

Scanning Transmission Electron Microscopy in a
Scanning Electron Microscope: Electron-Beam
Broadening, Contamination,
and Investigation of ZIF-8 by Correlative Electron
Microscopy

Zur Erlangung des akademischen Grades einer
DOKTORIN DER NATURWISSENSCHAFTEN (Dr. rer. nat.)

von der KIT-Fakultät für Physik des
Karlsruher Instituts für Technologie (KIT)
angenommene

DISSERTATION

von

M. Sc. Milena Hugenschmidt

Tag der mündlichen Prüfung: 04. Februar 2022

Referentin: Prof. Dr. Dagmar Gerthsen
Korreferent: Prof. Dr. Hans-Joachim Kleebe



This document is licensed under a Creative Commons Attribution-ShareAlike 4.0 International License (CC BY-SA 4.0): <https://creativecommons.org/licenses/by-sa/4.0/deed.en>

Contents

Constants, Symbols, and Acronyms	i
1. Introduction	1
2. Fundamentals	3
2.1. Electron-Sample Interactions	3
2.1.1. Single Scattering	6
2.1.2. Multiple Scattering and Diffusion	9
2.1.3. Electron Diffraction	13
2.1.4. Beam Damage	14
2.2. Electron Microscopy	16
2.2.1. Transmission Electron Microscopy (TEM)	17
2.2.2. Scanning Electron Microscopy (SEM)	26
2.2.3. Scanning Transmission Electron Microscopy (STEM)	30
2.2.4. STEM-in-SEM (TSEM)	34
3. Instrumentation and Methods	39
3.1. Transmission Electron Microscopes	39
3.2. Scanning Electron Microscopes	40
3.2.1. STEM Measurements in STEM-in-SEM	40
3.2.2. Quantitative Intensity Measurements	42
4. Beam Broadening	47
4.1. Introduction to Beam Broadening	47
4.2. Fundamentals of Beam Broadening	49
4.2.1. Definition of Beam Broadening	49
4.2.2. Theoretical Description of Beam Broadening	50
4.3. Experimental Methods	56
4.3.1. Simulation of the Angular Distribution of Scattered Electrons	57
4.3.2. Sample Preparation	57
4.3.3. Determination of Beam Broadening	58
4.3.4. Error Analysis	61
4.4. Results and Discussion	63
4.5. Summary	68

5. Electron-Beam-Induced Carbon Contamination	69
5.1. Introduction to Carbon Contamination	70
5.2. Fundamentals of the Contamination Process	72
5.2.1. Processes and Parameters	72
5.2.2. Theoretical Description of Contamination	82
5.2.3. Cleaning Strategies	85
5.3. Measurement and Quantitative Evaluation of Contamination	86
5.3.1. Requirements Regarding the Experimental Setup	87
5.3.2. Preparation of Carbon Support Films	88
5.3.3. Measurement Setup	89
5.3.4. Contamination-Mitigation and Sample-Cleaning Strategies	91
5.3.5. Monte Carlo Simulations	93
5.3.6. Imaging and Evaluation of Image Data	96
5.3.7. Error Estimation	98
5.4. Results: Influence of Imaging Parameters and Characteristics of Contamination Growth	99
5.4.1. aC Films	99
5.4.2. Contamination Thicknesses	101
5.4.3. Influence of Imaging Parameters	107
5.4.4. Contamination Morphology	116
5.4.5. TEM-like Contamination: Comparison with Theory	118
5.5. Results: Cleaning Strategies	121
5.5.1. Beam Showering	121
5.5.2. Sample Baking	125
5.5.3. Plasma Cleaning	125
5.5.4. Comparison of Contamination-Mitigation Strategies	126
5.6. Summary	128
6. Direct Synthesis and Subsequent Analysis of ZIF-8 on TEM Grids	131
6.1. Introduction to MOFs and ZIF-8	132
6.2. Fundamentals: Electron Microscopy of MOFs	134
6.2.1. Preparation for TEM	134
6.2.2. Beam Sensitivity	135
6.3. Methods	135
6.3.1. Synthesis	135
6.3.2. Analysis by Electron Microscopy	137
6.4. Results and Discussion	141
6.4.1. Morphology	141
6.4.2. Crystallinity	147
6.4.3. Nanoparticle Incorporation	150
6.5. Summary	153

7. Summary	155
Bibliography	167
Publications and Conference Contributions	189
Instrumentation List	193
Appendix	195
A. Cross-Section for Scattering through Angles Larger than θ^*	195
B. Detector Correction in Monte Carlo Simulations	196

Physical Constants

a_{H}	$=$	$5.291\,772\,109\,03(80) \cdot 10^{-11} \text{ m}$	Bohr radius ¹
k_{B}	$=$	$1.380\,649 \cdot 10^{-23} \text{ J K}^{-1}$	Boltzmann constant
e	$=$	$1.602\,176\,634 \cdot 10^{-19} \text{ C}$	Elementary charge
ϵ_0	$=$	$8.854\,187\,812\,8(13) \cdot 10^{-12} \text{ A s V}^{-1} \text{ m}^{-1}$	Vacuum electric permittivity
h	$=$	$6.626\,070\,15 \cdot 10^{-34} \text{ Js}$	Planck constant
N_{A}	$=$	$6.022\,140\,76 \cdot 10^{23} \text{ mol}^{-1}$	Avogadro constant

¹The reference for all physical constants is the NIST Reference on Constants, Units, and Uncertainty [Tie+20].

Symbols

A	Atomic mass
α	Beam (semi-) convergence angle
$A(\vec{u})$	Aperture function
$A(x, y)$	Wave amplitude
b	Beam broadening
β	Electron source brightness
\vec{B}	Magnetic field
c	Geometrical correction factor for the HAADF-STEM detector
C_c	Chromatic aberration coefficient
χ	Phase shift from the objective lens
C_s	Spherical aberration coefficient
d	Interplanar lattice spacing
Δ	Defocus spread due to C_c
δ	SE yield
Δf	Defocus value
D	Diffusion constant
d_{probe}	Electron probe diameter
E	Electron energy
E_0	Primary electron energy
E_{des}	Desorption energy
\vec{E}	Electric field

$E(\vec{u})$	Envelope function
$f(x, y)$	Specimen function
$g(\vec{r})$	Image function
H	Hurst exponent of anomalous diffusion
$h(\vec{r})$	Point-spread function
$H(\vec{u})$	Contrast transfer function
I	Electron beam current
I_b	STEM black-level intensity
I_{rel}	Relative intensity
I_0	STEM intensity of the incident electron beam
j	Current density
J	Mean ionization potential
λ	Wavelength
Λ	Mean free path length
Λ_{el}	Elastic mean free path length
l_{pd}	Distance between pole piece and STEM detector
m	Mass
n	Number of scattering events
$n(\vec{r}, T)$	Areal density of contaminants, depending on the position and time
ν	Adsorption constant
N	Number of atoms per unit volume

$d\Omega$	Solid angle into which the electron is scattered
$\phi(x, y)$	Wave phase
P_l	Legendre polynomials
P	Partial pressure
R	Fraction of overall intensity included in the beam diameter and scattering angle θ^*
r	Radius
ρ	Material density
\vec{r}	Position vector
σ_c	Cross-section for the decomposition and cross-linking of contaminants
σ_d	Cross-section for electron-beam-driven desorption
σ_{diss}	Dissociation cross-section
σ_{ion}	Ionization cross-section
σ_q	Dose <i>or</i> surface charge density
$\sigma_{\text{t,el}}$	Total elastic screened Rutherford cross-section
σ	Total scattering cross-section
$\sin(\chi)$	Phase contrast transfer function
$S_1(\theta)$	Single-scattering function
S	Sticking coefficient
$S(E)$	Stopping power, depending on the electron energy
τ_0	Residence time
t_c	Contamination thickness
\bar{t}_c	Mean contamination thickness
ϑ	Temperature
θ	Scattering angle
θ_B	Bragg angle

θ^*	Scattering angle that contains the R fraction of the overall intensity
θ_0	Screening angle
t	(Sample) thickness
T	Time, irradiation time
u_0	Point resolution
U	Acceleration voltage
u	Spatial frequency
\vec{u}	Reciprocal lattice vector
\vec{v}	Velocity
Φ	Work function
x	Mass thickness
(x, y)	Spatial coordinates
Z	Atomic number

Acronyms

ABSF	Average background subtraction filter
aC	Amorphous carbon
ADF	Annular dark field
AE	Auger electron
AFM	Atomic force microscopy
Au	Gold
Be	Beryllium
BF	Bright field
BS	Beam showering
BSE	Backscattered electrons
C	Carbon
C ₃ H ₈	Propane
CCD	Charge-coupled device
CHNX	Elemental analysis in organic chemistry of the ratio of C, H, N, and others (X), often by combustion
CMOS	Complementary metal-oxide-semiconductor
CTF	Contrast transfer function
Cu	Copper
DDEC	Direct-detection electron-counting
DF	Dark field
DP	Diffraction pattern
EBID	Electron-beam-induced deposition
EDXS	Energy-dispersive X-ray spectroscopy
EELS	Electron energy loss spectroscopy
EFTEM	Energy-filtered transmission electron microscopy
ETD	Everhart-Thornley detector
FEG	Field emission gun
FIB	Focused ion beam

FT	Fourier transform
FWHM	Full width half maximum
Ga	Gallium
Ge	Germanium
HAADF	High-angle annular dark field
HAADFp	DFa-c and HAADF detector at the Strata microscope
HRTEM	High-resolution transmission electron microscopy
ICE	In-chamber electron detector (similar to ETD)
iDPC	Integrated differential phase-contrast
KIT	Karlsruhe Institute of Technology
lbl	Layer-by-layer
LEM	Laboratory for Electron Microscopy
Low-energy STEM	<i>see</i> STEM-in-SEM
MC	Monte Carlo
MgO	Magnesium oxide
MOF	Metal-organic framework
NBED	Nano-beam electron diffraction
nMAE	Normalized mean average error
NP	Nanoparticle(s)
PC	Plasma cleaning
PCA	Principal component analysis
PCTF	Phase contrast transfer function
Pd	Palladium
PE	Primary electrons
RD	Rhombic dodecahedon
ROI	Region of interest
SAD	Selected-area diffraction
SE	Secondary electrons
SEM	Scanning electron microscopy
Si	Silicon
Si ₃ N ₄	Silicon Nitride

SNR	Signal-to-noise ratio
SR-CS	Differential screened Rutherford cross-section
SrTiO ₃	Strontium Titanate
STD	Standard deviation
STEM	Scanning transmission electron microscopy
STEM-in-SEM	Scanning transmission electron microscopy in SEM
SURMOF	Surface-anchored metal-organic framework
TEM	Transmission electron microscopy
TLD	Through-lens detector
TSEM	<i>see</i> STEM-in-SEM
WD	Working distance
WPOA	Weak phase-object approximation
XRD	X-ray diffraction
ZIF	Zeolitic imidazolate framework

Chapter

1. Introduction

The microscope is one of the few technical instruments with its own stellar constellation. Although *microscopium* is rather unspectacular, it hints towards the enormous value of the microscope for science. Microscopy bridges the scales from the world that our eyes can resolve down to the hidden atomic structure of matter.

Knoll and Ruska built the first transmission electron microscope in 1932 [KR32]. The first scanning transmission electron microscope by Ardenne followed in 1938 and again imaged electron-transparent specimens [Ard38]. In 1942, Zworykin, Hiller, and Snyder described a scanning electron microscope that allowed the studying of solid surfaces [Oat82]. In the decades since then, transmission electron microscopy and scanning transmission electron microscopy reached atomic resolution. The scanning electron microscope was mostly used for solid samples, with its ability to generate 3D-like images of their topography and a large number of different available detectors.

In recent decades, the transmission mode in scanning electron microscopy (SEM) is re-emerging. Already in 1968, Crewe, Wall, and Welter described the use of a commercial SEM instrument in transmission mode. The resolution and contrast of the technique was discussed by Kimoto and Hashimoto in the same year [KH68]. However, it was not used frequently at that time since the resolution was much poorer compared to transmission electron microscopy (TEM), and the setups were custom-made [KBF12; KH68; Cal+18; SBS69; CL70]. With improved electron optics and electron guns, and commercially available scanning transmission electron microscopy (STEM) detectors, transmission imaging in SEM has been greatly improved and is now more commonly used [Cal+18; van+07].

The transmission mode in SEM is often abbreviated as low-keV STEM, TSEM (transmission scanning electron microscopy) or, more precisely, STEM-in-SEM, to distinguish it from regular STEM [KBF12]. The advantages of STEM-in-SEM lie in the lower cost of ownership compared with “dedicated” STEM, more straightforward operation, larger field of views, more flexibility in sample handling, the large number of different detectors, and enhanced contrast generation for light materials due to the lower electron energies [Gui+04; KBF12; Sun+20].

However, two obstacles of electron microscopy are amplified at the lower SEM energies (typically ≤ 30 keV): Electron-beam broadening and carbon contamination. The former describes the widening of the focused electron beam in the sample due to electron-sample interactions, which degrades the spatial resolution of imaging and spectroscopy [Rei98; HS19]. After the fundamentals and basic methods of this work were illustrated in Chapter 2 and 3, Chapter 4 will focus on beam broadening. A recent theoretical model based on anomalous diffusion allows calculating beam broadening for a range of materials, sample thicknesses, and electron energies [GR16]. It has been tested for thin carbon films but the applicability to other samples remained an open question [Dre+17]. This question is tackled by an extensive experimental STEM-in-SEM study of beam broadening depending on the electron energy and the sample material and comparison of this data set with the theoretical model.

Electron-beam-induced carbon contamination impedes the imaging process as the contamination growing under the electron irradiation covers structures of interest, distorts chemical analyses of the sample by energy-dispersive X-ray spectroscopy (EDXS, also abbreviated as EDS or EDX) and electron energy loss spectroscopy (EELS), and can lead to charging problems, especially at low electron energies [Ege19; Hei63; Rei98]. Although carbon contamination was the subject of many studies in the past, its systematical investigation in STEM-in-SEM is still missing. A reproductive approach to test the contamination growth and understand the influence of different parameters is needed. Chapter 5 presents a workflow for quantitative STEM-in-SEM measurements of carbon contamination depending on different imaging parameters. The concept of measurements is then employed to test the effect of contamination-mitigation strategies. After mainly theoretical reflections on the contamination process, the chapter will end by deriving practical tips for contamination reduction.

The third topic of this dissertation was investigated within the excellence cluster 3DMM2O (3D matter made to order) and thus focuses on a different, material-related topic: The metal-organic framework ZIF-8 [Par+06b] (Chapter 6). By a newly-developed synthesis technique, we have grown it surface-mounted on electron-transparent carbon films on typical TEM sample grids. This technique aims to enable STEM and TEM studies of pristine surface-mounted ZIF-8, which is usually synthesized on bulk support from which it needs to be removed in a potentially damaging process. The question of whether the synthesis and the intended incorporation of nanoparticles is successful was answered by a combination of electron microscopy techniques. The study of morphology and development during synthesis by SEM and STEM-in-SEM is complemented by high-resolution TEM and diffraction investigations of the material's crystallinity, 3D-reconstruction, and chemical analysis by EDXS that altogether give a comprehensive picture of the surface-mounted ZIF-8 material.

Chapter

2.

Fundamentals

This chapter provides an overview of the basics of this work. It starts with the interaction processes between the electron beam and the sample and the signals and artifacts that they produce. The second part focuses on the different microscopy techniques that were used to obtain the results described in the result chapters (Chapter 4 - Chapter 6). The design of electron microscope types and the generation of image contrasts are discussed. More specific basics and state of knowledge regarding the topics beam broadening, carbon contamination, and ZIF-8 are given in the result chapters.

2.1. Electron-Sample Interactions

As the beam electrons pass the sample, they can undergo several interactions with it. Many of the generated signals can be used for analysis in electron microscopes and give us a wide range of information, for instance, on the morphology, the composition, and the crystallinity of the sample. A straightforward interpretation of the signals is not always possible, as often a number of the sample's properties influence one signal simultaneously. Understanding signal generation by theoretical descriptions and simulations is therefore essential for interpreting the images produced by electron microscopes.

The electrons in the primary electron beam are called primary electrons (PE). When such a beam propagates through a sample, the electrons interact with it and are scattered in different directions or stimulate secondary signals. Figure 2.1 shows the possible signals that are emitted from the specimen. Those that are important in this work are highlighted in blue. Some transmitted electrons have kept the incident direction, without or with very little interaction with a thin specimen; others have experienced different scattering processes. Some electrons leave the specimen in forward direction (scattering angle $< 90^\circ$). On the upper side of the specimen, backscattered electrons (BSE, scattering angle $> 90^\circ$) and other characteristic signals can be found: Secondary electrons (SE) are differentiated from the BSE by defining their energy as < 50 eV [Rei98]. When the electrons change their direction, they also generate Bremsstrahlung X-rays, which are typically not a valuable signal

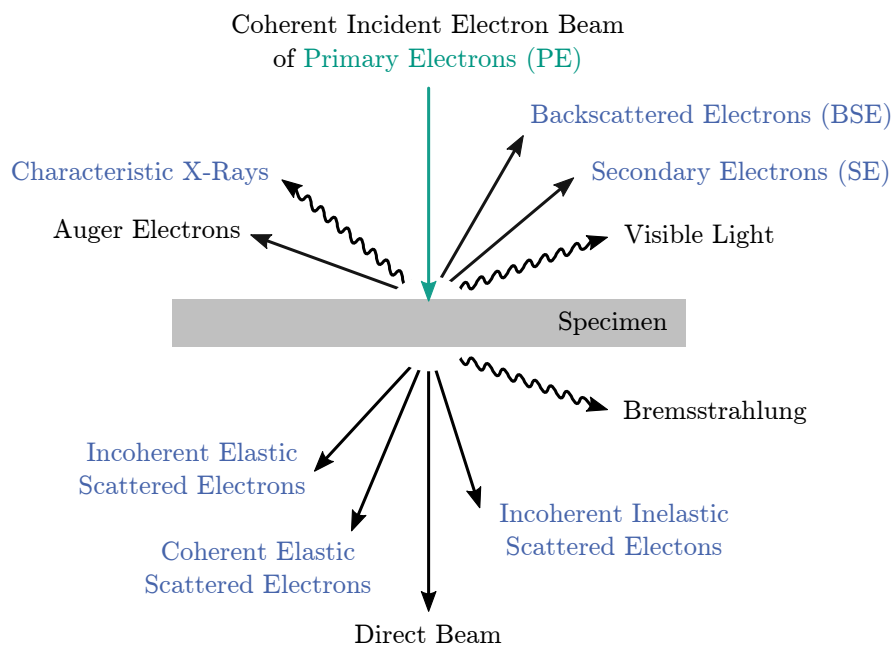


Figure 2.1. Signals generated by the interaction between the specimen and the electron beam [WC09]. The signals which are relevant for this work are highlighted in blue.

for material sciences [WC09]. Characteristic X-rays arise when the beam electrons excite inner-shell electrons of atoms to states with higher energy. When they relax, photons with characteristic energy can be emitted and used by EDXS. The energy may also be transferred to another atomic electron that leaves the specimen as an Auger electron (AE). This process is called Auger-Meitner effect. Both signals can be used to identify the material's composition [Rei98]. Lastly, the interaction of beam electrons with the specimen can also cause the emission of visible light [WC09].

Figure 2.2 shows a scheme of the energy distribution of electrons measured above a relatively thick sample. The maximum measured energy is the energy of the PE. Apart from the signals described above, plasmon losses are marked. They arise when plasmons, collective longitudinal charge-density waves of the sample's electrons, are excited. The peak of the SE is in the range of 2 – 5 eV [Rei98].

Figure 2.1 shows a distinction of transmitted electrons in four main types. It is not enough to only see electrons as particles to understand this distinction, but a property of waves, the coherence, becomes essential. Electron waves are called coherent if they have a well-defined phase relationship and are able to interfere [Rei98; HS19]. Electron sources are designed to make the incident beam as coherent as possible. The electrons transmitted through a thin specimen undergo different scattering processes that can be understood by thinking about electrons in terms of particles *and* waves. Electrons, which maintain their propagation direction (0° scattering angle) belong to the direct beam [WC09]. Elastically scattered electrons change

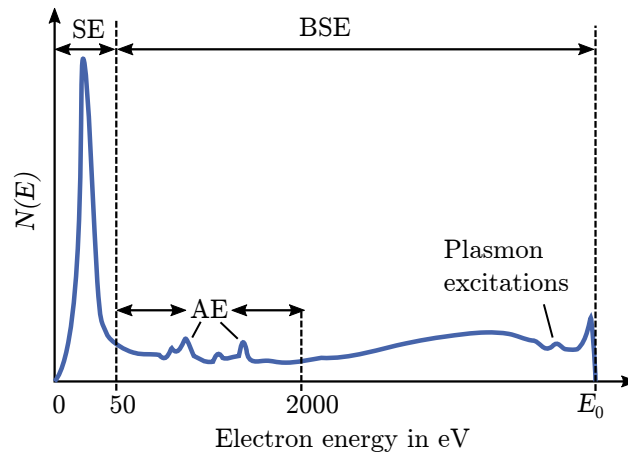


Figure 2.2. Schematic energy spectrum of electrons emitted from a bulk sample. It shows the number of electrons $N(E)$ as a function of their energy. The spectrum contains contributions from secondary electrons (SE) with $E < 50$ eV, backscattered electrons (BSE), peaks from Auger electrons and plasmon excitations (after [Rei98]).

their propagation direction to typically relatively low angles but do not lose energy. The elastically scattered electrons are usually coherent if the specimen is thin and crystalline. The higher the scattering angle, the more coherence is lost, and the electrons become incoherent. On the other hand, inelastically scattered electrons change their direction and lose some of their kinetic energy in the scattering process. They are usually incoherent and occur at very low scattering angles, apart from phonon-scattered¹ electrons [WC09]. Similar to the distinction between particles and waves, “scattering” describes an interaction between a particle (electron) and the specimen. “Diffraction” describes the interaction of a wave with an object. Electrons can undergo multiple scattering events, especially in thicker specimens. A general rule is that the total scattering angle increases with the number of scattering events. So when the specimen gets thicker, fewer electrons are in the direct beam or forward scattered, and more are backscattered [WC09].

Elastic and inelastic scattering processes lead to a zig-zag electron path in the sample until it leaves the sample or is absorbed [Rei98]. This is shown in Figure 2.3, representing a selection of the interactions in a bulk sample, which is the typical case in an scanning electron microscope. Due to their low energy, SE can only escape from the sample’s surface. Those that are produced by the PE stem from close vicinity of the incident beam and are called SE 1. SE 2, produced by BSE, are less localized since they can come from a larger distance from the incident beam. SE 3 (not shown in Figure 2.3) are electrons that are generated by BSE from the sample that hit surfaces in the microscope chamber, leading to SE production there. Hence, they do not carry information of the sample [Gol+18].

¹Phonons are collective oscillations of atoms in a solid, equivalent to heating the sample.

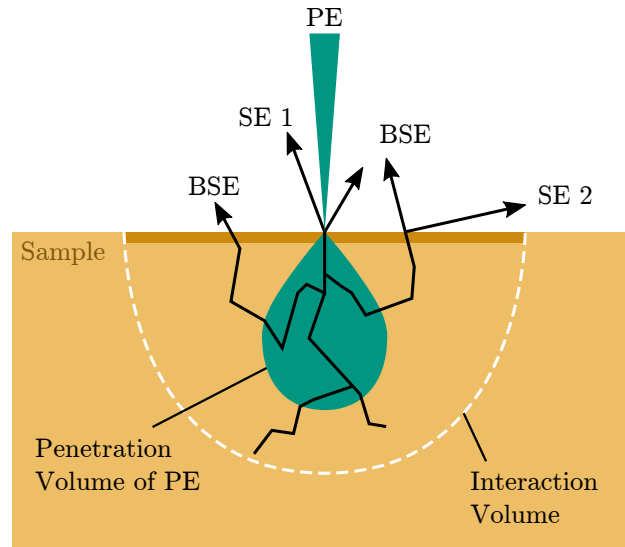


Figure 2.3. Schematic representation of the interaction volume from which signals emerge and the teardrop-shaped penetration volume of the PE. The area from which SE leave the sample is marked in a darker color (after [Rei98]).

2.1.1. Single Scattering

In the most straightforward case of single scattering, the electron undergoes only one interaction with the sample's atoms. Single scattering is described as the scattering of one electron in the potential of an atom. In the case of elastic scattering it is assumed that the electron only changes its initial direction, but no energy is transferred to the atom. In reality, there will always be a small energy transfer. If the energy transfers are considered, we speak about inelastic scattering [WC09].

2.1.1.1. Elastic Scattering

Scattering can only be described precisely by quantum mechanics. However, the scattering model by Rutherford, based on classical mechanics, is widely used and often precise enough. Geiger and Marsden found an unexpected reflection of alpha particles in thin metal plates in 1909 [GM09]. From this result, Rutherford deduced a theory of scattering of alpha radiation (helium nuclei) and beta radiation (electrons) in matter in 1911 [Rut11]. He assumed that scattering to angles larger than 1° is caused by scattering at the atom nucleus. The Rutherford model treats the electron as a particle with mass $m_e = 9.109 \cdot 10^{-31}$ kg and charge $-e = 1.602 \cdot 10^{-19}$ C, passing the nucleus in a distance b (Figure 2.4). The nucleus is considered as a particle with charge $+Ze$, remaining in rest due to its bigger mass. Z is the atomic number. The interaction of the electron with the electrons of the atomic shell is

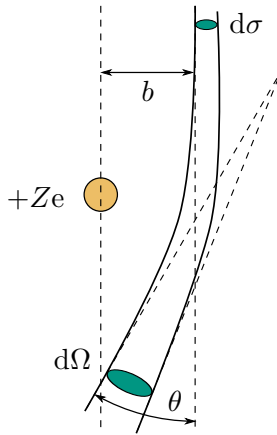


Figure 2.4 Visualization of elastic scattering at an atom. Electrons that pass the nucleus through area $d\sigma$ in distance b are scattered through an angle θ to a solid angle $d\Omega$.

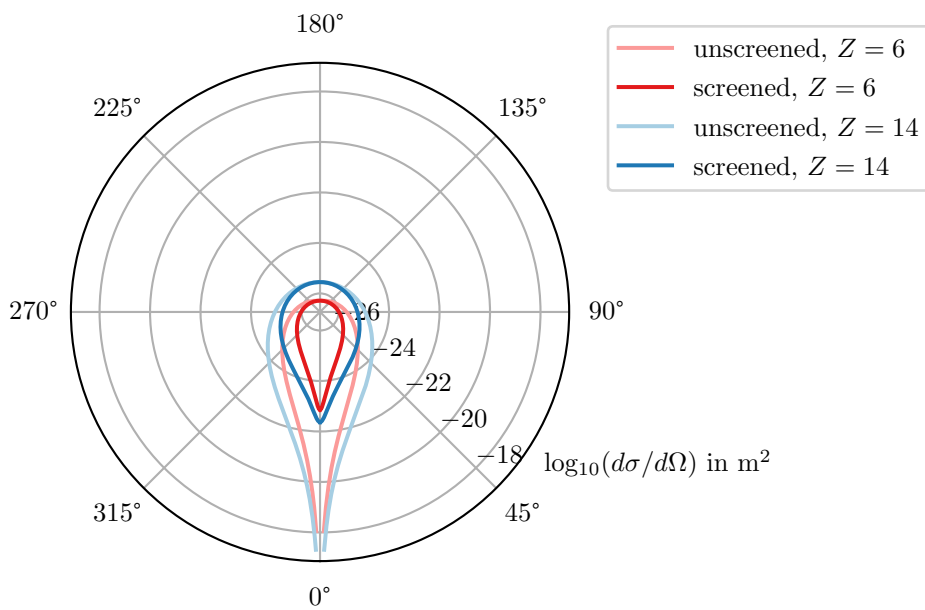


Figure 2.5. Comparison of the differential unscreened and screened Rutherford cross-section, Equation (2.2) and Equation (2.3), at 30 keV for Carbon ($Z = 6$) and Silicon ($Z = 14$).

neglected. The electron is then attracted to the atom by the Coulomb force

$$\vec{F} = -\frac{e^2 Z}{4\pi\epsilon_0 r^2} \vec{u}_r . \quad (2.1)$$

ϵ_0 is the vacuum permittivity, and \vec{u}_r denotes a radial unit vector. This attractive force results in a hyperbolic trajectory of the electron (Figure 2.4) [Rei98]. The differential elastic Rutherford cross-section by an unscreened nucleus results from this interaction. It describes the scattering at the nucleus to a solid angle $d\Omega$ [Rei98]

$$\frac{d\sigma}{d\Omega} = \frac{e^4 Z^2}{4(4\pi\epsilon_0)^2 \underbrace{m^2 v^4}_{4E_0^2} \sin^4(\theta/2)} , \quad (2.2)$$

with e being the elementary charge, Z the atomic number of the atom (average atomic number in a compound), ϵ_0 the vacuum permittivity, m the mass of the electron, \vec{v} the speed of the electron and θ the scattering angle (see Figure 2.4). The screening of the nucleus' charge by the electrons of the atom is neglected here, as it does not have a big influence if the beam electrons pass the nucleus at a small distance. But if the electrons pass in a larger distance, the long-range Coulomb field of the unscreened nucleus causes the unscreened Rutherford cross-section to diverge at $\theta \rightarrow 0$, as shown in Figure 2.5 [Rei98].

The singularity can be avoided by taking the screening effect into account. The charge of the nucleus is “shielded” by the electron shell, making the nucleus less visible for beam electrons that pass the atom in a larger distance b . Thus screening is only important if the electron passes far from the nucleus, in which case the scattering angles are small [WC09]. The differential screened Rutherford cross-section (SR-CS) take screening into account by introducing the screening angle θ_0 [Rei98]:

$$\frac{d\sigma}{d\Omega} = \frac{e^4 Z^2}{4(4\pi\epsilon_0)^2 m^2 v^4} \frac{1}{[\sin^2(\theta/2) + \sin^2(\theta_0/2)]^2} . \quad (2.3)$$

The screening angle θ_0 is defined as

$$\sin(\theta_0/2) \simeq \theta_0/2 = \frac{\lambda}{4\pi R} \quad (2.4)$$

with the Planck constant h , $R = a_H Z^{-1/3}$ denoting the screening radius of the atom, and the Bohr radius $a_H = h^2 \epsilon_0 / \pi m e^2 = 0.0529 \text{ nm}$ [Rei98; Tie+20]. Finally, Equation (2.4) includes the de Broglie wavelength λ

$$\lambda = \frac{h}{mv} . \quad (2.5)$$

which becomes

$$\lambda = \frac{h}{\sqrt{2m_0 eV \left(1 + \frac{eV}{2m_0 c^2}\right)}} , \quad (2.6)$$

including relativistic effects [WC09, p. 14]. When the scattering angle is $< \theta_0$, the scattering cross-section is modified and has no singularity at small scattering angles θ (Figure 2.5). For $\theta > \theta_0$ the electron-electron interactions become less relevant, and scattering can again be described by the pure electron-nucleus interactions in the unscreened Rutherford cross-section (Equation (2.2)).

The Rutherford cross-sections neglect relativistic effects and spin-orbit coupling. Therefore, they show deviations from the experimental results for high electron

energies and higher atomic numbers ($Z > 30$) [WC09]. Relativistic effects and spin-orbit interaction are considered in the exact Mott cross-sections after Mott and Massey [MM65]. They are derived from the numerical solution of the relativistic Schrödinger or Pauli-Dirac equations. Although being more precise, the drawback of Mott cross-sections is that they are no analytic equations but numerical values that have to be calculated [Czy+90]. The results are similar to the screened Rutherford cross-section for low atomic numbers, large electron energies, and large scattering angles. However, for low electron energies and high atomic numbers, the results differ strongly [Rei98].

2.1.1.2. Inelastic Scattering

Inelastic scattering gradually reduces the electron energy. It usually leads to lower scattering angles than elastic scattering [HS19]. The energy of the beam electrons can be high enough to excite atomic electrons to higher energy states (inter-band transitions) and cause X-ray emission. Other interactions are the excitation of Plasmons and Phonons. The transferred energy can even be high enough to kick an electron out of the atomic shell which ionizes the atom. A special case of ionization is Compton scattering, quasi-free collisions between electrons that occur when the binding energy of the atomic electron is small compared to the transferred energy [Gol+18; Rei98; WC09].

In short, there are two main groups of inelastic interactions:

- Electron- and X-ray-generating electron-electron interactions (band transitions, ionization of atoms, Auger-Meitner effect), and
- interactions with the atoms in the solid as a whole (Plasmons and Phonons).

Those processes cause characteristic energy losses that can be measured in electron energy loss spectra [Rei98]. They contain information about the chemistry and electronic structure of the sample. The amount of energy lost by ionization is specific for each element and the ionized shell. Free inner shells are refilled by electrons from higher shells, which emit the energy difference as an X-ray photon. These characteristic X-rays are used in EDXS to analyze the composition of samples. The energy loss by ionization of the innermost K-shell in the atom depends on the element and ranges from 0.11 keV for Be to 80 keV for Au [Rei98].

2.1.2. Multiple Scattering and Diffusion

The beam electrons usually experience more than one scattering event in the specimen. The average distance that each electron travels between two scattering events

is the mean free path length Λ . Neglecting energy loss, the elastic mean-free path length Λ_{el} is [Rei98]

$$\Lambda_{\text{el}} = \frac{1}{N\sigma_t} = \frac{A}{N_A\rho\sigma_t} \quad (2.7)$$

with the number of atoms per unit volume $N = N_A\rho/A$ and the total elastic screened Rutherford cross-section $\sigma_{\text{t,el}}$ [Rei98]:

$$\sigma_{\text{t,el}} = \int_0^\pi \frac{\partial\sigma}{\partial\Omega} \sin\theta d\theta \quad (2.8)$$

$$= \frac{e^4}{\pi(4\epsilon_0)^2} \left(\frac{Z}{E_0}\right)^2 \frac{1}{\left(1 + \sin^2\left(\frac{\theta_0}{2}\right)\right)^2 - 1} \quad (2.9)$$

$$\simeq \frac{e^4}{\pi(4\epsilon_0)^2} \left(\frac{Z}{E_0}\right)^2 \frac{1}{\theta_0^2}, \quad (2.10)$$

by using Equation (2.3) and the approximations $\sin(\theta_0/2) \approx \theta_0/2$ and $\theta_0^4 \approx 0$ for small θ_0 . The integral is evaluated by using the substitution $u = \cos(\theta) \Leftrightarrow \sin(\theta)d\theta = -du$. Inserting $\sigma_{\text{t,el}}$ into Equation (2.7), the elastic mean-free path length becomes

$$\Lambda_{\text{el}} = \left(\frac{E_0\theta_0}{Z}\right)^2 \frac{A}{\rho N_A} \frac{(4\pi\epsilon_0)^2}{\pi e^4}. \quad (2.11)$$

The assumption of negligible energy loss holds for thin and electron-transparent specimens. However, multiple inelastic scattering events in thicker and bulk samples cause a gradual energy loss of the electron energy, which reduces the mean-free path length until the electron is absorbed or leaves the sample. The maximum penetration depth, the electron range, depends on the initial electron-beam energy E_0 and sample properties, like composition and material density [MHG20]. The intensity I of the direct beam in a simplified expression is

$$I = I_0 e^{-N\sigma t}, \quad (2.12)$$

with the sample thickness t , the initial intensity I_0 of the beam and the total scattering cross-section σ that comprises all elastic and inelastic scattering events [Rei98]. The number of scattering events

$$n = \frac{t}{\Lambda} = tN\sigma, \quad (2.13)$$

with the total mean-free path length Λ , is used to define different scattering regimes: n is 0 or 1 in the case of no or single scattering, $1 < n < 25$ for plural scattering, and $n \geq 25$ for multiple scattering [Rei98]. Finally, the diffusion regime is reached when the beam electrons scatter isotropically [MHG20].

Continuous-slowng-down approximation The energy lost by an electron while traveling through the sample can be calculated by the stopping power $S(E)$, also called Bethe equation, which describes a continuous-slowng-down approximation

$$S = \frac{dE}{ds} = \frac{4\pi e^4 N_A \rho Z}{(4\pi\epsilon_0)^2 A m_0 v^2} \ln \frac{m_0 v^2}{J} . \quad (2.14)$$

This is an energy loss dE per traveled path ds , with the mean ionization potential J of the material [Bet; Rei98]. The following expression is sufficient for non-relativistic energies

$$\frac{dE}{ds} = 785 \frac{\rho Z}{A} \frac{1}{E} \ln \left(1.166 \frac{E_0}{J} \right) \text{ eV } \text{Å}^{-1} \quad (2.15)$$

with E_0 and J in eV. The mean ionization potential J increases with increasing Z and is approximated in the empirical fit

$$J = \left(9.76Z + 58.8Z^{-0.19} \right) \text{ eV} \quad \text{for } Z \geq 13 , \quad (2.16)$$

$$J = 11.5Z \text{ eV} \quad \text{for } Z < 13 , \quad (2.17)$$

which does not depend on the primary electron energy E_0 [BS64; JL89; Rei98]. The energy-dependence was added by Joy and Luo, who replaced J in Equation (2.15) by a new expression J'

$$J' = \frac{J}{1 + kJ/E_0} , \quad (2.18)$$

where k is a material-dependent factor ranging from 0.77 for C to 0.85 for Au [JL89].

Angular distribution of electrons The profile of the electron beam within the sample, or the beam profile at the exit surface of a thin specimen, is determined by all scattering events that the beam has experienced. The calculation of electron's angular distribution starts with the intensity $I_1(\theta)$ scattered into a solid angle $d\Omega$ by a single scattering event

$$I_1(\theta)d\Omega = I_0 N t \frac{d\sigma}{d\Omega} d\Omega = I_0 \frac{t}{\Lambda} S_1(\theta)d\Omega, \quad (2.19)$$

with the incident intensity I_0 , the number of atoms per unit area Nt , the differential scattering cross-section $d\sigma/d\Omega$, and the newly defined single-scattering function $S_1(\theta) = (1/\sigma)d\sigma/d\Omega$ with $\int S_1(\theta)2\pi \sin(\theta)d\theta = 1$ (see Equation (2.13)) [Rei98]. The scattering function of m scattering events is an m -times convolution (\otimes) of the single

scattering function

$$S_m(\theta) = S_{m-1}(\theta) \otimes S_1(\theta) . \quad (2.20)$$

Calculating the angular distribution after passing a sample of thickness t with n scattering events first requires the definition of the Poisson coefficients $\Pi_m(n)$ [Rei98]. They give the probability of m -fold scattering in a film of thickness t with a mean number n of scattering events

$$\Pi_m(n) = \frac{n^m}{m!} e^{-n} \quad \text{with} \quad \sum_{m=0}^{\infty} \Pi_m(n) = 1 . \quad (2.21)$$

The angular distribution after passing a sample thickness t with a mean number $n = t/\Lambda$ of scattering events is then

$$I(\theta)d\Omega = I_0d\Omega \sum_{m=0}^{\infty} \Pi_m(n) S_m(\theta) . \quad (2.22)$$

This expression is numerically evaluated by developing the single-scattering function $S_1(\theta)$ in a series of Legendre polynomials P_l [GS40; Rei98]

$$S_1(\theta)d\Omega = \frac{d\Omega}{4\pi} \sum_{l=0}^{\infty} (2l+1) a_l P_l(\cos\theta) \quad \text{with} \quad a_l = \int_0^\pi S_1(\theta) P_l(\cos\theta) 2\pi \sin\theta d\theta . \quad (2.23)$$

This allows evaluating the convolution in Equation (2.20) which results in

$$S_m(\theta)d\Omega = \frac{d\Omega}{4\pi} \sum_{l=0}^{\infty} (2l+1) a_l^m P_l(\cos\theta) . \quad (2.24)$$

The angular distribution in Equation (2.22) thus becomes

$$I(\theta)d\Omega = I_0 \frac{d\Omega}{4\pi} \sum_{l=0}^{\infty} (2l+1) e^{-n(1-a_l)} P_l(\cos\theta) , \quad (2.25)$$

which is the basis of the simulations based on the evaluation of the transport equation as described in Section 4.3.1 on page 57.

A facilitated result is retrieved if one assumes independence of successive scattering events and neglects large-angle scattering and energy losses:

$$I(\theta)d\Omega = I_0 \frac{d\Omega}{\pi\bar{\theta}^2} e^{-\theta^2/\bar{\theta}^2} \quad (2.26)$$

with the mean-square scattering angle

$$\bar{\theta}^2 = 1.2 \cdot 10^7 \frac{Z^{2/3}}{AE_0} x \text{ rad}^2 , \quad (2.27)$$

with E_0 in eV and the mass thickness x , defined as

$$x = \rho t , \quad (2.28)$$

in g/cm^2 [Rei98]. In this case, the transmitted intensity follows a Gaussian distribution.

2.1.3. Electron Diffraction

The previous discussion treated electrons as particles and ignored their wave nature. In the particle model, the crystallinity of the specimen is not relevant. However, the wave features phase and coherency are needed to describe diffraction in crystal lattices. If the number of scattering events that an electron undergoes in the specimen is small enough, its coherence is conserved and electron diffraction, an interference effect, occurs in crystalline specimens. Bragg and Bragg described diffraction in 1913 as reflections of X-rays in the crystal [BB13]. Even before, von Laue and others had the idea to investigate the crystalline structure of matter by using diffraction methods [Lau13; WC09]. Von Laue used the theory that was known from light-optics. It tells that two elementary waves of an incident wave front scattered at adjacent centers must have a path difference that is an integral multiple n of the wavelength λ for constructive interference. He derived three scattering conditions, the Laue equations, from this assumption (one for each dimension in space) [WC09]. The Braggs simplified the Laue equations by a model of scattering at adjacent lattice planes. The diffraction condition, known as Braggs' law, can be derived geometrically with Figure 2.6 [BB13]. The basic assumption is the same as von Laue's: The path difference between two waves that are diffracted at adjacent lattice planes must be an integral multiple n of the wavelength λ to make them interfere constructively. The path difference in the Figure is $\overline{AB} + \overline{BC}$ and equals $2d \sin \theta$ for a lattice plane distance d . The Bragg condition for constructive interference at these planes is thus

$$n\lambda = 2d \sin \theta_B \quad (2.29)$$

θ_B is the Bragg angle. It is a semi-angle, which is essential to keep in mind. Although the model is physically wrong, as there is no deflection of electrons at lattice planes, it is beneficial: When looking at Equation (2.29), it becomes clear that smaller lattice distances give rise to larger scattering angles. This reciprocal relationship allows interpreting diffraction patterns: As λ is known (by the electron energy) and θ_B can be measured, the lattice-plane distance is determined.

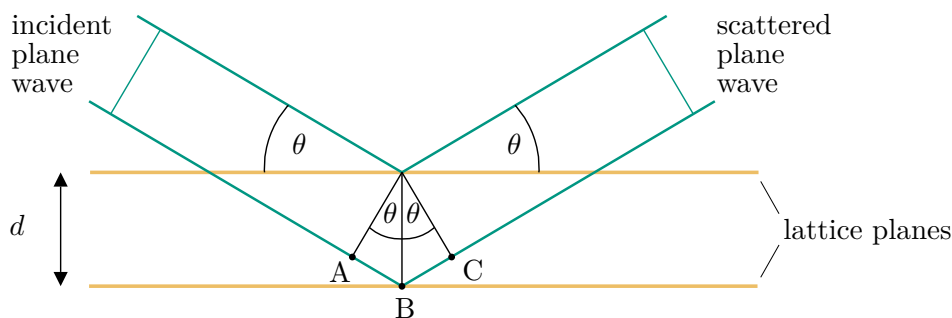


Figure 2.6. Bragg description of diffraction between two lattice planes after Williams and Carter [WC09].

2.1.4. Beam Damage

The interactions between the incident electron beam and the sample produce signals that allow the analysis of the sample. At the same time, the interacting electrons introduce artifacts. Typical types of sample damage by the electron beam are knock-on displacement, sputtering, ionization damage (radiolysis), charging, carbon contamination, etching, and sample heating by the electron beam [Ege19]. Strictly speaking, electron-beam-induced carbon contamination is not damaging the sample but hinders its examination as well. Chapter 5 is dedicated to carbon contamination, and the relevant basics are given there.

Knock-on displacement, also called knock-on damage, is the displacement of an atom in the sample by scattering. It occurs whenever an electron transfers an energy $E > E_d$ to an atom in the sample. E_d is the atomic displacement energy that determines the threshold energy E_0^{th} of primary electrons, below which knock-on damage does not occur. However, there is no sharp threshold in reality [Ege19]. The displacement and threshold energy depend on the position of the atom: They are higher for those in a compact crystal ($E_0^{\text{th}} = 150 - 1500 \text{ keV}$) than those atoms next to a pore or on an external surface ($E_0^{\text{th}} = 30 - 300 \text{ keV}$) [Ege19]. This lowered displacement energy at surfaces gives rise to the phenomenon of electron sputtering, the removal of atoms from the sample's surface [ER76; BZ89; CMS90]. Knock-on damage is the main damaging process in metals, conducting and inorganic specimens, while radiolysis dominates for poorly conducting samples [Ege19; Ege12].

Radiolysis occurs when an inelastic scattering event ionizes an atom, and the generated vacancy in the initial state of the atomic electron cannot be filled fast enough, such that chemical bonds are broken. Radiolysis is the primary damaging process in insulators and some semiconductors. While it is reduced at higher E_0 , knock-on damage behaves oppositely [Ege12; WC09]. The reduced knock-on damage at low electron energies motivated the development of transmission electron microscopes that provide atomic resolution at low electron energies [Kai+11]. However, radiolysis was identified as dominant for the metal-organic framework (MOF) ZIF-8

in TEM at 300 keV [Gho+19]. In a related class of porous materials, the zeolites, beam damage was found to be a superposition of radiolysis and knock-on damage, whereby the ratio depends on the primary electron energy. The lowest damage in TEM was observed for $E_0 = 80$ keV [Ugu+11]. The sensitivity of MOFs under electron irradiation is discussed in more detail in Section 6.2.2 on page 135.

Electric charging of the sample is induced by the escape of SE or BSE or by the absorption of beam electrons. It occurs when the sample is poorly conducting and the removed or implanted charges cannot be compensated [Ege19; Jia16a; JJ96]. The escape of SE usually charges insulating samples positively within the irradiated area, which can induce an opposite negative charge in the surrounding region [Ege19; RH18]. However, also negative charging (of carbon films) in the irradiated area has been observed and explained by the desorption of adsorbates [Het+18]. The induced electric field might not only disturb imaging (e.g., change in defocus in TEM [RH18]) but also may damage the sample [Jia16a; Jia16b].

In SE-SEM imaging of bulk samples, the scanned area may either look brighter than its surrounding, indicating a negative charging, or darker, indicating positive charging [JJ96]. This darkening can be misinterpreted as a built-up of contamination. Negative charging occurs at high primary electron energies, where more charges are injected into the sample than can escape due to the electron yield (SE and BSE) at increased energies [LJ05]. Positive charging occurs at lower energies when the yield is large enough to cause a net removal of charges from the sample. The sample does not charge in the special case where the injected and escaping charges balance out, and no contrast change is observed. This typically happens between 0.5 and 3 keV [JJ96; FMD94].

Chemical reactions induced by the electron beam can cause **etching** of the sample's surface. Section 5.2.1.3 in the chapter on carbon contamination gives some details on this topic.

The final beam damage mechanism to mention here is the **heating** of the sample by the electron beam the electron-induced excitation of phonons [WC09]. Heating does not necessarily damage the sample but can soften it in the case of polymers or melt it in extreme cases [Ege12; ELM04]. The rise of the sample temperature due to phonon excitation depends on the areal dose and is higher for a smaller beam diameter [ELM04]. Beam heating is usually a problem for high currents, but can also be worrisome at lower currents when the sample's thermal conductivity is low. It quickly reaches a steady-state and is usually insignificant: Egerton, Li, and Malac determined a temperature increase of ≤ 1.4 K of a carbon film irradiated with 5 nA at 200 keV. The beam diameter ranged from 1 μm to 1 nm [ELM04]. In SEM, the heat dissipation occurs in three dimensions and the temperature rises, again, by a few degrees, even for polymers, although most of the beam energy is deposited in the sample [ELM04; Rei98]. With scanning irradiation, the temperature increases

even less. However, the investigation of thin films in the SEM at energies ≤ 2 keV can lead to higher temperature rises if the total beam energy is deposited in the film since the heat flow is only two-dimensional. Again it is strongly reduced if the beam is scanned [ELM04].

2.2. Electron Microscopy

The history of light microscopy began with magnifying glasses in medieval times. Abbe formulated already in the 19th century that the wavelength of light restricts the spatial resolution of the classical visible-light microscope to around 300 nm, depending on the used wavelength [Abb73; WC09]. Electron microscopes go below this resolution limit since the wavelength of electrons is significantly smaller², which was described by de Broglie in 1927 [Bro27]. Today, electron microscopes are indispensable in life sciences, chemistry, geosciences, material sciences, and solid-state physics. The first transmission electron microscope of Knoll and Ruska in 1932 was the practical implementation of de Broglie's principle [KR32]. In a transmission electron microscope, a thin specimen is irradiated with an (ideally) parallel beam, which passes a system of projection lenses after the interaction with the specimen. They project the image of the specimen onto a fluorescence screen, an image plate, or a camera [WC09].

The first scanning electron microscope by Ardenne in 1938, which outperformed the resolution of classical visible-light microscopy, also used the transmission mode for imaging but scanned the specimen with a focused beam [Ard38]. Unlike modern scanning transmission electron microscopes, it had no post-specimen projection lenses, which makes it more similar to modern scanning electron microscopes. Different detectors collect the signal generated by subsequently irradiated spots on the sample in a scanning electron microscope or scanning transmission electron microscope. Those signals generate the intensity of each pixel in the image, corresponding to the properties of the irradiated position. In STEM, areal integrating STEM detectors collect the signals of direct and diffracted beams that become bright field (BF) and dark field (DF) images [WC09]. Zworykin, Hiller, and Snyder described a new scanning electron microscope that enabled the analysis of solid surfaces in 1942 [Oat82]. In SEM, the sample is scanned by a focused beam. Usually, multiple SE and BSE detectors are implemented in scanning electron microscopes and convert the locally detected electrons into the local image intensity. Compared to TEM and STEM, the maximum primary electron energies are usually considerably lower and limited to 30 keV.

²For example, $7 \cdot 10^{-3}$ nm for electrons with 30 keV energy.

In the decades since their invention, TEM and STEM have reached atomic resolution. The SEM was mostly used for solid samples, with its ability to generate 3D-like images of their topography. With improved electron optics and electron guns, and commercially available STEM detectors, transmission imaging in SEM, STEM-in-SEM, has been greatly improved and is now more commonly used [Cal+18; van+07]. This section starts with the basics of TEM, SEM, and STEM before it introduces the technique of STEM-in-SEM that has been primarily used in this work. Essential microscope components like the electron source and the lenses with their lens aberrations are very similar in all electron microscopes. They are discussed in the following section about TEM but also account for SEM and STEM.

2.2.1. Transmission Electron Microscopy (TEM)

A transmission electron microscope is set up from different parts along the electron beam. In the microscopes from most manufacturers, the beam travels from top to bottom, and this is the orientation that is considered here too. An electron gun generates the electron beam that is shaped by condenser lenses and the upper objective lens before it propagates through the specimen. The lower objective lens (which is usually meant by “objective lens” in TEM), and a system of projection lenses finally generates an image or diffraction pattern on the detector. The microscope column is pumped to high vacuum to avoid interactions of electrons with air molecules along the beam. Apart from the image detectors, transmission electron microscopes can be equipped with SE detectors and detectors for element-characteristic X-rays and electron-energy loss spectra or energy-filtered imaging.

2.2.1.1. Electron Source

An electron source consists of a cathode that emits the electrons, and an anode, that accelerates them by an acceleration voltage U . The energy gained by an electron when it passes an electrical potential difference of $U = 1\text{ V}$ is one electron volt, 1 eV , and this is the energy unit used in electron microscopy. Typical primary electron energies in a TEM are between 80 and 300 keV. The smallest beam cross-section at the electron source, the crossover, is what is in practice regarded as the electron source. To be emitted from the cathode, the electrons need to overcome an energy barrier, the work function Φ . The different methods to overcome this energy define the two types of electron sources: Thermionic and field-emission sources. In a thermionic source, the source material is heated to such high temperatures ($\approx 1700 - 2700\text{ K}$) that the electrons gain enough energy to overcome Φ . The source can be a tungsten filament, which can bear high temperatures, or a LaB_6 crystal with low Φ [WC09]. The principle behind field-emission sources, mostly called field-emission guns (FEGs)

is the increased electric field at sharp tips. Those tips are usually made from tungsten. A potential applied to such a tip results in a strong electric field, which lowers Φ and allows the electrons to tunnel out of the material by field-emission. A FEG needs to be in an ultra-high vacuum since already small amounts of contamination on the tip disturb the field-emission process. In return, the source can be kept at ambient temperatures (300 K, cold FEG) [WC09]. An alternative approach is the heating of the FEG that reduces contamination of the tip and facilitates the emission process. This type of source is called Schottky FEG (operating temperature ≈ 1700 K). Both types of FEGs still need ultra-high vacuum in the gun region. The advantages of FEGs are a smaller energy spread ($\Delta E = 0.3$ eV for cold FEGs and ≈ 0.7 eV for Schottky FEGs at 100 keV) and an increased lifetime [WC09].

The energy spread is connected to the temporal coherence of the emitted electrons: Small energy spread means high temporal coherence, and perfect temporal coherence means that all electrons have the same energy/wavelength. More important is the spatial coherence, which relates to the size of the source: For perfect spatial coherence, all electrons would have to emanate from a single point. This means that smaller sources provide higher spatial coherence. A measure for the quality of a source directly connected to the spatial coherence is its brightness β , which is the areal current density j per unit solid angle. β again is higher for FEGs than for thermionic sources [WC09].

2.2.1.2. Working Principle and Setup

Electromagnetic lenses are used to shape the beam in the electron microscope, analogous to glass lenses in light microscopes. Their working principle is based on the Lorentz force

$$\vec{F} = q(\vec{E} + \vec{v} \times \vec{B}) , \quad (2.30)$$

with the electric field \vec{E} , the magnetic field \vec{B} , and the electron's velocity \vec{v} . Most lenses work with the magnetic field \vec{B} , induced by currents in the coils of the magnetic lens. The magnetic field forces the electrons on helical trajectories along the optical axis. The coils of the lenses are embedded in a magnetic material, typically iron, with two cylinder-symmetrical polepieces that each have a small hole (bore) through which the electron beam enters and exits [WC09].

The condenser system consists of different electromagnetic lenses and apertures that shape the beam and direct it onto the specimen. The last lens before the specimen is the upper objective lens. The aim is to reach a parallel illumination of the specimen, with a minimal (half) opening angle α . Other parameters that the user of the TEM can change are the beam's intensity and diameter.

The lens system below the specimen allows for two different modes: The diffraction mode and the image mode (Figure 2.7). The diffraction mode produces a diffraction pattern (DP) on the detector (screen, image plate, or camera). The DP shows the angular distribution of diffracted and scattered electrons, which means that the distances in the DP correspond to scattering angles [WC09]. For crystalline specimens, the Bragg reflections appear, which fulfill Equation (2.29) on page 13. The Bragg equation shows that the angles in the DP have an inverse relationship with the lattice-plane distance d : The DP shows the reciprocal space. The selected area diffraction (SAD) aperture allows selecting a region of the image in the intermediate image plane.

In image mode, the intermediate lens is switched such that its object plane is the image plane of the objective lens, and a magnified image of the specimen appears on the screen. An objective aperture in the back-focal plane of the objective lens can select which scattering angles contribute to the image (Figure 2.7). If only the undiffracted direct beam (zero-order beam) is selected (red), the image is a BF image. Selecting diffracted beams (blue or green) generates DF images.

2.2.1.3. Lens Aberrations

The magnetic lenses in an electron microscope have lens errors, similar to the glass lenses in light optics. The most critical lens aberrations are the spherical and chromatic aberration, and astigmatism.

- **Spherical aberration:** This is the name of the aberration that causes electrons that have a larger distance from the lens center (the optical axis) to be focused closer to the lens. Instead of an infinitely small focal point, this leads to an error disk with a diameter of

$$d_s = 0.5 C_s \alpha^3 \quad (2.31)$$

in the plane of least confusion [Rei98; WC09]. C_s is the spherical aberration coefficient of the lens and α the semi-convergence angle of the incident beam. C_s is a property of the lens and is often constant, approximately equal to the focal length of the lens. However, it can be tuned to close to zero or other desired values in spherical aberration-corrected TEMs [Len+02].

- **Chromatic aberration:** This aberration means that the focal length of a lens depends on the wavelength of the electrons. Hence the smallest diameter reachable with a chromatic aberration constant C_c depends on the energy

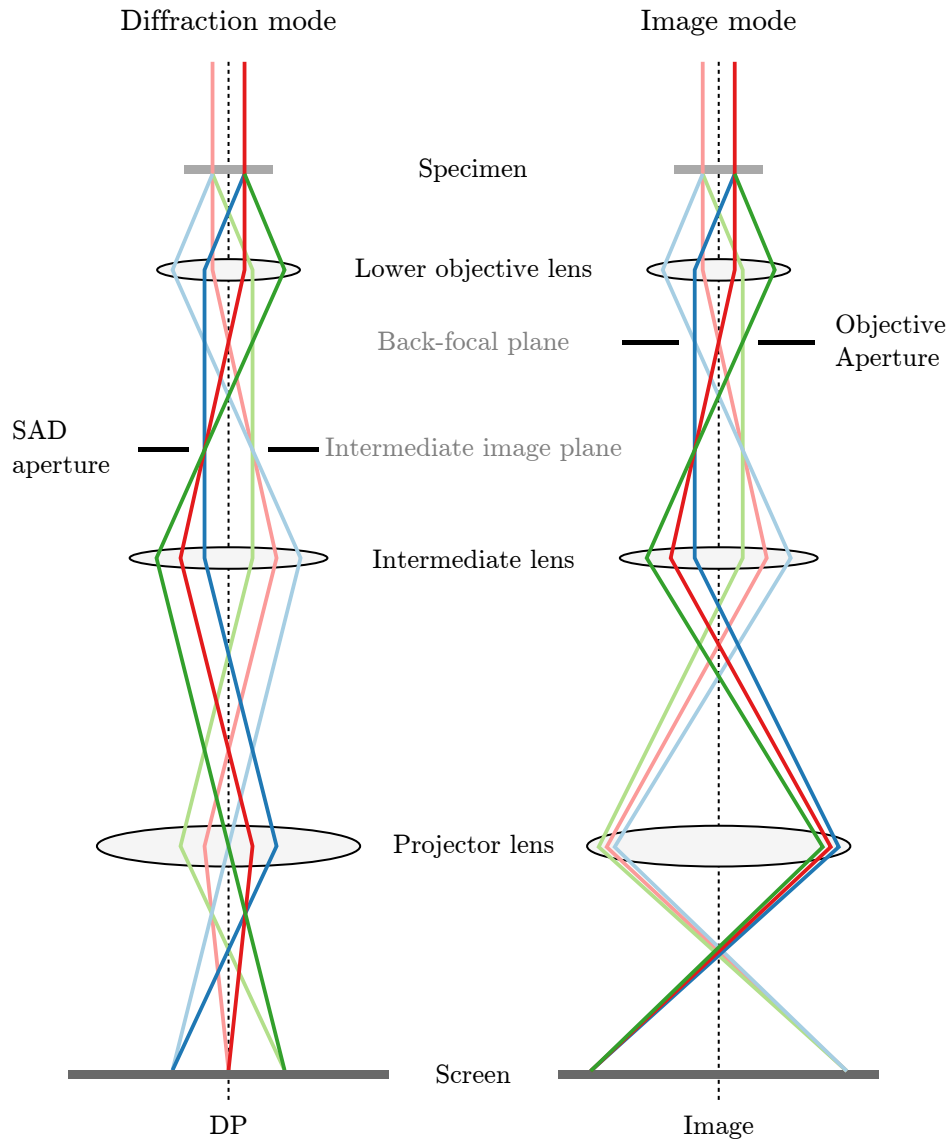


Figure 2.7. Ray diagram illustrating the imaging lens system of a TEM in diffraction and imaging mode. Beams diffracted from different points in the specimen are distinguished in pastel/full shade. Those diffracted to different angles are distinguished by their hue (green/red/blue) (after [WC09]). The diffraction mode produces a diffraction pattern (DP) on the screen, while the image mode projects an image of the specimen.

spread ΔE

$$d_c = C_c \frac{\Delta E}{E_0} \alpha . \quad (2.32)$$

C_c also is approximately equal to the lens' focal length [Rei98; WC09].

- **Astigmatism:** Several factors can cause asymmetries in the focusing field: Magnetic inhomogeneities of the polepieces, non-circular bores of the polepieces, and charging effects of bores and apertures due to contamination [Rei98]. These asymmetries in the magnetic field cause an astigmatic, elliptical beam. However, stigmators, which are octupole lenses, can correct astigmatism.

2.2.1.4. Contrast Generation

The main types of image contrast in TEM are mass-thickness contrast, phase contrast and diffraction contrast. The latter may arise due to changes in diffraction conditions or differences in the sample thickness [WC09; FH08]. While mass-thickness contrast is related to the amplitude of the electron wave and also understandable in the particle picture, only the wave picture can explain phase and diffraction contrast. This section focuses on the phase contrast in high-resolution TEM that makes lattice fringes and atomic structures visible.

Mass-thickness contrast This type of contrast generation is important when the specimen is amorphous or oriented such that the Bragg reflections are not excited strongly, if it is crystalline. If there are strongly excited Bragg reflections, diffraction and phase contrast dominate. The intensity of the direct beam decreases while it passes the specimen and the sample thickness t increases (Equation (2.12) on page 10). The cross-section σ , which describes the probability of scattering between the beam electrons and the atoms, increases with the atomic number Z and material density ρ . So the contrast generated by the decreasing intensity of the direct beam is called mass-thickness contrast. It allows a relatively easy interpretation of the intensities in the image: Considering constant Z , areas with lower mass-thickness x appear brighter in a BF image. However, this straightforward interpretation is only possible if diffraction is negligible.

Diffraction contrast Variations in the local intensity of diffraction in a specimen lead to diffraction contrast when the variation in the *intensity* of the diffracted waves is measured. This is contrary to phase contrast, where the *phase* is measured. The objective aperture can select the undiffracted or diffracted beam in the back-focal

plane (see image mode in Figure 2.7). The selection decreases the image intensity in those areas that do not fulfill the selected diffraction condition, while areas that fulfill the condition appear bright. The technique is referred to as TEM-BF or -DF imaging. For DF imaging, one of the diffracted beams is selected. Diffraction contrast is often used to image crystalline defects like dislocations [FH08].

Phase contrast The contrast generation in high-resolution TEM (HRTEM) can also be described in the wave-optical view. The phase contrast arises due to the interference of at least two reflections, typically the zero-order beam and one or more Bragg reflection, that is visible at high magnifications [FH08]. A plane wave passing the specimen undergoes an amplitude (intensity) change and a phase change. The wave after the interaction with the specimen can thus be described by

$$f(x, y) = A(x, y) \cdot e^{-i\phi(x, y)} \quad (2.33)$$

with the spatial coordinates $(x, y) = \vec{r}$, the amplitude $A(x, y)$, and the phase $\phi(x, y)$ [WC09]. $f(x, y)$ is called specimen function. In HRTEM, the specimen is, in a first approximation, assumed only to modify the phase and thus $A(x, y) = 1$ (phase object). An imaging system modifies the specimen function and forms an image $g(\vec{r})$. The modification is expressed in a point-spread function $h(\vec{r})$. The image function $g(\vec{r})$ is the convolution of $f(\vec{r})$ with $h(\vec{r})$

$$g(\vec{r}) = f(\vec{r}) \otimes h(\vec{r} - \vec{r}') \quad (2.34)$$

and the image intensity is given by [WC09]

$$I = |g(\vec{r})|^2 . \quad (2.35)$$

\vec{r}' highlights that each point in the image has contributions from multiple points in the specimen. With the reciprocal lattice vector $\vec{u} = 1/\vec{r}$ and the Fourier transforms of $g(\vec{r})$, $f(\vec{r})$, and $h(\vec{r})$, $G(\vec{u})$, $F(\vec{u})$, and $H(\vec{u})$, this convolution becomes

$$G(\vec{u}) = F(\vec{u}) \cdot H(\vec{u}) . \quad (2.36)$$

This is equivalent to the situation in the back-focal plane, as the objective lens performs a Fourier transform which is visible in the back-focal plane. $H(\vec{u})$ is called contrast transfer function (CTF) and consists of three parts [WC09]

$$H(\vec{u}) = \underbrace{A(\vec{u})}_{\text{Aperture function}} \cdot \underbrace{E(\vec{u})}_{\text{Envelope}} \cdot \underbrace{B(\vec{u})}_{\text{Abberation function}} . \quad (2.37)$$

The aperture function $A(\vec{u})$ describes the cut-off of spatial frequencies $|\vec{u}|$ by the objective aperture for $|\vec{u}| > u_{\max}$. The envelope function describes the damping of the wave and is a product of the damping envelopes caused by chromatic and spherical aberration, the specimen drift and vibration, and the detector [WC09]. Here, only the damping connected to chromatic and spherical aberration $E(\vec{u}) = E_c(\vec{u}) \cdot E_s(\vec{u})$ is discussed. The damping by the chromatic aberration is

$$E_c(\vec{u}) = e^{-0.5(\pi\lambda\Delta)^2 u^4} \quad (2.38)$$

with the defocus spread Δ due to the chromatic aberration. The image is focused (zero defocus) when the object plane of the objective lens is exactly the plane of the specimen. Δ depends on the instabilities of the objective lens current $\Delta I/I_0$, the instabilities in the acceleration voltage $\Delta V/V_0$, the energy spread of source itself $\Delta E/E_0$, and the chromatic aberration coefficient C_c [WC09, p. 495]

$$\Delta = C_c \sqrt{4 \left(\frac{\Delta I}{I_0} \right)^2 + \left(\frac{\Delta V}{V_0} \right)^2 + \left(\frac{\Delta E}{E_0} \right)^2} . \quad (2.39)$$

The damping connected to the spherical aberration for a Gaussian-shaped distribution of electrons is

$$E_s(\vec{u}) = \exp \left(- \left(\frac{\pi\alpha}{\lambda} \right)^2 (C_s \lambda^3 u^3 + \Delta f \lambda u)^2 \right) , \quad (2.40)$$

with the spherical aberration coefficient C_s and the semi-angle α that characterizes the convergence of the electron beam [WC09, p. 496].

The aberration function is

$$B(\vec{u}) = e^{i\chi(\vec{u})} \quad (2.41)$$

and contains the phase shift χ from the objective lens

$$\chi(\vec{u}) = \pi \Delta f \lambda u^2 + \frac{1}{2} \pi C_s \lambda^3 u^4 \quad (2.42)$$

due to the defocus Δf and the spherical aberration C_s [WC09, p. 485].

The phase-object approximation is usually used to simplify Equation (2.33) [WC09, p. 486]: Absorption is taken into account by a function $\mu(\vec{r})$, such that the rest of the specimen transfer function is a “phase object”

$$f(\vec{r}) = \exp(-i\sigma V_t(\vec{r}) - \mu(\vec{r})) . \quad (2.43)$$

V_t is the projected potential of the specimen and σ the interaction constant. This can be further simplified assuming that the specimen is very thin and thus $\mu(\vec{r}) = 0$

and $V_t(\vec{r}) \ll 1$. A Taylor expansion of Equation (2.43) then gives

$$f(\vec{r}) \approx 1 - i\sigma V_t(\vec{r}) , \quad (2.44)$$

which is the *weak* phase-object approximation (WPOA). With this approximation, the aberration function (Equation (2.41)) can be set to

$$B(\vec{u}) = 2 \sin(\chi(\vec{u})) . \quad (2.45)$$

$\sin(\chi)$ is sometimes called the phase contrast transfer function (PCTF) [HS19]. The contrast transfer function is then given by

$$H(\vec{u}) = A(\vec{u}) \cdot E(\vec{u}) \cdot 2 \sin(\chi(\vec{u})) \quad (2.46)$$

[FH08, p. 546], [WC09, p. 487]. This means that the contrast transfer cannot be easily interpreted as it varies with the spatial frequency $u = |\vec{u}|$. Specimen structures appear dark on bright background for $\sin(\chi) < 0$ and vice versa for $\sin(\chi) > 0$. Thus a HRTEM image is not interpretable anymore after the first zero crossing of $\sin(\chi)$. The corresponding value of $1/u_0$ is called point resolution. The aim is therefore to push the zero crossing to maximum values of u .

Figure 2.8 shows $\sin(\chi)$ for different defocus values for $E_0 = 300$ keV and $C_s = 0.013$ mm, which is a typical value for a transmission electron microscope with an implemented C_s corrector. Depending on C_s , the following characteristic defocus values can be derived:

- The defocus of **minimum contrast** is for $C_s = 0$ the Gaussian focus ($\Delta f = 0$). For $C_s \neq 0$ it is

$$\Delta f_{\text{mc}} = -0.44(C_s\lambda)^{1/2} \quad (2.47)$$

This is the only defocus value that can directly be recognized when tuning the defocus [FH08, S. 569].

- The **Scherzer defocus**

$$\Delta f_{\text{Sch}} = -(C_s\lambda)^{1/2} \quad (2.48)$$

pushes the point resolution to higher values of u [RK08, S. 220]. However, the typically used setting is the...

- **Extended Scherzer defocus**

$$\Delta f_{\text{Sch, ext}} = -1.2(C_s\lambda)^{1/2} . \quad (2.49)$$

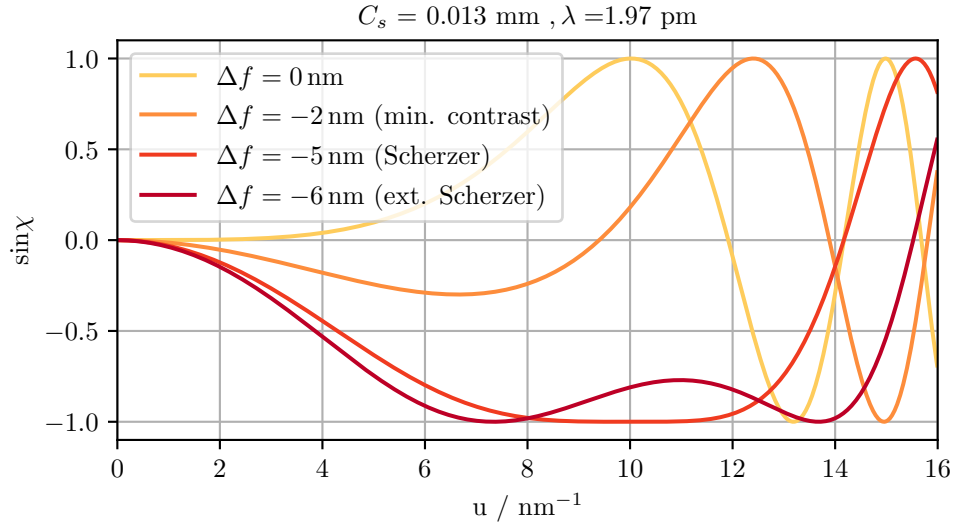


Figure 2.8. $\sin(\chi)$ plotted for different defocus values with $\lambda = 1.97 \text{ pm}$ for 300 keV according to Equation (2.6) on page 8.

The extended Scherzer defocus maximizes u_0 and reaches a point resolution of $1/u_0 = (\frac{C_s}{6}\lambda^3)^{1/4}$ [FH08, S. 550]. In the example in Figure 2.8, it is 0.6 \AA . The contrast of smaller features cannot be interpreted intuitively. Hence the objective aperture function $A(\vec{u})$ should cut off higher values of u .

Figure 2.8 visualizes why defocusing causes a stronger contrast in an image: Low spatial frequencies, which means large real-space frequencies, have a stronger contrast transfer for increasing negative values of Δf . However, the point resolution deteriorates for $\Delta f < \Delta f_{\text{Sch, ext}}$.

The transmitted intensities can already be damped at $u < u_0$ due to the damping envelope functions $E(u)$ (see Equation (2.46)), as shown in Figure 2.9. In spherical aberration-corrected microscopes, C_s can be tuned such that the point resolution is extended to the information limit, which is defined as the value of u where the envelope drops to a level of $e^{-2} = 13.5\%$ [Len+02; OKe92]. This information limit defines the size of the smallest detail that can be observed with a particular microscope [BT08].

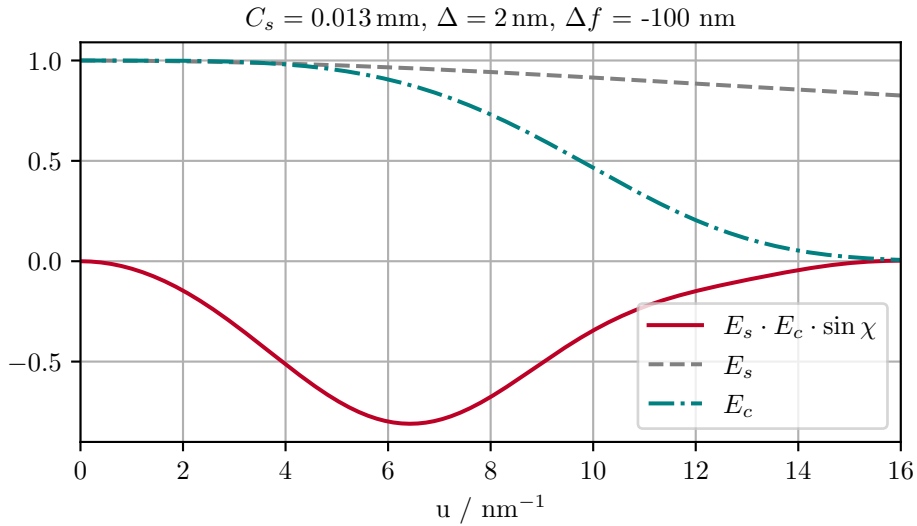


Figure 2.9. Contrast transfer function $H(\vec{u})$ plotted for 300 keV, defocus spread $\Delta = 2 \text{ nm}$, defocus $\Delta f = 100 \text{ nm}$ according to Equation (2.46), Equation (2.40), and Equation (2.38).

2.2.2. Scanning Electron Microscopy (SEM)

The imaging process in SEM and STEM works fundamentally different than for TEM imaging: Instead of a parallel beam, the beam electrons are focused and form a probe with a minimized diameter. Instead of collecting the image directly by a detector, a computer assembles the image point by point from a detector signal while the focused beam scans the sample. The magnification is determined by the size of the scanned region on the sample.

The primary electron energy in an SEM is usually between 0.1 keV and 30 keV [HS19]. In contrast to the TEM, the sample chamber is large and accommodates several detectors above the sample, collecting SE and BSE or X-rays. In addition, many SEMs are equipped with a focused ion beam (FIB) column that enables surface modifications and the preparation of electron-transparent specimens from bulk material.

This section focuses on the probe formation and resolution in SEM, the contrast generated by SE and BSE, and the different available detectors and imaging modes.

2.2.2.1. Probe Formation and Spatial Resolution

The spatial image resolution of an SEM is determined by the size and shape of the incident electron probe, the limitation by the noise (signal-to-noise ratio, SNR), the beam and sample positional stability, the size of the interaction volume, and the information depth depending on the type of detected electrons [Rei98]. The X-ray spatial resolution is approximately equal to the interaction volume of electrons but will not be further discussed here [FHN77].

Probe size The demagnification of the electron-gun crossover forms the electron probe. The finite source size, spherical and chromatic lens aberrations, and diffraction at the probe-forming aperture determine the probe diameter d_{probe} at the specimen surface, considering the sample is in focus

$$d_{\text{probe}} = \sqrt{d_0^2 + d_d^2 + d_s^2 + d_c^2} . \quad (2.50)$$

d_0 is the diameter due to the finite size of the source, d_d is the diameter of the diffraction disc from the probe-forming aperture, and d_c and d_s are the error discs due to the chromatic and spherical aberration (see Section 2.2.1.3 on page 19) [RK08, p. 94]. This results in

$$d_{\text{probe}} = \sqrt{\left(\left(\frac{4I}{\pi^2\beta}\right)^{1/2} \frac{1}{\alpha}\right)^2 + \left(\frac{0.6\lambda}{\alpha}\right)^2 + (0.5C_s\alpha^3)^2 + \left(C_c \frac{\Delta E}{E_0} \alpha\right)^2} , \quad (2.51)$$

with beam current I , source brightness β , beam convergence angle α , wavelength λ , relative energy spread $\Delta E/E_0$, and the chromatic and spherical aberration constants C_c and C_s . Equation (2.51) shows there exists an optimum α that results in a minimum d_{probe} [WM20]. As mentioned in Section 2.2.1.3, C_c and C_s are proportional to the focal length of the probe-forming objective lens. If the sample is in focus, the focal length equals the working distance (WD), which is the distance between the lower end of the pole piece and the sample surface. Hence, a lower WD reduces the probe diameter.

The comparably low primary electron energies E_0 in SEM increase the ratio $\Delta E/E_0$ for a given energy spread of the source. The increased ratio worsens the beam diameter of SEM compared to STEM, which operates at higher energies (like TEM). A monochromator can reduce ΔE and the beam diameter [HS19].

The second, diffraction-dependent term in Equation (2.51) determines the lower limit for d_{probe} for small α [WCH91]. For example, $0.6\lambda/\alpha = 0.8$ nm with the values found in Section 6.3.2.4 on page 140. The spherical aberration and d_0 typically determine the beam diameter in SEM, but also the contribution of C_c increases at low energies due to the larger ratio $\Delta E/E_0$, as mentioned above. SEMs with thermionic sources reach probe diameters around 5 nm at conventional energies (5–30 keV), while SEMs with FEGs can reach probe diameters below 1 nm [HS19].

Spatial resolution for SE/BSE imaging The low energies of SE result in a small exit depth of the order of a few nanometers (Figure 2.3 on page 6). Therefore, the part of SE that is excited by primary electrons (SE 1) has a spatial resolution of $\approx 1 - 10$ nm, depending on the probe diameter. However, Figure 2.3 on page 6 clarifies that this resolution is worsened by the SE 2 generated by BSE [Rei98]. BSE provide a poorer resolution than SE due to the larger exit depth and the escape

from larger distances to the primary electron beam. However, their exit depth is reduced at lower beam energies, enhancing the resolution [Rei98].

2.2.2.2. Signal-to-Noise Ratio

The beam current I influences not only the beam diameter but also the achievable signal-to-noise ratio (SNR), as a number of

$$n = f \cdot \tau \frac{I}{e} \quad (2.52)$$

electrons produce a signal S , with the fraction $f < 1$ of electrons that the detector records, the electron charge e , and the recording time τ for one image point in SEM and STEM. The noise signal is $N = \sqrt{n}$ [RK08]. According to the Rose criterion, the signal-to-noise ratio S/N must fulfill

$$\frac{S}{N} = \frac{n}{\sqrt{n}} \leq \kappa, \quad (2.53)$$

with κ around 3 to 5 [Ros48]. If a signal difference of ΔS on the background signal S should be detected, this determines the minimum I for a fix τ or vice versa [RK08, p. 96]

$$\frac{\Delta S}{S} \geq \kappa \frac{\sqrt{n}}{n} = \frac{\kappa}{\sqrt{f I \tau / e}}. \quad (2.54)$$

The SNR in an image can thus be improved by either increasing the recording time or the current (or both). Both a longer recording time and a higher current increase the potentially damaging electron dose the sample is exposed to. This general rule also holds for TEM imaging.

2.2.2.3. SE and BSE imaging

The secondary electron yield δ depends on the tilt angle of the sample surface and is enhanced at edges and for small particles. In addition, the measurable signal is lower if an object blocks the direct way between the examined position and the detector, which leads to a shadowing effect [Rei98]. The dependency on the tilt angle and the shadowing render SE-SEM a technique to image a sample's topography in a 3D-like manner. SE-SEM can also visualize charging of the sample's surface: Due to their low energy, SE are retained by a positive charge or repelled by a negative charge (see Section 2.1.4 on page 14) [JJ96]. SE can also generate material contrast as their emission depends on the work function Φ of a surface. By careful quantification, SE images can even allow identifying various material components

of a given sample [Caz10]. Lastly, SE can cause magnetic contrast as the magnetic field of magnetic domains in a sample influences them [Rei98].

The SE yield δ varies depending on the electron energy and has a maximum at about $E_0 = 1$ keV, depending on the material [LJ05; Caz10]. Notably, the contrast of SE images is always influenced by the BSE signal, as BSE generate SE 2 (see Figure 2.3 on page 6) [Rei98].

Like SE emission, the BSE emission depends on the surface tilt and can be shadowed, enabling topography imaging. However, the BSE carry mainly material contrast when detected at high take-off angles. One meaningful application of BSE is imaging grains in polycrystalline materials due to the dependence of the BSE yield on the angle between the incident electrons and the lattice planes, called channeling contrast. Finally, also BSE can generate magnetic contrast [Rei98].

2.2.2.4. Detectors

The best-known detector in SEMs is the Everhart-Thornley detector (ETD), typically used to detect SE. It collects SE by a positively biased collector grid (between +100 V and +200 V), behind which the SE are accelerated towards a scintillator and the resulting photons are then detected by a photomultiplier [Rei98]. As the detector is usually positioned above and aside from the sample, images collected by it look as if the sample was illuminated from the side.

When the grid is charged negatively, such that it repels all SE, only BSE can reach the ETD. However, the detection efficiency is low as they move on nearly straight trajectories and are not “soaked in” by the grid like the SE. A dedicated annular scintillator/photomultiplier or semiconductor BSE detector without an acceleration grid is better suited for BSE detection. BSE detectors are preferably installed at high take-off angles with a large solid angle, for example, below the objective-lens polepiece [Rei98].

In-lens or through-lens detectors (TLD) are also used for SE and BSE imaging, but generate different-looking images due to the different geometry: As the name suggests, such detectors are placed inside the electron column and the electrons have to travel through the polepiece of the objective lens. This means that the solid detection angle is narrow. The signal is still high enough, as the electrons emitted by the sample are trapped by the field of the objective lens and spiral up the electron column, which works best in the immersion mode described in the next section. In the electron column, they have to be deflected off the optical axis towards the detector [HS19; Nag+87]. The resolution of in-lens detector images is usually better than in ETD images as no SE 3 are detected. In-lens detectors can be used for SE and BSE imaging; some even allow more specific energy filtering [Gol+18]. Due to

their position in the electron column, the image looks as if the sample was irradiated from above.

Besides scintillation-photomultiplier detectors, semiconductor detectors are in use. They directly detect electrons which generate electron-hole pairs in the detector material [Rei98]. STEM detectors are usually of the semiconductor type in scanning electron microscopes while scintillator/photomultiplier STEM detectors are common in high-energy STEM. Semiconductor STEM detectors are discussed in Section 2.2.3.2.

The electron beam excites X-rays that are characteristic of the sample's elemental composition. Those X-ray photons can be detected by EDXS. An energy-dispersive spectrometer measures the energy of X-ray photons and can collect the whole X-ray spectrum simultaneously. It measures the photon energy by the number of electron-hole pairs that X-ray photons generate in a semiconductor [Rei98; Gol+18].

2.2.2.5. Imaging Modes

A scanning electron microscope typically provides three different imaging modes: A field-free mode, a semi-in-lens/immersion mode, and a mixture which is used for EDXS mappings. The latter will not be further discussed here. In the field-free mode, the magnetic field is restricted to the pole piece, and thus the microscope chamber is field-free. In the semi-in-lens mode, the sample is “immersed” in the magnetic field reaching out of the strongly excited objective lens. The working distance ($WD = \text{focal length of the lens}$) is reduced to 1 – 2 mm, which leads to a larger convergence angle α . This results in smaller C_c and C_s and thus in a best resolution of $< 1 \text{ nm}$ in the semi-in-lens mode [Rei98]. The detector typically used in the semi-in-lens mode is an in-lens detector, as the field guides more electrons up the electron column and nearly no signal reaches the ETD. The user of the microscope can easily switch between these modes.

A full in-lens mode further improves the beam diameter. However, it requires a modified microscope setup where the specimen is introduced between the polepiece of the objective lens and a counter-polepiece [Nag+87].

2.2.3. Scanning Transmission Electron Microscopy (STEM)

A scanning transmission electron microscope scans the sample with a focused electron probe, similar to SEM, and thus the probe formation works as described in Section 2.2.2.1. Contrary to SEM, the electrons propagate through a thin specimen and the signal is detected below, after the imaging lenses. It is important to note that many transmission electron microscopes can switch to the STEM mode. Less common are dedicated STEM instruments that cannot use the conventional

TEM mode. The majority of instruments is set up for TEM and STEM with operation voltages typically from 60 keV to 300 keV. The most commonly used detector in STEM is the STEM detector, a radially segmented annular semiconductor detector [HS19]. Other possible detectors are angular-segmented detectors, pixelated detectors, and detectors for SE, X-rays or energy loss spectroscopy. The following overview covers the spatial resolution in STEM, the STEM detector, imaging modes, and nanobeam diffraction.

2.2.3.1. Spatial Resolution

The achievable spatial resolution in STEM depends on the probe diameter d_{probe} (Equation (2.51)), the signal-to-noise ratio, the beam and sample positional stability, and, different than in SEM, the beam broadening within the specimen (i.e. the specimen thickness) and the beam divergence due to the convergence angle of the probe [FHN77; WM20; JVD18; HEM08].

The spatial resolution d is thus

$$d = \sqrt{d_{\text{probe}}^2 + d_{\text{SNR}}^2 + d_{\text{bb}}^2 + d_{\alpha}^2} \quad (2.55)$$

with the limitation through noise d_{SNR} , beam broadening d_{bb} , and the beam divergence d_{α} [JVD18; HEM08]. The beam divergence is a geometrical effect of the probe, which leads to a wider beam in the specimen parts that are not in focus. It is more pronounced for spherical-aberration-corrected microscopes that have a shorter focus depth of field [HEM08]. Beam broadening and divergence increase with the specimen thickness t . For small t , d is small enough to achieve atomic resolution [HS19]. Contrary to the TEM mode, magnification in STEM is not controlled by the projection lenses but by the size of the scanned region on the specimen, like in SEM [WC09].

2.2.3.2. STEM Detector and Image Formation

The STEM detector is placed below the specimen, symmetrical to the optical axis. It is a semiconductor or scintillator detector that is segmented in a central, circular bright field (BF) segment, and annular dark-field (ADF) segments around it. The average number of generated electron-hole pairs in a semiconductor is $\bar{n} = E/\bar{E}$ with the electron energy E and the mean electron-hole excitation energy \bar{E} (3.6 eV in Si). The electron-hole pairs are separated in the semiconductor's reversely biased pn-junction and generate a current I_p [Rei98]. This incident electron current I_p

creates a charge-collection current I_{cc} in the detector:

$$I_{\text{cc}} = I_{\text{p}} G \epsilon . \quad (2.56)$$

ϵ is the charge-collection efficiency of the detector. G is the detector gain that contains the threshold energy E_{th} in the range of a few keV, below which the detector is insensitive due to its protective metal coating

$$G = (1 - \eta) \cdot \frac{E - E_{\text{th}}}{\bar{E}} . \quad (2.57)$$

The factor η takes the loss of electron-hole pair generation due to electron backscattering into account. The detector finally measures a current

$$I_{\text{det}} = I_{\text{cc}} + I_{\text{b}} \quad (2.58)$$

that is a sum of the charge-collection current (the actual signal) and the dark-current I_{b} , which results from noise in the detector and its electronics [Rei98].

In STEM mode, the projection lenses are operated such that the STEM detector is in the diffraction plane. Due to the convergence of the beam, the diffracted beams do not appear as spots (like for parallel TEM irradiation), but as diffraction discs with a beam convergence angle-dependent diameter.

The segments of the STEM detector spatially integrate the signal of the diffraction pattern. Figure 2.10 shows a schematic side view of the detection-angle ranges of different segments of a STEM detector. The central BF segment detects the direct beam with unscattered electrons or those scattered into low angles. The narrow segment (or multiple segments) that are placed concentrically around the BF segment are the DF segments. The outermost and widest segment is the high-angle annular dark field (HAADF) segment. For STEM in a transmission electron microscope, different lenses are positioned between the specimen and the detector (see Figure 2.7 on page 20), and the electron trajectories are no straight lines. Imaging lenses between the specimen and the STEM detector facilitate the change of the camera length and, therefore, the change of the detection-angle range [HS19]. An exception is the linear electron trajectories in field-free low-energy STEM-in-SEM, described starting from page 34, with no lenses between the specimen and the STEM detector, which means that the detection-angle range is almost fixed.

2.2.3.3. Image Contrasts

Images obtained with the STEM detector carry different information on the specimen by showing mass-thickness contrast, Z -contrast, or diffraction contrast [WC09]

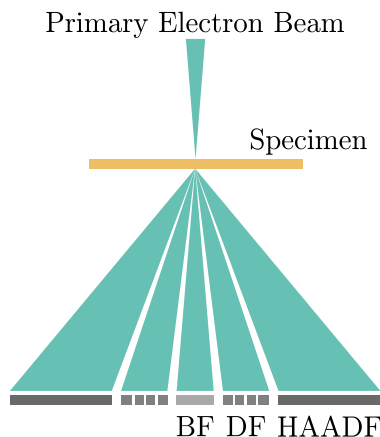


Figure 2.10 Scheme of the STEM detector's imaging principle. The detector comprises a BF segment, narrow DF segments, and a wide HAADF segment.

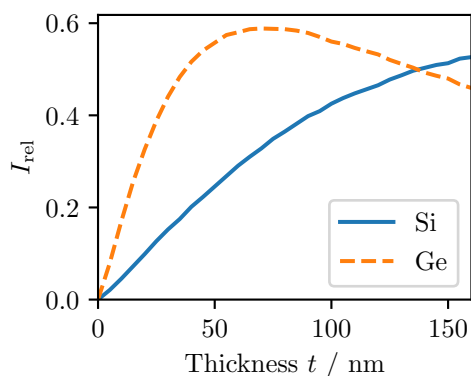


Figure 2.11 Simulated relative HAADF-STEM intensities as a function of sample thickness (Monte Carlo simulation), normalized with the intensity of the incident electron beam. $E_0 = 20$ keV, Si and Ge as exemplary materials. Evaluated scattering angle range: 168 mrad – 617 mrad.

As the BF segment collects the direct beam and the annular DF segments collect the diffracted beams, the produced image contrast is approximately complementary. The HAADF signal increases with increasing sample thickness as an increasing number of electrons are scattered to higher angles and reaches the HAADF segment. At the same time, the BF signal decreases. However, there is a contrast reversal in HAADF images for even higher sample thicknesses when the electrons are increasingly absorbed in the specimen or scattered even beyond the angles covered by the HAADF segment (Figure 2.11, Ge). As the contrast reversal occurs at smaller thicknesses with decreasing electron energy, it is most important when using low electron energies. The change in the intensity depending on the thickness is due to mass-thickness contrast, which dominates for amorphous specimens and for crystalline specimens if no Bragg reflection is strongly excited (kinematical diffraction condition) [WC09]. The HAADF segment covers high scattering angles, dominated by incoherent Rutherford scattering. Hence, the signal is less dependent on the crystal orientation. As Rutherford scattering is highly dependent on the atomic number Z , the contrast obtained by the HAADF segment is often referred to as Z -contrast (Equation (2.3) on page 8). Z -contrast allows distinguishing different materials for a constant sample thickness, as depicted in Figure 2.11: For a sample thickness of 50 nm, the intensity of Ge ($Z = 32$) is more than two times higher than the intensity of Si ($Z = 14$), as the heavier material causes stronger scattering to the large HAADF angles. A practical example is the distinction of strongly scattering

heavy atoms or particles from a low-scattering (e.g., carbon) support [WC09; HS19]. However, caution is necessary in identification of the heavier material as brighter due to the decrease of intensities for large specimen thicknesses (Figure 2.11). Considering two materials that should be distinguished have the same thickness, there is a material contrast inversion when the curves in Figure 2.11 cross. For increasing electron-beam energies, the curves are stretched along the x-axis and the contrast reversal occurs for higher sample thicknesses. The interpretation of TEM images is less straightforward as there is contrast reversal with defocus. This reversal does not occur in STEM images, which is particularly useful for the automatic acquisition of tilt series for STEM tomography.

With a suitable specimen and a small enough probe, STEM images from both BF and (HAA)DF detectors can have atomic (column) resolution. In addition, BF-STEM can image lattice fringes by phase contrast, even if the probe diameter is larger than the fringe distance: If the diffraction discs overlap, coherent interference can occur. If the BF segment then covers a small enough area not to average out those interferences, the signal becomes dependent on the beam position. In this case, lattice fringes become visible [HS19].

2.2.3.4. Nanobeam Diffraction

The technique where the diffracted electron intensities from a nanometer-size area are not integrated by a STEM detector but recorded by a camera is called nano-beam electron diffraction (NBED). It can be used for crystallographic examinations like identification of the structure, as in Section 6.4.3, or strain measurements [Usu+04; Béc+09].

2.2.4. STEM-in-SEM (TSEM)

Scanning electron microscopes are usually used to investigate bulk samples. However, it is possible to get signals from transmitted electrons from electron-transparent specimens with special detectors and sample holders. The technique is then called STEM-in-SEM [BG20; Hol21], TSEM [KBF12] or Low-energy STEM/low-keV STEM [Dre+17; HMG19; Čal+19]. This technique was mostly used in this work. However, as the main principles of electron sources, scanning of the sample, and STEM detectors were already introduced in previous sections, this section is rather short. It focuses on the setup, working principle, and pros and cons of the technique. In STEM-in-SEM, a STEM detector with BF and ADF segments integrates the intensity of electrons transmitted through thin specimens with respect to their scattering angle and provide images similar to those known from classical STEM. A camera or a fluorescent screen is sometimes available to record the transmitted

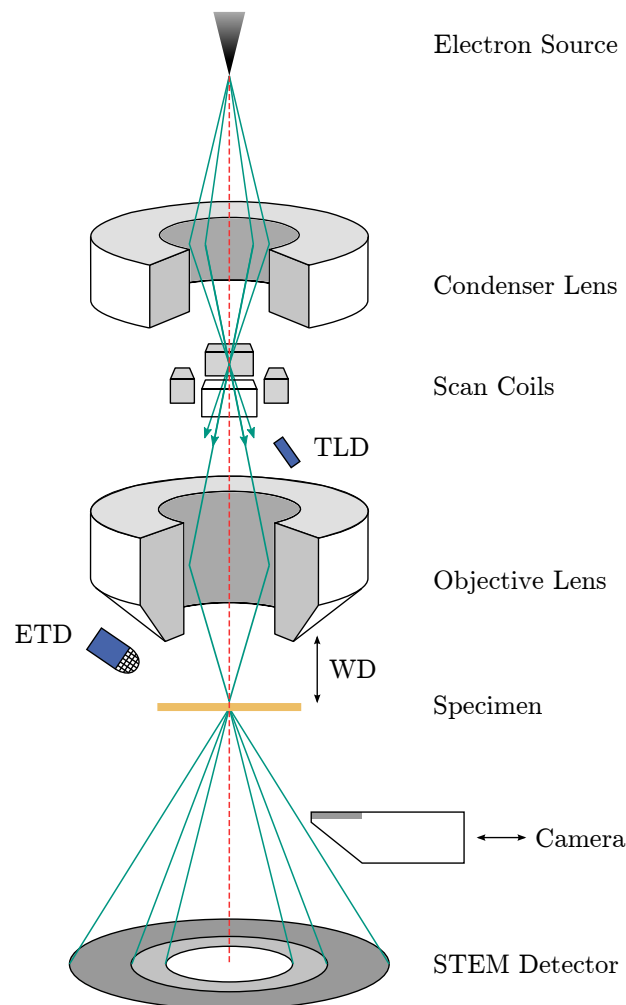


Figure 2.12. Scheme of a scanning electron microscope equipped with a STEM detector for STEM-in-SEM, and a retractable on-axis camera for the acquisition of diffraction patterns. The optical axis is shown in red. The condenser and objective lenses form a small electron probe on the specimen surface. The scan coils move the beam across the specimen. Typical SEM detectors, like the Everhart-Thornley detector (ETD) and through-lens detector (TLD), collect surface images complementary to transmission imaging. The working distance (WD) is the distance between the lower end of the objective lens and the specimen's surface.

diffraction patterns. Although there is no system of projection lenses, this is possible because the distance between the specimen and the STEM detector is large enough, such that far-field Fraunhofer diffraction occurs in the detector plane [WC09].

2.2.4.1. Setup and Working Principle

A STEM-in-SEM setup is shown in Figure 2.12. It requires a specific sample holder that allows the transmission of the electron beam and a STEM detector. In some instruments, a camera or fluorescence screen is mounted below the specimen (Figure 2.12) [BDG13; Hol21]. Some setups deviate further from the standard SEM setup as they comprise an objective lens part below the specimen for a full in-lens mode [Kon+14]. Apart from the lower acceleration voltages ($E_0 \leq 30$ keV), the main difference between the setup of a regular TEM/STEM and the STEM-in-SEM is, as mentioned above, the missing projection-lens system. This means that the camera length can only be changed physically, not by switching some lenses: Either the specimen or the detector has to move in z-direction [Mül+20].

Today, STEM-in-SEM has in many ways become closer to “classical” TEM and STEM: The spatial resolution has been improved such that lattice fringes imaging and high-resolution imaging of 2D-materials have become possible by BF-STEM imaging [Kon+14; Sun+16]. The diffraction pattern (spot-like or transmission Kikuchi patterns) can be accessed by cameras or fluorescence screens below the specimen [BDG13; Sch+20a; GRK13; Mül+20]. Caplins, Holm, and Keller developed a programmable digital micromirror device that can switch between imaging and diffraction mode just as fast as in TEM. In addition, it enables a flexible selection of detection angles for STEM imaging. Recently, fast pixelated cameras (some with direct electron detection) have been implemented, allowing for 4D-STEM techniques [Mül+20; Hol21; Ore+03]. Lastly, STEM-in-SEM instruments can be equipped with EELS detectors [Bro+19].

2.2.4.2. Advantages and Disadvantages

STEM-in-SEM has several advantages: Parallel to taking STEM images, it is possible to get surface-sensitive or material-sensitive SE-SEM and BSE-SEM images of the same specimen region, which is denoted as correlative imaging [BDG18; Sun+20]. A large number of available SEM detectors combined with transmission imaging renders the STEM-in-SEM technique a powerful combination for the investigation of samples like nanoparticles, grain textures, and crystalline defects [Hol21; Sun+19; Kle+11; GSP11; GRK13]. BF-STEM enables lattice fringe resolution; at the same time, SEM bridges length scales up to centimeters [Kon+14; Sun+16]. Besides, SEMs are usually a lot cheaper than TEM/STEM or dedicated

STEM instruments³. The implementation of a FIB in many instruments allows the investigation of a freshly prepared specimen without bringing it into contact with ambient air. The large chamber size and several access ports facilitate the implementation of custom sample holders (e.g., sample carousels for the fast investigation of multiple specimens), in-situ experiments, and detectors [GSP11]. Contrary to TEM, the specimen diameter is not necessarily limited to 3 mm. The illumination can be changed from nearly parallel to convergent (< 1 mrad to > 60 mrad), although it is not as easy as in TEM [Hol21]. A Faraday cup for beam-current measurements is a frequent accessory in a scanning electron microscope in contrast to transmission electron microscopes. This is advantageous because the knowledge of the precise current is necessary for some EDXS quantification methods [WW06].

Lower electron energies lead to larger scattering cross-sections, resulting in a shorter mean free path length. Therefore the electrons experience more scattering events on their way through a specimen. On the one hand, this yields a better contrast for weakly scattering materials like polymers and life-science samples [GSP11]. On the other hand, the enhanced scattering requires thinner specimens compared to high-energy STEM⁴.

The low electron energies reduce knock-on damage. However, radiolysis is enhanced at lower energies, making STEM-in-SEM less suited for the investigation of specimens susceptible to this kind of sample damage (for the types of beam damage, see Section 2.1.4 on page 14). Another disadvantage is the less flexible camera length, as mentioned above. As discussed in the introduction of this work, the reduced energies in SEM cause increased beam broadening and beam-induced carbon contamination that hamper STEM-in-SEM investigations. Beam broadening worsens the resolution and contrast in images [MM07]. It cannot be avoided, but it is helpful to have suitable models to estimate its effect. Chapter 4 focuses on this topic. Carbon contamination depends on several factors, some of which can be used to reduce or mitigate the deposition of contamination layers during sample investigation. Chapter 5 addresses the contamination topic.

The main disadvantage of STEM-in-SEM compared to TEM and classical STEM is the reduced spatial resolution. Yet, where atomic resolution is not needed, STEM-in-SEM can fulfill many transmission imaging and diffraction tasks.

³Which only use the STEM mode

⁴For comparison: Around 50 nm is regarded the maximum thickness of standard TEM specimens [WC09], but the allowed thickness depends on many parameters.

*Chapter***3.**

Instrumentation and Methods

This chapter describes the instruments used in this work and the technique of quantitative STEM measurements in STEM-in-SEM setups. As most of the remaining methods were solely used in one of the results chapters, they are outlined there, aiming for each chapter to be a sealed unit best possible. The description of the microscopes follows the order in the fundamentals, starting with the description of the TEM/STEM instruments and continuing with the STEM-in-SEM instruments.

3.1. Transmission Electron Microscopes

HRTEM analysis was performed with a FEI TITAN³ 80-300 (FEI Company, today Thermo Fisher Scientific), which is equipped with a spherical-aberration corrector in the image lens system (CEOS GmbH), a monochromator, and a Gatan Tridiem 865 ER imaging filter (Gatan Inc.). Since the analysis of the beam-sensitive material investigated in Chapter 6 is limited by beam damage rather than the achievable spatial resolution of the TEM, the image corrector was not aligned. The monochromator was used to reduce the dose rate, but not for its intended purpose (reducing the beam's energy spread).

The TITAN can also be used in STEM mode, which was utilized to obtain NBED patterns and for STEM tomography. For the latter, the TITAN is equipped with a Fischione single-tilt tomography holder, allowing a tilt-angle range of 140° (E.A. Fischione Instruments Inc.). The HAADF-STEM signal was collected with a Fischione Model 3000 ADF detector. During the time range of this work, the camera of the microscope was changed from a Gatan Ultrascan 1000 CCD camera with relatively low detection efficiency and slow readout to a more sophisticated TVIPS TemCam-XF416(R) CMOS camera (Tietz Video and Image Processing Systems GmbH). The frame rate of the latter is 24 frames per second for 4096 × 4096 pixels. Due to its high detection efficiency and fast frame rates, the camera is well suited for low-dose

imaging [OGT18]. TEM images were also acquired in the PHILIPS CM200 FEG ST (Philips, today Thermo Fisher Scientific), a dedicated TEM instrument.

The FEI TECNAI OSIRIS is a TEM/STEM instrument optimized for high-efficiency EDXS analysis with ChemiSTEM technology [Sch+10]. It combines four 30 mm² windowless silicon-drift detectors for a large detection solid angle and high detection efficiency with a high-brightness electron source (X-FEG). All other used electron microscopes are equipped with (conventional) Schottky-FEGs.

3.2. Scanning Electron Microscopes

The SEM and STEM-in-SEM investigations in this work were performed in a Thermo Scientific HELIOS G4 FX NANOLAB and a FEI STRATA 400S scanning electron microscope, which are equipped with an annular-segmented STEM detector (STEM 3 and STEM 4, respectively). Apart from that, they comprise a Ga⁺-ion column for FIB sample modifications like the preparation of electron-transparent specimens from bulk material. Both microscopes are equipped with a specialized sample holder for transmission imaging, different SE and BSE detectors and an EDXS detector.

SEM imaging was only performed as SE-SEM imaging in the HELIOS microscope, using the TLD and a so-called in-chamber electron (ICE) detector, which is similar to a classical ETD detector. It provides a higher detection efficiency because the photomultiplier is positioned within the vacuum chamber, resulting in reduced optical couplings [MDG08]. The HELIOS employs a retractable counter-polepiece, which enables a “full” in-lens/immersion mode with an increased convergence angle and smaller probe diameter (see SEM imaging modes, Section 2.2.2.5).

3.2.1. STEM Measurements in STEM-in-SEM

The Strata 400S and the Helios G4 FX microscope both contain a STEM detector with a BF segment and four DF segments. The HAADF segment is azimuthally divided into 6 parts. Figure 3.1 shows a scheme of the STEM detector in the STRATA microscope (STEM 3). The detector in the HELIOS is in principle the same, but it is covered by an aperture that reduces the effective radius of the BF segment and hence the detection angles¹ (STEM 4, see Figure 3.3 on page 45). The signals of individual detector segments can be added (or subtracted) in the microscope’s user interface by reading them out simultaneously. In the HELIOS microscope, it is possible to activate all segments simultaneously, while the BF and DF0 can only be

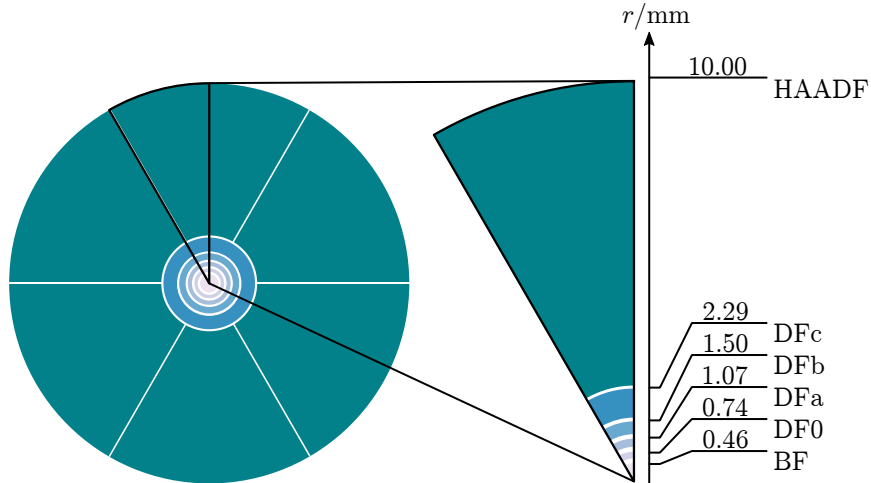


Figure 3.1. Scheme of the STEM detector implemented in the STRATA microscope, comprising a BF segment, DF segments (DF0, DFa - DFc), and the radially sub-segmented HAADF segment (to scale). The zoom-in on a part of the detector on the right is labeled with the detector names and their outer physical radius in mm. The HAADF detector is 2 cm in diameter and has the largest surface area among all the segments.

used alone in the STRATA. The other segments (DFa-c and HAADF) can be used at the same time and were labeled as “HAADFp” by the developers.

Each segment of the STEM detector covers different scattering angles, determined by the segment’s inner and outer physical radii r and the distance between the specimen and the detector (Figure 3.2 a). Moving the specimen up and down (in z -direction) changes the detected scattering angles and also the WD between the lower end of the pole piece and the specimen. The distance l_{pd} between the pole piece and the detector is fixed. For the STRATA, it is $l_{pd} = 18.3$ mm, whereas it is $l_{pd} = 40.0$ mm in the HELIOS microscope. This results in a different coverage of scattering angles by the STEM detector at STRATA and HELIOS, as shown in Figure 3.2 b: The angles detected by the HAADF segment at the HELIOS microscope are considerably smaller than in the STRATA microscope. As the range of WD is limited, it is not possible to reach identical HAADF detection angle ranges in the two microscopes.

The detection angle θ_{det} as a function of the geometry of the microscope can be expressed in a short formula:

$$\theta_{det} = \arctan \left(\frac{r}{l_{pd} - WD} \right), \quad (3.1)$$

¹The reason for this and the large distance between the pole piece and the detector at HELIOS is the same: The goal is to minimize the BF segment’s detection angle. The technically possible radius has a lower limit, so those two tricks are used. A small detection angle is desired for high-resolution imaging when the beam diameter is larger than the atomic distance. High-resolution BF-STEM imaging in SEM is an exciting topic but beyond the scope of this work.

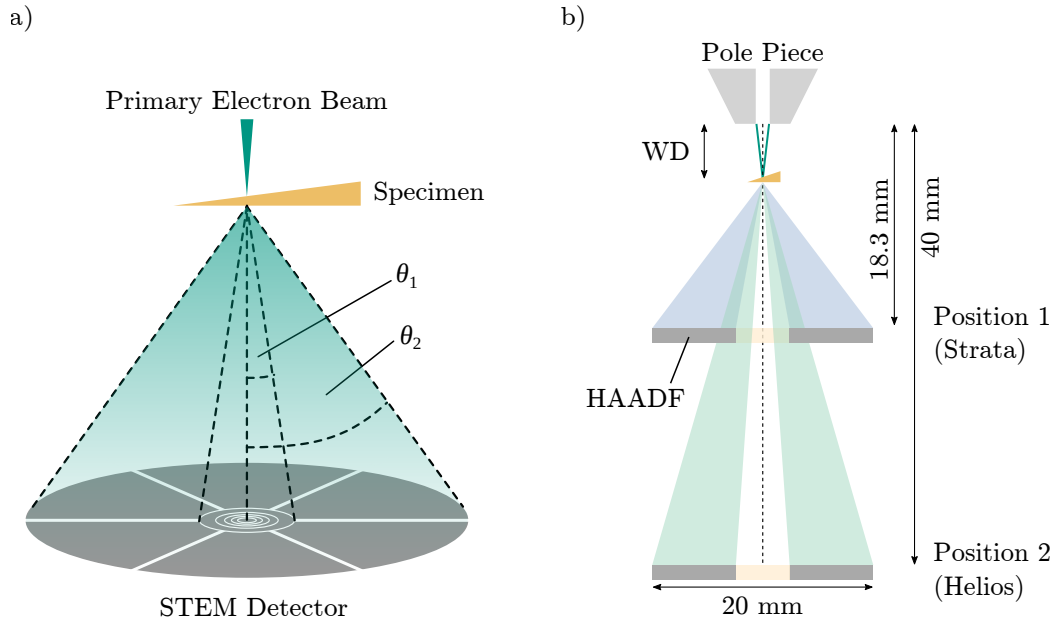


Figure 3.2. Schematic representation of the STEM detector and the detection angles in STEM-in-SEM. a) Principle of measurement, showing two scattering/detection angles ranges. The scattering angle θ refers to the angle to the optical axis. b) Correlation between detection angles and the distance between pole piece and detector. The width of the HAADF segments and the distances to the lower end of the pole piece are to scale. The detection angles are drawn for $WD = 5$ mm.

where $l_{pd} - WD$ is the camera length. The detection angle interval of the HAADF segment in the HELIOS is $68 \text{ mrad} - 272 \text{ mrad}$ for a typical WD of 4.2 mm . This is in fact so small that it is still influenced by coherent Bragg diffraction, even at 30 keV . The (220) reflection of Si, for example, is found at $2\theta_B = 36 \text{ mrad}$, which means that the second order (440) already falls on the HAADF segment. The detection-angle range of the HAADF detector in the Helios often prevents pure atomic-number (Z) contrast in HAADF-STEM images [Yam+18]. The large l_{pd} in HELIOS is presumably used in the HELIOS to minimize the collection angle on the BF segment together with the aperture to allow for BF-STEM lattice-fringe imaging. Due to the smaller l_{pd} in the STRATA, the detection-angle range there is $168 \text{ mrad} - 617 \text{ mrad}$ for $WD = 4.2 \text{ mm}$.

3.2.2. Quantitative Intensity Measurements

For quantitative measurements with the STEM detector, contrast and brightness settings need to be carefully set such that the intensity is neither under-saturated nor over-saturated. It also makes sense to use the full range of available gray values and save the images as 16 bit, corresponding to 65536 gray values. For calculating relative intensities, these gray values (intensities) I_{exp} of the image are normalized with the highest and lowest gray values I_0 and I_b under the chosen microscope

settings. They are determined by directly scanning the STEM detector without the specimen, as shown in Figure 3.3. The black-level intensity I_b is then subtracted from the image intensity values I_{exp} before the normalization with the corrected intensity I_{corr} of the direct electron beam:

$$I_{\text{rel}} = \frac{I_{\text{exp}} - I_b}{I_{\text{corr}} - I_b}. \quad (3.2)$$

The correction of I_0 takes into account the case where a certain proportion of the nominal detector area is physically covered or is less active and thus cannot (fully) contribute to the measured intensity [HMG19].

There are two possible ways to determine I_{corr} from I_0 :

1. For the **HAADF** segment: Normalizing I_0 with the ratio c between the actually active area and the nominal HAADF area, defined by the inner and outer detection angles.

$$I_{\text{corr}} = c \cdot I_0 \quad (3.3)$$

In the case of the HELIOS microscope, an aperture covers 7.95 % of the nominal HAADF area, thus c is 0.9205. The aperture with the shielding bars is highlighted in Figure 3.3a. To make the HAADF segment visible and determine I_0 , the detector has to be decentered, as the pole piece limits the view (marked by an orange circle in Figure 3.3a). The STEM detector of the STRATA microscope does not have an aperture, thus $c = 1$.

Averaging over large regions of the STEM detector when determining I_0 , including dark spots or lines on the active detector segment (see Figure 3.3b), considers less responsive areas, assuming that their distribution is homogeneous. Focusing on the detector is not needed. The defocused image leads to automated averaging of brighter and darker areas of the active area. Subtracting the less active areas completely from the active area, as it is done for the aperture above, can over-correct the problem, as their intensity is larger than I_b .

This method to correct the highest gray value I_0 by multiplying with c (Equation (3.3)) makes sense if only one STEM detector segment is evaluated, as in Chapter 5.

2. If **more than one** segment is used at the same time, the less active areas between them need to be taken into account. Figure 3.4 shows the STEM detector of the STRATA microscope with the three outer DF segments and the HAADF segment activated. In this microscope, parts of the HAADF segment are visible without decentering the detector. Especially at higher primary electron energies (here 30 keV), the connecting rings between the active segments

as well as the conducting tracks of the detector electronics are not entirely black. Their gray level is $I_{\text{gray}} \geq I_{\text{b}}$ and can be measured in the image of the detector (Figure 3.4). In Chapter 4, the STRATA microscope is used, and the signals from all STEM segments are added, if possible by activating them simultaneously during imaging. However, not all detector segments can be active simultaneously at STRATA (see Section 3.2.1). The signals hence need to be added during the evaluation process (Section 4.3.3 on page 58). The signal of the inactive circular regions between the added segments gradually drops to I_{b} at the border to the inactive segments (see arrow “inactive” in Figure 3.4). The corrected intensity I_{corr} is therefore

$$I_{\text{corr}} = I_0 \cdot a_0 + I_{\text{gray}} \cdot a_{\text{gray}} + I_{\text{b}} \cdot a_{\text{b}} , \quad (3.4)$$

taking into account the share of fully active (a_0), less sensitive (a_{gray}), and inactive (a_{b}) detector segments from the nominal area of the detector segments [HMG19]. Those areal ratios add to

$$a_0 + a_{\text{gray}} + a_{\text{b}} = 1. \quad (3.5)$$

The method described here can be used to normalize and quantify any measured STEM intensity if the black and white intensity value of the detector, and its geometrical characteristics are known (see Equation (3.3) and Equation (3.4)). When Equation (3.2) is used to quantify the STEM intensities of each pixel in an image, it yields an image with relative intensity values $0 \leq I_{\text{rel}} \leq 1$.

The normalized intensities allow determining the beam broadening as described in Chapter 4. Furthermore, experimental values of I_{rel} can be compared to simulated values, which was used for the determination of contamination thicknesses in Chapter 5.

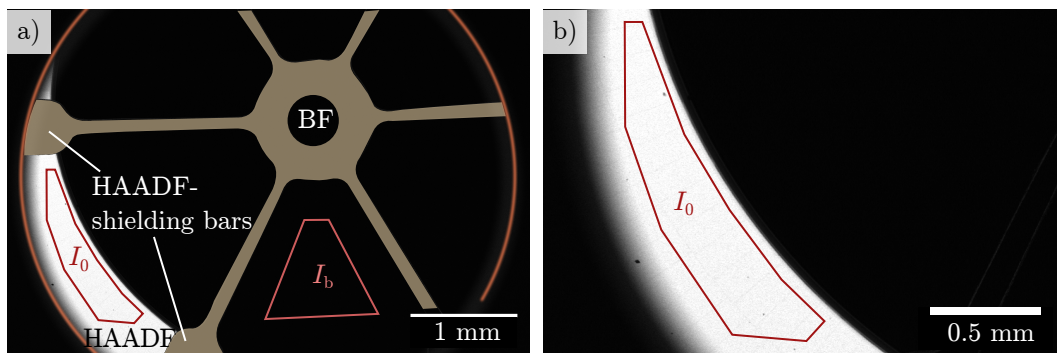


Figure 3.3. 20 keV HAADF-STEM image of the STEM detector in the HELIOS microscope, obtained by scanning the entire field of view at the lowest magnification with the HAADF segment active. The HAADF segment thus appears bright. a) The pole piece (marked by an orange circle) limits the view, and only a small part of the HAADF segment is visible. To make it visible, the detector was intentionally decentered with the STEM centering mode. b) Zoom-in on the HAADF segment in a), revealing its inhomogeneities.

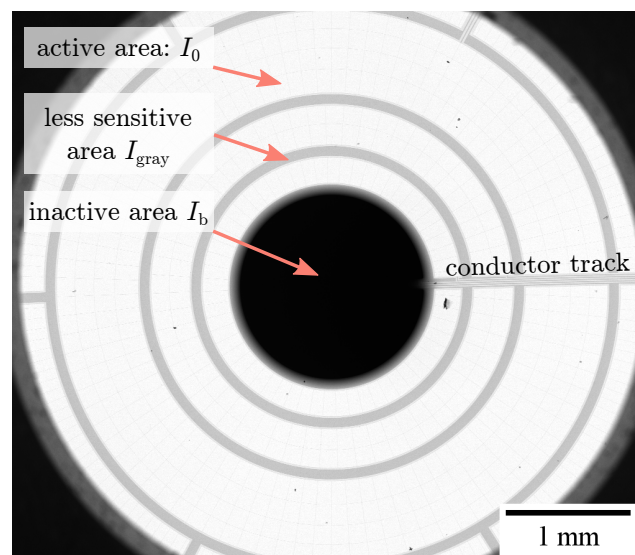


Figure 3.4. 30 keV STEM image in the STEM detector at the STRATA microscope. It was obtained by focusing the electron beam on the detector and scanning it with activated DF_a-c and the HAADF segment, which appear bright. Again the pole piece limits the view, and only the innermost part of the HAADF segment is visible [HMG19].

Chapter

4. Beam Broadening

In this chapter, the measurement of beam broadening in thin samples is described and compared to a recent theoretical model. Beam broadening is a key factor that has to be kept in mind when discussing lateral resolution in STEM. The specified beam diameter is only valid at the top of the sample. Interactions between the electrons and the sample lead to a change of their propagation direction and to broadening of the beam in the sample. Beam broadening impedes the interpretation of images since it worsens the lateral resolution of a STEM image, especially for features that are in deeper regions of the sample (top-bottom effect) [JVD18]. It is therefore helpful to quantify beam broadening depending on parameters like the sample's material and thickness, and the electron-beam energy. This chapter is based on the publication: M. Hugenschmidt, E. Müller, and D. Gerthsen. “Electron beam broadening in electron-transparent samples at low electron energies”. In: *Journal of Microscopy* 274.3 (2019), pp. 150–157. DOI: 10.1111/jmi.12793, but gives more detailed insights into different beam broadening models. In Section 4.2, the fundamentals of beam broadening will be outlined. The method Section 4.3, starting from page 56, will then describe the simulations, the preparation of test samples, and the evaluation of the measurements. Section 4.4, starting from page 63, finally shows the experimental and simulated values of beam broadening and classifies them in comparison with one of the theoretical models.

4.1. Introduction to Beam Broadening

Analytic equations for beam broadening b in amorphous samples can be derived based on single elastic Rutherford scattering [Gol+77], or random walk models [GR16], but also the spread of a Gaussian that describes the distribution of electrons in the beam [DLF80; Rei98; RK08]. Numerical solutions are obtained from the Boltzmann transport equation [Gro75; Ros75; MHG20] and Monte-Carlo simulations [FN78; HEM08; Sou+09; Dem+12].

Goldstein et al., Reimer, and Gauvin and Rudinsky derived analytical equations

beam broadening from single scattering, assuming a Gaussian distribution, and random walk, respectively. All three models neglected energy loss and lead to different equations that have a proportionality of $b \propto t^{1.5}$ (in the last case only for the multiple scattering regime) [Gol+77; Rei98; GR16]. These models are described in more detail in Section 4.2.2 on page 50.

Rez used the Boltzmann transport equation to calculate projected angular distributions at the bottom surface of samples. His model considered the angular distribution of inelastic scattering but neglected energy loss. Evaluating the full width half maximum (FWHM) of those projected distributions, he found a power-law dependence on the sample thickness t as well, however with a larger exponent $b \propto t^{1.88}$ [Rez83]. Similarly, Demers et al. found in their Monte-Carlo simulations of beam broadening in amorphous carbon for $t \leq 5 \mu\text{m}$ that the $t^{1.5}$ proportionality overestimates the beam diameter at smaller thicknesses and underestimates it at large thicknesses [Dem+12]. This may suggest a larger exponent as well.

Recently, Müller, Hugenschmidt, and Gerthsen published their simulations of the angular distribution of electrons in the sample by solving the transport equation without neglecting energy loss [MHG20]. Regarding beam broadening, their main statement was that the mean penetration depth of the electrons, corresponding to t , is always smaller than the traveled path length, which is the correct parameter for calculations of beam broadening. This difference increases with t and explains why their results diverge from the analytical models neglecting energy loss when the maximum penetration depth of the electrons is reached. t then approaches a constant value, whereas the traveled path length increases further, and with it the beam diameter. Interestingly, their simulations reproduce the $t^{1.5}$ proportionality for lower sample thicknesses.

EXPERIMENTS

Jonge, Verch, and Demers measured beam broadening in 200 keV STEM by evaluating the intensity profiles of Au nanoparticles (NP) embedded in different horizontal layers in an Al matrix of 0.6 μm and 1 μm thickness [JVD18]. They found that the resolution of NP is independent of the vertical position for those NP close to the upper surface, but beam broadening then quickly worsens the resolution. The authors compared their experimental results to the single scattering model, the Gaussian-based model, and the model based on anomalous diffusion [Gol+77; Rei98; GR16], and found the best agreement with the random walk model. A similar approach of deriving beam broadening from NP as test objects had already been used earlier for quantifying the top-bottom effect [GGR74; RR87]. Drees et al. studied beam broadening in thin amorphous carbon films with $t < 120 \text{ nm}$ at beam energies up to 30 keV, estimating that the mean number of scattering events was only up to 2.5. For this case of thin samples, they found $b \propto t^2$, which agreed with their Monte-Carlo simulations and the anomalous diffusion model for the case of thin samples by Gauvin and Rudinsky [GR16] (see page 52). However, they found that both

simulations and the theory underestimate beam broadening with decreasing beam energy. They speculated this is caused by thermal-diffuse scattered electrons, which are not considered in the calculations.

Many works analyze beam broadening concerning its influence on X-ray spatial resolution and sensitivity [FN78; FHN77; Gol+77; Wil+92], a topic that this work is not further focusing on. Beam broadening is of particular importance in the field of liquid cell imaging and STEM tomography of biological samples, where the sample thickness is large [Jon+10; HEM08; Jon18], and for STEM imaging at low beam energies, especially when aberrations are corrected [Sas+14].

Although it is seldom discussed, it also occurs in TEM, since every single ray in the parallel beam can undergo multiple scattering as well [Gro75]. Due to the theorem of reciprocity, the top-bottom effect is inverted in TEM, and details at the bottom of a specimen are imaged with better spatial resolution [GGR74; RR87].

This study on beam broadening now aims to continue the studies by Jonge, Verch, and Demers [JVD18] and by Drees et al. [Dre+17] by expanding the range of investigated materials, sample thicknesses and/or primary electron energies, which allows testing the anomalous diffusion model in more detail.

4.2. Fundamentals of Beam Broadening

The fundamentals needed for this chapter start with defining beam broadening. The focus is then on the different theoretical models to describe beam broadening, from the widely used Goldstein equation to the more recent anomalous diffusion model.

4.2.1. Definition of Beam Broadening

As the electrons penetrate the sample, they are scattered in different directions. Considering electrons as particles, they follow different paths that are visualized using a Monte-Carlo simulation in Figure 4.1. In the upper region of the sample, forward scattering dominates and the electrons are relatively close together. Reaching deeper areas of the sample, the electrons are scattered multiple times and the distribution of electrons gets blurry. In this work, beam broadening b is defined as the diameter of the beam in the sample, neglecting the initial diameter of the beam hitting the sample. Figure 4.1 shows that the beam broadening is not uniquely defined, since the electron distribution has no clear boundary and is rather blurred. It is thus reasonable to define the beam diameter as the diameter of the passed disc area that contains a certain fraction R of the overall electrons for a defined depth in the sample. This fraction was chosen to be $R = 68\%$ here, mainly due to the evaluation method that will be described in further detail in Section 4.3.3 starting from

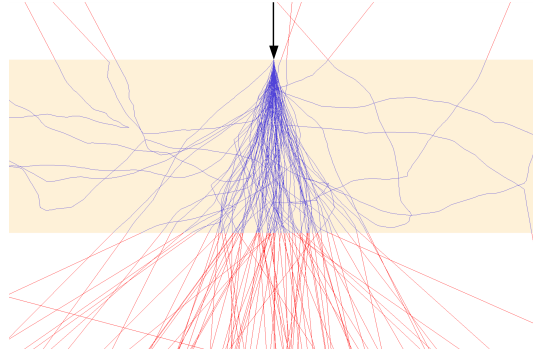


Figure 4.1. Visualization of electron paths in a 1500 nm thick Si sample, simulated with Monte-Carlo simulation for $E_0 = 30$ keV. Electrons in the sample are shown in blue, electrons outside are shown in red.

page 58. However, various definitions of R can be found in the literature. Apart from $R = 68\%$ [Dre+17], whereby 68% corresponds to one standard deviation σ of the normal distribution, $R = 90\%$ is the most often used definition [GR16; Ree82; Wil+92]. Other authors use the FWHM as definition of beam diameter [Rez83; HEM08]. Beam broadening b is expected to increase with increasing thickness t of the sample and decreasing primary electron energy E_0 . Additionally, it depends on the material's properties like atomic number Z , material density ρ , and atomic mass A :

$$b = b(t, E_0, Z, \rho, A) . \quad (4.1)$$

4.2.2. Theoretical Description of Beam Broadening

Goldstein Model A theoretical description of beam broadening was published by Goldstein et al. already in 1977 [Gol+77]. The authors neglected the screening of the nucleus by orbital electrons by using the unscreened elastic differential Rutherford cross-section (Equation (2.2) on page 7). The integrated cross-section for scattering in angles $> \theta^*$ can be calculated from the differential cross-section (appendix, Section A):

$$\sigma(\theta^*) = \frac{\pi e^4 Z^2}{(4\pi\epsilon_0)^2 m^2 v^4} \cot^2 \left(\frac{\theta^*}{2} \right) . \quad (4.2)$$

With the number of atoms per unit area $Nt = \frac{N_A \rho}{A} t$ [Rei98], the probability p of scattering through an angle $> \theta^*$ is:

$$p = N \cdot t \cdot \sigma(\theta^*) \quad (4.3)$$

$$\begin{aligned} &= \frac{\pi e^4 N_A}{(4\pi\epsilon_0)^2} \frac{Z^2}{A} \frac{1}{E_0^2} \cot^2\left(\frac{\theta^*}{2}\right) \rho t \\ &= 1 - R, \end{aligned} \quad (4.4)$$

with the characteristic¹angle θ^* including the fraction R of the beam (here 68%). The calculation of beam broadening is now based on the assumption that the electrons are scattered once at the center of the sample into a cone with an opening angle θ^* (Figure 4.2). This geometrical relation gives

$$b = t \tan(\theta^*) . \quad (4.5)$$

In the last step, small angles θ^* are assumed, such that $\cot(\theta^*/2) \approx 2/\theta^*$ and $b \approx t \cdot \theta^*$, which gives $\cot(\theta^*/2) \approx \frac{2t}{b}$. Inserting this into Equation (4.4) finally leads to the

Goldstein Equation

$$b = \frac{\sqrt{\pi e^4 N_A}}{2\pi\epsilon_0} \frac{1}{\sqrt{1-R}} \frac{Z}{E_0} \sqrt{\frac{\rho}{A}} t^{3/2} . \quad (4.6)$$

Combining all constants in a factor a , this simplifies to

$$b = a \cdot \frac{Z}{E_0} \sqrt{\frac{\rho}{A}} t^{3/2} . \quad (4.7)$$

With sample thickness t and beam broadening b in units of nm, the (average) atomic number Z , the material density ρ given in units of g cm^{-3} , the (average) atomic mass A in g/mol , E_0 in keV, and $R = 0.68$, the factor is $a = 0.11$ in units of nm keV . A second model by Reed considers single scattering as well, but with a uniform probability of the scattering event taking place along the depth of the sample [Ree82]. By then integrating with respect to depth, Equation (4.7) with a changed factor $a = 0.13 \text{ nm keV}$ is retrieved.

¹The term “characteristic” does not indicate a particular physical process here. It rather means that θ^* is characteristic for the chosen R fraction.

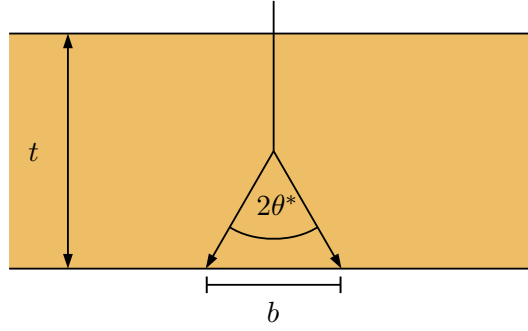


Figure 4.2. Illustration of the determination of beam broadening b in a sample of thickness t after Goldstein et al. [Gol+77]. The relation $b = t \tan(\theta^*)$ can be derived from this figure. The characteristic scattering angle θ^* is the opening angle of the scattering cone and corresponds to the scattering angles in Figure 4.7.

Reimer Model Reimer assumed a Gaussian electron intensity distribution (compare Equation (2.26))

$$I(r) \propto \exp\left(-r^2/r^2\right) \quad (4.8)$$

as a function of distance r from the optical axis at a certain depth in the sample to describe beam broadening. This results in a beam width expressed through the root-mean-square value r_{RMS}

$$b_{\text{RMS}} = 2r_{\text{RMS}} = 2\sqrt{2} \cdot 1.05 \cdot 10^5 \frac{Z}{E_0} \left(\frac{\rho}{A}\right)^{0.5} t^{3/2} \quad (4.9)$$

with the beam diameter b_{RMS} and the sample thickness t in cm, E_0 in eV, ρ in g/cm^3 and atomic mass in g/mol [Rei98; RK08]. Though the used model differs substantially from the Goldstein model, the same parameter proportionalities are retrieved. The R fraction is not used here because the definition of the beam diameter is inherent in the definition of the Gaussian intensity distribution.

Anomalous Diffusion Model A more general approach to describe beam broadening was introduced by Gauvin and Rudinsky [GR16]. They used a random walk model, where beam broadening is defined as the lateral distance between the particle's position and the point where it entered the sample (Figure 4.3). This definition leads to an equation defining the beam diameter b as

$$\frac{b}{2} = \sum_{i=1}^n r_i, \quad (4.10)$$

where n is the number of scattering events and r_i is the traveled lateral distance for a single scattering event. Therefore, one main parameter of the model is the number of scattering events n . It equals the ratio between sample thickness t and mean free

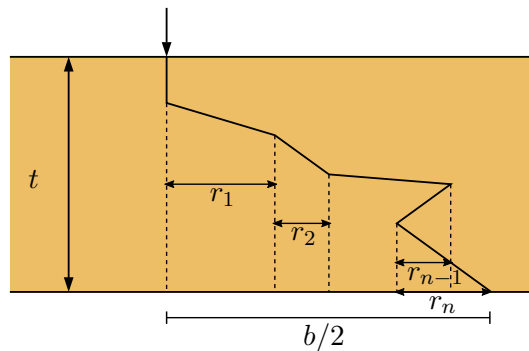


Figure 4.3. Illustration of the determination of beam broadening b in a sample of thickness t after Gauvin and Rudinsky, used for the anomalous diffusion model [GR16]. r_i are the projected distances of each collision, leading to the relation $b/2 = \sum_{i=1}^n r_i$.

path length Λ (see Section 2.1.2 on page 9)

$$n = \frac{t}{\Lambda} . \quad (4.11)$$

n is 0 or 1, if zero or one scattering event occurs, but also describes plural scattering ($1 < n < 25$) up to the multiple scattering/diffusion regime ($n \geq 25$) [Rei98]. Before going back to Equation (4.10) and expressing its right side depending on the scattering regime, a few words on the theoretical background are needed. Random walks are the basis of this model for beam broadening and can be described with the help of anomalous diffusion and fractal theory [HB02]. Anomalous diffusion is usually expressed by a power-law:

$$\langle x^2(T) \rangle \simeq K_\alpha T^\alpha = K_\alpha T^{2H} , \quad (4.12)$$

where $\langle x^2(T) \rangle$ is the mean squared distance after a time T , depending on the anomalous diffusion exponent α and the diffusion coefficient K_α [Met+14]. Gauvin and Rudinsky use the Hurst exponent $H = \alpha/2$ instead of α . This Hurst exponent was originally introduced by Mandelbrot and Ness to describe fractional Brownian motions, and lies between 0 and 1 [Mv68]. It serves to distinguish the different diffusion regimes, as shown in Figure 4.4. $H = 0.5$ is the case of normal diffusion or Brownian diffusion, where the mean displacement increases linear with time. This is the case when the sample thickness is larger than the mean free path length ($t/\Lambda > 1$). According to Gauvin and Rudinsky, $H = 0.5$ is reached when the number of scattering events 'is large' [GR16]. The definition given above ($t/\Lambda \geq 25$) may be a guiding value. $0 < H < 0.5$ characterizes the subdiffusion regime, where the diffusion is slower. $H > 0.5$ characterizes the superdiffusion regime [MK00], where the mean squared distance increases faster than for normal diffusion. This regime is typically not termed as diffusion in electron microscopy, because it involves additionally directed transport of electrons (incident beam). The special case where $H = 1$ char-

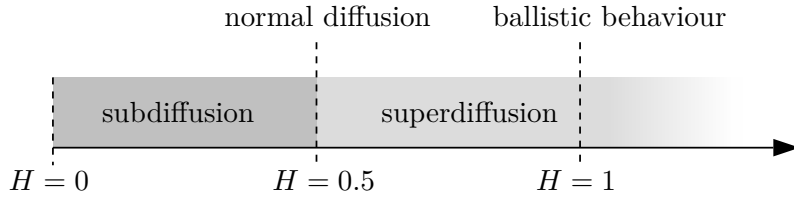


Figure 4.4. Domains of anomalous diffusion after Metzler and Klafter [MK00].

acterizes the ballistic regime of $t/\Lambda \rightarrow 0$, where the electrons move encounter no or only few interactions.

How does the anomalous diffusion model now help to calculate the beam broadening, or, more specifically, the right side of Equation (4.10)? The following description goes into some details of the model and the final equation in the box a few pages onward. Having said that, the derivation of the final equation is inevitable to understand the limitations of the anomalous diffusion model, and thus worth reading.

Gauvin and Rudinsky propose an equation for the sum of lateral distances, similar to the power-law Equation (4.12) that describes the mean squared deviation after a time T :

$$\sum_{i=1}^n r_i = \langle r_i \rangle n^H, \quad (4.13)$$

where $\langle r_i \rangle$ is the mean lateral distance for each collision [GR16]. Equation (4.10) then becomes

$$\frac{b}{2} = \langle r_i \rangle n^H, \quad (4.14)$$

which is the generalized description of beam broadening covering superdiffusion (0 or 1 scattering events) as well as normal diffusion ($H = 0.5$) and subdiffusion (more scattering events).

The mean projected lateral distance $\langle r_i \rangle$ in the bottom plane for each scattering event is

$$\langle r_i \rangle = \frac{t}{2} \tan(\theta^*) \approx \frac{t}{2} \theta^* \quad \text{for small } \theta^*, \quad (4.15)$$

with the characteristic scattering angle θ^* as defined in Figure 4.2. Note that this correlates to one single scattering in the center of the sample again, as in the Goldstein model. This leads, inserted to Equation (4.14), to

$$b = \theta^* \cdot \frac{t^{1+H}}{\Lambda^H}. \quad (4.16)$$

The angle θ^* and the mean free path length Λ need to be expressed based on known

parameters. The path length was already defined (Equation (2.7)): $\Lambda_t = \frac{A}{N_A \rho \sigma_t}$. θ^* contains a defined fraction of all beam electrons, in this work $R = 68\%$ by convention. It can be calculated for single scattering solving the equation

$$R = \frac{\int_0^{\theta^*} \frac{\partial \sigma}{\partial \Omega} \sin \theta d\theta}{\int_0^\pi \frac{\partial \sigma}{\partial \Omega} \sin \theta d\theta} \quad (4.17)$$

[GR16] using the screened Rutherford cross-section (Equation (2.3)). The denominator is the total screened Rutherford cross-section (Equation (2.10))

$$\sigma_t \simeq \frac{e^4}{\pi(4\epsilon_0)^2} \left(\frac{Z}{E_0} \right)^2 \frac{1}{\theta_0^2} \quad (4.18)$$

for $\sin(\theta_0/2) \approx \theta_0/2$ and $\theta_0^4 \approx 0$ if the screening angle θ_0 is small. The numerator of Equation (4.17) is calculated using the substitution $u = \cos(\theta) \Leftrightarrow \sin(\theta)d\theta = -du$. After some transformations, this becomes

$$\cos(\theta^*) = 1 - \frac{2 \frac{\theta_0^2}{4} R}{1 + \frac{\theta_0^2}{4} - R} . \quad (4.19)$$

By assuming $\frac{\theta_0^2}{4} \ll 1$ and developing $\cos(\theta^*) \approx 1 - (\theta^*)^2/2$ with the Taylor expansion for small θ^* , finally

$$\theta^* = \sqrt{\frac{R}{1-R}} \theta_0 , \quad (4.20)$$

is obtained, the characteristic angle that contains a given fraction of the beam electrons. For the screening angle the expression

$$\theta_0 = \frac{0.1167 Z^{1/3}}{\sqrt{E_0}} \quad (4.21)$$

is used, with E_0 in keV [GR16; WC09]. With this equation and Equation (4.16), (2.7), (4.18), and (4.20) everything is there to calculate the beam broadening as a function of physical parameters and H . This leads to the general formulation of the Gauvin/Rudinsky equation:

$$b = K' \cdot \frac{Z^{(1+4H)/3}}{E_0^{(1+2H)/2}} \cdot \left(\frac{\rho}{A} \right)^H \cdot t^{1+H} \quad (4.22)$$

with the factor

$$K' = 0.1167^{1-2H} \cdot (\pi e^4 N_A)^H \cdot (4\pi\epsilon_0)^{-2H} \cdot \sqrt{\frac{R}{1-R}} \quad (4.23)$$

The equation is in SI units (except for E_0 in keV) and becomes clearer if Gaussian

units are used, with b and t in cm, and $4\pi\epsilon_0 = 1$. The equation then reduces to

Beam Broadening from the Anomalous Diffusion Model

$$b = 0.1167^{1-2H} \cdot (39437)^H \sqrt{\frac{R}{1-R}} \cdot \frac{Z^{(1+4H)/3}}{E_0^{(1+2H)/2}} \cdot \left(\frac{\rho}{A}\right)^H \cdot t^{1+H} \quad (4.24)$$

with the materials density ρ given in g cm^{-3} , the (average) atomic mass A in atomic mass units, E_0 in units of keV, and b and t in cm [GR16].

In the case of plural and multiple scattering, the behavior of the electrons becomes a random walk, characterized by $H = 0.5$. Equation (4.24) then reduces to the Goldstein Equation (4.6) with the $t^{1.5}$ proportionality but with a different numerical factor a . As already mentioned, $H = 1$ is valid for $t/\lambda \rightarrow 0$ and describes the ballistic regime. In this case, the equation becomes $b = K' \frac{Z^{5/3}}{E_0^{3/2}} \frac{\rho}{A} t^2$. This equation has been confirmed in experiments on thin amorphous carbon films [Dre+17].

Notably, all beam broadening models that were described here have a general limitation: They use the sample thickness t as the key parameter. However, the traveled path length is the correct parameter for describing beam broadening, as the distance traveled by the electrons differs from the sample thickness. The traveled path length and depth in the sample are in fact only similar up to some scattering events when the zig-zag behavior of scattered electrons is not yet that strong. This topic has been addressed in a recent work published by our group [MHG20].

4.3. Experimental Methods

One main parameter of beam broadening is the traveled distance in the sample, which depends on the sample thickness, as long as the mean penetration depth does not reach a constant value [MHG20]. Thus specimens with precisely known thickness, apart from known composition, are needed for experimental studies. The determination of beam broadening then needs precise measurements and a microscope with well-known geometry, as well as careful evaluation of experimental STEM intensities. Simulations of scattered intensities are also used to test theoretical models.

4.3.1. Simulation of the Angular Distribution of Scattered Electrons

The scattering behavior of electrons in the sample is simulated by the numerical solution of the electron transport equation by using an expansion in Legendre polynomials, similar to the approach by Negreanu [Neg+05]. This is appropriate for electron energies below 30 keV as well as higher electron energies and for single, multiple, and plural scattering, but does not take crystal structures into account. The basics of this calculation are described in Section 2.1.2 on page 9. For details, see the work by Müller, Hugenschmidt, and Gerthsen [MHG20]. The calculations are implemented in the program CeTE1.4 (Computation of electron Transport Equation), which was developed in our group [MHG20]. It allows computing the angular distribution of scattered electrons for given material parameters (Z , ρ , A), sample thickness t , and primary electron energy E_0 . Compared to Monte-Carlo simulations, the computation time is considerably shorter. However, the sample geometry is limited to one homogeneous material and the simulation of layers of different materials is not possible yet. Mean values of material parameters are used for chemical compounds.

CeTE1.4 allows choosing different scattering cross-sections. In this work, the differential screened Rutherford cross-section was used to describe elastic scattering since it adequately describes the experimental STEM intensities. Inelastic scattering is taken into account by the implementation of the continuous-slowing-down approximation of Joy and Luo (Equation (2.15) and Equation (2.18)) [JL89].

4.3.2. Sample Preparation

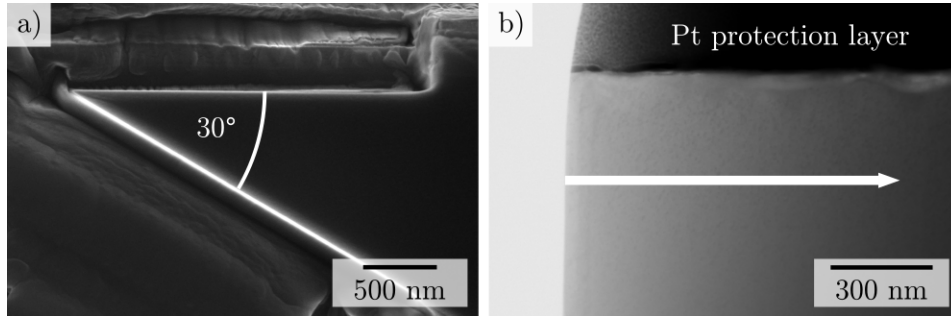
Beam broadening was studied in MgO, Si, SrTiO₃, and Ge, which cover averaged² atomic numbers from $Z = 10$ to 32. All materials either consist of a single element or have a known stoichiometric composition. The relevant material parameters are shown in Table 4.1.

TEM specimens from these materials with known thickness are needed for measuring the beam broadening. Most suitable for this are wedge-shaped specimens that cover a range of different thicknesses. They were prepared with a DualBeam Strata 400S system (former FEI, now Thermo Fisher Scientific) using a focused Ga⁺ ion beam. The sample was first covered with a protecting Pt layer before cutting out a typical TEM lamella, from which a wedge with a defined angle was prepared. Figure 4.5 shows such a wedge sample. The wedge angle and the sharpness of the wedge tip can be seen in the top view SEM image (a). The wedge has a constant angle, apart from the rounded wedge tip, and its thickness is thus well known. However, mainly

²Weighted by the fraction of the total number of atoms associated with each element

Table 4.1. Material properties of sample materials for the determination of beam broadening [Lid05]

Material	(mean) atomic number Z	Material density ρ / $\frac{\text{g}}{\text{cm}^3}$	(mean) atomic mass A / u
MgO	10	3.6	20.15
Si	14	2.33	28.09
SrTiO ₃	16.8	5.1	36.70
Ge	32	5.32	72.64

**Figure 4.5.** A MgO wedge for the measurement of beam broadening. a) 30 keV SE-SEM micrograph in topview, b) 30 keV (BF+DF+HAADF)-STEM image, showing the side perspective of the wedge. The thickness increases along the arrow [Hug18].

the Pt-protection layer is visible in top-view in Figure 4.5 a and slight deviations in the slope of the underlying material cannot be excluded. The same wedge is imaged by the combination of the BF-, DF, and HAADF-segments in (b), where the arrow indicates the direction of increasing thickness. The Pt-protection layer appears dark in the upper area of the image.

4.3.3. Determination of Beam Broadening

Measurements of the angular distribution of transmitted electrons are needed for the experimental determination of beam broadening. For this, STEM images of the wedge-shaped specimens are taken at a DualBeam Strata 400S FIB-SEM microscope by FEI. The probe diameter of the incident electron beam is around 1 nm and the convergence angle α is around 2 mrad [Sun+19]. Both values are considered small enough to neglect their contribution to beam broadening [HEM08].

The transmitted electron intensity as a function of the scattering angle can be accessed by using a multi-segmented STEM detector below the specimen [Dre+17]. As described in Section 3.2.1, the detector in the Strata 400S microscope comprises one BF segment, four narrow DF segments, and an azimuthally segmented HAADF segment, all of which can be controlled separately. The scattering angle covered

by one STEM detector segment is determined by the inner and outer radius of the segment and by the working distance (see Figure 3.2 on page 42).

The measurement and evaluation of scattered intensities is a 4-step procedure:

1. A specific working distance is set.
2. A wedge-shaped sample with defined thickness is imaged with the different detector segments. As the HAADF segment and the outer three DF segments are used together, 3 images are obtained (BF, DF 0, DF a-c + HAADF) (see Section 3.2.1). These images are evaluated by an intensity line profile at identical positions in the direction of increasing thickness (see Figure 4.5 b), yielding measured intensities as a function of sample thickness t . The line scan is averaged over the width of some pixels to reduce noise.
3. These measured intensities are normalized by the intensity of the incident electron beam, as described on page 42, and relative intensity values I_{rel} as a function of t are obtained (Figure 4.6). The curves do not start at $t = 0$ nm since the small thicknesses are missing due to the thickness offset at the wedge tip, and since additional values have to be dismissed at the rounded wedge tip, where the thickness cannot be calculated correctly. The distance from the tip after which the wedge thickness increases linearly was determined by imaging the wedges in top view by SEM (see Figure 4.5a) and by energy-filtered transmission electron microscopy (EFTEM) imaging.
4. The relative intensities measured by consecutive detector segments are summed up and yield the integrated scattered intensity from 0° up to a maximum outer angle defined by the outermost segment (Figure 4.7 on page 61).

When this is repeated for six different working distances, six curves are obtained. Each shows the scattered intensity contained in different maximum scattering angles θ^* . As an example, this is shown for MgO at 20 keV in Figure 4.7. The curves do not begin at a sample thickness t of 0 nm since the wedge is not ideally sharp. However, it seems that the approximately linear curves would cross at $t = 0$ nm, $I_{\text{rel}} = 1$, which agrees with 100 % transmittance of the beam in vacuum. The intensity curves drop faster for smaller outer scattering angles θ^* because the electrons are scattered beyond the surveyed angle already at smaller thicknesses. The relative intensity of 68 %, which is used for the definition of the beam diameter in this work, is marked by a solid horizontal line. The intersections of this line with the intensity curves are clearly separated and yield value pairs for (θ^*, t) , as highlighted by the vertical lines. In this example, beam broadening can be determined for Si for sample thicknesses between 460 nm and 680 nm. It becomes also clear that the typical definition of the beam containing 90 % of all electrons is not suitable here because

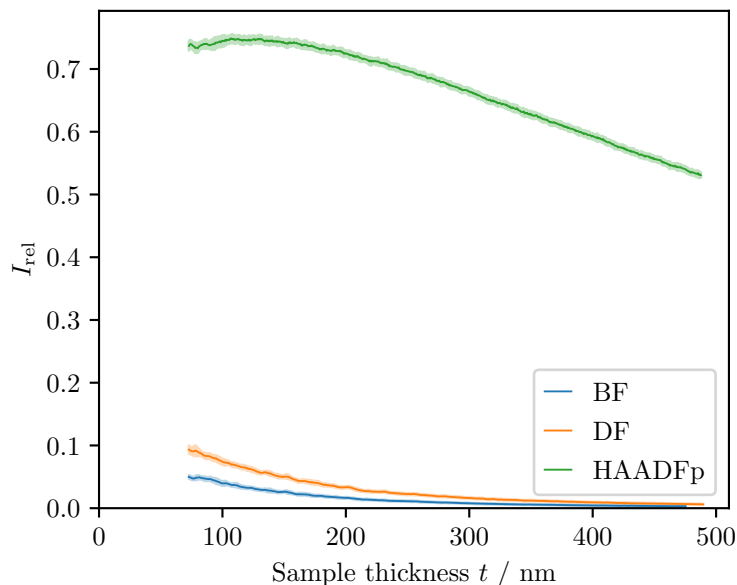


Figure 4.6. Normalized STEM intensities (BF, DF 0, and DF a-c + HAADF (HAADFp)) as a function of sample thickness for MgO at 20 keV and WD = 5 mm. DF 0 is abbreviated as DF here, DF a-c + HAADF as HAADFp. The missing data for smaller sample thicknesses is due to the rounded and not ideally sharp wedge tip. The standard variation resulting from averaging over the width of the linescans, as described in step 2, can be seen as half-lucent background of the intensity curves.

the intersections with the dotted line are not well separated and the covered sample thicknesses are too close together (between 130 nm and 190 nm). The value pairs (θ^*, t) and Equation (4.5) (page 51) are then used to calculate the experimental values for beam broadening b , assuming that the electrons are on average scattered in the center of the sample (see Figure 4.2 on page 52). The very same evaluation procedure is used to evaluate the beam broadening for different primary electron energies (15 keV to 30 keV) and materials (MgO, Si, SrTiO₃, and Ge). It is also applied to obtain simulated values for beam broadening from simulated scattered intensity distributions as described in section Section 4.3.1 on page 57.

As none of the theories in this chapter considers coherent scattering from crystalline samples, the influence of the crystalline structure during the measurement was aimed to be minimal. This was checked by investigating each material under different tilt angles towards the electron beam (6° apart). As the obtained STEM intensities did not differ considerably, the influence of crystallinity was found to be negligible. Two-beam conditions can furthermore be excluded by checking the BF-STEM image for thickness contours. If they are visible, the sample is tilted until the thickness contours disappear to avoid a strong influence of Bragg diffraction on the measurement. In general, Bragg scattering gets less dominant with larger sample thicknesses. That means it should not have a large influence on the intensities measured here.

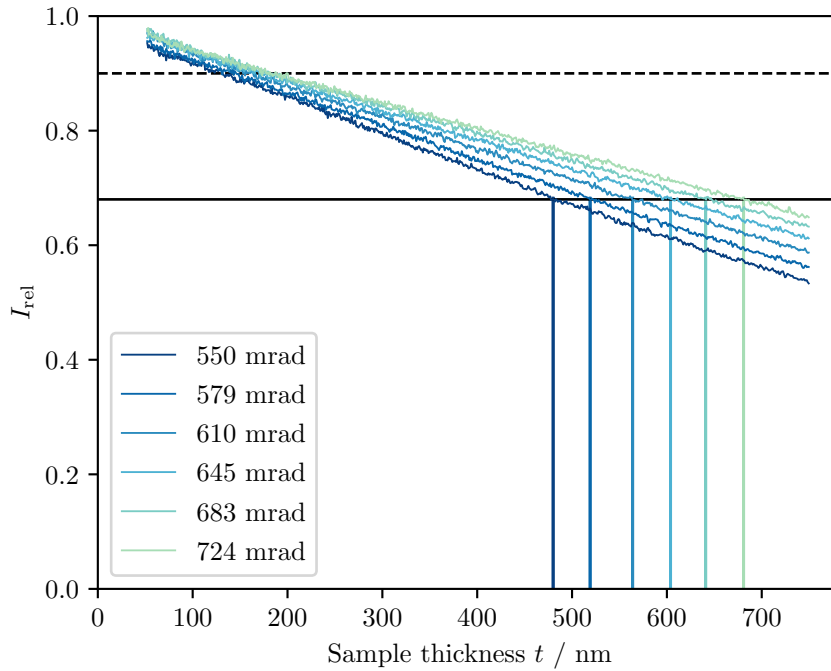


Figure 4.7. Normalized STEM intensities below maximum scattering angles (given in the legend) as a function of sample thickness for Si at 25 keV. Normalization was performed with respect to the incident electron intensity according to Equation (3.4) on page 44. Solid vertical lines indicate the thicknesses where the intensity curves intersect with 68% of the total intensity, marked by the solid horizontal line. The dashed line marks 90% of the total intensity.

4.3.4. Error Analysis

4.3.4.1. Propagation of Uncertainty

The main possible error that influences the determination of beam diameter is the uncertainty of the sample thickness. The uncertainty of the measured scattering angle, is neglected because it is smaller than the influence of the thickness error. The two parameters influencing the thickness error are the thickness offset at the wedge tip and the wedge angle. The thickness offset was determined to be 38, 30, 27, and 23 nm for the MgO, Si, SrTiO₃, and the Ge wedge, respectively, by SEM top-view images. The assumed uncertainty of this offset value is $\sigma_{\text{offset}} = 10$ nm. Note that the uncertainties σ are always positive by definition of the confidence interval. The confidence interval x of a measurement is defined as $x = \bar{x} \pm \sigma$, where \bar{x} is the experimentally determined value and σ is the uncertainty. The angle α of the wedge has to be determined in a top-view image too, as shown in Figure 4.5 on page 58. The angles range between $\alpha = 30^\circ$ and 16° , with an assumed uncertainty of $\sigma_\alpha = 0.5^\circ$. Because $t = x \cdot \tan(\alpha)$ and with the maximum real wedge angle being

$\alpha_{\max} = \alpha + \sigma_\alpha$, the absolute uncertainty caused by σ_α is

$$\sigma_{t,\alpha} = x (\tan(\alpha_{\max}) - \tan(\alpha)) \quad (4.25)$$

$$= x (\tan(\alpha + \sigma_\alpha) - \tan(\alpha)) \quad (4.26)$$

for each distance x from the wedge tip. The error gets larger with increasing sample thickness due to the influence of x . The resulting error of the sample thickness is then calculated by a square sum of the contribution of the angle and the thickness offset of the wedge:

$$\sigma_t = \sqrt{\underbrace{(\tan(\alpha + \sigma_\alpha) - \tan(\alpha))^2 \cdot x^2}_{\sigma_{t,\alpha}^2} + \sigma_{\text{offset}}^2} . \quad (4.27)$$

When adding the intensities measured by different detector segments, as described in step 4 on page 59, the resulting associated thickness errors are again calculated by a square sum from the errors in the individual measurements. To impede further errors due to the rounded wedge tip, where the slope is not linear, measured intensity values near the wedge tip are discarded. This linearity was checked both in SEM top view images as well as by EFTEM imaging in a Titan³ 80-300 Transmission electron microscope (FEI) using a Tridiem 865 ER image filter by Gatan. The uncertainties on the intensity values, caused by the line scan, are small enough to be neglected in the error calculation (see Figure 4.6 on page 60). The error of the sample thickness determination thus finally propagates with

$$\sigma_b = |\tan(\theta^*) \cdot \sigma_t| \quad (4.28)$$

to calculate the uncertainty σ_b of each beam broadening value $b = t \tan(\theta^*)$ (Equation (4.5) on page 51) with the outer scattering angle θ^* .

4.3.4.2. Measure of Fit Quality

In this chapter, the normalized mean absolute error (nMAE) quantifies the goodness of a fit. It is defined as

$$\text{nMAE} = \frac{\sum_{i=1}^n |Y_i - \hat{Y}_i|}{\sum_{i=1}^n Y_i} \quad (4.29)$$

with n being the number of measured/predicted values, Y_i the measured values, and \hat{Y}_i the predicted values. Its range is 0 to $+\infty$, with 0 indicating a perfect fit [Yu+06].

4.4. Results and Discussion

Figure 4.8 shows the measured beam diameter for the investigated materials and the exemplary primary electron energy of 25 keV. Looking at the material properties in Table 4.1 on page 58, we see that the beam diameter increases with increasing atomic number, as expected. Although MgO has a smaller average atomic number than Si, it shows stronger beam broadening, probably due to the higher material density. With beam broadening values between 100 nm and 600 nm, neglecting the primary beam diameter in the calculations is justified. The anomalous diffusion model of beam broadening is fitted to the experimental values by varying the Hurst exponent H (dashed curves). This is possible because all other parameters are known or have been determined. The shape of the theoretical curves (Equation (4.24), page 56) fits generally well to the experimental values and the fits yield H -values of 0.754 ± 0.003 (MgO), 0.753 ± 0.006 (Si), 0.811 ± 0.004 (SrTiO₃), and 0.758 ± 0.04 (Ge) [HMG19]. A closer look at the data points belonging to one material (data with the same color) reveals that they tend to lie below the theoretical curve for lower sample thicknesses and above for larger sample thicknesses. The slope of individual data sets is therefore not perfectly represented by the fit curve. This may be explained by the increasing energy loss of electrons with increasing sample thickness, which is not considered in the theoretical models in this chapter.

The evaluation shown in Figure 4.8 gives an impression of the absolute beam diameters of different materials at one specific beam energy. The significance of H determined in these fits is, however, limited. A value of H for the measurements of one material at all electron energies can be obtained by multiplying the experimental b and the theoretical curve with the energy-dependent factor $E_0^{(2H+1)/2}$. The theoretical curve then reads

$$b \cdot E_0^{(1+2H)/2} = 0.1167^{1-2H} \cdot (39437)^H \sqrt{\frac{R}{1-R}} \cdot Z^{(1+4H)/3} \cdot \left(\frac{\rho}{A}\right)^H \cdot t^{1+H} \quad (4.30)$$

As the right side of the equation is independent of E_0 , this allows combining the measurements of one material for all E_0 . Figure 4.9 shows the results for SrTiO₃. Measured and simulated beam diameters b are evaluated according to the left side of Equation (4.30). The experimental data is shown with error bars, while the simulated data are marked by dots. All data points lie in good agreement on the theoretical curve according to the right side of Equation (4.30) when $H = 0.81$ is used for both the evaluation of the experimental data and the theoretical curve. The best-fitting value for H was determined by minimizing the error measure nMAE according to Equation (4.29) (page 62) for different H . Again the tendency of the theoretical curve underestimating the slope of individual data sets (energies) can be seen. Repeating the same evaluation for the other materials yields the values for H

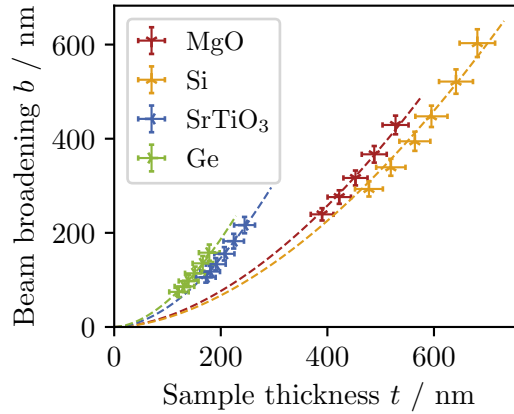


Figure 4.8. Experimentally determined beam broadening as a function of the sample thickness for MgO, Si, SrTiO₃, and Ge at 25 keV. Fitted curves (dashed) according to the anomalous diffusion model (Equation (4.24), page 56). The error bars were calculated according to Section 4.3.4.1 on page 61.

Table 4.2. Hurst exponents and the normalized mean absolute error nMAE as a measure of deviations between Equation (4.30) and the experimental and simulated data.

Material	Measured beam diameters		Simulated beam diameters	
	H	nMAE	H	nMAE
MgO	0.75	2 %	0.80	1 %
Si	0.76	2 %	0.80	1 %
SrTiO ₃	0.81	1 %	0.80	1 %
Ge	0.74	2 %	0.82	1 %

shown in Table 4.2. Beam broadening for all materials can be described well with the anomalous diffusion model, as indicated by the small nMAE values, e.g. 1 % for the experimental values in Figure 4.9. The values for H from the measured beam broadening are around 0.75 for MgO, Si, and Ge. Only for SrTiO₃, a 8 % higher value is obtained. The simulated beam diameters yield $H = 0.80$ for all materials except for Ge, which yields $H = 0.82$.

Finally, a single value for H is obtained by bringing all material-related parameters on the left side of Equation (4.30) too, which leads to

$$\frac{b \cdot E_0^{(1+2H)/2}}{c_{\text{mat}}} = 0.1167^{1-2H} \cdot (39437)^H \sqrt{\frac{R}{1-R}} \cdot t^{1+H} \quad (4.31)$$

with $c_{\text{mat}} = Z^{(4H+1)/3} \left(\frac{\rho}{A}\right)^H$. Plotting the experimental data according to the left side of this equation, using $H = 0.75$, yields the graph shown in Figure 4.10 a. It comprises the measured data from all observed materials and primary electron energies. Data points from different materials are shown in different colors. In addition to the experimental data, it shows the theoretical curve according to Equation (4.31) with $H = 0.75$, which yields the best agreement for the complete measured data set

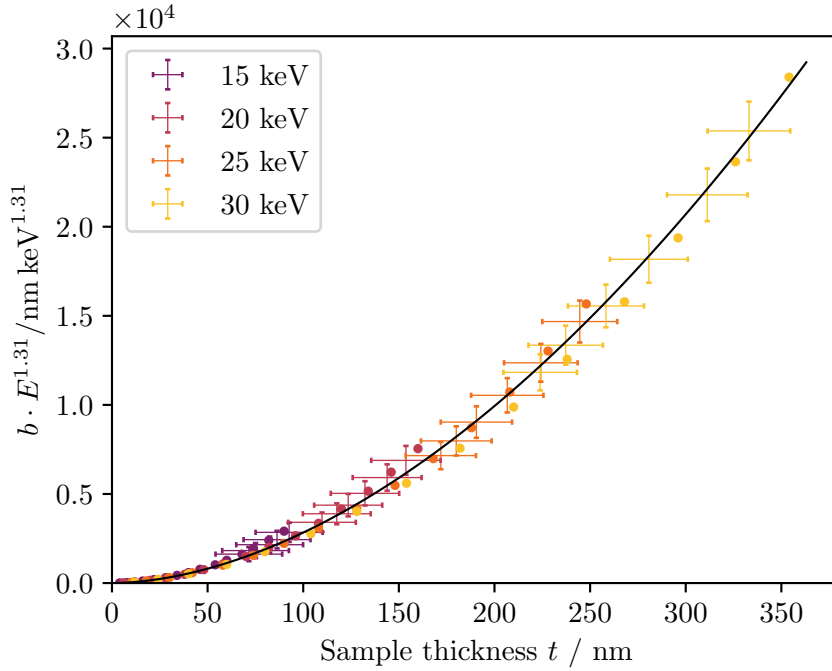


Figure 4.9. Compilation of the data for SrTiO₃ by $b \cdot E_0^{(2H+1)/2}$ with $H = 0.81$. The data points with error bars show experimental beam diameters, the points without error bars show simulated beam diameters. The black curve is the theoretical behavior according to the anomalous diffusion model (Equation (4.30)) [HMG19].

and the theoretical curve. It describes the data points well (nMAE = 1%) however the stronger slope of individual data sets is again visible. As the data points in (a) are very dense for low sample thicknesses, Figure 4.10 b presents a zoom-in on this area up to 200 nm sample thickness, where again the fit is in good agreement with the measured data. The full set of simulated beam diameters is shown in Figure 4.11, with the best-fitting curve for $H = 0.80$ (nMAE = 0.4%). It thus differs by 7% from the Hurst exponent determined for the experimental data. Equation (4.24) of beam broadening from the anomalous diffusion model is concretized as

$$b = 0.1167^{-0.5} \cdot 39437^{0.75} \sqrt{\frac{R}{1-R}} \cdot \frac{Z^{4/3}}{E_0^{1.25}} \left(\frac{\rho}{A}\right)^{0.75} \cdot t^{1.75} \quad (4.32)$$

using $H = 0.75$ from the experimentally determined beam broadening. To now classify this result, it is important to know the scattering regimes which were covered in this measurement. The elastic mean free path length Λ_{e1} and number of scattering events n are calculated from Equation (2.11) on page 10 and Equation (4.11) on page 53. The minimum and maximum sample thickness covered in the measurement of each material are used to determine if single $n = 1$, plural ($n < 25$), or multiple scattering/diffusion ($n \geq 25$) was dominant in the measurements. Table 4.3 lists the resulting values for 15 keV and 30 keV, with n ranging from 6 to 30 scattering events. Beam broadening was thus mainly determined for the plural scattering

Table 4.3. Elastic mean free path lengths Λ_{el} , calculated with Equation (2.11). The minimum and maximum number of scattering events n_{min} , n_{max} at 15 and 30 keV were calculated using the minimum and maximum sample thickness at which the beam width was measured.

Material	$E_0 = 15 \text{ keV}$			$E_0 = 30 \text{ keV}$		
	$\Lambda_{\text{el}} / \text{nm}$	n_{min}	n_{max}	$\Lambda_{\text{el}} / \text{nm}$	n_{min}	n_{max}
MgO	13	11	17	27	21	30
Si	18	9	13	36	19	25
SrTiO ₃	9	8	10	17	13	20
Ge	7	6	9	14	13	18

regime here. Equation (4.32) differs from the Goldstein Equation (4.6) [Gol+77]. Gauvin and Rudinsky stated that their model (Equation (4.24)) should converge towards the Goldstein equation when reaching the diffusion regime [GR16]. However, their Monte-Carlo simulations also showed that H depends not only on the number of scattering events $n = t/\Lambda_{\text{el}}$ but also on the diameter-defining parameter R (Figure 5 in [GR16]). In fact, their simulations show that $H = 0.5$ for $t/\lambda_{\text{el}} > 1$ holds only for $R = 99\%$ and increases with decreasing R , up to $H = 0.62$ for $R = 90\%$. The larger value of $H = 0.75$ for $R = 68\%$ determined here fits into this scheme, as H may further increase with decreasing R . A possible explanation for this behavior is that smaller R means that only electrons closer to the center of the beam are considered in the evaluations. Those are transmitted under a smaller scattering angle and might therefore have experienced fewer scattering events. Reaching the diffusion regime with $H = 0.5$ would therefore need larger sample thicknesses. Overall, the anomalous diffusion model with the Hurst exponent H is found to be well suited to describe beam broadening, which is in line with the study on thin amorphous carbon films by Drees et al. [Dre+17].

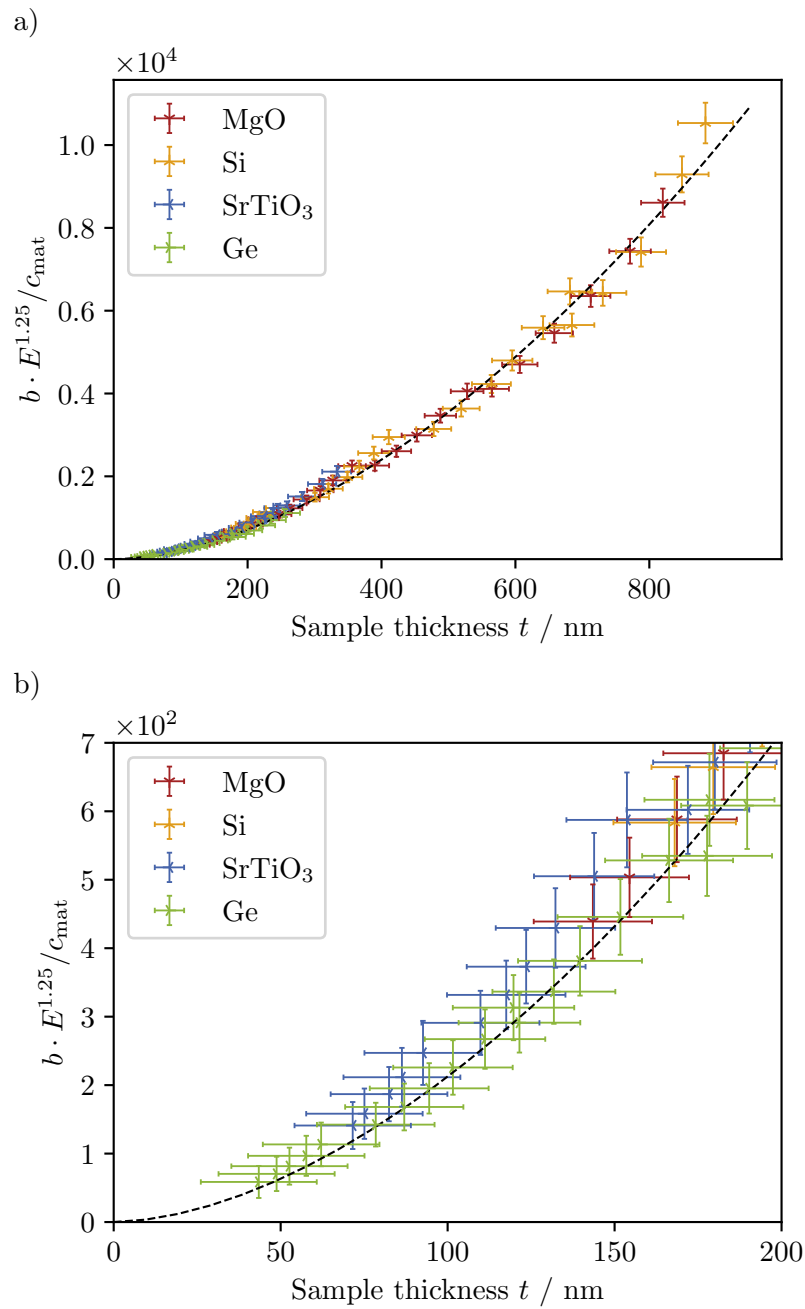


Figure 4.10. Compilation of all experimental data (all materials and primary energies) by $b \cdot E_0^{(2H+1)/2} / c_{\text{mat}}$ with $H = 0.75$. The black curve describes the theoretical behavior according to the anomalous diffusion model (Equation (4.31)). a) Overview of the full sample thickness range, b) zoom-in on the thickness interval up to 200 nm [HMG19].

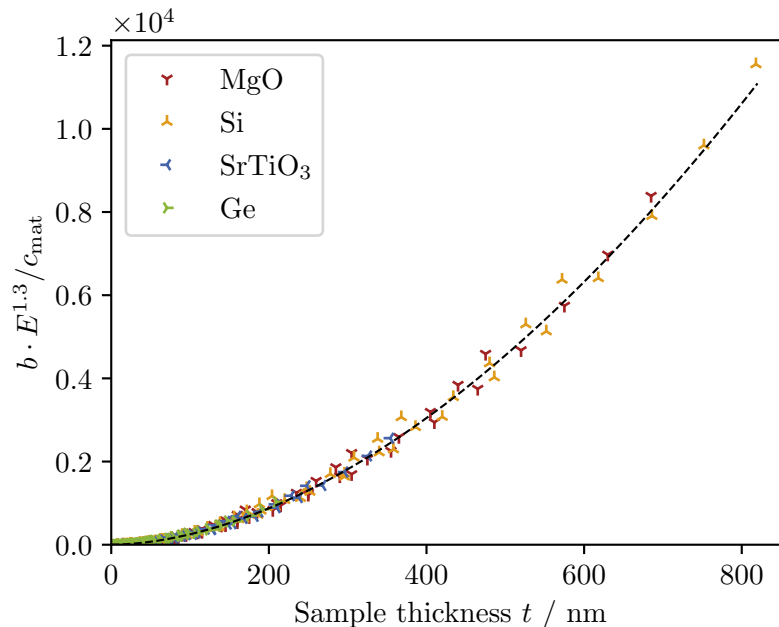


Figure 4.11. Compilation of all simulated data by $b \cdot E_0^{(2H+1)/2} / c_{\text{mat}}$ and the fit curve with $H = 0.80$ [HMG19].

4.5. Summary

This chapter presented experimental results and the discussion of beam broadening, with a focus on the anomalous diffusion model by Gauvin and Rudinsky. Beam broadening was measured at primary electron energies between 15 keV and 30 keV, for materials with average atomic numbers ranging from 10 up to 32 (MgO, Si, SrTiO₃, and Ge). Sample thicknesses up to 900 nm were covered in the measurements. Beam broadening was also simulated by Monte-Carlo methods, showing good agreement with the experimental data. Both the experimental and simulated data can be described well by the anomalous diffusion model (p. 56). It allows distinguishing between different scattering regimes, in contrast to the widely used Goldstein equation (p. 51), introducing the Hurst exponent H , which ranges from 1 (ballistic scattering) to 0.5 (diffusion). Besides, simulations have shown that H is influenced by the fraction R that defines the beam diameter, as it increases with decreasing R . The measured beam diameters could be fitted with $H = 0.75$ for the fraction $R = 68\%$ that was used here. Simulated beam diameters can be well described by $H = 0.80$. The model has also been shown to be accurate for very thin samples in earlier work [Dre+17]. However, its limitations lie in the negligence of energy loss during scattering. Due to the underlying Rutherford scattering theory, it is furthermore not suited for the description of beam broadening in crystalline samples, where coherent scattering effects like beam channeling may occur [Wu+17].

*Chapter***5.**

Electron-Beam-Induced Carbon Contamination

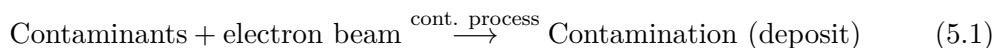
Electron-beam-induced carbon contamination is always present when using electron microscopes. Most of the time the growth of amorphous carbon is unwanted because it worsens the resolution of micrographs by covering structures that are of interest, may lead to charging problems, and impedes analytical studies by EDXS or EELS [Ege19; Hei63]. STEM-in-SEM techniques at primary beam energies ≤ 30 keV have been more and more used in recent years. As carbon contamination appears to be increased at those energies [KHS81; Hir+94], compared to the higher energies used in classical STEM and TEM, a systematic investigation of contamination-growth processes and cleaning methods is particularly interesting in such a setup. This chapter thus focuses on contamination on thin films, mainly amorphous carbon, at ≤ 30 keV. It deals with the concept and the results of a contamination-test experiment that allows testing parameters of contamination growth as well as cleaning methods in a reproducible way. After the introduction (Section 5.1), the theoretical background of electron-beam-induced carbon contamination is discussed (Section 5.2), before the measurement process and its requirements are presented (Section 5.3, starting from page 86). The first results part then focuses on the contamination thicknesses obtained by SEM-like or TEM-like irradiation and on the influence of imaging parameters (section 5.4, starting from page 99). Finally, the concept of measurement is applied to test different sample-cleaning strategies (Section 5.5, starting from page 121). Within this project on carbon contamination, the bachelor thesis of Katharina Adrion¹ and the master thesis of Aaron Marx² were conducted. Katharina Adrion continued to work on the project with me in the course of a student assistant contract. Their respective contributions are indicated in the following.

¹ORCID: 0000-0001-9837-4155²ORCID: 0000-0001-9475-4652

5.1. Introduction to Carbon Contamination

CONTAMINATION PROCESS

As already stated by Watson in 1947, the starting material for carbon contamination are contaminants, which are assumed to be mostly hydrocarbon molecules [Wat47; Rei98; Hil48]. Carbon contamination forms when the contaminants are polymerized by the electrons, which results in an immobile deposit on the sample [Wat47; Ste34]



In the early days of contamination studies, the contaminants were often assumed to be directly polymerized from the residual gas [Hei63; Wat47]. However, other and especially later studies showed that the dissociation takes place on the sample's surface [LJ06; Hil48; KHS81]. Many authors stated that the supply of contaminants via surface diffusion is a key factor in contamination growth, and it will be considered in all following discussions [Het+17; Kno76; RW78; Amm96; RWF07; Hir+94; Mül69]. However, there is also the opposite opinion stating that diffusion is negligible and the contaminants solely stem from the initial coverage or adsorption from the residual gas [KHS81].

SOURCES + COMPOSITION OF CONTAMI- NANTS

Contaminants are present on the sample itself as well as in the residual gas of the microscope [Lov+81; Rei98]. Since modern electron microscopes use oil-free pumps such as scroll, turbo-molecular, and ion pumps, the backstreaming of outgassing oil molecules to the microscope chamber, that was strongly contributing to contamination, has been reduced [Ban+78; TBH68; Kon79]. Another source of hydrocarbons can be vacuum grease, rubber gaskets, and plastic tubing inside the chamber [Enn54; Lov+81]. Some authors consider the vacuum to be the main source of contaminants [YHE83], yet others concluded the sample is the main source of contamination [Het+17; Hre78]. The contaminants on the sample and sample holder can stem from the ambient air during storage and from preparation steps, especially when they involve solvents or the sample is touched with bare hands [VC05; Lov+81]. Hence, some contaminants are brought into the microscope chamber with every sample exchange. It was already mentioned above that mostly hydrocarbons are considered to cause contamination. They are denoted as C_xH_y , indicating that they are of unknown type and composition. Most important, according to Reimer, are -CH, -COOH and -CNH₂ compounds [Rei98]. Mass analyzers attached to the microscope chamber allow investigating the composition of the residual gas by mass spectrometry [Hei63; Wan+10; Goh+20; HKM70; Pos96; Tom+79]. However, contaminants on the sample cannot be detected and it is known that molecules can be fragmented during the ionization in the mass analyzer that is required for the measurement process, such that the original molecule may not be detected [Wan+10]. Apart from typical constituents of ambient air, like N₂, O, CO₂, H₂O, and Ar,

Wanzenboeck et al. found higher atomic masses in their spectrum (> 60 u), which they attributed to fragments of hydrocarbons. In particular, they highlighted peaks at 70 u, 98 u, 119 u, and 170 u as contaminants, without identifying them. Goh et al. assigned masses from 25 u to 55 u to organic molecules, and 55 u to 59 u to pump oil hydrocarbons. However, their spectrum ends at 65 u and allows no insights on higher masses [Goh+20]. Hart, Kassner, and Maurin found the hydrocarbons CH_4 , C_2H_6 , $(\text{C}_2\text{H}_5)_2\text{O}$, C_4H_8 , $\text{C}_3\text{H}_6\text{O}$ (acetone), C_4H_{10} , and C_5H_{10} and considered them as potential contaminants [HKM70]. From his findings on the low volatility and high diffusion activation energy of the hydrocarbons, Mitchell assumed that the contaminants include long-chain hydrocarbons, aromatics, or plasticizers [Mit15]. In other works, a range of different hydrocarbons have been considered: C_4H_6 , C_6H_{14} , and C_9H_{20} [Ryk+08; Tot+07; Lob+08].

The deposit resulting from the contamination process consists mostly of amorphous carbon, but may contain other elements like H, O, or N [Hil48; Rei98; Lau+10; Het+17; KHS81; Roe+09]. Bret et al. investigated deposits grown with different organic precursors, and found that their composition is alike, close to $\text{C}_9\text{H}_2\text{O}_1$, independent of the precursor. The bonding type of the C-C bonds is mostly sp^2 [Bre+05; Het+17]. Depending on many factors like the type of irradiation, focused stationary, SEM-like (scanning), or TEM-like, the properties of the sample and the hydrocarbons, the contamination deposit can have different shapes. In the case of a stationary, focused beam without the use of a precursor gas, usually cones [CL75; Kan+90] are formed. Kanaya et al. and others described a transition from cone to ring with increasing beam diameter [Kan+88; Hre78], explained by the different relation between diffusion coefficient and beam radius, as discussed in more detail in Section 5.2.1.4. Depending on factors like the beam current, the contamination rings even show no noticeable contamination in the center [RW78; Hri+14]. Contamination effects size measurements of particles in TEM, even if the support does not show visible contamination [Kön48; Wat47; Cos47].

Another important parameter for the deposit's shape is the current density, causing a transition between growth/etching and by this also from cones to rings [Tot+07; Pin16; Lob+08]. Similar results have been found when the irradiation time is varied [Amm96]. Utke, Hoffmann, and Melngailis showed by theoretical considerations that the interplay of current and diffusion leads to the transition between cones and rings too, even if etching is not considered [UHM08]. When an etch precursor was used, even combinations of cones and rings were found [Tot+07].

For a scanning focused beam as in SEM and STEM, the shape of the deposit follows more or less the dimensions of the scanned area [Roe+09; Hir+94; Wan+10; GW10]. Its thickness is often more homogeneous as when a large area is irradiated with a static beam (TEM), which was explained by the replenishing of hydrocarbons during the refresh time of the scanning [UHM08]. However, pronounced growth at the bor-

ders can also occur [Hir+94; VP05; VPV01; VPP08; Wan+10; Lau+10; Roe+09]. Just like in TEM, this effect can be explained by the diffusion process: Hydrocarbons that reach the irradiated area are mostly cracked immediately and cannot reach the center of the area. The scanning pattern may also be directly visible in the deposit. Typical is a larger rim where the beam waits for synchronization before each scan line [Mit15; Roe+09], but even the individual scan lines were seen [Lau+10]. In general, the deposit grows on both sides of a thin specimen if the electron beam propagates through it [Hre78; Kan+90]. Further material characteristics of carbon contamination, like chemical stability and mechanical properties have been collected by Pinard, but are not of importance here [Pin16].

EBID

Many microscopists experience the effects of carbon contamination as an obstacle for their measurements. In contrast, some people induce contamination deliberately to grow structures on the sample's surface [vH08; ELM04; Din+05; FRR05; Joy06; LJ06; Lob+08; Mit+05; RFR06; UHM08; Smi07; Koo88], for example for the production of tips for scanning tunneling microscopy [Hüb+92]. The technique is called electron-beam-induced deposition (EBID) and is mostly performed in electron microscopes with a focused electron beam, using a precursor gas. As EBID is an intended process, it is not the focus of this work. However, some of the findings in this field can be transferred to carbon contamination. Another application of contamination is found in the preparation process of thin samples with FIB: A pad of contamination can be grown to protect the region of interest of the sample before any treatment with the ion beam. For this, either the ever-present contaminants from the vacuum and the sample itself or again a precursor gas can be used [Cór14; SSR12].

5.2. Fundamentals of the Contamination Process

The following fundamentals introduce the processes leading to carbon contamination, a theoretical model to describe them, and finally give an overview of available strategies to mitigate contamination.

5.2.1. Processes and Parameters

Contaminants adsorbed from the residual gas atmosphere of the microscope chamber get weakly bonded to the sample's surface by physisorption, or form a stronger bond by chemisorption [UHM08]. The physisorbed molecules can thus desorb again, with a finite residence time on the sample. As this weak binding type is thought to be dominant, a dynamic equilibrium is reached, where desorption and adsorption on the sample balance out, leading to a constant mean areal density of contaminants on

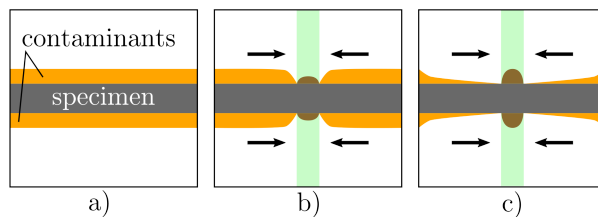


Figure 5.1. Scheme showing the contamination growth and diffusion of contaminants on an electron-transparent sample. a) Initial state without electron irradiation. b) Start of irradiation, contaminants are converted into contamination (dark orange), additional contaminants diffuse into the irradiated area. c) steady state between the decomposition and inflow of new hydrocarbons. Adapted from Hettler et al. [Het+17].

the sample (Figure 5.1a) [Het+17; UHM08]. For thin samples, both sample surfaces are covered by contaminants.

The electron beam in the electron microscope disturbs this equilibrium by decomposing the hydrocarbon molecules into fragments, which is also referred to as cracking. The cracked hydrocarbons are cross-linked (polymerized) on the sample and a carbon-rich deposit starts to grow [Rei98; Wat47; Ste34]. This process leads to a depletion in hydrocarbon concentration that results in the diffusion of surrounding hydrocarbons into the illuminated area due to the concentration gradient, mainly via the specimen surface (Figure 5.1b) [Het+17; Kno76; RW78; Amm96; RWF07; Hir+94; Mül69]. After some time, a steady state between the inflow of hydrocarbons and their decomposition is expected to be reached (Figure 5.1c) [Het+17]. In the following, the individual processes and contamination parameters are discussed in more detail.

5.2.1.1. Adsorption and Desorption

The total amount of molecules adsorbed from the gas depends on the number of molecules impinging on the sample's surface [Chr60]. The probability of a molecule to be adsorbed is described by the sticking coefficient S , which depends on the sample, the type of hydrocarbon, the pressure, gas coverage, the involved bonding processes (e.g. chemisorption/physisorption), and the temperature of the system [Wet+98; Tay+92; HKM70; UHM08; vH08; GS13]. For low temperatures, the sticking coefficient was found to be close to unity, for example at 105 K for the adsorption of C_2H_2 on Si(100) [Tay+92]. It decreases as the sample temperature increases, and is larger for longer-chain hydrocarbons at a specific temperature, as examined for different hydrocarbons on Au by Wetterer et al. [Wet+98]. At higher temperatures, the sticking coefficient approaches zero [Wet+98]. Hart, Kassner, and Maurin proposed a dependency of the form $S \propto \exp(a/\vartheta)$, with the temperature ϑ . The opposite process, the thermal desorption of molecules from the surface, can

be stimulated thermally or by the electron beam. Thermal desorption is described by the mean residence time τ_0 between adsorption and desorption, i.e. a larger τ_0 means less desorption. τ_0 is considered to have an Arrhenius-like dependency on the temperature ϑ of the surface and the desorption energy E_{des} [Chr60; vH08]:

$$\tau_0 \propto \exp\left(\frac{E_{\text{des}}}{k_B \vartheta}\right), \quad (5.2)$$

with the Boltzmann constant k_B . E_{des} increases linearly with the length of long-chain hydrocarbons [Wet+98].

The impacting electron beam can stimulate the desorption of hydrocarbons as well, in a competing process to polymerization of hydrocarbons that will be discussed below. This electron-beam-driven desorption is described by the desorption cross-section σ_d [Hir77]. Not only the primary electrons but also SE can contribute to the removal of adsorbed species, especially when their emission is higher at low beam energies [LJ06].

5.2.1.2. Cracking and Polymerization

Cracking is the decomposition of hydrocarbons into smaller molecules, which is followed by polymerization and cross-linking, finally leading to the formation of a carbon-rich deposit on the surface of the specimen [Rei98]. The two main processes involved in cracking are electron impact ionization and dissociation [ARB00; Enn53]. Alman, Ruzic, and Brooks stated that not only the direct dissociation but also ionization can cause dissociation of bonds, in 80 % of the processes [ARB00]. They used the same formula to describe the ionization and dissociation cross-section as a function of the electron energy E :

$$\sigma_{\text{diss/ion}} = \begin{cases} 0 & \text{for } E < E_{\text{th}} \\ \sigma_{\text{max}} \left(1 - \frac{(E_{\text{max}} - E)^2}{(E_{\text{max}} - E_{\text{th}})^2}\right) & \text{for } E_{\text{th}} < E \leq E_{\text{max}} \\ \sigma_{\text{max}} \exp\left(\frac{-(E - E_{\text{max}})}{\epsilon}\right) & \text{for } E > E_{\text{max}}, \end{cases} \quad (5.3)$$

with the threshold energy $E_{\text{th}} \approx 10$ eV, below which the cross-sections are zero, the maximum value of the cross-section σ_{max} at the energy E_{max} , and the constant ϵ that describes the decrease of the cross-sections at larger energies. Measurements of cross-sections for CH_y and C_2H_y were used to describe the parameters in a generalized form. The two cross-sections increase with the number of C and H atoms:

$$\sigma_{\text{max,diss}} = (2.36C + 0.413H - 0.631) \cdot 10^{-16} \text{cm}^2 \quad (5.4)$$

$$\sigma_{\text{max,ion}} = (1.89C + 0.33H - 0.505) \cdot 10^{-16} \text{cm}^2. \quad (5.5)$$

the other parameters are identical for ionization and dissociation:

$$E_{\max} = (7.71C + 1.31H + 67) \text{ eV} \quad (5.6)$$

$$\epsilon = (-64.3739C + 35.3963H + 668.358) \text{ eV} . \quad (5.7)$$

Both cross-sections are shown for C_3H_8 in Figure 5.2. σ_{ion} contains pure ionization as well as dissociative ionization, with is believed to have a share of 80 % [ARB00]. Hence, σ_c from Section 5.2.2 has contributions from σ_{diss} and σ_{ion} . Both cross-sections decrease exponentially with the electron energy beyond E_{\max} , which means that low-energy electrons have the largest influence on cracking and contamination growth. They describe the probability for cracking hydrocarbons under electron irradiation characterized by its current density.

The current density on the specimen surface has contributions from PE, SE, BSE and Auger electrons:

$$j = j_{\text{PE}} + j_{\text{SE}} + j_{\text{BSE}} + j_{\text{Auger}} . \quad (5.8)$$

j_{PE} can be measured, e.g. with a Faraday cup, the other terms depend on the used primary electron energy and the specimen. Considering the typical energies of the different types of electrons (c.f. Figure 2.2 on page 5), we see that the electrons with the lowest energy, SE and other electrons in the < 1000 eV-range, have the highest cracking probability. Early studies have shown that even 5 eV-electrons form contamination layers [Poo53; Hir60]. However, the peak energy of SE is in average below the energy threshold of the cross-sections [Rei98]. The relative contribution of the different types of electrons is therefore unclear [Sch93]. Different, constant dissociation cross-sections for different hydrocarbons and electron energies are found in the literature [RWF07; HKM70; Hir77; Lob+08]. As other than PE contribute to the contamination growth, contamination can grow outside the irradiated area, as the spatial distribution of SE, BSE and Auger electrons at the surface is larger than the directly irradiated region [Rei98].

The cracked hydrocarbons form a stable contamination deposit by polymerization and cross-linking [Chr60; Enn53; HKM70; Wat47; Lin66; Poo53; Rei98]. Polymerization is the process of converting monomers into polymers, whereas cross-linking is the formation of a bond between existing macromolecules, in this case polymers [Jen+96]. This results in a deposit consisting mostly of amorphous carbon, as mentioned before. From the polymerization and cross-linking process, it contains bonds and double-bonds, such as $\text{C}=\text{O}$, $\text{C}=\text{C}$, $\text{C}-\text{O}$, $\text{C}-\text{H}$, $\text{C}-\text{N}$, and $\text{Si}-\text{C}$ [KHS81; Bre+05].

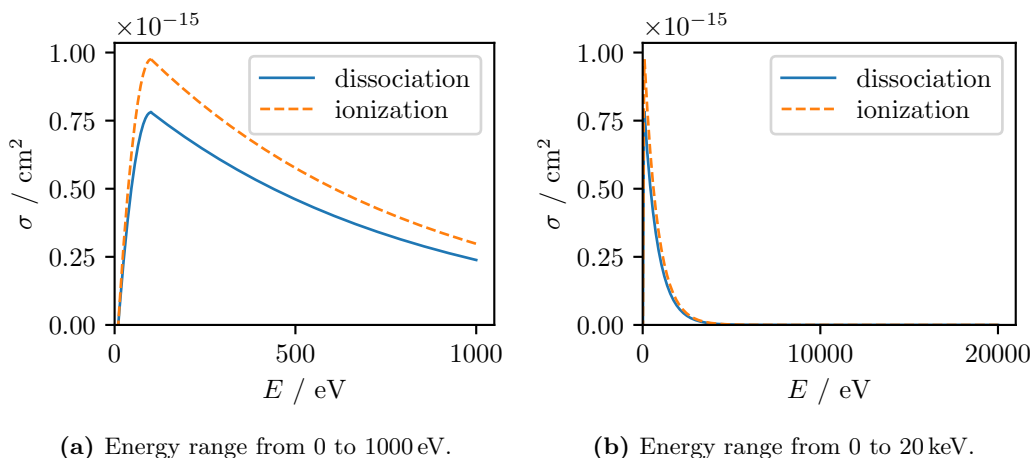


Figure 5.2. Cross-section of electron-impact-induced dissociation and ionization as a function of the electron energy E for C_3H_8 with $E_{\text{max}} = 101 \text{ eV}$ (Equation (5.3)).

5.2.1.3. Etching and other effects

Etching of the sample is a competing process to the deposition of material, especially when using a precursor gas [vH08; Tot+07; Lob+08]. Instead of growing a deposit, etching removes already deposited contamination or even (carbonaceous) material from the sample [Hei63; Hre79; RS66]. Besides specific etching precursors, the residual gases O_2 , H_2 , and H_2O , or adsorbed H_2O are thought to cause etching [Hei63; ER76]. The excited gas molecules and ionized atoms and bonds of the sample or present contamination undergo a chemical reaction that releases gases [Hre79]. It is unclear if the activation of the etching molecules or the specimen material is the main process. Heide stated that the ionization of adsorbed gas species dominates over the effect of ionized residual gas around the specimen [Hei63]. Egerton and Rossouw found that the ionization of surface carbon atoms is the dominant process if the ionization cross-section of C is larger than that of the adsorbed molecules [ER76].

The transition between contamination and etching depends on many factors, like beam current, sample temperature, partial pressure of precursors, diffusion coefficient, and etching cross-section. It is usually less severe at low beam currents [Lob+08]. Etching can be disturbing, but can also be intentionally used for removing present contaminants or contamination [Mik+16], or for creating nanostructures [Lob+08].

Polarization of poorly conducting specimens was considered to introduce a drift force on contaminants when an electric field is present on the sample (e.g. due to charging of an insulator) [Fou78]. Charging of the sample might also cause defocusing of the electron probe [Hri+15]. Other effects, like beam heating and sputtering, are described in Section 2.1.4. They can become of importance at high beam currents [Mit15]. The cracking of hydrocarbons and the etching process lead to depletion of

hydrocarbons in the irradiated area and the formation of a concentration gradient [Hir+94; Hre79].

5.2.1.4. Surface diffusion

Although the supply of hydrocarbons to the irradiated area from the vacuum was considered to be the dominant process [KHS81], it is usually regarded to depend mainly on surface diffusion, driven by the concentration gradient between the irradiated and non-irradiated regions [RW78; Amm96; RWF07; Het+17; Kno76; Hir+94; Mül69]. One argument for the dominance of surface diffusion is the often observed saturation of contamination growth rates after a short time, which can be explained by surface diffusion rather than by adsorption from the vacuum [Het+17; Mit15; CL75; YHE83]. The transition from cone to ring with increasing spot radius using stationary irradiation can be attributed to the relation between the spot's radius and the diffusion coefficient [Kan+88; Hre78]. In the case of a large radius, like in TEM or with a defocused beam in SEM, the diffusion constant is small compared to the radius, and the hydrocarbons are cross-linked before they reach the center of the spot, leading to the typical appearance of contamination rings [RW78; Kan+88]. The pinning of contaminants around the irradiated area before the measurement to reduce the number of diffusing molecules is the working principle of beam showering (see Section 5.2.3).

An increased sample temperature increases the mobility of adsorbents and thus the speed of diffusion [HKM70; Hre78]. This allows more molecules to reach the irradiated area in a constant time interval and leads to an increase in contamination thickness. The influence of the sample temperature ϑ on the diffusion coefficient D is expressed as

$$D(\vartheta) = D_0 \exp\left(-\frac{E_{\text{diff}}}{k_B \vartheta}\right), \quad (5.9)$$

with the activation energy E_{diff} for diffusion and the maximal diffusion coefficient D_0 , which depends on the adsorbed species and the substrate [UHM08]. The similarity with the residence time that describes desorption (Equation (5.2)) is caused by the similarity of the process: For both movements, a bond with the sample has to be ruptured [UHM08]. Notably, a higher surface temperature also causes a reduction of contamination thickness by increased contaminant desorption, which explains why both sample cooling and heating can help to reduce contamination [Hre78]. The contradictory opinion of Kumao, Hashimoto, and Shiraishi on the role of contamination, which was cited above, is that ring-shaped deposits are formed due to a steep decrease of temperature from the center of the irradiated area to the outside. They suggested that there would be more contaminants at the cooler edges, causing an increased contamination thickness [KHS81]. Considering the low temperature

increase caused by the electron beam, this seems unlikely (see Section 2.1.4).

A range of values for the diffusion coefficient are found in literature, ranging from 10^{-11} to $10^{-19} \text{ m}^2 \text{ s}^{-1}$ [Het+17; HKM70; Mal+05; Wal80; Ryk+08].

5.2.1.5. Growth regimes: Irradiation time and current density

The contamination thickness t_c in the initial state follows a power law $t_c \propto T^a$ with irradiation time T and an exponent $a \leq 1$ [RWF07; Het+17]. Rykaczewski, White, and Fedorov performed simulations of the growth process and distinguished between two contamination growth regimes depending on the current density j [vH08; RWF07; Chr60]:

- **Reaction-limited regime.** The current density is so low that more hydrocarbons reach the illuminated area than can be decomposed and a linear thickness increase with time is expected ($a = 1$). This growth regime is also called electron-limited or reaction-rate regime [vH08; Smi07; RWF07]
- **Precursor-limited regime.** At a higher current density, all hydrocarbons that reach the illuminated area can be decomposed. The deposition process is then precursor-limited and independent of the beam current, the exponent is $a < 1$. In this precursor-limited (also mass transport-limited or diffusion-limited) regime, the contamination thickness depends on the number of molecules reaching the irradiated area by diffusion and adsorption and is independent of j [vH08; Smi07; RWF07; Roe+09].

In reality, the growth regimes will not be clearly separated but have a transition in between [RWF07]. The transition between the linear and power-law-like growth as a function of beam current can nicely be seen in the work of Conru and Laberge [CL75]. After some time, depending e.g. on the surface diffusion constant and the initial density of contaminants, the system reaches the steady state [Het+17]. The constant areal density of contaminants in the steady state means that a constant number of molecules per time is converted to contamination. Thus a linear increase of contamination thickness with time ($a = 1$) is found once the steady state is established, regardless if the system is in the reaction- or precursor-limited regime [vH08]. Figure 5.3 shows the hypothetical contamination thickness after a specific irradiation time T as a function of j , distinguishing the two growth regimes. In the steady state, the growth regimes can only be distinguished by different slopes of the linear thickness increase, when the contamination growth is examined as a function of time at a fixed value of j as a function of T [vH08]. In the reaction-limited regime, it is described by

$$t_c \propto j \cdot T \cdot \frac{dE}{ds} . \quad (5.10)$$

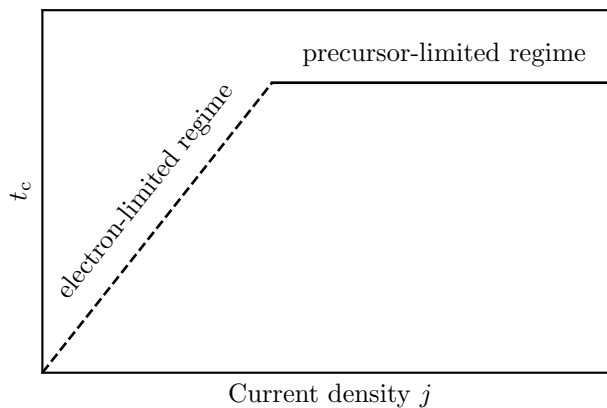


Figure 5.3. Schematic plot of the contamination thickness t_c as a function of the electron-beam current density after a fixed irradiation time T , distinguishing between the electron-limited and the precursor-limited regime. Adapted from van Dorp and Hagen [vH08].

$\sigma_q = j \cdot T$ is the collected dose per area, dE/ds is the energy loss per traveled distance (stopping power), which indicates the strength of interaction between beam and sample [Rei98]. In the precursor-limited regime, t_c is independent of the current density j .

The linear growth of contamination has been found in many studies, indicating that the steady state was reached so fast that the initial state was not recorded [CL75; KHS81; Hir+94; Enn53; Mül69]. Hettler et al. could measure the time it took to reach the steady state. They found a power-law dependency on the irradiation time only for the first 30 s of irradiation, after which the growth continued linearly [Het+17]. A similar short time to reach linear growth was found by Conru and Laberge and Amman [Amm96]. However, Mitchell found a power-law dependency

$$t_c \propto T^a \text{ with } a = 0.5 \quad (5.11)$$

for irradiation times T up to 15 min (the maximum observed time), indicating that the steady state had not been reached yet [Mit15]. He also found an incubation time in the first seconds, during which the contamination is considerably slower. Others found a power-law dependency with $a < 1$ for the full time of irradiation as well [Enn53; Mit15; Kno76; CL75; Tom+79; Sch93].

For spot irradiation and the growth of contamination cones, it is often not enough to only look at contamination thickness or height, since the volume might continue to increase, while the thickness saturates [CL75]. However, the thickness and volume of the contamination cones can also behave similarly [Kno76; Pin16], while the diameter of the cones seems to saturate faster in some cases [Kno76; Sch93; Tom+79; Pin16].

5.2.1.6. Electron energy

Contamination is typically experienced as particularly disturbing at low electron energies because the electron-induced dissociation probability of adsorbed molecules increases with lower electron energies, until it reaches a maximum in the 100 eV range, as visible from Equation (5.3) [ARB00; FRR05; vH08; Mit+05], and due to a lower SE yield at higher electron energies [LJ05; Smi07]. Reimer suggested Equation (5.12) to describe the contamination thickness t_c as a function of the electron energy E_0

$$t_c \propto qS \propto E_0^{-0.8}, \quad (5.12)$$

with the primary electron energy E_0 , the collected charge q , and the energy dependence $S \propto E^{-0.8}$ of Bethe's stopping power [Rei98; Bet]. This formulation implies that contamination depends mainly on the SE yield δ , which is proportional to the stopping power. As the primary electron energy in SEM and S(T)EM is larger than the threshold energies for contamination (Section 5.2.1.2), Ennos concluded that contamination growth is independent of the electron energy [Enn53]. They indeed found no dependence of the contamination on the electron energy between 40 keV and 75 keV using TEM-like irradiation. Similar results were obtained for 0.1 keV – 0.5 keV and 0.5 keV – 30 keV, in the latter case using a focused beam for EBID [Hir60; UY04]. Pinarid found an unclear behavior of the height, volume, width, and diameter of the deposit grown by a stationary, focused beam in his microprobe system with 3 keV – 30 keV [Pin16]. Contrary, many authors observed the decrease of contamination thickness with increasing primary electron energy, in experiments with 50 keV – 2000 keV, 1 keV – 25 keV, 0.5 keV – 30 keV, and 100 keV – 200 keV [KHS81; Hir+94; Roe+09; BZK66]. In the study of Roediger et al., investigating the case of square-shaped SEM deposits, the volume showed the opposite behavior: increasing with higher beam energy. Again this ambivalent behavior is more pronounced for deposits from a stationary, focused beam (cone/ring or combination) [Pin16; Sch93]. Schiffmann and Hübner et al. and measured an increasing height while the diameter or cone angle of the cone-shaped deposits decreased with higher beam energy [Sch93; Hüb+92]. This behavior might be explained by the decreasing probe diameter with increasing acceleration voltage (see Equation (2.51) on page 27).

At very low beam energies < 100 eV, even a cleaning effect was observed in STEM-in-SEM [Mik+16].

5.2.1.7. Influence of the substrate

Hillier speculated after his measurements on different specimens that the contamination growth is independent of the substrate [Hil48]. Indeed Poole found no influence on the contamination of different metallic target materials in their electron optic system [Poo53], yet in most cases, the contamination was found to be dependent on the substrate. Many parameters that were discussed above depend on the substrate material: The sticking coefficient, the residence time, the diffusion coefficient, and the emission of SE and BSE [GS13; LJ05; Rei98; UHM08]. Ranzetta and Scott observed in investigations of bulk metal substrates (Al, Fe, Ni, Cu, and Au) that contamination increases with the atomic number, which was assigned to the enhanced generation of BSE. Others made the same connection of a change in BSE emission with a change in the deposit's shape [Wen80; Amm96]. The BSE emission depends on the atomic number, atomic mass, and density of the substrate [Amm96]. From contamination measurements of different bulk substrates, the growth was found to be nearly zero on B and Si and highest on the transition metals, and higher on Pb than on Au, which led the authors to conclude that materials with lower heat conductivity contaminate less since they heat up under the electron beam [BH86; Wen80]. Hirsch stated that metallic surfaces might even act as catalysts for contamination growth [Hir60]. Pinard compared several data sets of contamination on different substrates, yet it was not possible to find a clear connection between substrate properties and contamination [Pin16].

5.2.1.8. Systematical SEM and STEM Studies

The overview on different imaging parameters shows that SEM and STEM-in-SEM, with the combinations of low energies and scanning irradiation, which can lead to contamination pads with homogeneous thickness, are particularly affected by contamination. Concluding this overview, the following highlights three systematical studies of contamination grown by scanning irradiation.

Hirsch et al. examined the relative thicknesses of SEM contamination deposits on bulk Cu and Si with BSE images that were normalized with the BSE-intensity of clean sample regions, and by evaluation of SE signals. They found that contamination increases with the beam current and with decreasing electron energies between 25 and 1 keV with a trend to frame-like contamination patterns. They also observed contamination to be a dose-rate (current) effect rather than a dose effect, related to the influence of surface diffusion of hydrocarbons [Hir+94].

Roediger et al. used atomic force microscopy AFM to investigate the thickness of SEM contamination deposits on bulk Si. They found that contamination decreases with increasing beam current, and deposits become more inhomogeneous, indicating

a precursor-limited growth regime. For electron energies between 1 keV and 25 keV, they found a nearly linear increase of the deposit's volume with increasing beam energy, in contrast to the results by Hirsch et al. [Hir+94]. However, the mean thickness of contamination decreases with increasing E_0 , indicating an enlarged contaminated area. They stated that the cleanliness of the sample is of smaller importance than the residual gas in the microscope (in their case with an oil-free pump system). According to their experience, maintenance with a long chamber opening increases the contamination strongly, and it requires around 2 months to restore clean conditions. Contamination thickness and shape were found to strongly differ in different microscopes using the same irradiation parameters, ranging from homogeneous deposits with large average thickness to frame-like contamination [Roe+09].

Mitchell evaluated contamination grown on amorphous carbon (aC) films and other specimens by 200 keV-STEM using scanning irradiation. Thickness maps of the deposits were obtained by EFTEM. As mentioned above, he found that the contamination thickness increases proportionally to the square root of the contamination time. An increase of the contamination thickness with beam current was observed, and a reduction of the contamination thickness for higher beam currents in contrast to work performed at lower electron energies. Mitchell assigned this reduction to beam-induced sputtering at high currents [Mit15].

5.2.2. Theoretical Description of Contamination

A partial differential equation to describe the areal density of molecules on the sample $n(\vec{r}, T)$ at a position \vec{r} and time T was published by Müller in 1969 [Mül69]. It is important to be aware that $n(\vec{r}, T)$ is not a measure of the contamination that is grown on the surface, but of the “starting material”, the hydrocarbons/contaminants. The differential equation includes contributions from adsorption, desorption, electron-beam irradiation, and diffusion:

$$\frac{\partial n}{\partial T} = \underbrace{\frac{P}{\sqrt{2\pi m k_B \vartheta}}}_{= \nu, \text{ Adsorption}} - \underbrace{\frac{n}{\tau_0}}_{\text{Desorption}} - \underbrace{\frac{j}{e} \sigma(E_0) n}_{\text{Irradiation}} + \underbrace{D \Delta n}_{\text{Diffusion}}. \quad (5.13)$$

ν describes the adsorption of contaminants on the surface. It comprises the partial pressure of contaminants P , the mean molecular mass m of the hydrocarbons, the Boltzmann constant k_B , and the temperature ϑ . The molecular mass is given by dividing the molar mass M (unit g/mol) through the number of particles/molecules in one mol N_A : $m = M/N_A$. The parameter τ_0 is the residence time on the surface between adsorption and desorption. The irradiation term describes the reduction of contaminants by growth of contamination and by beam-induced desorption. It depends on the current density j , on the elementary charge e , and on the total cross-section $\sigma(E_0) = \sigma_c + \sigma_d$, being a sum of the cross-sections for decomposing

and cross-linking the contaminants (σ_c), and the cross-section of electron-beam-driven desorption (σ_d). σ depends on the primary electron energy E_0 [ARB00; FRR05; vH08]. The diffusion term with its diffusion constant D characterizes the diffusion of contaminants, driven by the concentration gradient. In the equilibrium state with no irradiation (see Figure 5.1a on page 73), $\partial n/\partial T$, Δn , and j are zero. The equilibrium concentration

$$n_\infty = \nu \cdot \tau_0 \quad (5.14)$$

solves Equation (5.13) in this case [Mül69; Hir+94]. If the current density $j \neq 0$, Equation (5.13) can be solved analytically for the steady state with $dn/dT = 0$ (Figure 5.1 on page 73c). Further assumptions can be made both for the case with a rectangular SEM-like irradiation, and for the case of circular, TEM-like irradiation.

Rectangular irradiation In the first case of rectangular, scanning irradiation like in SEM, an irradiated area with side lengths $a \ll b$ can be assumed, allowing to write Equation (5.13) as a one-dimensional equation with direction x and $\Delta = \partial^2/\partial x^2$ [Hir+94]. The refreshing time of each scan is assumed to be so fast that it can be described by a homogeneous, static irradiation, where $j \neq 0$ inside the irradiated area is constant value. For the steady state $\partial n/\partial T = 0$, Equation (5.13) becomes

$$0 = \nu - \left(\frac{1}{\tau_0} + \frac{\sigma(E_0) \cdot j}{e} \right) \cdot n + D \frac{\partial^2 n}{\partial x^2} \quad (5.15)$$

The solution of this equation for the irradiated area is [Hir+94]

$$n_1(x) = \nu \cdot \tau_0 \left(\frac{1}{1 + \frac{\sigma \tau_0 j}{e}} + c_1 \cdot \cosh \left(\frac{x}{a \cdot \xi_1} \right) \right) \quad (5.16)$$

with $\xi_1 = \xi(1 + \sigma \tau_0 j/e)^{-1/2}$. The constant c_1 results from boundary conditions³.

Circular irradiation In the second case of circular, static irradiation like in TEM, the Laplace operator can be written in polar coordinates: $\Delta = \partial^2/\partial r^2 + (1/r)\partial/\partial r$, where r is the radial distance from the center of the irradiated area. In the stationary case ($\partial n/\partial T = 0$), Equation (5.13) becomes

$$0 = \nu - \left(\frac{1}{\tau_0} + \frac{\sigma(E_0) \cdot j}{e} \right) \cdot n + D \left(\frac{\partial^2}{\partial r^2} + \frac{1}{r} \frac{\partial}{\partial r} \right) n, \quad (5.17)$$

³Note that in their paper, Hirsch et al. are missing a closing bracket after n'_0 in Equation 14a.

which is solved by⁴

$$n_1(r) = \nu \cdot \tau_0 \left(\frac{\kappa_0^2}{\kappa^2} + C \cdot I_0 \left(\frac{r}{\kappa_0} \right) \right) \quad (5.18)$$

with the modified Bessel function I_0 [Mül69], and

$$\kappa = \sqrt{\tau_0 D}, \quad \kappa_0 = \frac{\kappa}{\sqrt{1 + \frac{j\sigma}{eD} \cdot \kappa^2}} \quad (5.19)$$

The constant C_1 is calculated from boundary conditions again [Mül69].

$$C_1 = \kappa_0 K_1 \left(\frac{R}{\kappa} \right) \frac{1 - \frac{\kappa_0^2}{\kappa^2}}{\kappa_0 \cdot I_0(R/\kappa_0) \cdot K_1(R/\kappa) + \kappa \cdot I_1(R/\kappa_0) \cdot K_0(R/\kappa)}, \quad (5.20)$$

with the radius R of the irradiated region, and the modified Bessel functions I_1 , K_0 , and K_1 . Notably, different parameters influence the shape of n_1 similarly. For instance, the partial pressure of the residual gas, which is contained in the adsorption constant ν , and the residence time τ_0 enter Equation (5.18) in a multiplicative way, and τ_0 also influences κ_0^2/κ^2 and the shape of I_0 .

Calculation of the contamination thickness Using the areal density n_1 of contaminants in the irradiated area, either from the solution for rectangular or circular irradiation, the resulting contamination thickness t_c can be calculated. It is a function of irradiation time T , and the distance r (or x for the one-dimensional case) from the center of the irradiated area.

$$t_c(r, T) = \frac{m_c}{\rho_c} \cdot \frac{\sigma_c j}{e} \int_0^T n_1(x, t) dt \quad (5.21)$$

$$= \frac{m_c}{\rho_c} \cdot \frac{\sigma_c j}{e} \cdot n_1(r) \cdot T \quad (\text{for stationary } n). \quad (5.22)$$

m_c and ρ_c are the mean mass and density of the deposited contamination [Hir+94]. This equation can be used to theoretically investigate the influence of parameters like the diffusion coefficient D . In Figure 5.4, Equation (5.22) is plotted for the rotational symmetric solution (Equation (5.18)) for two different values of D . Details on the values for the other parameters can be found in Section 5.4.5. In Figure 5.4a, D is by one magnitude smaller than in b, which results in a smaller mean contamination thickness \bar{t}_c of 19 nm, compared to 71 nm for the larger diffusion constant. This can be understood because less hydrocarbons reach the irradiated area in a given time. The smaller diffusion constant leads to pronounced ring-like contamination and t_c is nearly 0 at the center of the irradiated area, as expected because most contaminants

⁴The solution for $n_1(r)$ differs slightly from the one found in the work by Müller [Mül69], where κ^2 (denoted as ρ^2 in his work) was missing, likely due to a printing error. Thank you to Aaron Marx (LEM, KIT) for finding those typos.

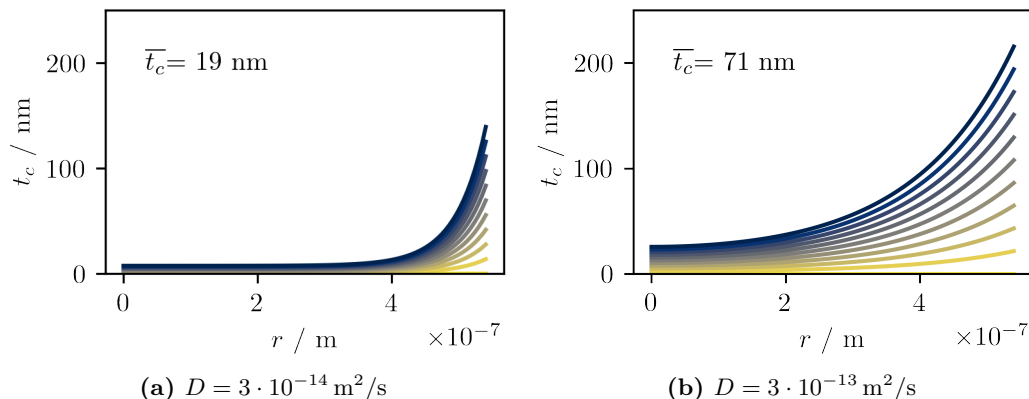


Figure 5.4. Calculated contamination thicknesses according to the Müller model (Equation (5.18) and (5.22)) for irradiation times from 1 min (yellow) to 10 min (dark blue). \bar{t}_c is the mean contamination thickness in the irradiated area. A partial pressure of $P = 4.5 \cdot 10^{-5}$ Pa, $m = 7.32 \cdot 10^{-26}$ kg, $\vartheta = 290$ K, $\tau_0 = 10$ s, $R = 0.54 \mu\text{m}$, $j = 65.49$ A/m², and $\sigma = 4.06 \text{ \AA}^2$ are assumed.

are pinned before they reach the center of the area if D is small.

The Müller and the Hirsch model are based on the same differential equation (5.13), taking adsorption and desorption of contaminants into account. Replenishment of contaminants from the vacuum and their desorption is also considered in the theory of Kanaya et al. [Kan+90]. Other theories neglect adsorption and desorption, as surface diffusion is regarded as the main contribution to contamination [Amm96; RWF07].

5.2.3. Cleaning Strategies

Besides the understanding of the growth mechanisms, the mitigation of carbon contamination is of interest. A variety of sample-cleaning methods is available, reducing the contamination that is caused by the sample itself. Those sample-cleaning techniques are sample baking [Dyc+18; Goh+20; McG+12; Mit15], plasma cleaning [GW10; Hor+09; Isa+99; McG+12; VPV01; Mit15], UV cleaning [Hoy+11; SWH12; Het+17; Mit15], washing the sample in solvents [Hir+94], or a mixture of ethanol and activated carbon [Li+21], pre-bombardment with argon ions [Kan+88], mechanical cleaning (tested on graphene) [Sch+20b], and irradiation with < 100 eV electrons [Mik+16]. Another attempt to reduce contamination is to enhance the quality of the vacuum in the sample chamber of the microscope. Common strategies are the use of cold traps [Enn53; Hil48; Hei63; RS66], a dry nitrogen leak, or nitrogen purge systems on the microscope (Postek.1996). Qualitatively it was noticed that the vacuum is improved when examining metallic Li in the microscope, which could be explained by the getter activity of Li [CS08]⁵. Lastly, there are attempts to hinder the contamination growth by applying in-situ heating [Enn53; Het+17; Yam+16],

⁵Thank you to Johannes Schmiege (formerly LEM, KIT) for sharing this experience.

sample cooling [ER76; Hir+94; Mit15; BH21; Wal80], beam showering [Dyc+18; Het+17; Amm96; Mit15; Bru97], and gas jets [Ban+78; Hei60; Bru97]. The goal of baking the sample in vacuum is to desorb volatile contaminants, including water and light organic molecules [Mit15]. For beam showering, a large area around the actual region of interest (ROI) is irradiated with a high dose to pin contaminants that would otherwise be able to diffuse into the ROI. Different gases can be used to produce a plasma for plasma cleaning. Typical are O₂, Ar, and N₂ or mixtures [Isa+99; McG+12; ZKH97; Kut+09; WC09; VKC20]. The energetic electrons and ions in the plasma bombard the surfaces and break C-H bonds there or form new bonds between ions and atoms of the specimen [WC09; Kut+09]. Free molecules are then pumped away. The plasma cleaner can either be a separate instrument or attached directly to the microscope chamber [WC09; VKC20]. A drawback of plasma cleaning is the possible damaging of the specimen, especially organic materials, parallel to the removal of contaminants. It should thus only be used for short times [WC09]. Ar plasma modifies the sample less as it cannot chemically react with the surface [Isa+99].

Mitchell performed a detailed analysis of contamination-mitigation strategies for 200 keV-STEM, testing the efficiency of sample baking, plasma cleaning, beam showering, UV cleaning, and sample cooling on different samples, among them C and NiO thin films [Mit15]. He identified sample baking as moderately effective, however needing long times (best overnight) and a clean heating/pumping station, and only working when the adsorbed species reach relatively high vapor pressures. Cooling the samples to liquid-nitrogen temperature prevented contamination completely. Plasma cleaning reduced contamination strongly when only applied for 1 min, with stagnant effectiveness afterward (for aC films). A similar result, with lower effectiveness, was found for UV cleaning. Beam showering for 5 to 10 min was highly effective and rapid, yet the effect is not permanent due to in-diffusion of further hydrocarbons. Mitchell's study clarifies that a cleaning method does not have the same effect on each sample, and the suitability should be assessed before application. A combination of different cleaning methods may be the best option [Mit15].

5.3. Measurement and Quantitative Evaluation of Contamination

The introduction and fundamentals section of this chapter have shown that contamination depends on a vast number of parameters, and not all of them can be controlled. In this work, the focus is on contamination in STEM-in-SEM, where it is a severe problem due to the low electron energies and the scanning irradiation, which leads to more homogeneous deposits than in TEM. The experiments presented here

test the dependencies of beam-induced carbon contamination on different parameters as

- initial state of the sample and the microscope (chamber pressure, residual gas, age of the sample),
- primary electron energy E_0 ,
- electron-beam current I (dose rate) and total dose σ_q ,
- irradiation time T ,
- substrate material,
- and applied cleaning methods.

The requirements of reliable measurements are discussed in the following.

5.3.1. Requirements Regarding the Experimental Setup

A suitable measuring procedure should be close to “reality”, meaning the situation where we usually face contamination problems. It should preferably be possible to grow the contamination and evaluate its properties in one instrument. As carbon contamination is pronounced at low primary electron energies [ARB00; FRR05; vH08], the STEM-in-SEM instruments HELIOS G4 FX and STRATA 400S DUAL-BEAM were chosen as a testing environment. Quantitative HAADF-STEM images in combination with Monte-Carlo simulations furthermore allow the calculation of absolute thicknesses of thin samples and contamination when their composition is known. The initial state of the microscope and the sample can not be kept constant over time. Thus it is impossible to change only one parameter at a time, and a reference measurement has to be established to facilitate the comparison of contamination experiments that are performed on different days.

The specimen that is used for contamination tests should be close to “reality” too. An amorphous carbon film on a TEM grid is a reasonable test specimen since it serves as support for all kinds of materials. The carbon films should be clean and with a flat topography. Additionally, it must be possible to repeatedly produce these films with the same quality. The preparation method that meets these requirements is discussed in the following section.

Thin amorphous carbon films are the most widely used support material for TEM and STEM investigations. However, it is also interesting to investigate the contamination behavior on Au, Pd, or Si_3N_4 thin films because of their different physical properties. A 10 nm Si_3N_4 membrane⁶, 2-3 nm Au⁷, and 2-3 nm Pd films⁸ were

⁶EM-Tec 10 nm silicon nitride membrane, 0.1 x 0.1 mm window, 200 μm frame

⁷SubstratekTM 2-3 nm Au on 400 mesh Au TEM grid

⁸SubstratekTM 2-3 nm Pd on 400 mesh Au TEM grid

chosen for this purpose.

5.3.2. Preparation of Carbon Support Films

The preparation of amorphous carbon (aC) films on TEM copper grids has to be done in a clean environment to provide a clean and smooth surface. It was found that it is not necessary to go to a clean room. However, all tables and tools should be kept as dust-free and clean as possible. In a first step, the original copper grids are carefully cleaned in an ultrasonic bath with acetone, then washed with isopropyl alcohol and distilled water and in the last step dried on a microscope slide on a hotplate for around 12 min at 120 °C to remove remaining solvents.

To produce the carbon films, freshly cleaved mica sheets, providing a very flat surface, are put in a LEICA EM ACE 600 high-vacuum coater. A carbon layer (nominally 10.7 nm) is then evaporated on the mica sheets by adaptive carbon-thread coating. A small glass funnel with a flat bottom is placed on another glass vessel. A tailored piece of dust-free cloth covers the bottom of the funnel, which is then filled with distilled water (Figure 5.5). The small outlet of the funnel and the cloth on it ensure that it takes some minutes before the water has flowed off. The cleaned TEM grids are put on the bottom of the vessel on top of the cloth. The aC films are released from the mica by dipping the mica sheets at a flat angle into the water until the films float on the water surface. As the water slowly drains, the floating aC films approach the TEM grids on the bottom of the funnel. Finally, the aC films sink on the TEM grids, which need to be positioned below. They are then removed from the vessel and air-dried for two days in a breathable dust cover, after which they are separately stored in typical sample boxes between paper sheets in ambient air Figure 5.6.

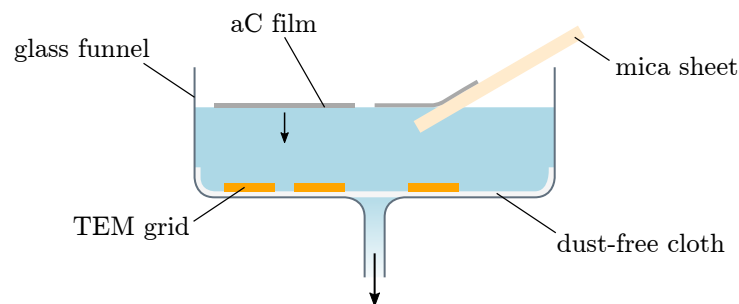


Figure 5.5. Scheme of the floating process to deposit thin aC films on TEM copper grids.

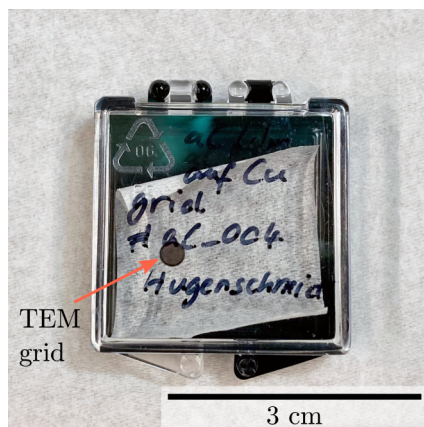


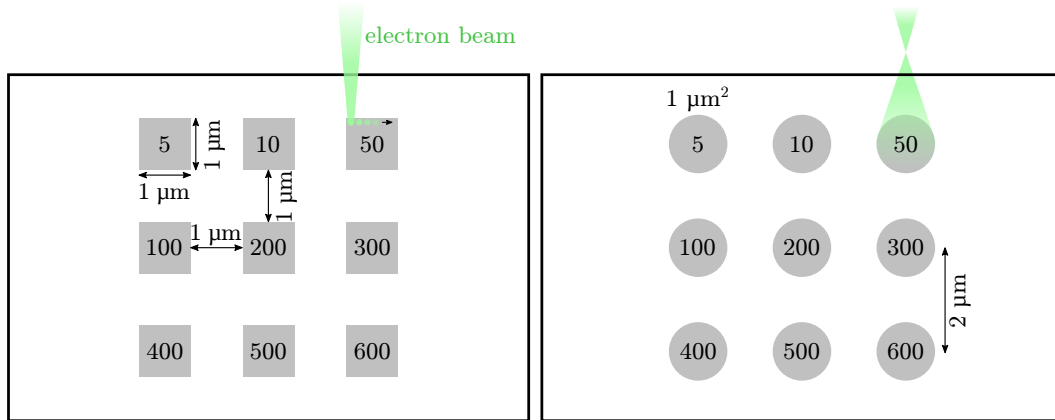
Figure 5.6. Storage box for aC films on TEM grids that serve as contamination test specimens.

5.3.3. Measurement Setup

A reproducible test procedure to grow and evaluate contamination was established. Before each measurement, all tools and surfaces that will touch the sample are wiped with a dust-free cloth and ethanol. Subsequently, they are dried with an air gun or a manual blower. The sample holder is cleaned with a plasma cleaning device in the microscope or with a separate plasma cleaning tool before loading the sample on it. After inserting the sample into the microscope and the last movement of the stage, some time is needed for the stabilization of the stage and the reduction of specimen drift. Two scanning electron microscopes, the Thermo Scientific HELIOS G4 FX, and the FEI STRATA DUAL BEAM, both equipped with a STEM detector, are used to grow and image contamination.

Three different types of test patterns are set up to grow contamination on the support films:

- **SEM-like irradiation.** The focused electron beam scans 3×3 squares of $1 \mu\text{m} \times 1 \mu\text{m}$ size for different time intervals between 5 s and 10 min (Figure 5.7a). The square pattern simulates imaging in the SEM with a scanning beam.
- **SEM-like irradiation (single square).** A single, continuously scanned $1 \mu\text{m} \times 1 \mu\text{m}$ square is used for the test of contamination-mitigation strategies instead of the SEM-like pattern with 3×3 squares. The total irradiation time of the single square is 20 min or 36 min, interrupted every 120 s for the acquisition of a HAADF-STEM image for contamination-thickness determination. This allows testing strategies depending on the time that has passed after their application.
- **TEM-like irradiation.** A strongly defocused and stationary electron beam irradiates 3×3 circles with an area of $1 \mu\text{m}^2$. The defocused beam mimics the



(a) Square contamination pattern with SEM-like irradiation. The beam scans the patterns with a defined pitch, as indicated in the upper-right square.

(b) Circular contamination pattern with uniform, TEM-like irradiation. The beam is broadened by defocusing to achieve a uniform irradiation.

Figure 5.7. Scheme of the contamination test patterns. The green markings indicate how the patterns are irradiated. The irradiated area is $1 \mu\text{m}^2$ for both the squares and the circles. The numbers in the squares/circles denote the irradiation time in seconds.

homogeneous, circular irradiation in TEM (Figure 5.7b). Notably, the beam has a larger convergence angle than in transmission electron microscopes. The irradiation time ranges from 5 s to 10 min as for the experiments with SEM-like irradiation. This pattern meets the assumptions of the model by Müller and is used since the models by Müller and Hirsch et al. cannot describe scanning irradiation [Mül69; Hir+94].

Test parameters Apart from the parameters that can only be influenced to a small extent, some can be controlled and tested regarding their influence on contamination. These are imaging parameters of the microscope as primary electron energy E_0 , electron-beam current I , irradiation time T , and total dose σ_q . These tests were performed with the square scanning pattern, as it is closest to the reality in SEM and STEM investigations. The scan has a step size (pitch) of 1 nm and a pixel dwell time of 1 μs . The other value ranges covered by the experiments are given in Table 5.1.

The conditions of the microscope and the samples can change over time, for example when the microscope is opened for maintenance or the sample contaminates during storage. To monitor the resulting changes of contamination growth, a reference test with SEM-like irradiation and constant imaging parameters (given in the right column of Table 5.1) is performed before any contamination experiment. The beam energy $E_0 = 20 \text{ keV}$ is selected because this relatively high energy is often used in STEM-in-SEM measurements. It was also found suitable for the evaluation of the contamination thickness. However, the parameters of contamination growth and

Table 5.1. Parameters for measurements of beam-induced carbon contamination with the SEM-like pattern shown in Figure 5.7a.

Parameter	Values	Values for reference measurements
Irradiation time	5 s to 10 min	5 s to 10 min
Primary electron energy E_0	0.35 – 30 keV	20 keV
Beam current I (nominal)	13 – 800 pA	40 or 50 pA ⁹
Dose rate	$1.6 \cdot 10^{-3} - 4.5 \cdot 10^{-1} \text{ C cm}^{-2} \text{ s}^{-1}$	
Maximum total dose σ_q	1.8 and 3.6 C cm^{-2}	
Support material	aC, Si ₃ N ₄ , Pd, Au	aC
Cleaning strategies	Beam showering, sample baking, plasma cleaning	no cleaning

imaging for thickness evaluation can be chosen independently. The reference value of the nominal current is 40 pA or 50 pA due to the available current values in the software of the STRATA and HELIOS microscope. The real beam current can vary. Hence it is always measured using a Faraday cup. In the following, nominal current values are shown for the sake of clarity, if not stated differently.

In another set of experiments, the circular static pattern was used to enable the comparison of experimental contamination data with calculated data from the model of Müller (Section 5.2.2 on page 82 and Equation (5.22)). The comparison of theoretical and experimental contamination thicknesses allows, to some extent, conclusions on the parameters in Equation (5.13). These conclusions are difficult to make since the typical shape of the contamination is influenced by different parameters in a similar way, as discussed in Section 5.2.2.

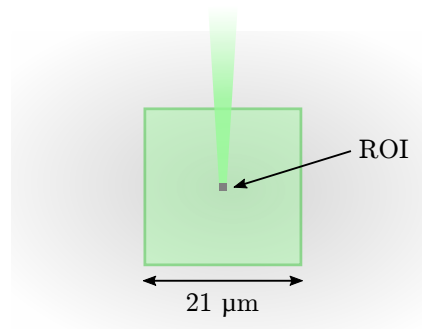
5.3.4. Contamination-Mitigation and Sample-Cleaning Strategies

In addition to the contamination experiments, three contamination-mitigation techniques were regarding their efficiency in preventing contamination. Using aC films as test samples, the following methods were applied:

1. **Beam Showering (BS):** Directly before the actual measurement, the electron beam scans over a large area around the ROI, acting as a shower that pins mobile contaminants. They should then form a thin layer of contamination, reducing the contamination growth when imaging the ROI at higher magnifications since fewer mobile contaminants are available to diffuse into the ROI. In this work, the electron beam scanned 10 min over an area of $\sim 21 \mu\text{m} \times 21 \mu\text{m}$ on the aC film using different measured beam currents I of 32 pA, 2050 pA,

⁹Depending on the pre-settings of the microscope

Figure 5.8 Schematic representation of beam showering. The large green square marks the area that is irradiated for 10 min during beam showering. Immediately after the showering, the contamination is measured in the dark square, the ROI.



and 7280 pA at 20 keV. The scanned area varies slightly as it was chosen just as large as a window in the Cu grid that supports the aC film. After the beam showering, contamination is grown and measured for 36 min with the single-square SEM test pattern as described on page 89. Figure 5.8 shows the principle of beam showering.

Frame showering: This test is very similar to regular beam showering, but the small ROI is not scanned during beam showering: Leaving out the central $3\ \mu\text{m} \times 3\ \mu\text{m}$ protects the ROI from being damaged before the actual imaging process. This is achieved by putting together four rectangles of different sizes using the e-beam patterning options of the microscope and scanning them simultaneously. The outer dimensions of the showered area are $\sim 25\ \mu\text{m} \times 25\ \mu\text{m}$. Bruenger proposed a similar test with alternating showering and measurement [Bru97].

2. **Sample Baking:** A vacuum heating setup¹⁰ bakes the specimen on the sample holder of the HELIOS microscope at 100 °C for 15 min at a pressure of $4 \cdot 10^{-3}$ mbar. This ex-situ method has the disadvantage that the holder and specimen need to be transferred to the microscope after baking. During this time, molecules from the surrounding air can adsorb and contaminate the sample again. The whole transfer process takes approximately 3 min: 2 min for venting the vacuum heating recipient and 1 min for inserting the holder into the microscope. Although sample baking is typically applied for longer times [Mit15], we selected this short time here to make the time-effort of the cleaning method comparable to the other methods.
3. **Plasma Cleaning (PC):** The in-chamber plasma cleaner¹¹ at the HELIOS microscope produces a reactive plasma from the residual gas in the microscope after increasing the pressure to around 50 Pa by venting the chamber with nitrogen. The plasma is active for 15 min in this experiment. After pumping the chamber down again, the contamination is measured.

¹⁰Klaus Binder Labortechnik, TS 716

¹¹FEI plasma cleaner, power 19 W

5.3.5. Monte Carlo Simulations

HAADF-STEM imaging is used to evaluate the thickness of contamination deposits, as described in the next section. For the quantitative evaluation of the sample thicknesses, the connection between relative HAADF intensities I_{rel} (see Equation (3.2) for definition) and the sample thickness t has to be known. It is simulated using a modified version of NISTMONTE1.2 [Rit05], a Monte Carlo (MC) simulation program. The relevant modification for this work, concerning the efficiency of the detector, is described below.

Relative image intensities $I_{\text{rel, sim}}$ as a function of the sample thickness t are obtained by normalizing the number of electrons within the detection-angle range of the HAADF segment with the total number of simulated electrons. The detection angles are $68 < \theta \leq 272$ mrad for the HELIOS and $168 < \theta \leq 617$ mrad for the STRATA microscope at $\text{WD} = 4.2$ mm. The composition and density of the material and suitable scattering models need to be known for reliable simulations. The differential screened Rutherford cross-section (SR-CS) is suitable to describe scattering in aC at energies between 15 keV and 30 keV as found by Volkenandt, Müller, and Gerthsen and is used for the MC simulations [VMG14]. Both the support film and the contamination are assumed to be pure carbon, although contamination contains C, H, O, and N, as outlined in Section 5.1 [Hil48; Rei98; Lau+10; Het+17; KHS81; Roe+09]. Assuming the same material for the support film is justified if both show the same intensity for the relevant HAADF scattering angles at 20 keV, used for the thickness evaluations.

The HAADF-STEM intensities for 20 keV were checked with a cross-section TEM sample prepared by FIB milling. The grid with the aC film was coated from both sides with Pt using the same high-vacuum coater to protect the support and contamination deposit. The film was again coated from both sides at the specific take-out side using Pt deposition induced by the electron and ion beam in the HELIOS microscope. Finally, the FIB was used to cut out and thin a lamella. A HAADF-STEM image of the lamella at 20 keV is shown in Figure 5.9. As the support film is not distinguishable from the contamination, it is reasonable to assume the same material for film and contamination in the simulations.

The material density ρ is unknown and the literature's values for aC vary considerably between 1.75 g cm^{-3} and 2.3 g cm^{-3} [Iwa02; Sch+05; Wan+06]. The simulation is calibrated by comparing the measured relative intensity I_{rel} with the simulated intensity $I_{\text{rel, sim}}$ for a carbon film with known thickness, and varying the material density ρ until both values agree. The calibration also compensates for possible deviations from pure carbon due to the impurities of the film and contamination. The thickness of one carbon film with contamination deposit was determined by TEM from the same cross-section lamella, imaged at 200 keV in a PHILIPS CM200

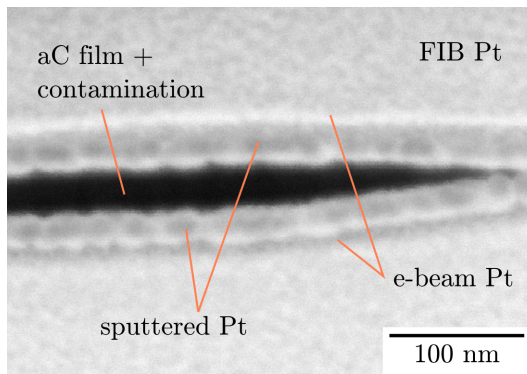


Figure 5.9. 20 keV HAADF-STEM image of the cross-section lamella prepared from the support film with contamination deposit. The different protective Pt deposits from the high-vacuum coater, the e-beam, and the FIB are visible above and below the dark carbon.

transmission electron microscope for better spatial resolution (Figure 5.10). The measured thickness of $t = 10.1 \pm 0.3$ nm is close to the nominal thickness. The measured relative intensity $I_{\text{rel}} = 7.2\%$ of this film is compared with $I_{\text{rel, sim}}-t$ -curves simulated with different ρ , with the best agreement for $\rho = 1.63$ g cm $^{-3}$ (Figure 5.11). This value can differ from the true density since deviations from the assumed values of the average atomic number or scattering behavior influence it.

The MC simulation package takes account for the energy dependence of the detector's detection sensitivity [Čal+19]. It normalizes the simulated signal with the simulated primary electron intensity, including the reduced detection efficiency of the detector at very low energies due to a protecting layer on its surface. The details are given in the appendix, Section B on page 196. The cutoff energy, below which the detection efficiency decreases, was determined to be 3 keV for the STRATA and 0.5 keV for the HELIOS microscope.

¹²Scattering angle range $68 \text{ mrad} < \theta \leq 272 \text{ mrad}$

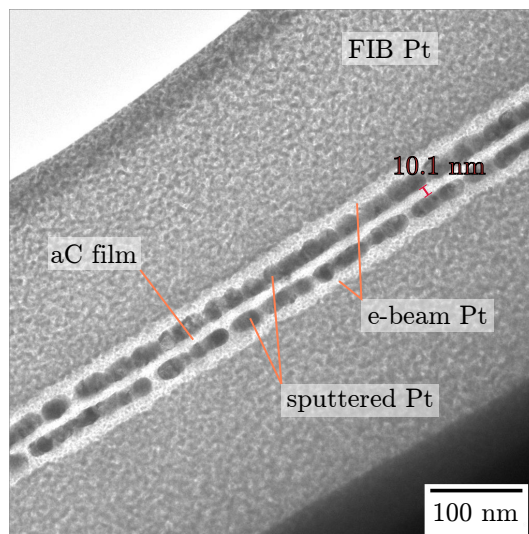


Figure 5.10. 200 keV TEM image of the cross-section lamella prepared from the support film. Again the different protective Pt layers are visible. The Pt layer deposited with the electron beam looks brighter than the Pt deposited with the FIB, which indicates that the former contains more light elements from the precursor gas.

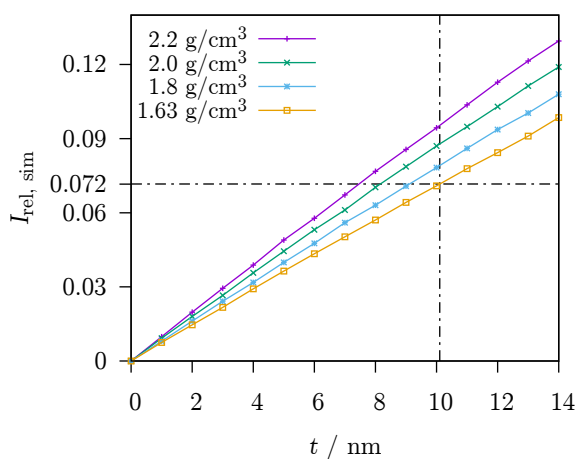


Figure 5.11. Simulated relative HAADF-STEM intensities at 20 keV for aC^{12} . The experimentally determined sample thickness t and corresponding $I_{rel} = 0.072$ are marked with dashed-dotted lines. The simulated curve intersects this point for $\rho = 1.63 \text{ g cm}^{-3}$.

5.3.6. Imaging and Evaluation of Image Data

Quantitative HAADF-STEM imaging in combination with MC simulations is used to obtain contamination thickness maps. This section outlines the imaging and image evaluation process that is illustrated in Figure 5.12. The properties of the deposits are discussed in Section 5.4. The contamination deposits on the aC film are directly imaged after growing them using HAADF-STEM at 20 keV and WD= 4.2 mm in the same microscope (Figure 5.12a). At this WD, the HAADF detectors of both microscopes cover the detection angles given above (Section 5.3.5). The HAADF-STEM imaging provides an experimental gray value intensity I for each pixel in the image, from which relative intensities I_{rel} are calculated as described in Section 3.2.2, Equation (3.3). The intensity of the incident beam I_0 and the black-level intensity of the STEM detector I_b need to be known for this calculation (Figure 5.12b).

The comparison of the resulting experimental values I_{rel} (Figure 5.12 c) with the values from the MC simulation (Section 5.3.5 and Figure 5.12d) yields the thickness of the aC film and the contamination deposit. As we are interested in the contamination thickness only, the average film thickness is subtracted and effectively set to zero (Figure 5.12e). However, determining the contamination thickness in every single pixel by subtracting the average background thickness is only valid if the thickness variation of the support film is negligible compared with the thickness of the contamination. Our aC films have a homogeneous thickness. Thus, the error is small here (see Section 5.4.1).

The average thickness \bar{t}_c of each contamination pad is used to compare the results from different experiments. It is determined by

$$\bar{t}_c = \frac{A_{\text{pixel}}}{\underbrace{A_{\text{irr}}}_{1/N_{\text{irr}}}} \cdot \sum_i N_i \cdot t_i . \quad (5.23)$$

The ratio $A_{\text{pixel}}/A_{\text{irr}}$ of the area of one pixel and the irradiated area yields the inverse number of irradiated pixels $1/N_{\text{irr}}$. N_i is the number of evaluated pixels with a thickness t_i , represented as a histogram in Figure 5.12f. The normalization with the number of irradiated pixels is needed to include all contamination deposited by the irradiation as the area that is evaluated by Equation (5.23) is always larger than the initially irradiated area ($N_i > N_{\text{irr}}$). This evaluation considers smeared-out contamination that is outside the irradiated area, e.g., due to sample drift. If the number of evaluated pixels were used for normalization, the result would depend on the size of the evaluated area, and the comparison would be impossible. The calculation of mean contamination thicknesses \bar{t}_c is shown in Figure 5.12f and g for the contamination deposit with the longest irradiation time.

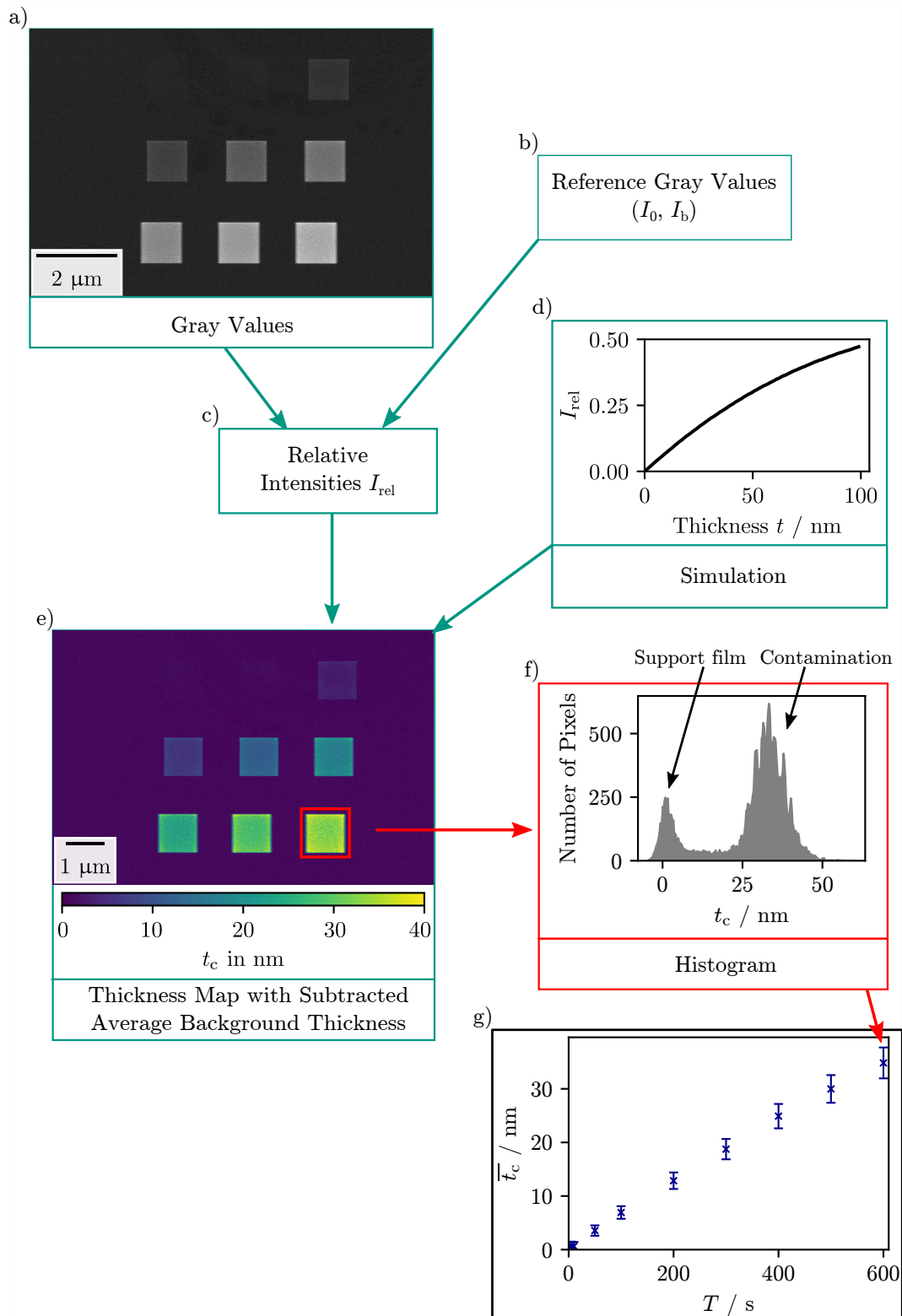


Figure 5.12. Schematic overview on the evaluation of contamination thicknesses. In this example, contamination was grown at 20 keV with a beam current of 50 pA in the HELIOS microscope. A gray value image and the reference gray values (white value I_0 and black value I_b) allow the calculation of relative intensities I_{rel} for every pixel. The comparison with a MC simulation, which connects values of I_{rel} with sample thicknesses t , results in a thickness map. The thickness values of the pixels of every deposit are evaluated according to Equation (5.23), resulting in a plot that shows the mean contamination thickness \bar{t}_c as a function of irradiation time T . See Section 5.3.6 for the more detailed description.

5.3.7. Error Estimation

The uncertainties of the relative intensities I_{rel} , the black and white intensity I_0 and I_b , the geometrical correction factor c , and finally, the uncertainty of the simulation influence the precision of the calculated I_{rel} and \bar{t}_c values (see Equation (3.2) and Equation (5.23)). For simplicity, the simulated $I_{\text{rel}}-t$ relation is assumed to be linear,

$$I_{\text{rel}} = m \cdot t \quad \Leftrightarrow \quad t = \frac{I_{\text{rel}}}{m}, \quad (5.24)$$

which approximately holds for carbon thicknesses up to 40 nm for the HELIOS microscope and up to 180 nm for the STRATA microscope (Figure 5.13). The fit curves yield a linear slope of $m_{\text{Helios}} = 0.0066$ and $m_{\text{Strata}} = 0.0019$. The different shape of the two curves is due to the different HAADF scattering angle ranges in the microscopes. The assumed uncertainty of this value is 6% and comprises uncertainties of the material density ρ , atomic number Z , and scattering models. Table 5.2 lists the other assumed uncertainties.

The starting values of the uncertainty evaluation are now the manually determined mean gray values $\overline{I_{\text{exp}}}$ of each contamination pad (without surrounding). Linear error propagation theory assuming no correlation between the variables first results in uncertainties on $\overline{I_{\text{rel}}}$ (based on Equation (3.2) and Equation (3.3)), then in the uncertainties of \bar{t}_c assuming $\bar{t}_c = \overline{I_{\text{rel}}}/m$. Figure 5.12 (bottom-right) shows the uncertainties as error bars. They increase with \bar{t}_c , and the relative error is typically around 6%. Section 5.4.2.1 gives a more detailed discussion of the uncertainties.

Table 5.2. Parameters of the contamination thickness evaluation and their uncertainties.

Parameter	relative uncertainty
I_b	$\pm 1.2\%$
I_0	$\pm 0.9\%$
$\overline{I_{\text{exp}}}$	$\pm 0.8\%$
m	$\pm 6\%$
c	0

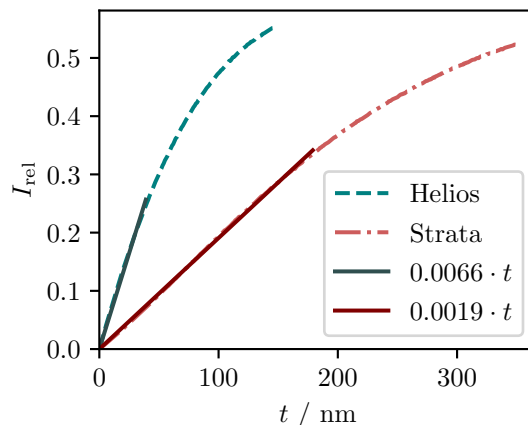


Figure 5.13. Simulated relative HAADF-STEM intensities I_{rel} as a function of aC thickness t ($I_{\text{rel}}-t$ curve) for the HELIOS and STRATA microscope, simulated as described in Section 5.3.5.

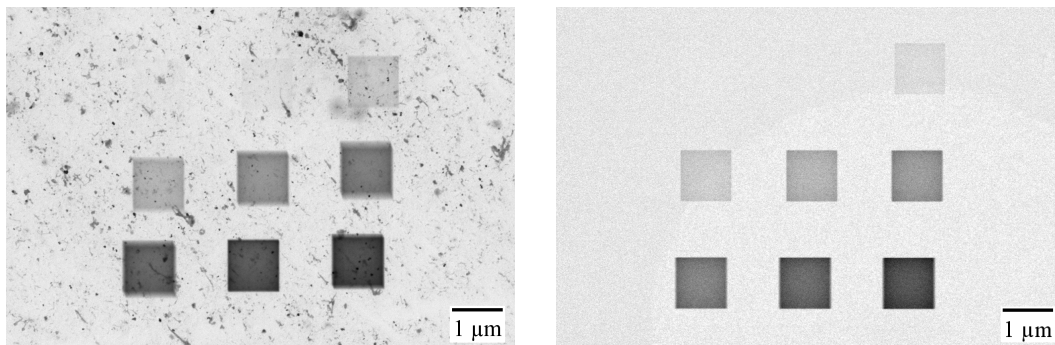
5.4. Results: Influence of Imaging Parameters and Characteristics of Contamination Growth

This section shows the results of the carbon contamination experiments. It starts with discussing the quality of the carbon films that serve as a substrate for the contamination and were prepared according to Section 5.3.2. The description of contamination test results starts with the reference measurements and some findings on the reproducibility of the tests. SEM-like contamination test patterns give insights into the influence of different imaging parameters and the morphology of contamination. TEM-like test patterns are the prerequisite to compare experimental and calculated contamination thicknesses. The last part examines the effectiveness and handleability of different contamination-mitigation strategies.

5.4.1. aC Films

The aC films have to be clean and with a uniform thickness for reliable and reproducible contamination tests. Figure 5.14 shows a comparison between a commercial carbon film¹³ and one that was prepared in this work with the procedure described in Section 5.3.2, both with 9 contamination patches. The self-made carbon films are very clean compared to the commercial ones, and the contamination particles of the film in Figure 5.14a are even visible within the contamination test deposits. In contrast, the self-prepared aC film is a more homogeneous substrate for the contamination deposit. A circular-shaped brighter area of the film in Figure 5.14b indicates that the film is thinner there. As these clean self-prepared films show nearly no detail, focusing has to be done at the borders of each window in the film-supporting

¹³Plano GmbH (product number S160-3, carbon film on 300 mesh Cu grids)

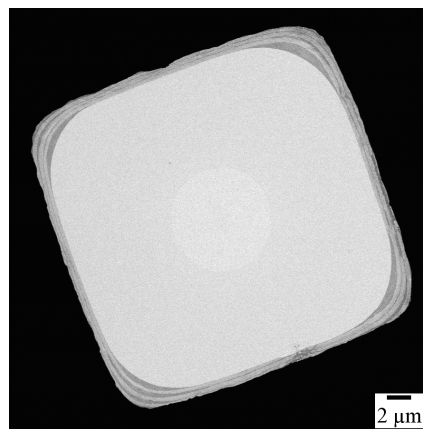


(a) BF-STEM image of a commercial carbon film with contamination pattern at 20 keV. Product: Plano GmbH, S160-3. Image courtesy of K. Adrion.

(b) BF-STEM image of a self-made carbon film with contamination pattern at 20 keV.

Figure 5.14. Comparison between a commercial and a self-made carbon film. In (a), the 9 square-shaped contamination deposits show contamination particles of the dirty film, which disturbs the evaluation process. The image width is 10 μm in both cases.

Figure 5.15 BF-STEM image of a TEM grid window covered by an aC film. In addition to the film (in the bright regions), there is some contamination visible in the vicinity of the Cu grid (black area in Figure 5.15). The circular region in the center appears the brightest, indicating that the film is thinnest there.



TEM grid where some contamination remains from the drying process. Figure 5.15 shows such a window. Some contamination is observed in the vicinity of the Cu grid (black area in Figure 5.15). The drying process also seems to leave an additional layer, except for the region in the center of the window, which appears as the brighter circle that was already visible in Figure 5.14b. The image evaluation shows that the thickness of the film in Figure 5.15 is 9.9 nm in the center. In the surrounding part, the film is 0.6 nm thicker. Those small differences in thickness stem from inhomogeneities of the film or previous contamination. They are taken into account in the error estimation in the uncertainty on I_{exp} Section 5.3.7. The uncertainty is assumed to be only 0.8% there as Figure 5.14b shows an example with a relatively thick additional layer. In addition, the contamination test pattern is usually placed in the center of such a bright circle, such that the film thickness below each contamination deposit is more or less the same.

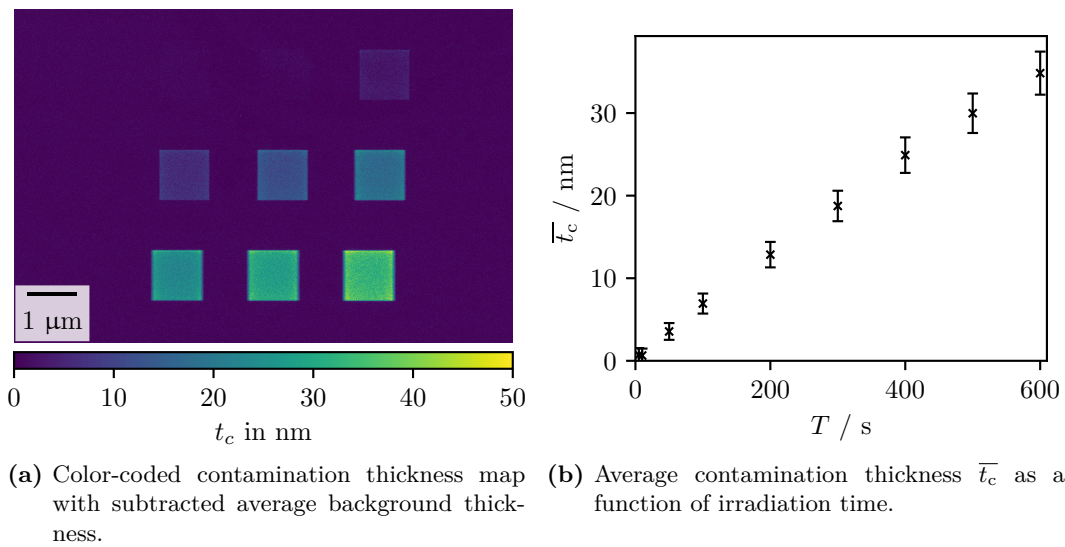


Figure 5.16. Contamination reference test at the HELIOS microscope irradiated with 20 keV electron energy and 50 pA beam current using the SEM-like pattern (Figure 5.7a) with irradiation times from 5 s to 600 s.

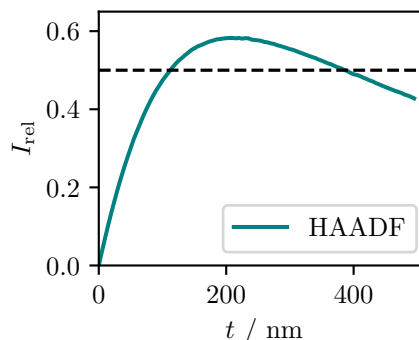
5.4.2. Contamination Thicknesses

First we take a look on the typical result of a reference measurement (aC film, 20 keV, 40/50 pA, SEM-like irradiation, see Table 5.1 on page 91), before checking the changes of results with time and the chosen microscope.

5.4.2.1. Typical Result of a Reference Measurement

Figure 5.16 shows a typical contamination thickness map together with the mean thickness \bar{t}_c of each contamination pad, which results in a plot of \bar{t}_c as a function of the irradiation time T . The contamination pads in Figure 5.16a show a nearly homogeneous thickness, only the edges and corners of the square are a bit thicker. This can be explained by the replenishment of mobile contaminants that reach the irradiated area at its borders. This behavior is expected to be stronger for scanning irradiation, as replenishing can take place also in the central part of the irradiated area when the focused electron beam is at another spot [UHM08]. The squares are not perfectly aligned to each other due to sample drift during the growth procedure in direction left-down. Figure 5.16b shows a nearly linear increase of mean contamination thickness \bar{t}_c with time T , without saturation in the examined time interval of up to 10 min.

Figure 5.17 Simulated relative intensities I_{rel} on the HAADF detector of the HELIOS microscope as a function of sample thicknesses t up to 500 nm at $\text{WD} = 4.2$ mm, 20 keV, and for an aC thin film with the properties described in Section 5.3.5. The dashed line highlights the ambiguity of I_{rel} values, if sample thicknesses larger than the thickness at the maximum (here ≈ 205 nm) occur.



5.4.2.2. Reliability of the Thickness Determination

The errors in Figure 5.16b were calculated according to Section 5.3.7 and increase with \bar{t}_c . In the shown example, the relative uncertainties are between 6.1% and 6.2%, which means in absolute values an uncertainty of ± 0.8 nm for the first data point and ± 2.6 nm for the last one. In the following plots of \bar{t}_c over T , the error bars are omitted for clarity. The result in Figure 5.16b demonstrates that the thickness determination based on quantitative HAADF-STEM intensities and MC simulations is reasonably reliable with sub-nm precision for very thin specimens in our case. As the simulation uncertainty dominates the uncertainty of the calculated thicknesses, the precision can be considerably better if the material's properties are known with higher accuracy. For example, the uncertainty of the material density ρ and the material composition is negligibly small for many crystalline specimens.

The method is valid up to the specimen thickness where the HAADF curve shown in Figure 5.17 begins to decrease, as this leads to ambiguities: The relative intensity I_{rel} can match to more than one thickness value t (dashed line). Hence it should be possible to exclude that thicknesses near to the maximum of the HAADF curve and larger occur in the examined specimen. The reliability of the method is the best for the approximately linear area of the curve for small thicknesses. Close to the maximum of the HAADF curve, the uncertainty of thickness determination is larger than for thinner specimens, as a specific value and uncertainty of I_{rel} match a broader value range of t for less steep sections of the curve.

5.4.2.3. Reproduceability

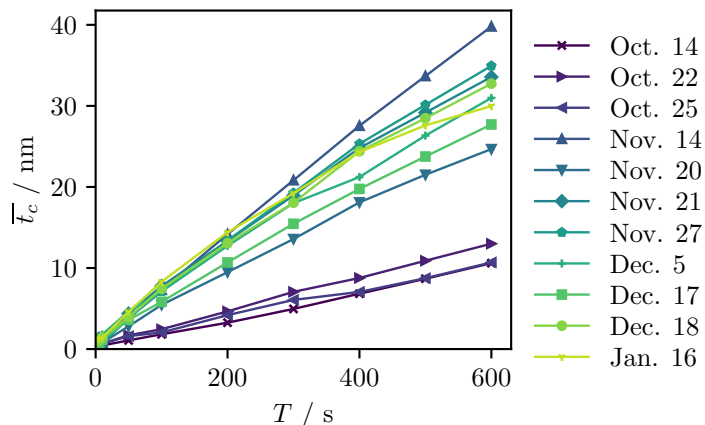
The comparability of the microscope and sample conditions were always tested by a reference measurement before experiments were performed. This procedure was applied on each day when measurements took place, and when a new sample or different microscope was used. Another problem is the drift of the stage during the long contamination times. Finally, it has to be tested if the distance and irradiation sequence of the irradiated areas changes the contamination growth.

Reference measurements over a longer period Repeated reference measurements on one sample and in the same microscope can reveal changes in the state of the microscope or sample with time. Figure 5.18 shows the evaluation of reference measurements over a period of four months on one single sample. This sample was produced shortly before the first measurement and stored in a box in ambient air between the measurements. In Figure 5.18a, we see the mean contamination thickness as a function of irradiation time for the different measurement dates. For better readability, the error bars are not shown here and in the following. Also here and in the following, the points of each measurement are connected with straight lines without indicating a fit, if not stated otherwise. Figure 5.18b shows the microscope chamber pressure¹⁴ observed during the measurements at the different days. The time span is divided in three parts, highlighted by a colored background. The first three measurements were performed before a long service break, where the chamber was vented and open for a longer time. All other measurements took place after the service break. Although the chamber pressure is mostly above average for the first three measurements (Figure 5.18b), they show a low contamination thickness, reaching about 10 nm after 10 min of irradiation (Figure 5.18a). Directly after the service break (Nov. 14), contamination was strongly increased, reaching 40 nm. It was then again much lower on Nov. 20, after which the values reach between 28 nm and 35 nm. A noticeable change in the growth occurs at Jan. 16. The values are nearly identical with the previous measurements until 500 s are reached. This is when the growth seems to saturate and the curve does not remain linear. There is no obvious link between the different slope of these curves and the chamber pressure shown in Figure 5.18b. Also, the differences don't show a direct connection with the aging of the sample, as the contamination is not consistently increasing over the 3 months.

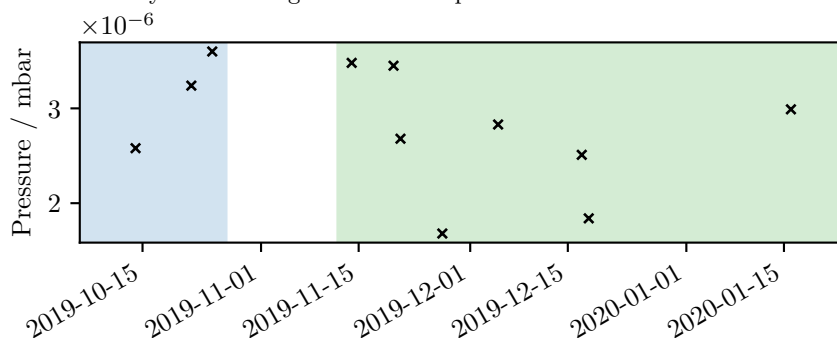
It is helpful to see the contamination patterns behind the curves to understand what causes this behavior. Figure 5.19 shows thickness maps from Nov. 21 and Jan. 16, respectively. The corresponding mean contamination thicknesses \bar{t}_c of the first date one show approximately linear contamination growth while \bar{t}_c saturates on the second date (Figure 5.18a). In the first case (Figure 5.19), the contamination patches show a rather homogeneous thickness, although it is slightly enhanced at the edges. The shape of the contamination changed completely 2 months later: Now the contamination is dominant at the edges of the squares and reaches around 50 nm there after 10 min of irradiation. In the inner patch regions, the contamination thickness is much lower and around 10 nm (right side of Figure 5.19).

The most obvious explanation for this change in contamination growth could be a change in the contaminants on the film. Though the sample was stored at the same place in the time between the measurements, it was also used for measurements

¹⁴Measured by the Penning gauge attached to the microscope



(a) Mean contamination thickness \bar{t}_c over the irradiation time T , showing changes in the reference test on different days when using the same sample.



(b) Changes in the chamber pressure over the time span shown in (a). The date format on the x -axis is year-month-day.

Figure 5.18. Contamination growth on one sample and chamber pressure in the HELIOS microscope over a period of 3 months (aC film, 20 keV, 50 pA).

between these two dates, and the humidity of the ambient air may have changed. A change in the composition of contaminants could change their diffusion constant, too. It has been discussed in Section 5.2.2 that a lower diffusion constant leads to a stronger frame formation (see Figure 5.4 on page 85).

In this case, the mean contamination thicknesses \bar{t}_c from the reference test gave a hint that some conditions have changed. The contamination thickness maps confirm that the sample did not show the typical contamination pattern anymore on Jan. 16. That leads to conclusion that measurements performed on this day cannot be directly compared with results from other days.

Influence of the microscope The measurements in this chapter were performed using two microscopes, the HELIOS and STRATA STEM-in-SEM instruments. It is interesting to compare how the contamination grows in one or the other microscope using the same sample on the same day. Figure 5.20 shows this comparison. As the beam current is not the same, the \bar{t}_c values are normalized with the measured beam current I to obtain reliable results. These measured currents are $I_{\text{Helios}} = 40$ pA and

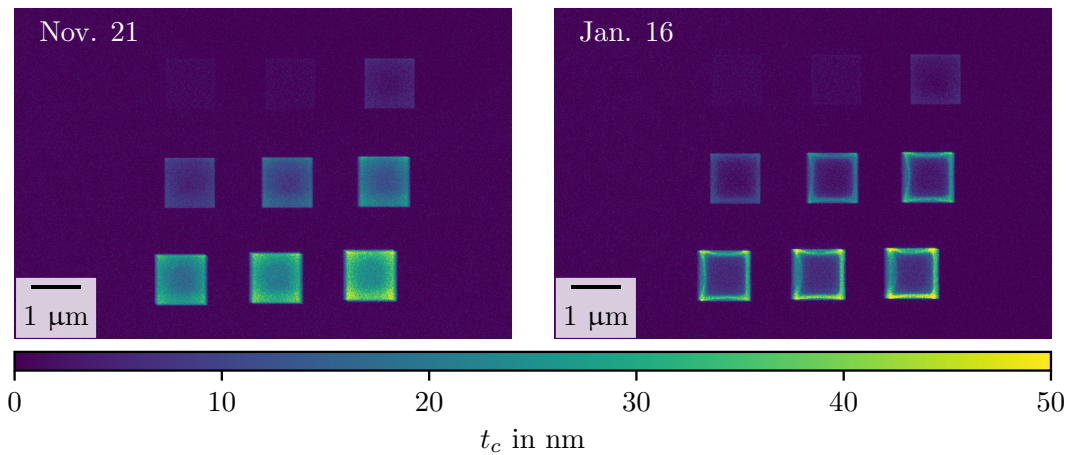


Figure 5.19. Contamination thickness maps of reference measurements on the same sample on two different dates (Nov. 21 and Jan. 16, aC film, HELIOS, 20 keV, 50 pA). Figure 5.18a shows the average thicknesses \bar{t}_c from these thickness maps.

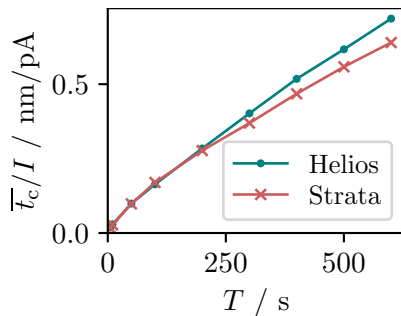


Figure 5.20 Mean contamination thickness \bar{t}_c measured on the same day and the same sample in the HELIOS and STRATA microscope (aC, 20 keV). The values are normalized with the measured beam current I .

$I_{\text{Strata}} = 27$ pA for the nominal current values 50 pA and 40 pA, respectively. It is important to note that the actual current values may change over time, e.g., with position changes of apertures and cross-over or due to aging of the electron source. The contamination in the two microscopes shows no difference in the first 2 min (Figure 5.20). The contamination in the HELIOS then continues slightly faster than in the STRATA microscope. The relative deviation of \bar{t}_c/I after 10 min of irradiation is +13%. Although this deviation is not too large, the results on beam showering in Section 5.5.1 will indicate that the microscope can significantly influence the contamination growth. Notably, both curves have a power-law appearance in the first minutes, indicating that the time to reach the steady state is visible here.

Influence of sample drift and pattern distance It is essential to answer whether the chosen pattern for contamination measurement allows general findings or if the results are undesirably dependent on factors like sample drift and pattern distance. Figure 5.21 shows the evaluation method applied to deposits with significant sample drift compared to the associated reference measurement with nearly negligible drift. The sample drift smears out the contamination pads, which gives them a 3D-like appearance (Figure 5.21a). In this example, it is even so large that

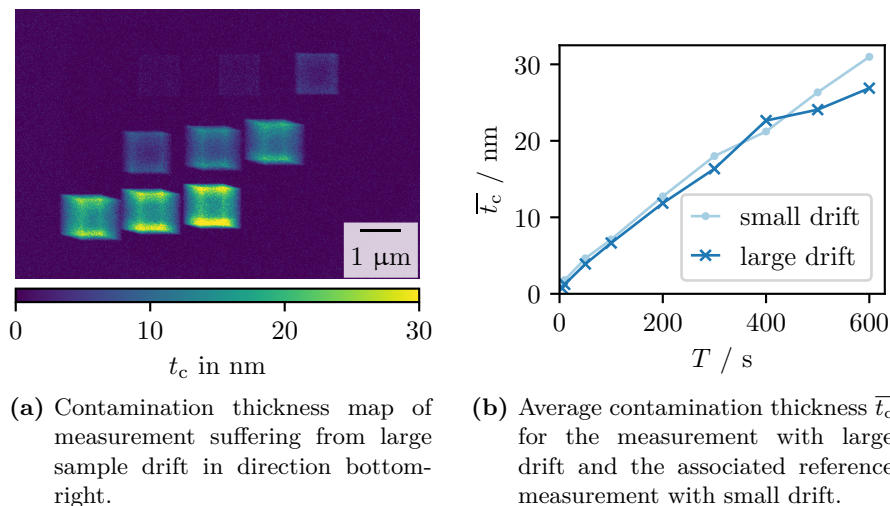


Figure 5.21. Test of the evaluation method’s stability towards sample drift (aC film, HELIOS, 20 keV, 50 pA).

the deposits begin to overlap. However, the \bar{t}_c curves for small and large drift differ only slightly (Figure 5.21b). This indicates that the chosen concept of measurement is not affected by sample drift. The bearable upper limit of sample drift is just before the deposits begin to overlap. In this case, \bar{t}_c is not reliable anymore. The sample drift of the results in this chapter was generally significantly lower than in Figure 5.21.

Figure 5.22 shows the comparison of two measurements with the SEM-like pattern (c.f. Figure 5.7a on page 90) and the same pattern with a square distance of $0.5\ \mu\text{m}$ instead of $1\ \mu\text{m}$. This experiment was carried out to test if the successively irradiated patterns influence each other due to a too-small distance. In this case, halving their distance should lead to changed \bar{t}_c values. However, the difference between the two curves in Figure 5.22 is small and indicates that the squares grow independently. Another test with $2\ \mu\text{m}$ distance between the squares lead to the same conclusion as it had no significant influence on the contamination.

We can thus conclude that the contamination measurement method as outlined in Section 5.3 is a reliable tool to test contamination growth. As some uncontrollable conditions of the microscope or sample may change over time, the reference test is inevitable to compare results from different days, samples, or microscopes.

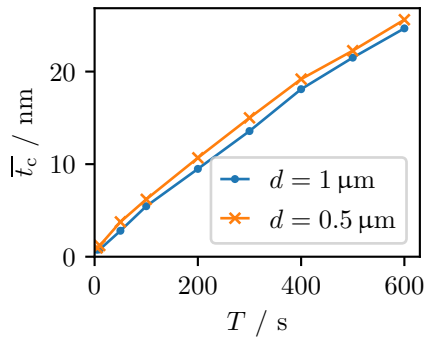


Figure 5.22 Mean contamination thicknesses grown with the SEM-like pattern using the usual distance d of $1 \mu\text{m}$ and a smaller distance of $0.5 \mu\text{m}$ between the squares (aC film, HELIOS, 20 keV, 50 pA).

5.4.3. Influence of Imaging Parameters

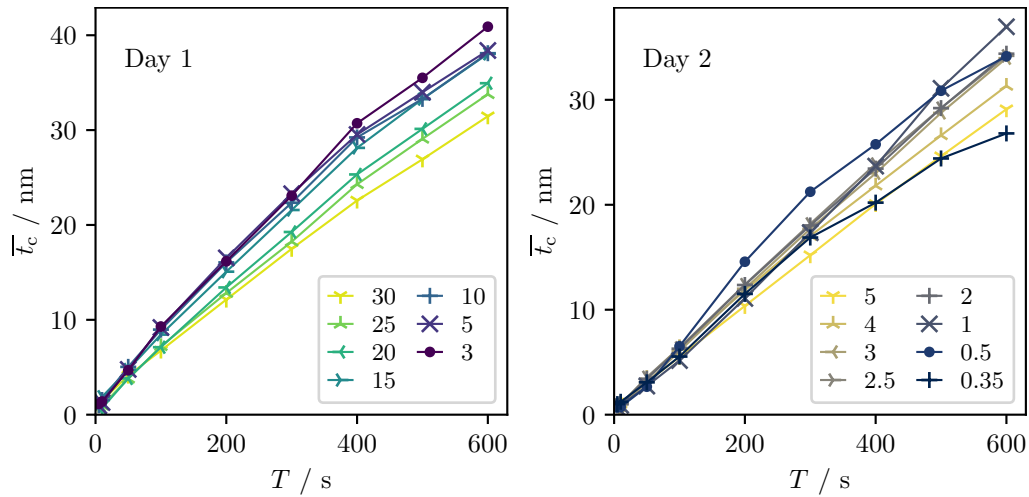
The following results include mostly comparisons of different measurements. Directly compared results were measured within one day, in one microscope, and on one sample. This section discusses the influence of different imaging parameters, like primary electron energy, beam current, total dose, scan dwell time, and irradiation time. Each parameter section includes tips to reduce contamination by optimal imaging settings. Lastly, it shows the change of contamination when using another substrate material.

5.4.3.1. Electron Energy

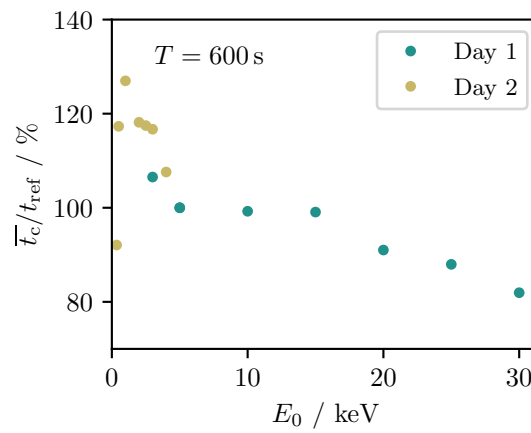
The primary electron energy E_0 is a crucial contamination parameter, as Section 5.2 and especially Section 5.2.1.6 have pointed out. Figure 5.23 comprises two data sets that show the energy dependence of contamination growth. Figure 5.23a splits the results into two subfigures, representing measurement day 1, covering electron energies from 30 keV to 3 keV, and day 2, covering energies down to 0.35 keV. From 30 keV to 3 keV \bar{t}_c increases with decreasing E_0 . The second data set down to 0.35 keV reveals a more complex behavior. \bar{t}_c continues to increase with lower E_0 until the behavior changes at 0.5 keV: For the two lowest energies, the \bar{t}_c - T curves are less linear, and the final contamination thickness is reduced. This reduction complies qualitatively with the theoretical cross-section. However, the theory predicts the maximum at a lower electron energy ($E_{\text{max}} \approx 0.1 \text{ keV}$, c.f. Figure 5.2 on page 76). Figure 5.23b comprises both data sets. The \bar{t}_c values after irradiation for 10 min are normalized with the contamination thickness at 5 keV (t_{ref}) and plotted as a function of E_0 . Due to the normalization, both data sets intersect at $E_0 = 5 \text{ keV}$ (100%). Figure 5.23b shows the decrease of contamination with increasing E_0 , which would already be expected from the dissociation and ionization cross-section (Figure 5.2 on page 76 and Equation (5.3)). However, the cross-sections drop too fast with increasing energy (Figure 5.2b on page 76) to explain the still significant contamination thicknesses at 10 keV and above. The likely explanation for the slow

decrease of \bar{t}_c with increasing E_0 is that the contamination growth is mainly caused by SE rather than the primary electrons. The SE yield $\delta \propto E_0^{-0.8}$ decreases slower than the dissociation cross-section (see Equation (5.12) on page 80). At 20 keV, δ is still 0.08 for carbon and may be multiplied by two due to the two surfaces of our aC film [LJ05].

Figure 5.23b also shows the maximum of contamination at 1 keV more clearly. To understand this behavior, it is helpful to take a step back and look at the underlying thickness maps. Figure 5.24 shows the thickness maps for 4 keV and 0.35 keV. While the contamination looks as usual for 4 keV, the appearance has changed completely at 0.35 keV: It spreads around the irradiated area and is more concentrated at the edges and corners inside the irradiated area. The spread of contamination may be connected to electric charging of the support film, caused by a high number of absorbed primary electrons at such low energies. In this case, the charges are not transported away fast enough if the film's conductivity is low. The localized charges may lead to a inhomogenous electric field that disturbs the electron beam and causes the spread of contamination. A second possible reason is the increased emission rate of SE and BSE at lower beam energies. The SE emission rate has its maximum just at 0.4 keV for carbon [LJ05]. As a result of the changed regional distribution of contamination at 0.35 keV, the contamination thickness in the irradiated area is reduced, which indicates a change in the contamination growth at very low energies. However, a cleaning effect, as mentioned in Section 5.2.3 for 0.1 keV electrons is not visible. The possible charging effects below 1 keV possibly disturb the imaging process. Hence, lowering the beam energy for reduced contamination does not seem to be a good advice. Similar \bar{t}_c values as for 0.35 keV result from $E_0 \geq 20$ keV. It is thus advisable to maximize E_0 for reduced contamination.



(a) Mean contamination thickness \bar{t}_c as a function of irradiation time T for the two different measurement days (left and right) and using different electron energies denoted in the legends in keV.



(b) \bar{t}_c at $T = 600$ s, normalized with the mean contamination thickness t_{ref} at 5 keV at day 1 and 2, respectively.

Figure 5.23. Energy dependence of contamination between 0.35 keV and 30 keV. The datasets stem from two different days, denoted as Day 1 and Day 2 (aC, HELIOS), 50 pA.

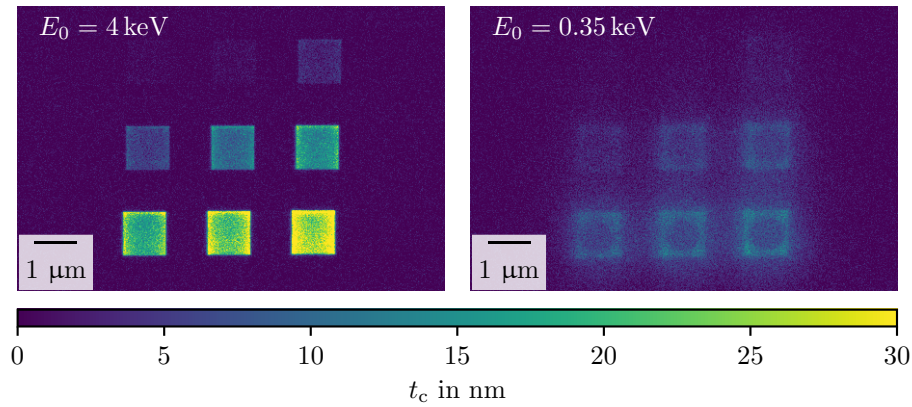


Figure 5.24. Contamination thickness maps of deposits grown on the same sample using the same setting except $E_0 = 4$ keV on the left side and 0.35 keV on the right side (aC, HELIOS, 50 pA).

5.4.3.2. Influence of the Beam Current and Total Dose

The influence of the total dose on the contamination thickness was first investigated by simply increasing the beam current using the SEM-like pattern while keeping the number of irradiated pixels per scan line constant. If contamination would be a pure dose effect and independent of the dose rate, a doubled beam current I should double the contamination thickness (Figure 5.25). Instead, Figure 5.25 shows a saturation of \bar{t}_c with increasing beam current. For lower currents, \bar{t}_c increases with I , indicating the electron-limited regime. However, around 366 pA, the \bar{t}_c saturates, indicating that the precursor-limited regime is reached. The measurement thus illustrates the transition between the two extremes (see Section 5.2.1.5 on page 78). Notably, the growth regimes were defined using the current density j in Section 5.2.1.5. For a stationary beam irradiating a defined area, j is defined as the dose rate per beam area. However, for SEM-like irradiation like in this section, it should not be understood as dose rate per *beam* area of the focused beam, but as dose rate (current) per irradiated area, here $1 \mu\text{m}^2$.

The saturation behavior becomes clearer in Figure 5.26. The relation between dose rate and contamination thickness is tested here by the variation of the dose rate while keeping the overall dose σ_q constant. This is accomplished by increasing the irradiation time and decreasing the beam current, as shown in Figure 5.26a and Table 5.3. All squares in Figure 5.26a were irradiated with the same total dose $\sigma_q = 1.8 \text{ C cm}^{-2}$ but different dose rates (with the unit $\text{C cm}^{-2} \text{ s}^{-1}$). The dose rate is the highest for square 1 with the smallest contamination thickness and decreases until square 9 with the highest contamination deposit. This thickness map and Table 5.3 show that contamination is reduced when a high beam current is applied in a short irradiation time rather than a low current in a long time. Figure 5.26b

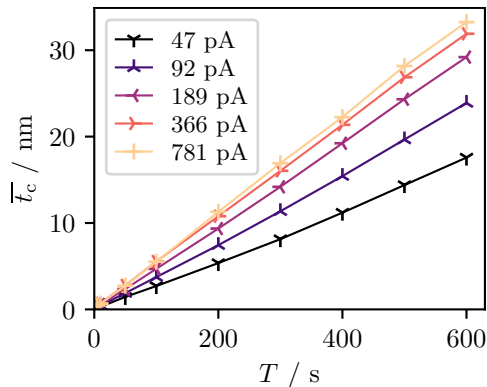


Figure 5.25 Mean contamination thickness as a function of irradiation time for different measured beam currents, given in the legend (aC, HELIOS, 20 keV).

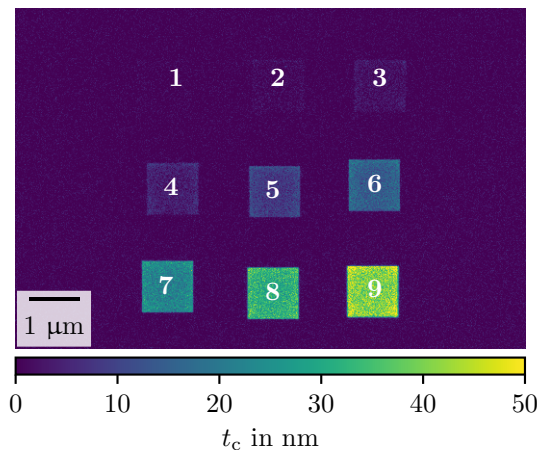
Table 5.3. Parameters for measurements of the dose rate dependence of the contamination thickness in Figure 5.26a.

Rectangle no.	Measured current / pA	Time / s	dose rate / $\text{C cm}^{-2} \text{s}^{-1}$	total dose / C cm^{-2}
1	4520	4	$4.5 \cdot 10^{-1}$	1.808
2	2220	8	$2.2 \cdot 10^{-1}$	1.776
3	1110	16	$1.1 \cdot 10^{-1}$	1.776
4	549.2	32	$5.5 \cdot 10^{-2}$	1.757
5	268.4	68	$2.7 \cdot 10^{-2}$	1.825
6	135.8	134	$1.4 \cdot 10^{-2}$	1.820
7	65.8	276	$6.6 \cdot 10^{-3}$	1.816
8	32.7	555	$3.3 \cdot 10^{-3}$	1.815
9	16.1	1121	$1.6 \cdot 10^{-3}$	1.805

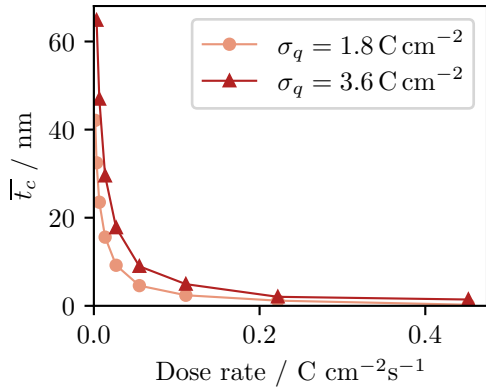
and c) show the \bar{t}_c values belonging to the thickness map and another measurement with doubled irradiation time. The transition from a strong dependence on the dose rate at low dose rates (electron-limited regime) to the saturation behavior is well visible. The possible temperature rise of the sample at higher currents might additionally contribute to the saturation [KHS81]. The evaluation shows that it is advisable to reduce contamination growth while keeping a certain total dose (e.g., for high counts in an x-ray spectrum) by using a high current and short irradiation time.

5.4.3.3. Influence of the Irradiation Time

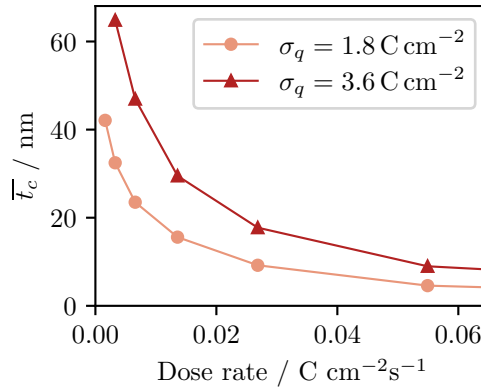
All contamination measurements shown by now resulted in (nearly) linear \bar{t}_c - T curves, indicating that the steady state is reached so fast that it could not be observed (see Section 5.2.1.5 on page 78). To observe the contamination growth over a longer time, A. Marx irradiated a single square of $1 \mu\text{m}^2$ continuously for 140 min. Every 10 min, he stopped the irradiation of the square for a short moment to take a HAADF-STEM image for thickness evaluation [Mar21]. Figure 5.27 shows the thickness development of this square. The orange area on the left marks the time



(a) Contamination thickness map for which the numbered squares were irradiated with different currents and for different times T as given in Table 5.3. The irradiation time was selected such that the total dose equals $\sigma_q = 1.8 \text{ C cm}^{-2}$ for each square. The dose rate is highest for square 1 and lowest for square 9.



(b) Mean contamination thickness as a function of the dose rate. The data points with $\sigma_q = 1.8 \text{ C cm}^{-2}$ stem from the pattern in Figure 5.26a. The dose was doubled for the second data series by doubling the irradiation time.



(c) Detail of the plot in (b): Contamination thickness for lower dose rates.

Figure 5.26. Contamination test with a variation of the dose rate and constant total dose (aC, HELIOS, 20 keV).

≤ 10 min covered by the measurements up to now. The \bar{t}_c - T curve still looks linear up to 50 min but begins to saturate afterward. Mitchell's power law (Equation (5.11)) is first tested to describe the experimental data, but the fit obtained by the non-linear least squares method strongly deviates from the experimental data (dashed curve in Figure 5.27). This is understandable since Equation (5.11) describes the initial diffusion of hydrocarbons into the irradiated area before the steady state is reached. In Mitchell's work, Equation (5.11) was used to describe contamination growth for up to 15 min [Mit15]. For the long irradiation times observed here, it is more likely that the initial behavior is not captured at all and the saturation rather indicates a depletion of mobile hydrocarbons. It seems thus more reasonable to fit a restricted growth function of the form $\bar{t}_c = S \cdot (1 - \exp(-cT))$, where S is the upper thickness limit and c is the growth constant. The thickness at $T = 0$ is assumed to be zero. The fit (again by non-linear least squares) yields the solid curve, which represents the experimental data well using the parameters $S = 156$ nm and $c = 0.01$ / min.

This result shows that the assumption of $\bar{t}_c \propto T$ is valid up to ≈ 50 min, but afterward, the growth saturates, presumably because the surface is strongly depleted of hydrocarbon molecules. The saturation indicates that there is also no endless supply of hydrocarbons from the atmosphere in the microscope chamber.

In Figure 5.18a and Figure 5.19 on page 105, the growth experiment performed on Jan. 16 showed a clear deviation from linear contamination growth in combination with frame-like contamination. The thickness maps after different times of irradiation that were evaluated for Figure 5.27 reveal a similar behavior (Figure 5.28): The contamination patch has a more homogeneous thickness after 10 min during linear increase of the contamination thickness. In contrast, a frame-like contamination pattern is observed after 100 min where a deviation from linear contamination-thickness increase is found. The connection between frame-like deposits and saturation of \bar{t}_c may be: When the mobile contaminants are increasingly depleted, less of them reach the irradiated area in a given time and most of them are directly pinned at the border. The contaminants are then not able to reach the center of the irradiated area, which results both in slower growth and frame-like deposits. The results of the long-time contamination measurement can thus be understood by diffusion of mobile contaminants on the surface.

5.4.3.4. Influence of the Scan Dwell Time

The main difference between SEM and TEM-like irradiation is that the electron beam irradiates either all points simultaneously or sequentially. For SEM-like irradiation, a specific dwell time on a pixel is used, leaving the mobile contaminants time to diffuse into the irradiated area [UHM08]. The dwell time was discussed in Section 5.4.2.1, where it could partly explain the homogeneous thickness of SEM

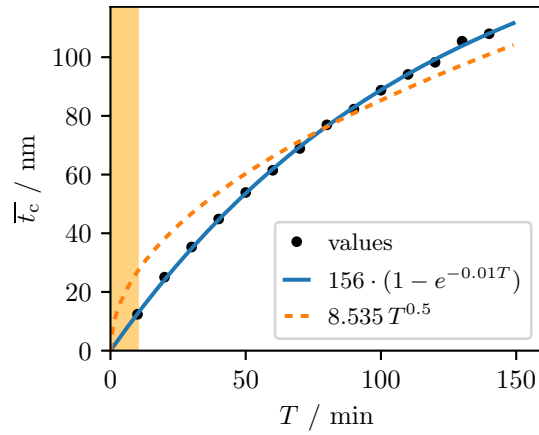


Figure 5.27. Mean contamination thickness \bar{t}_c of a single, continuously irradiated square of $1 \mu\text{m}^2$ for irradiation times up to 140 min (aC, STRATA, 20 keV, 40 pA). The orange region marks the time up to 10 min.

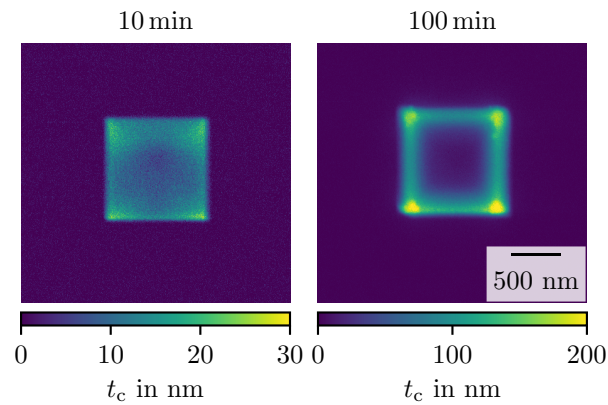


Figure 5.28. Contamination thickness maps of the irradiated patch evaluated in Figure 5.27 after 10 min and 100 min of irradiation (aC, STRATA, 20 keV, 40 pA). Please note that the color bars cover different thickness ranges. The scale bar applies to both thickness maps.

deposits. The question is now if SEM-like irradiation could mimic homogeneous irradiation if the dwell time was so short that the time that a pixel is not irradiated would be negligibly small. Figure 5.29 shows the comparison of scanning with a dwell time of 4 μs , 1 μs , and 0.25 μs . Both dose rate and total dose are kept constant. The scanned pixel distance in this measurement was a bit larger than the usually used value of 1 nm, namely 1.4 nm. The dwell time of 4 μs thus results in a scan refresh (loop) time of 1.05 s, 0.25 μs lead to a refreshing time of 0.1 s. The deposits in Figure 5.29 indeed indicate a change towards frame-like contamination for shorter dwell times. Their average contamination thickness \bar{t}_c is 13 nm, 16 nm and 10 nm, respectively.

However, the change towards frame-like growth was not reproduced in two independent repetitions of the experiment. A possible explanation for the non-repeatable findings is that on those measurement days, the diffusion coefficient of the contaminants was considerably larger, such that they were able to reach the center of the irradiated area even for the shortest tested dwell times (125 ns, refresh time 60 μs). The associated thickness maps of the measurement in Figure 5.29 and the repetition without frame-like growth support this assumption: The former reference measurement shows a frame-like behavior (Figure 5.19 on page 105, Jan. 16), indicating slow contaminants, whereas the latter shows contamination patches with homogeneous growth (similar to Figure 5.16a on page 101). If the contaminants diffuse very fast, the dwell time would always be long compared to the time scales of diffusion. This could explain why frame-like growth did not even appear for the shortest available dwell times in the repeated measurement.

Also the influence of dwell time on the mean contamination thickness in Figure 5.29 is unclear, as \bar{t}_c increases between 4 μs and 1 μs . At even shorter dwell times, the tendency seemed to be reversed. Again, repetitions of this experiment did not show this change of \bar{t}_c with dwell time. The influence of dwell time on the contamination in SEM-like irradiation thus needs further examination.

5.4.3.5. Influence of the Substrate

To test the influence of the substrate on contamination, K. Adrion applied the SEM-like reference test pattern to thin films of Au, Pd, and Si_3N_4 (see Section 5.3.1 on page 87) [Adr23; Adr12; Adr21]. These materials were chosen due to their different electrical conductivity, which is $45.5 \cdot 10^6 \text{ A V}^{-1} \text{ m}^{-1}$ for Au, $9.3 \cdot 10^6 \text{ A V}^{-1} \text{ m}^{-1}$ for Pd, and around $1 \cdot 10^{-14} \text{ A V}^{-1} \text{ m}^{-1}$ for Si_3N_4 , which means it is an electrical insulator [Win21; DKL17].

Figure 5.30 shows BF-STEM images of the Au and Pd film recorded directly after the irradiation. Notably, thinner samples lead to brighter gray values, while thicker

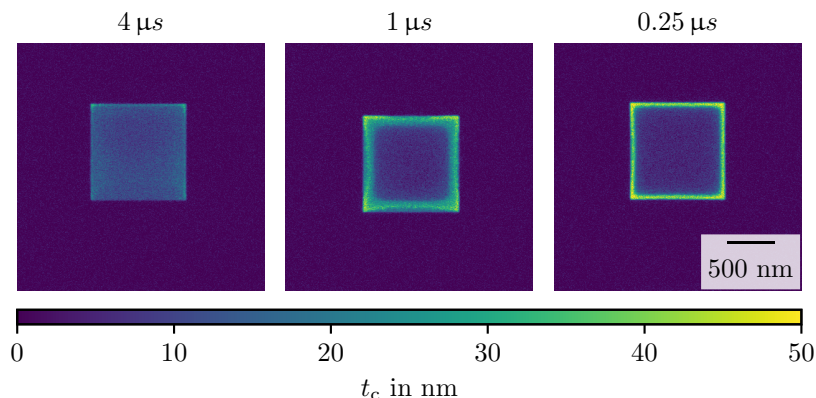


Figure 5.29. Contamination thickness maps of one patch irradiated with 4 μs , 1 μs , and 0.25 μs dwell time after irradiation for 200 s (aC, HELIOS, 20 keV, 50 pA). \bar{t}_c for 4 μs is 13 nm, for 1 μs 16 nm, and for 0.25 μs it is 10 nm.

samples show darker gray values in BF images. Both samples show granular background features. The Pd sample also shows spotted dark pre-contamination. In contrast to the aC films, the electron beam does not only apply contamination, but also thins the sample, indicated by brighter squares compared to the surrounding. The thinning could be explained by etching where the contaminants act as an etching precursor [RFR06]. In the case of Au, thinning is visible for up to 100 s. The Pd thin film in the irradiated squares does not even get darker than the untreated support during the full observed time interval, which could be explained by its catalytic activity.

The same contamination test on the Si_3N_4 film resulted in no visible changes of the film in the STEM images. Therefore, a smaller ($100\text{ nm} \times 100\text{ nm}$) area was constantly irradiated for 10 min (Figure 5.31). Although the areal dose here is larger than in the usual test, no contamination is visible. We can only speculate about the reasons for this behavior: Si_3N_4 is an insulating material, which could potentially lead to charging of the film and to the build-up of an inhomogeneous electric field. The field could disturb, deflect or defocus the electron beam and result in mitigation or spread of the contamination over a larger area. This behavior, however, was not intensely investigated and fully clarified.

5.4.4. Contamination Morphology

Figure 5.32 shows a side-view SE-SEM image and a thickness map of the same contamination deposit grown in 140 min (20 keV, 40 pA). Similar to the long-term irradiation in Figure 5.28, the deposit has a frame-like shape with stronger contamination at the edges than in the center. Again this morphology is explainable by the mobile contaminants that reach the irradiated area at the edges first and are mostly pinned there. Most electrons propagate through the thin aC films at 20 keV, thus

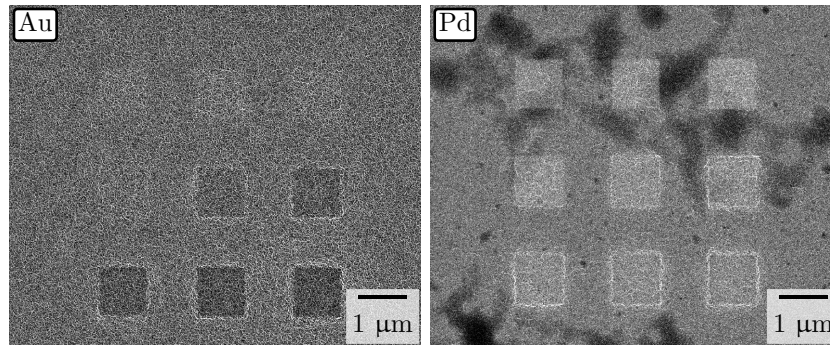


Figure 5.30. 20 keV BF-STEM images of an Au and a Pd thin film after the application of the SEM-like reference pattern with irradiation times between 5 s (upper-left square) and 10 min (lower-right square). 20 keV, 50 pA, STRATA.

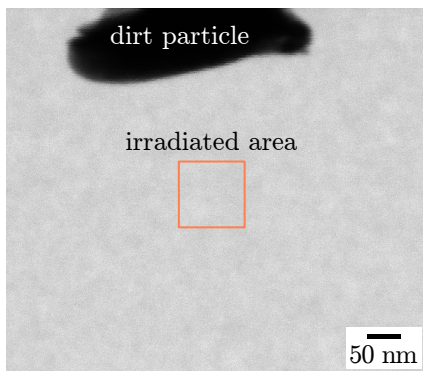


Figure 5.31 BF-STEM image (20 keV) of the Si_3N_4 film after irradiating an area of $100 \text{ nm} \times 100 \text{ nm}$ in the center of the image (orange marking) for 10 min with 20 keV, 40 pA (STRATA). The dark dirt particle facilitates focusing.

contamination growth is expected at both sides of the film [Hre78; Kan+90]. The growth on both sides is confirmed in Figure 5.33, which shows BF-STEM images of a cross-section TEM lamella of the contamination deposit shown in a). The same sample was used for Figure 5.9 on page 94, and the preparation is described there. Figure 5.33 confirms that contamination grows on both sides of the film, with no visible asymmetry.

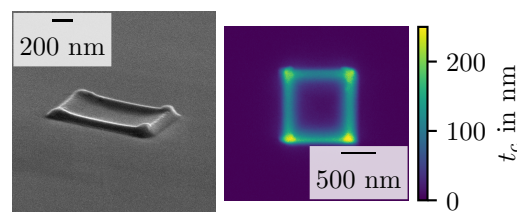


Figure 5.32. 3 keV SE-SEM and thickness map of a deposit grown in 140 min (20 keV, 40 pA, STRATA). The viewing direction of the SE image is tilted by 70° away from the top-view to reach a 3D-like impression.

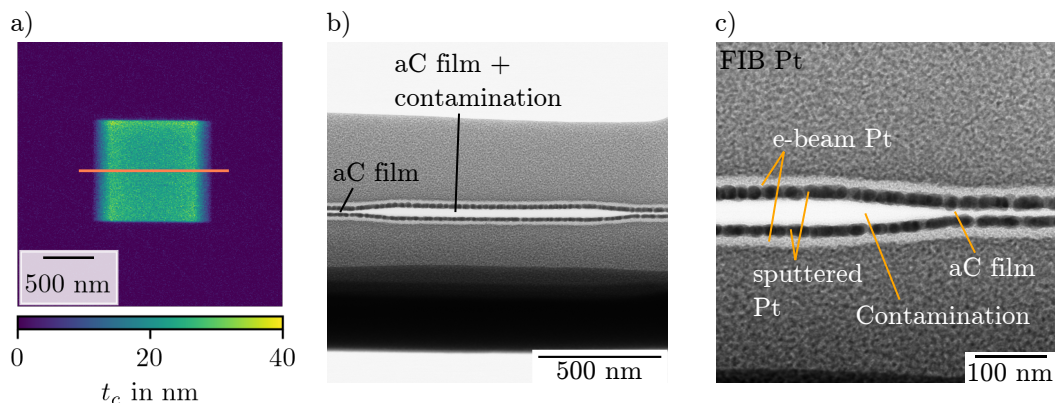


Figure 5.33. Morphology of a contamination deposit grown in 10 min (aC film, HELIOS, 20 keV, 50 pA) investigated by a cross-section TEM lamella. a) Thickness map of the deposit with unsharp left and right borders due to sample drift. The orange line indicates where the TEM lamella was taken out. b) Overview 200 keV BF-STEM image of the cross-section lamella where the aC film and aC film with contamination is visible as a bright horizontal line. c) Higher-magnification 200 keV BF-STEM image.

5.4.5. TEM-like Contamination: Comparison with Theory

The TEM-like test pattern (Figure 5.7b on page 90) provides the conditions needed for comparison with the theory by Müller (Section 5.2.2 on page 83). A. Marx conducted several contamination tests with this pattern, and Figure 5.34 shows a typical example [Mar21]. As expected from literature and the transport of contaminants mostly through diffusion (see Section 5.1 on page 70), the thickness map shows circular deposits where nearly all contamination is deposited at the rim of the exposed region (Figure 5.34a). Figure 5.34b shows the azimuthally averaged thickness of the bottom-right deposit ($T = 600$ s, red dots) in comparison with the theoretical contamination thickness from Equation (5.22) on page 84 and Equation (5.18) on page 84 (solid line). The theoretical curve was fitted to the experimental data using the set of parameters from Table 5.4 with the contaminants' residence time τ_0 as the fitting parameter. To reduce the number of free parameters down to τ_0 , we attempted to find realistic estimates for the unknown values, as described in the following.

A mass spectrum of the residual gas in the microscope¹⁵ helps identify possible contaminant species (Figure 5.35). Notably, molecules found in the mass spectrum can be fragments of larger molecules and are not necessarily found in the residual gas [Wan+10]. OH is the shortest hydrocarbon, which can result from the splitting of longer-chain carbons, Ga is a residual of the focused Ga ion beam of the microscope. H₂O, N₂, and O₂ are constituents of the atmosphere. The peak at 44 u

¹⁵Residual gas analyzer: QMG 250 PrismaPro quadrupole mass analyzer by Pfeiffer Vacuum. Spectrum measured by A. Marx.

could indicate C_3H_8 or CO_2 . As the concentration of CO_2 in the atmosphere and thus expectantly in the residual gas is fairly low, we assume for this comparison of theory with experiment that the contaminants species is C_3H_8 , which yields the assumed molecular mass¹⁶ of contaminants. The measured beam current of 32 pA determines the current density j . Throughout this chapter, the contamination is considered pure carbon with a density of 1.63 g cm^{-3} . The specimen temperature ϑ is set to 20°C , the diffusion constant D to $1.5 \cdot 10^{-14} \text{ m}^2 \text{ s}^{-1}$. Section 5.5.1.1 describes its determination from beam showering experiments. The beam-driven desorption cross-section σ_d is set to zero. The model by Alman, Ruzic, and Brooks (Equation (5.3) on page 74) allows calculating the contamination cross-section for C_3H_8 from direct dissociation and ionization, which they assume to lead to dissociation too, with a probability of 80 %. We used the mean energy $E = 25 \text{ eV}$ as the mean energy of SE, which contribute most to contamination. The other parameters for the cross-section are $E_{\text{max}} = 101 \text{ eV}$, $\lambda = 758 \text{ eV}$ from Equation (5.6) and Equation (5.7), and $E_{\text{th}} = 10 \text{ eV}$ [ARB00]. Lin and Joy determined the SE yield of carbon at 20 keV as 0.08, which is multiplied by two due to the two surfaces of our carbon film [LJ05]. All this leads finally to $\sigma_c = 0.76 \text{ \AA}^2$. The partial pressure of contaminants P is unknown, but $1 \cdot 10^{-7} \text{ mbar}$ seems a good guess as a fraction of the typical pressure in the microscope.

The residence time τ_0 is thus the only left parameter and is the fitting parameter for Figure 5.34. The fit by the non-linear least squares method yields $\tau_0 = 84 \text{ s}$, which agrees with the lower limit of 10 s formulated by Hirsch [Hir77]. This relatively long time explains why diffusion plays a significant role in the contamination process as it leaves the hydrocarbon molecules enough time to diffuse on the sample. However, the fit does not reproduce the experimental values perfectly. They have a steeper increase towards the border of the irradiated area, indicating a too small value of D . A smaller value for D would lead to a steeper increase in the theoretical curve and yield a larger value of τ_0 . As apparent from the large number of parameters, the comparison of experiment and theory and the fit depend strongly on reasonable assumptions for unknown parameters. Still, the comparison of the TEM-like deposits with the theory for circular irradiation helps confine the order of magnitude of otherwise completely unknown parameters.

¹⁶Molar mass divided by the number N_A of contaminants in one mol

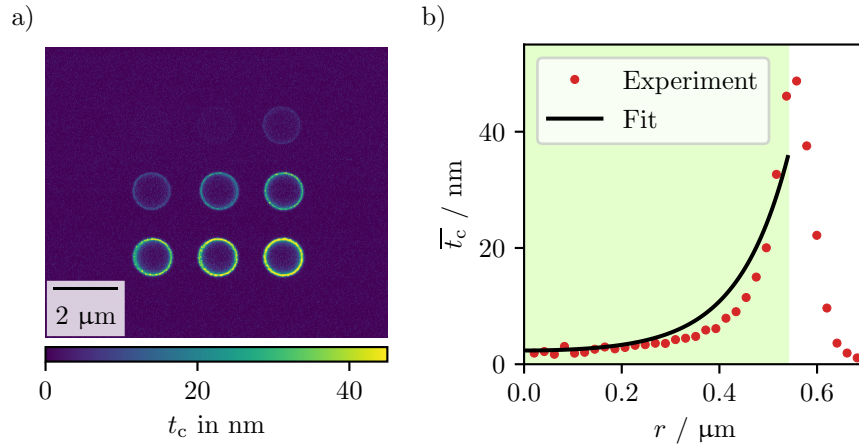


Figure 5.34. Comparison of measured and theoretical contamination thicknesses for TEM-like irradiation according to Figure 5.7b on page 90. a) Contamination thickness map (aC film, STRATA, 20 keV, measured current 32 pA). b) Azimuthally averaged contamination thicknesses (red dots) from the bottom-right circle in (a), and theoretical curve (solid line) fitted with τ_0 as the free parameter. The green background marks the radii inside the irradiated area.

Table 5.4. Parameters for the calculation of contamination thicknesses in Figure 5.34. The fit parameter τ_0 is highlighted in bold.

Parameter	Value	Name
j	35 A m^{-2}	Current density
R	0.54 μm	Irradiation radius
m	$7.32 \cdot 10^{-26} \text{ kg (C}_3\text{H}_8\text{)}$	Molecular mass of contaminants
m_c	$1.99 \cdot 10^{-26} \text{ kg (C)}$	Molecular mass of contamination
ρ	1.63 g cm^{-3}	Contamination material density
ϑ	293 K	Specimen temperature
D	$1.5 \cdot 10^{-14} \text{ m}^2 \text{ s}^{-1}$	Diffusion constant
σ_d	0 \AA^2	Desorption cross-section
σ_c	0.76 \AA^2	Contamination cross-section
P	$1 \cdot 10^{-7} \text{ mbar}$	Partial pressure
τ_0	84 s	Residence time

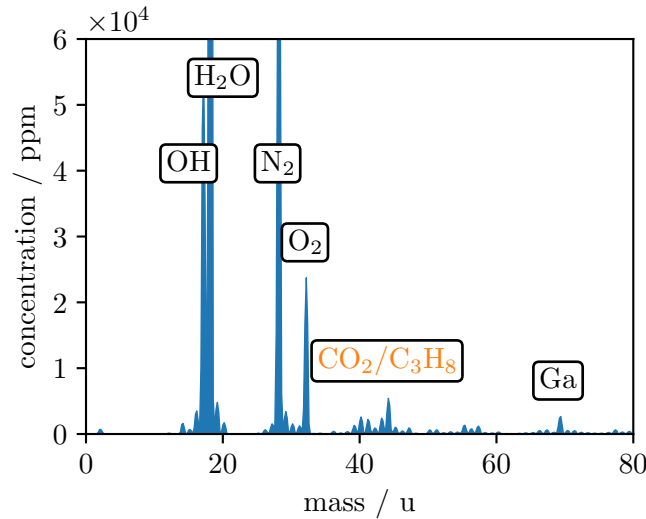


Figure 5.35. Mass spectrum of the residual gas in the STRATA microscope.

5.5. Results: Cleaning Strategies

This section focuses on contamination-mitigation and sample-cleaning strategies, from beam showering over sample baking to plasma cleaning. It discusses the efficiency of the different methods, also with regard to the ease of use. Beam showering experiments additionally allow estimating the diffusion constant D . After checking the results of each cleaning strategy individually, the section will end with a comparison of all methods.

A single, continuously irradiated $1\ \mu\text{m} \times 1\ \mu\text{m}$ square was used for these tests instead of the SEM-like pattern with 3×3 squares, as described in Section 5.3.3. Imaging for the evaluation of thicknesses was done at 20 keV and with 40 pA/50 pA, depending on the microscope. These imaging parameters will not be mentioned in each figure caption in the following. As a student assistant, K. Adrion performed a large proportion of the measurements in this section and helped in the data evaluation.

5.5.1. Beam Showering

Figure 5.36a shows the resulting average contamination thicknesses \bar{t}_c after the regular¹⁷ beam showering (BS) as described in Section 5.3.4 on page 91, compared to the reference measurement without cleaning. The curve labels indicate the measured showering current. The BS curves all show lower contamination thicknesses than the reference measurement. The effect increases with higher beam currents. However, the values of \bar{t}_c after 36 min reveal that the contamination reduction does not depend linearly on the showering current. The reference measurement shows the

¹⁷not leaving out the ROI

strongest contamination growth that reaches a linear increase after the first minutes of irradiation. The linearity up to 36 min is in good agreement with the saturation measurement (Figure 5.27 on page 114). Already beam showering with the lowest current (33 pA) reduces contamination growth compared to the reference measurement, especially in the first minutes after application. Beam showering with the two higher currents reduces contamination growth even more, again most effectively in the first 10 min. The showering even nearly suppresses contamination in the first minutes of contamination growth. However, it may be sufficient to shower with a low beam current when investigating beam-sensitive samples: Low currents are less damaging for the sample but still lead to some reduction of contamination. The slopes of all three curves converge after some time.

The convergence of the contamination curves becomes clearer in Figure 5.36b. It shows the slopes of the curves in (a) as a function of the time T' that has passed after beam showering. Only the slope of the reference measurement decreases with T' , which can be understood by the time it needs to reach the steady state. The BS curves reflect that beam showering is only effective for a limited time interval: The slopes start at low values, for the two highest currents even close to zero, and increase until they reach around the same value as the reference measurement. A colored background marks the time after which the slopes are approximately the same. The following section describes the determination of this time and its use to determine the contaminants' diffusion constant. The maximum of the 33 pA and 2050 pA measurement's slopes is not explainable by diffusion. Adsorption from the vacuum may play a role here and increase the contamination growth intermittently.

Notably, the effect of beam showering seems to depend on the microscope. Only a small and short-lasting (4 min) or even no effect of beam showering could be found in repeated tests of beam showering in the HELIOS microscope. Only showering a larger area on the sample yields a more significant effect of beam showering. The strongly varying effect of beam showering might be due to faster diffusing contaminants on the sample, which probably come from the sample holder. The different composition of contaminants could be caused by differences in the use of the microscope, like the diligence of sample handling, or the use of organic precursors for FIB and electron-beam deposition.

5.5.1.1. Diffusion Constant

Assuming that beam showering depletes most contaminants in the showered area, they begin to fill the showered area again by diffusion when the showering has stopped. Once they reach the ROI and have filled the depleted area, the contamination growth should continue as if no showering had been applied. The characteristic

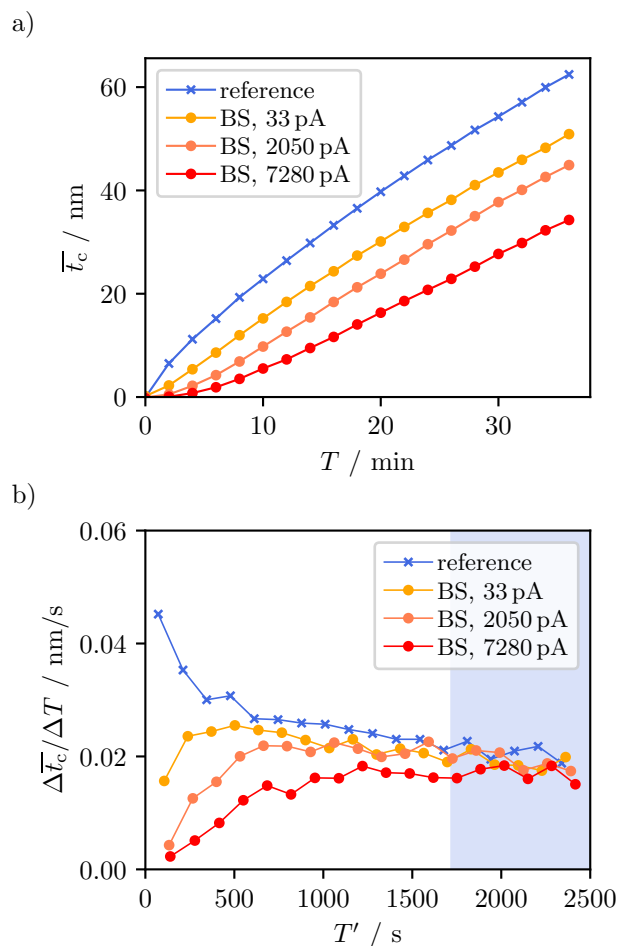
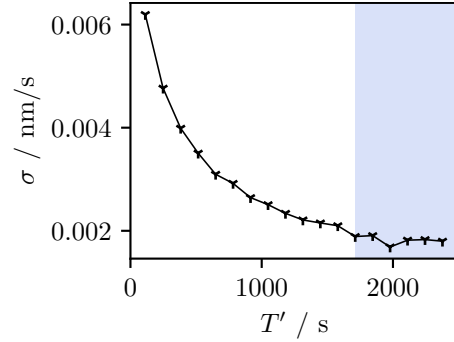


Figure 5.36. Result of BS measurements in comparison with the reference measurement (aC, STRATA, 20 keV, 40 pA). a) Mean contamination thickness \bar{t}_c as a function of the irradiation time T without cleaning (reference) and after beam showering with three different showering currents, given in the legend. b) Slope of the curves in (a) as a function of the time T' after the BS. The light-blue background marks the time when the slope is assumed to be constant.

Figure 5.37 Spread (standard deviations σ) of the slopes of the beam showering measurement in Figure 5.36b for each time T' after the beam showering (arbitrary units). The time after which the σ is considered to be constant is marked in bright blue.



time when this happens is denoted as T_D . To evaluate the deviation between the slopes quantitatively, the slopes at each (mean) time T' after cleaning are summarized as s and their spread is quantified by calculating the standard deviation (STD) $\sigma = \sqrt{\frac{1}{N} \sum (s_i - \bar{s}_i)^2}$ with $N = 4$. Figure 5.37 shows this STD between the slopes of the measurements in Figure 5.36 as a function of T' . A good guess for the time after which the standard deviations are nearly constant seems $T' = T_D = 1700$ s. This time is highlighted by the blue background.

The mean square displacement is the average diffusion distance of a molecule and is expressed as $x = \sqrt{k \cdot 2DT_D}$ [Cha+98]. In the beam showering experiment, x is the minimal distance that the contaminants have to diffuse to reach the ROI. It is around $10.2 \mu\text{m}$ from the border of the irradiated area to the ROI. The dimensionality of the system is $k = 2$. The estimated diffusion constant of contaminants in this experiment is thus

$$D = \frac{x^2}{2kT_D} = 1.5 \cdot 10^{-14} \text{ m}^2 \text{ s}^{-1} . \quad (5.25)$$

This value is considerably smaller than $D \approx 10^{-9} \text{ m}^2 \text{ s}^{-1}$ found for cyclic hydrocarbons (C_6H_6 and C_6H_{12}) on nickel [SA18]. However, it is closer to the estimation $D = 1.5 \cdot 10^{-15} \text{ m}^2 \text{ s}^{-1}$ for contaminants on aC and $\text{Pd}_{77.5}\text{Cu}_6\text{Si}_{16.5}$ thin films [Het+17], and $D = 7.5 \cdot 10^{-14} \text{ m}^2 \text{ s}^{-1}$ for contaminants on bulk Si [Ryk+08]. The large D variations are expected since the interaction between contaminants and substrate depends, for example, on their composition, surface configurations, and temperature.

5.5.1.2. Frame Showering

A variation of the regular beam showering is frame showering, as described in Section 5.3.4 on page 91. A $25 \mu\text{m} \times 25 \mu\text{m}$ area was showered for 10 min with 20 keV and 1880 pA, leaving out a square of $3 \mu\text{m} \times 3 \mu\text{m}$ in the center. Figure 5.38 shows the contamination without cleaning and after the application of frame showering, grown by continuous irradiation of the $1 \mu\text{m} \times 1 \mu\text{m}$ single-square ROI. The result is

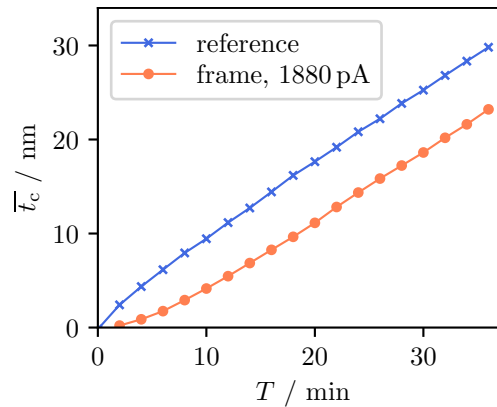


Figure 5.38. Mean contamination thicknesses \bar{t}_c after frame showering and without cleaning (reference) as a function of irradiation time T (aC, STRATA, 20 keV, 40 pA).

very similar to the regular showering with a comparable current (see 2050 pA in Figure 5.36). Frame showering is thus comparably effective as regular beam showering but protects the ROI from being damaged before the actual imaging. A disadvantage is the more complex setup of the showering pattern.

5.5.2. Sample Baking

Figure 5.39 shows the effect of baking the sample prior to the measurement for 15 min at 100 °C at $4 \cdot 10^{-3}$ mbar compared to the reference measurement. The main difference between baking and beam showering is that baking permanently reduces contamination growth. This becomes apparent as the baking curve looks like a re-scaled reference curve. The long-lasting effect is understandable since sample baking reduces the concentration of the contaminants all over the sample and even can affect the sample holder. This is in contrast to beam showering that only affects a limited area on the sample. At $T = 20$ min, the contamination reduction through sample baking is 26 %, despite the moderate baking temperature and relatively short baking time. In-situ sample heating on a heating holder in the microscope is expected to be more effective, as re-contamination during the transfer of the sample from the external baking recipient to the microscope is avoided.

5.5.3. Plasma Cleaning

Figure 5.40 shows the result of in-situ plasma cleaning for 15 min. A substantial reduction of contamination thickness is visible compared to the reference measurement. As the contamination after plasma cleaning increases approximately linearly, we can assume a long-lasting cleaning effect, similar to the effect of sample baking. Again plasma cleaning treats the whole sample, parts of the sample holder,

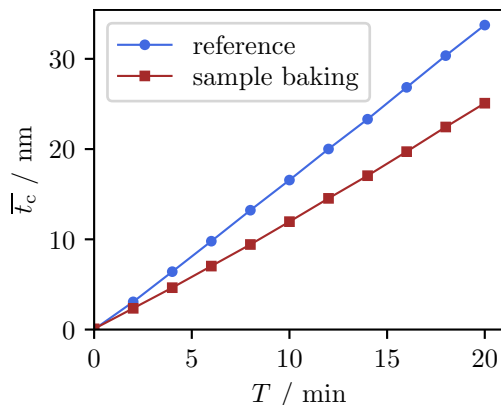


Figure 5.39. Mean contamination thicknesses \bar{t}_c after sample baking (15 min at 100 °C, $4 \cdot 10^{-3}$ mbar) and without cleaning (reference) as a function of irradiation time T (aC, HELIOS, 20 keV, 50 pA).

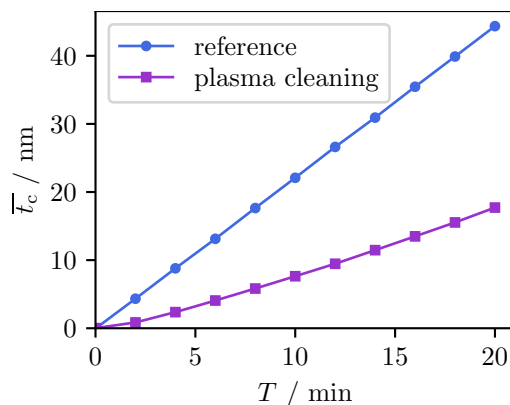


Figure 5.40. Mean contamination thicknesses \bar{t}_c after 15 min plasma cleaning and without cleaning (reference) as a function of irradiation time T (aC, HELIOS, 20 keV, 50 pA).

and even parts of the microscope, which explains the persistence of contamination reduction. However, caution should be exercised when applying plasma cleaning to organic samples which are likely to be damaged by the plasma, as mentioned in Section 5.2.3 on page 85.

5.5.4. Comparison of Contamination-Mitigation Strategies

Finally, the effect of regular beam showering, frame showering, sample baking, and plasma cleaning are compared. As the cleaning effect of the showering methods degrades with time, Figure 5.41 shows the reduction of contamination growth in the first 6 min. It was determined by fitting linear functions $m \cdot T$ for $T \leq 6$ min to the \bar{t}_c - T curves shown above and normalizing the fitted slope m with the value for the respective reference measurement. Assuming a linear growth is a substantial restriction but is approximately true for up to 6 min, enabling this comparison. The comparison separates the two used microscopes STRATA (Figure 5.41a) and HELIOS

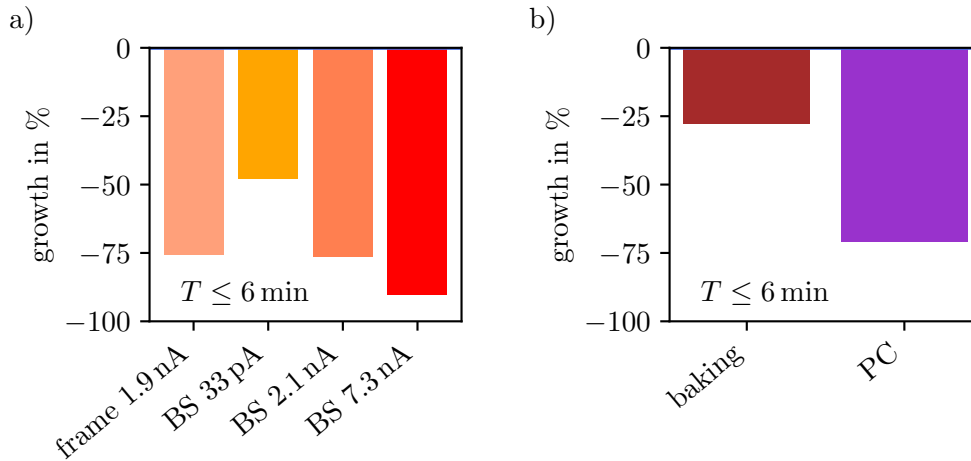


Figure 5.41. Comparison of contamination-mitigation strategies, separated for the two microscopes. It shows the relative growth reduction in % compared to the respective reference measurement, evaluated for up to 6 min of irradiation time. a) Regular beam showering (BS) and frame showering measurements with different currents in the STRATA microscope. b) Sample baking and plasma cleaning (PC) tested in the HELIOS microscope.

(b) as their result for beam showering was considerably different (see Section 5.5.1). Thus also the effect of baking and plasma cleaning may depend on the microscope. Figure 5.41a shows the effect of frame showering and beam showering (BS) tested in the STRATA microscope. Already regular beam showering with the lowest current (33 pA) reduces the contamination growth by 48 % during the first 6 min. Increasing showering currents reduce contamination more effectively, reaching a reduction of 90 % for 7.3 nA. The comparison confirms that frame showering and beam showering are equally effective (76 % reduction) for comparable beam currents. Frame showering is thus the better choice as it protects the sample. If the entire area is showered, the user needs to find a compromise between sample damage and cleaning effect to select the best beam showering current.

Figure 5.41b shows the effect of sample baking and plasma cleaning (PC), tested in the HELIOS microscope. Sample baking only reduces contamination moderately (28 %). Plasma cleaning is more effective (71 %). However, plasma cleaning yields a better result if irradiation times T up to 20 min are evaluated (Figure 5.42). Compared to Figure 5.41, the effect of all beam showering methods is considerably lower (now a reduction of 28 % to 67 %). The contamination reduction by sample baking and plasma cleaning remains nearly constant (now 27 % and 62 %). However, a decline of the cleaning effect is also visible for plasma cleaning, which is understandable if contaminants from some areas on the sample or sample holder that were not reached by the plasma reach the irradiated area after some time. These findings agree well with the results by Mitchell obtained at 200 keV (see Section 5.2.3 on page 85).

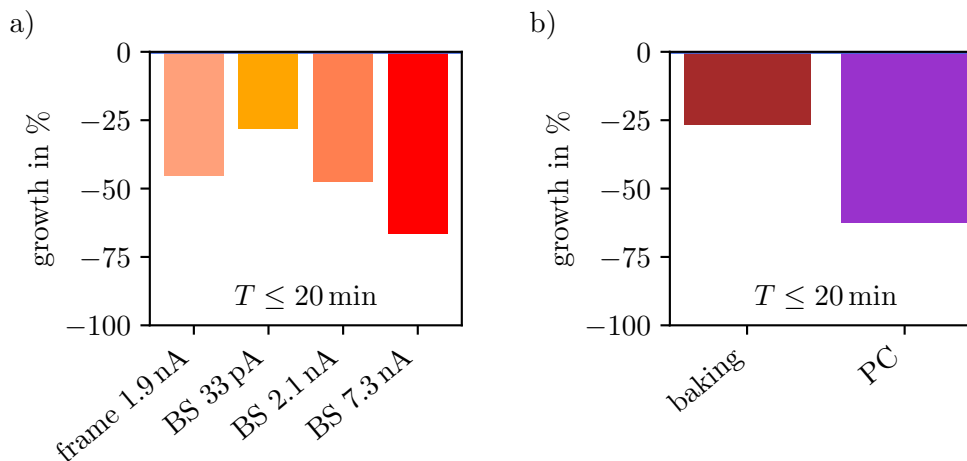


Figure 5.42. Comparison of contamination-mitigation strategies, separated for the two microscopes, evaluated for up to 20 min of irradiation time. a) Regular beam showering (BS) and frame showering measurements in the STRATA microscope. b) Sample baking and plasma cleaning (PC) tested in the HELIOS microscope.

5.6. Summary

This chapter presented an overview of contamination processes and growth and studies on this topic. A reliable and precise method was described to measure contamination on electron-transparent samples using quantitative HAADF-STEM imaging and MC simulations. Reference measurements with constant imaging parameters are performed before every examination of imaging parameters or cleaning methods. They ensure comparability between measurements and monitor changes of sample and the microscope parameters over longer time scales. An SEM-like test pattern was defined to test the growth of contamination depending on imaging parameters close to the reality in SEM imaging. A typical SEM contamination deposit has a relatively homogeneous thickness. Sometimes a more frame-like morphology is observed, attributed to slower-diffusing contaminants. A TEM cross-section lamella of a contamination deposit confirmed that contamination grows on both sides of an electron-transparent film. The parameter tests were performed on aC films, if not stated differently. The findings on imaging parameters can be summarized as follows:

- The primary **electron energy** has a strong influence on contamination growth. Higher electron energies lead to reduced contamination thicknesses. However, the morphology changes at very low energies (< 1 keV), which is mostly attributed to charging effects and increased SE generation. The primary electron energy should thus be maximized to reduce contamination if knock-on damage is no issue.

- Contamination decreases with increasing **dose rate** (beam current), which implies applying a constant dose rather with a high current in a short time than with a low current in a long time.
- **Irradiation time**: After showing a strong increase in the first minutes in some cases, contamination continues to grow approximately linearly. However, a saturation effect begins to be visible for long-time irradiation. The contamination then also changes its morphology from more homogeneous to frame-like. Both findings can be understood by the depletion of contaminants.
- Initial tests of the scan **dwell time** indicated that it is advisable to use a short dwell time, leading to frame-like contamination that leaves the center of the ROI free. However, these findings could not be reproduced later, and the dwell time's influence remains an open question.
- The contamination behavior depends strongly on the **material** of the support film. Whereas etching is only visible in the first minutes for the Au film, it dominates the picture for the Pd film. Contamination is completely absent on the Si_3N_4 film. We speculate that the electrical insulating property of the material might result in charging that mitigates contamination.

A TEM-like contamination test pattern with homogeneous, static irradiation was used to produce circular-shaped deposits. Their thickness is compared with calculated contamination thicknesses from the model by Müller [Mül69]. The model describes the experimental findings with acceptable agreement using the residence time of contaminants as the fit parameter. However, the assumed parameters influence the result strongly. Diffusion was found to be the dominating process throughout the contamination experiments. Thus an adapted model that neglects adsorption and desorption of contaminants might be more appropriate and would reduce the number of parameters.

A single, continuously irradiated square was used to test contamination-mitigation and sample-cleaning strategies and allows drawing the following conclusions:

- **Beam showering** reduces contamination growth strongly but has no permanent effect, as contaminants from outside the showered area reach the ROI after some time. Higher showering currents reduce contamination stronger than lower showering currents. However, the connection between current and contamination reduction is not linear, as saturation with high currents is visible. Beam showering can be used to estimate the diffusion coefficient of contaminants, which allows testing diffusion on other sample materials in the future. The effect of beam showering in our experiments depended highly on the used microscope. In some cases, it did not show a cleaning effect at all. This might

be understandable due to different types of contaminants reaching the sample from the sample holder.

- **Frame showering**, which means leaving out the ROI and its nearest surroundings during beam showering, is equally effective as regular beam showering. The likely explanation is that the irradiation quickly depletes the contaminants in the ROI, and the (pinned) contaminants from further away begin to dominate the contamination growth. Although it needs more work to set up the showering pattern for frame showering, it is the preferable alternative for beam-sensitive samples. Both showering techniques share the drawback that it is a localized and short-lasting technique that needs to be applied again if the analyzed region on the sample is changed.
- **Sample baking** in an external vacuum recipient is moderately effective when applied with 100 °C for 15 min. One reason may be that the sample is in contact with ambient air when brought to the microscope. Another possible reason is that the application time is too short or the temperature too low. A general drawback is that it requires a separate instrument and transfer of the sample before the investigation in the microscope, which makes it more cumbersome. It can still be an alternative to plasma cleaning if the sample cannot withstand plasma but elevated temperatures.
- **Plasma cleaning** is the most effective cleaning method among all tested methods. It needs a separate instrument but is easy to apply. Before using plasma cleaning, it should be considered if the sample withstands it.

The method for the determination of contamination thicknesses presented here can facilitate further contamination studies on sample-cleaning strategies and different support materials in the future. The TEM-like contamination test pattern may be used to test adapted carbon contamination models that reduce the number of free parameters and allow further conclusions on the contamination process.

Chapter

6.

Direct Synthesis and Subsequent Analysis of ZIF-8 on TEM Grids

This chapter differs from the others in this work, as it focuses on a material science topic, namely the properties of the metal-organic framework (MOF) ZIF-8. The chapter begins with an introduction on MOFs and ZIF-8, and their investigation by electron microscopy, including a brief overview of the current state of literature. The short fundamentals section sums up the two main challenges for electron microscopy on surface-mounted MOFs (SURMOFs): Preparation and beam sensitivity. This is followed by a methodology part, where the necessary information about the sample synthesis/preparation used here and a more detailed look into the microscopy techniques is given. The results section then sums up the main findings, e.g. regarding the growth of the material, crystallinity, and nanoparticle (NP) incorporation.

The work described here was a collaboration with Ksenia Kutonova (formerly at the Institute for Organic Chemistry, KIT), who provided the samples. The preparation technique described below was developed and realized by her. It was improved in an iterative process of testing the preparation and analysis of the obtained material, mainly by electron microscopy. The focus of this chapter is on the material characterization by electron microscopy, though the synthesis is described briefly. Details on the synthesis and other characterization methods can be found in the publication: M. Hugenschmidt et al. "Direct Synthesis of ZIF-8 on Transmission Electron Microscopy Grids Allows Structure Analysis and 3D Reconstruction". In: *Particle & Particle Systems Characterization* 37.11 (2020), p. 2000209. DOI: 10.1002/ppsc.202000209, on which this chapter is partly based.

6.1. Introduction to MOFs and ZIF-8

MOFs are crystalline, porous materials built from metal nodes and organic linkers [HW19; YLL95]. Due to the huge number of possible combinations of linkers and nodes, more than 70000 members of this material class had already been produced and characterized in 2017 [Mog+17]. The number of combinations also enables designable topology, porosity, and functionality [Kas16]. The attraction of MOFs is also caused by the characteristic to be crystalline and porous at the same time [HW19]. A particular advantage of large pores, that can be considered as nano-cages, is the incorporation of nanoparticles or other guest molecules [HW19].

SYNTHESIS AS
POWDER OR
FILM

MOFs can be prepared as powder, or they are used as a coating of another material. One strategy to obtain a powder MOF is a one-pot method called solvothermal synthesis, where the fluid constituents of the MOF are mixed and heated, which causes the MOF crystals to form in the solution [Val+16; Kas16; Par+06b]. The second possibility has recently gained more and more interest as it allows the formation of SURMOFs on various supports by several synthesis routes [She+11], for example by the liquid phase epitaxial layer-by-layer (lbl) deposition technique, where the reaction partners are consecutively applied to a substrate [She+07]. This can be done by dipping the substrate into the educt solutions, interrupted by washing in solvents [SE13; She+14]. The growth of the SURMOF on the substrate is facilitated by chemically activating the surface before the deposition. Depending on the support material this is achieved by ozone or plasma treatment, or by a self-assembled monolayer [Val+16].

ZIF-8

In this work, the focus is on ZIF-8, which is a member of the class of zeolitic imidazolate frameworks (ZIFs) that are topologically isomorphic with the zeolites [Par+06b]. It is synthesized from 2-methyl imidazole, serving as the linker, and Zn salts that form Zn-containing metal nodes [Par+06b]. Its structure formula is $C_{24}H_{30}N_{12}O_{10}Zn_3$, with Zn only contributing 3.8% to the overall atomic mass [Par+06a]. For the ZIF-8-SURMOF, gold or alumina are typical supports [She+14; Val+16]. ZIF-8 is an extensively studied material due to its good thermal and chemical stability in a humid atmosphere and in organic solvents (like methanol) [Par+06b; Zha19] and due to its high surface area, which is comparable to activated carbon [But+16; Sud+06]. These properties lead to many (potential) applications of ZIF-8, like

- separation of gases (e.g. H_2/CH_4 , C2–C3 hydrocarbon mixtures) [Val+20; Bux+09; PL11],
- removal of contaminants from water [Zho+19],

- separation of water and ethanol → purification of biofuels [Zha+14], or oil-water separation [Yan+20],
- electronic or chemical sensing [Che+14; Liu+11; Li+20],
- drug delivery [Che+14],
- as a catalyst for various reactions when combined with nanoparticles [Che+14],
- and as a base for materials in next-generation batteries [Ye+21].

Electron microscopy is an important technique for the characterization of MOF materials, especially for small quantities of materials that are not sufficient for performing X-ray diffraction (XRD) and CHNX elemental analysis [Hug+20; VJC10]. In contrast to spatially averaging methods like XRD, electron microscopy provides up to sub-nm spatial resolution, which is essential for defect and interface analysis and the understanding of crystal growth [Liu+13]. SEM is used to image the topography, size, orientation, and surface coverage of SURMOF (particles) [Hug+20; Tro+19; Cra+09; Cra+11; SE13; Yan+18; Bux+09; Jin+20; Lai+16]. From SEM studies of ZIF-8 obtained in solvothermal synthesis, it is known that ZIF-8 crystals develop from cubic particles, exposing (100) facets, over truncated rhombic dodecahedra to rhombic dodecahedra (RD), exposing (110) facets [Cra+12; Jia+15]. This RD shape is shown in Figure 6.1 on the next page along different projected directions, while the intermediate shape of a truncated RD is shown in Figure 6.2. Transmission electron microscopy (TEM) and scanning transmission electron microscopy (STEM) allow studying the shape and structure of ZIF-8 at higher magnifications [Cra+11; ZZ18]. Insights into the crystalline structure, interfaces, and orientation of crystals are obtained via HRTEM [Cra+09; Zha+18; Zhu+17]. Venna, Jasinski, and Carreon [VJC10] conducted an XRD and TEM study on the growth process of powder ZIF-8. They divided the crystallization of ZIF-8 powder into 3 stages: First, the nucleation stage, where the crystallinity increases slowly, then the growth stage, characterized by a fast increase of crystallinity up to nearly 100%, and finally the stationary phase, during which the crystallinity slowly reaches 100% and the ZIF-8 crystals grow larger. They suggested Ostwald ripening, characterized by a loss of small particles in favor of larger ones, as the process behind the strongly increasing particle size [VJC10]. Recently, Liu et al. [Liu+21] investigated the nucleation process of powder ZIF-8 by in-situ and cryo TEM. They divided the nucleation stage into three additional steps: Phase separation, condensation, and finally crystallization into nanocubes. Electron diffraction methods, NBED, are another possibility to analyze the structure and orientation of crystals [Hug+20; Esk+10; Cra+11; Rös+14; Liu+21]. High-resolution STEM, especially the emerging technique integrated differential phase-contrast (iDPC) STEM, offers new possibilities to image MOFs [Liu+20]. The local distribution of elements within the material can be analyzed by EDXS [ZZ18; Bux+09]. If SEM can not reveal the desired 3D

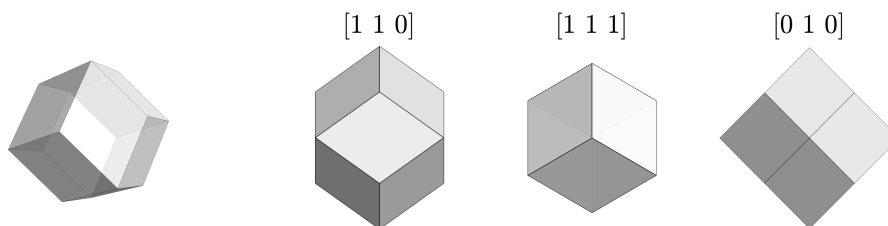
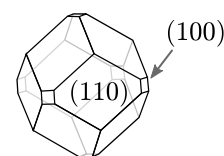


Figure 6.1. Scheme of the RD shape of ZIF-8 according to Cravillon et al. [Cra+12], with the rhombic planes being (110) facets. Left is an arbitrary viewing direction, on the right the RD is shown from different low-index viewing directions.

Figure 6.2 Scheme of the truncated RD shape undergone by ZIF-8 particles during their shape development from cubes to RD according to Cravillon et al. [Cra+12].



information, TEM or STEM tomography is used to reconstruct a volume, e.g. to obtain information about embedded nanoparticles [Hug+20; Esk+10].

6.2. Fundamentals: Electron Microscopy of MOFs

Whereas the preparation of powder MOFs for TEM is easy, as the powder can be floated on standard TEM grids, the preparation of SURMOFs for TEM is challenging. This short fundamentals section deals with this and another challenge of electron microscopy of MOFs: The sensitivity towards electron irradiation.

6.2.1. Preparation for TEM

Most of the literature cited above discuss the properties of powder ZIF-8, and there is only a limited number of (S)TEM works on lbl-synthesized other MOFs [Gu+16; Dar+10; Zha+15; Guo+16; Hei+15; Hug+20]. The reason for this might be the difficulties in the preparation of electron-transparent specimens of lbl-grown MOFs without introducing defects or destroying the material. Typically, the lbl MOFs are grown on bulk supports, from which they have to be detached before TEM or STEM imaging. This can be done, for example, by scratching the material off its support, PMMA-assisted shaving or by a laser-ablation technique [Dar+10; Guo+16]. All those processes bear the potential of damaging the MOF material and preservation of the pristine structural and compositional properties is not guaranteed.

6.2.2. Beam Sensitivity

Another difficulty in imaging MOFs is their high sensitivity towards electron irradiation, which limits the achievable resolution and renders electron microscopy imaging of their crystalline structures a challenge [Cra+09; Zha+18; Liu+20]. MOFs start to lose their crystallinity when the cumulative dose reaches around 10 – 20 electrons/Å² at 300 keV [Zha+18; Zhu+17; Liu+20], a value that is comparable to the limiting doses of cryo-electron microscopy of organic specimens [BR10]. Along with the destruction of crystallinity, shrinkage of MOFs on the structural level was observed [Gho+21; Liu+20]. The limited allowed dose is only enough to produce relatively noisy HRTEM images with low resolution using CCD or CMOS cameras, since they usually need hundreds of electrons/pixel to achieve a good SNR [Liu+20; Hug+20]. Direct-detection electron-counting (DDEC) cameras have thus greatly facilitated HRTEM imaging of MOFs [Zha+18; Zhu+17]. Zhang et al. further optimized the imaging process by a low-dose sample orientation tool and image processing [Zha+18].

Radiolysis was found to be the dominating process of damage to MOFs, which is typical for organic specimens [Gho+19; Ege12]. This is understandable because MOFs are largely organic and poorly conducting, which does not allow to transport charges away fast enough (see Section 2.1.4 on page 14). As radiolysis is stronger for lower primary electron energies, maximizing the primary electron energy was found to be advantageous for MOFs [Liu+20].

6.3. Methods

In this methodological section, a new preparation technique to obtain lbl-prepared ZIF-8 directly on amorphous carbon thin film and the subsequent analysis of the material by SEM and (S)TEM are described. The synthesis of ZIF-8 and Ag/ZIF-8 SURMOF is briefly introduced, followed by a more detailed description of electron microscopy techniques to analyze the material. More details on the synthesis can be found in Hugenschmidt et al. [Hug+20].

6.3.1. Synthesis

ZIF-8 SURMOF was directly synthesized on aC-covered TEM grids¹, using a lbl dipping method similar to the one used by the Wöll group at KIT before [Val+16; Val+20; Hug+20]. The aC film on the TEM grid has a nominal thickness of 6–10 nm. Importantly, lbl growth refers to the precise control of deposited material

¹Plano GmbH, Wetzlar, product number S160A

here, controlled by the number of dipping cycles, rather than to an epitaxial growth of a closed film. Before the deposition of ZIF-8, it is activated by UV irradiation, which should lead to OH groups on the surface, facilitating the nucleation process [Hug+20]. The dipping process was performed by a carousel dipping robot, which can hold up to 4 TEM grids at the same time. The TEM grids are immersed in four different solutions of the following 4-step-process to complete one deposition cycle (Figure 6.3 on the next page):

Preparation of ZIF-8

1. **Metal node:** 10 mmol l⁻¹ zinc dinitrate hexahydrate solution (300 s),
2. Rinsing solvent: Methanol (100 s),
3. **Linker:** 20 mmol l⁻¹ 2-methyl-1H-imidazole (300 s), and
4. Rinsing solvent: Methanol (100 s).

Each cycle can be followed by the next one, or the synthesis can be stopped by washing the sample in ethanol, drying it in ambient air, and storing it in a desiccator afterwards [Hug+20]. Samples with 25 to 100 deposition cycles were obtained in this way.

In addition to the synthesis of pure ZIF-8, an attempt was made to obtain Ag nanoparticles in the ZIF-8 pores, leading to a composite here denoted as Ag/ZIF-8, also described as “one NP @ one ZIF-8 pore”. Two synthesis steps have to be added to form the Ag NP, as reported by Jiang et al. [Jia+11]: AgNO₃ as the precursor solution for the Ag NP and NaBH₃ for the reduction of AgNO₃ to metallic Ag. This leads to an 8-step-synthesis scheme [Hug+20], as depicted in Figure 6.4.

Preparation of Ag/ZIF-8

1. **Metal node:** 10 mmol l⁻¹ zinc dinitrate hexahydrate solution (300 s),
2. Rinsing solvent: Methanol (100 s),
3. **Linker:** 20 mmol l⁻¹ 2-methyl-1H-imidazole (300 s),
4. Rinsing solvent: Methanol (100 s),
5. **Ag precursor:** 0.5 mmol l⁻¹ AgNO₃ solution (300 s),
6. Rinsing solvent: Methanol (100 s),
7. **Reduction:** 1 mmol l⁻¹ NaBH₄ solution (300 s), and
8. Rinsing solvent: Methanol (100 s).

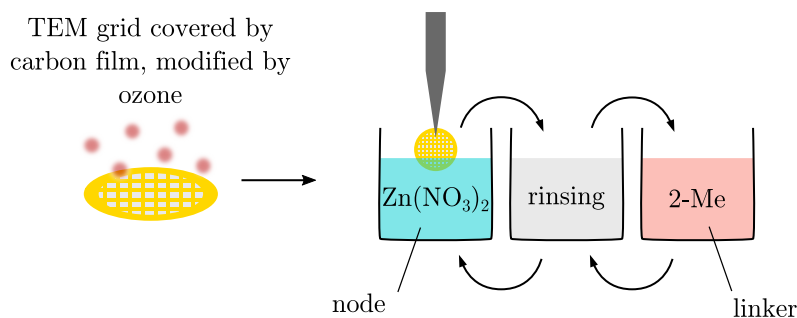


Figure 6.3. Scheme of the lbl-dipping synthesis of ZIF-8 on aC-covered TEM grid [Hug+20].

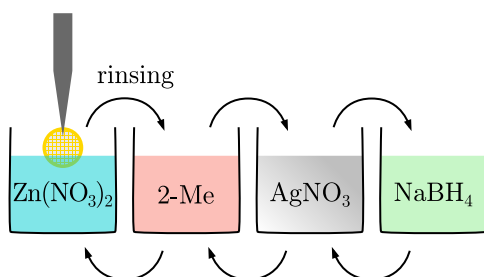


Figure 6.4 Scheme of the lbl-dipping synthesis of Ag/ZIF-8 on aC-covered TEM grid [Hug+20]. The rinsing steps are not shown individually.

Like in the procedure for ZIF-8, these steps can be repeated to add another deposition cycle, or the synthesis can be finished by washing and drying the sample. In theory, the size of the NP should be limited by the diameter of the pores they are embedded in. The upper limit should thus be a size of 1.2 nm.

6.3.2. Analysis by Electron Microscopy

This electron microscopic method section is divided into the different imaging techniques that were used to analyze the products of the synthesis described above: SEM and STEM-in-SEM, HRTEM, STEM (tomography), diffraction, and finally elemental analysis.

6.3.2.1. SEM and STEM-in-SEM

All ZIF-8-covered TEM grids were first imaged by SEM, to see if the support film was there, check for inhomogeneity on different areas on the grid, and see if individual particles or a closed film had formed. As mentioned on page 135, the material is expected to be particularly sensitive towards radiolysis through low-keV irradiation [Liu+20]. Thus the irradiated area should be kept limited and the positions protocolled if it is intended to image the sample by HRTEM later. Both the FIB-SEM instruments Thermo Scientific HELIOS G4 FX and FEI STRATA 400S were used for SE-SEM and STEM imaging. When imaging thin films by SE-SEM, it is

important to remember that, depending on the detector, also electrons from below the sample are contributing to the image signal. The resulting image is then not a pure SE image but a mixture between a STEM and a SE image, making deposits at the lower side of the film visible too and causing a misleading impression of topography signal. Therefore the TLD was used for most of the SE images in this chapter, as its small acceptance angle reduces the contribution of transmitted electrons. For SEM imaging, the primary electron energy was 5 keV or 10 keV and the immersion mode was on, a setting that was found to give the best topography contrast for those samples. For STEM-in-SEM imaging, the field-free mode was used and the primary electron energy was 20 keV or 30 keV. This electron energy leads to a strong contrast between deposits of a certain thickness and support film in BF-STEM images, while there are still differences in the gray values of an individual particle that allow conclusions on the particle shape beyond its contour. The advantages of BF imaging for particle analysis, particularly in a STEM-in-SEM setup, are:

- Strong contrast between particles and support film even for small particles due to fast decreasing BF-STEM with increasing thickness, especially for the low E_0 in STEM-in-SEM \rightarrow small particles are less likely to be overseen.
- No contrast inversion as for the HAADF-STEM intensities for larger sample thicknesses \rightarrow intuitive contrast interpretation and easier automatic segmentation of particles.
- Small pixel sizes (in the range of the beam diameter), together with large horizontal field widths that are possible in an SEM \rightarrow possibility to analyze a large number of particles already in a single STEM image.

All this is considered helpful for automated segmentation of particles that delivers information on particle sizes, shapes, and coverage of the sample. The segmentation method has been used within this work but was not applied for a systematical growth study of ZIF-8 SURMOF yet.

6.3.2.2. HRTEM

The crystallinity of the samples was examined by HRTEM in our FEI TITAN³ 80-300 microscope, described in Section 3.1 on page 39. The maximum electron energy of $E_0 = 300$ keV is used to reduce radiolysis (see Section 2.1.4 on page 14). Although the microscope is equipped with a relatively sensitive CMOS camera, a careful imaging strategy is necessary to preserve the crystal lattice. Most importantly, a trade-off between minimizing the dose to reduce sample damage and a large enough dose for a satisfactory SNR has to be found. Typical settings to achieve this are:

- Spot size 9

- 70 μm C2 aperture
- Monochromator value 30 to 50
- Magnification: 71000x
- Exposure time: 2-3 s

With a beam diameter of 1.1 μm that is just enough to homogeneously illuminate the camera, this leads to around 160 to 300 counts/pixel on the camera. Such a low beam current can not be measured anymore on the fluorescence screen of the microscope. It is also too low to be seen on the fluorescence screen, respectively the fluorescence screen camera, which makes it necessary to do the typical TEM alignments directly on the CMOS camera. For imaging, the sample stage was either moved blindly to a region that was not irradiated before, which can be done automatically in the camera software. Or the sample was imaged with very short exposure time (e.g. 200 ms) in 'live view' and stopped once a particle was found. The particles were then imaged without orienting them to a specific zone axis. During the imaging procedure, it is crucial to have the pre-specimen shutter (gun blanker) closed when the camera is not recording, which is ideally done automatically. This allows waiting for the stage to settle before imaging.

The imaged crystalline structures were then analyzed by converting them to diffractograms, using a 2D Fourier transform (FT). Analog to the Bragg reflections in a diffraction pattern, those diffractograms show spots representing the periodicities in the HRTEM image. The diffractogram consists of complex numbers z of which typically the absolute value

$$|z| = \sqrt{\text{Re}(z)^2 + \text{Im}(z)^2} \quad (6.1)$$

or the squared value $|z|^2$ (power spectrum) is shown. Each peak corresponds to a distinct interplanar lattice spacing d according to the Bragg equation Equation (2.29) on page 13. Those interplanar spacings, and also the corresponding set of lattice planes themselves, are labeled by the Miller indices (hkl). For example, if the diffracting planes are of the (100) type with a spacing d_{100} , the planes with d_{200} have the halved distance and appear in the doubled distance from the zero-order beam or spot in the diffraction pattern or diffractogram [FH08; IL03]. This is due to the reciprocal relation between real and Fourier space, as outlined in Section 2.1.3 on page 13 and visible in the Bragg equation. The zone axis is the direction normal to the lattice planes belonging to the reflexes in the diffraction pattern/diffractogram. It is labeled with square brackets (e.g., [010]).

The simulation of diffraction patterns and the comparison with experimental diffraction patterns or diffractograms enables the identification of crystalline structures. In this work, diffraction patterns were either calculated by *ImageJ/Fiji* or *Digital Mi-*

crograph (Gatan) [Sch+12]. Simulated diffraction patterns were obtained by *JEMS* [Sta87], and the comparison was performed in the same program (using **Indexing** → **Spot pattern**). This identification of crystalline structures is called “Indexing”. *JEMS* performs the simulation based on a file providing the theoretical crystalline structure (for example, as `.cif` file). For ZIF-8, the structure published by Park et al. was used [Par+06a].

6.3.2.3. STEM and STEM Tomography

Conventional STEM imaging was only rarely used for the ZIF-8 samples, as the information in addition to STEM-in-SEM is limited if atomic resolution cannot be achieved. For the Ag/ZIF-8 samples, however, it can be used to examine the presence and distribution of Ag NP. As STEM images are projections, they contain no (or only little) information about the distribution of NP in direction of the electron beam. More specifically, they do not yield information if the Ag NP are incorporated into the ZIF-8 material as desired, or if they are only deposited on the surface. To solve this problem, STEM tomography was performed at the TITAN microscope, using a Fischione single-tilt tomography holder and $E_0 = 300$ keV. The tilt series were collected by the built-in FEI STEM TOMOGRAPHY software tool that handles sample tilt, image acquisition, drift correction, and refocus automatically. The tilt angles ranged ideally between -75° and 75° in steps of 2° . Sometimes, this range cannot be exploited due to geometrical restrictions of the specimen. ETOMO/3DMOD (version 4.9.12, from the IMOD software package) has been used to process the resulting image stacks and to reconstruct the tomogram [MH17]. The tomogram was then visualized either by the AVIZO SOFTWARE FOR FEI SYSTEMS (version 9.2.0) or by the open-source application TOMVIZ (version 1.8.0) [Lev+18].

6.3.2.4. Nano-Beam Electron Diffraction (NBED)

NBED is useful to analyze the crystallinity of beam-sensitive materials, especially if HRTEM is not applicable, for example due to a camera that is not suited for low-dose imaging or if the sample is not in a low-indexed orientation. NBED was applied to Ag/ZIF-8 here, to check for the signal of Ag NP within the ZIF-8 matrix. Diffraction patterns can be obtained by scanning the beam over the sample during imaging to protect a single spot from beam damage. Additionally, the beam intensity should be reduced, which was achieved here by choosing the $50\ \mu\text{m}$ C2-Aperture and spot size 10. The NBED patterns were recorded at the TITAN microscope at $E_0 = 300$ keV with a beam-convergence semi-angle of 1.4 mrad and a camera length of 285 mm. The obtained diffraction patterns were indexed as described in Section 6.3.2.2.

6.3.2.5. Elemental Mapping using EDXS

Elemental mapping by energy-dispersive X-ray spectroscopy (EDXS) was used to check for Ag NP inside the Ag/ZIF-8 composite that could be too small to be resolved via STEM tomography. The mapping allows distinguishing if most of Ag is present on the surface of a particle or inside. In the first case, the signal for Ag for an approximately spherical particle should ideally be highest at the outline of the particle. In the second case, it should be highest in the center of the particle. EDXS mapping was performed at the FEI Tecnai OSIRIS microscope that is equipped with a Super-X quad silicon drift-detector for a high X-ray detection efficiency. Again, the beam intensity was reduced (70 μm C2 Aperture, spot size 9) and the total dose rather spread over the collection time of 58 min. The map was collected using the BRUKER ESPRIT software (version 1.9) with automated sample drift correction. The maps were then evaluated using the python-based HYPERSPY package and a JUPYTER notebook using principal component analysis (PCA) [La +19]. The notebook was based on a template by Lukas Grünewald (LEM, KIT) [Grü+20].

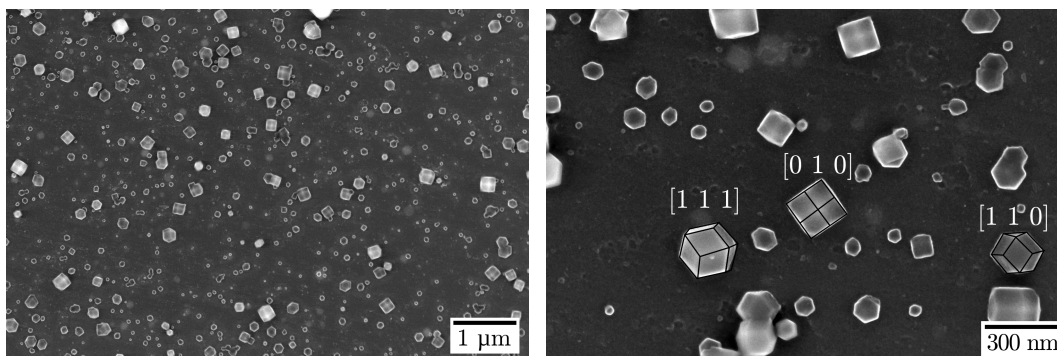
6.4. Results and Discussion

The electron microscopy techniques described above yield insights into the morphology and growth, crystalline structure, and composition of ZIF-8 and Ag/ZIF-8. This result section starts with the examination of 'pure' lbl-grown ZIF-8 by SEM, STEM-in-SEM, and HRTEM, followed by the search for Ag NP incorporated into ZIF-8 using tomography, NBED, and EDXS.

6.4.1. Morphology

Figure 6.5 shows the typical appearance of lbl-grown ZIF-8 SURMOF after 50 deposition cycles. In Figure 6.5a, we see an overview of a larger area with a lot of individual particles of different sizes appearing bright. The deposit is not a closed film, however, the faceting of the larger particles indicates the successful growth of crystalline material. The particles have an estimated size of a few 10 nm up to around 250 nm [Hug+20]. Details of some particles can be seen in Figure 6.5b. Several particles exhibit the RD shape that is expected for ZIF-8. This is indicated for three particles by tracing their edges with black lines and labeling the viewing directions according to Figure 6.1 on page 134.

SEM enables us to follow the shape change of ZIF-8 from cube to RD during growth. The shape evolution, that has been described by Cravillon et al. [Cra+12] for powder



(a) Overview image

(b) Higher magnification image of the same sample. Low-index orientations of the RD shape are highlighted and labeled.

Figure 6.5. SE-SEM micrographs of lbl-grown ZIF-8 on an aC film after 50 deposition cycles. The images were taken at 5 keV in the immersion mode using the through-lens detector (TLD) [Hug+20].

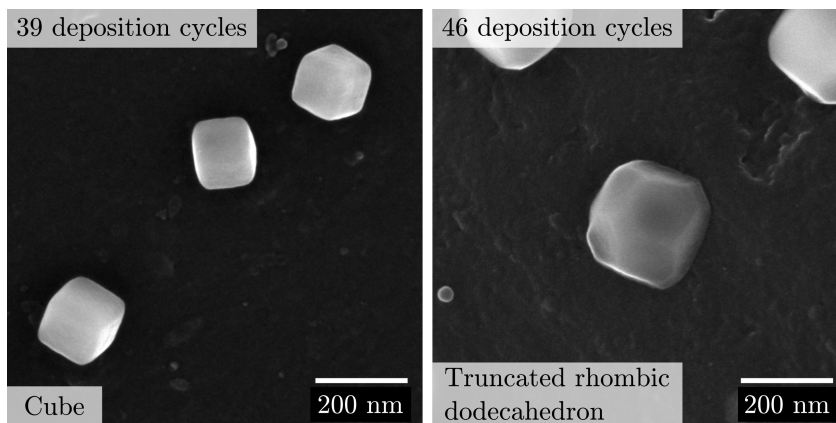


Figure 6.6. SE-SEM micrographs of lbl-grown ZIF-8 on aC film after (left) 39 and (right) 46 deposition cycles. The images have the same magnification and were taken from two specimens from the same sample batch at 5 keV in the immersion mode, using the TLD.

ZIF-8, occurs for our lbl-grown ZIF-8 too, as confirmed in Figure 6.6. It shows SE-SEM images of two samples from the same batch, one grown with 39 deposition cycles (left) the other one with 46 cycles (right). Indeed, the particles after 39 cycles have a cubic shape. The image for 46 deposition cycles shows a truncated RD, which is known as the intermediate shape between cube and RD, where the (100) facets of the cube grow smaller while the (110) facets of the RD grow larger (see Figure 6.2 on page 134) [Cra+12].

Up to now, we can conclude that the lbl-grown ZIF-8 SURMOF looks similar to powder ZIF-8. Is it then just powder ZIF-8 that has formed in the dipping solution and was eventually deposited as complete particles onto the aC support film? This hypothesis is falsified in Figure 6.7 on the facing page, showing a tilt series of a single

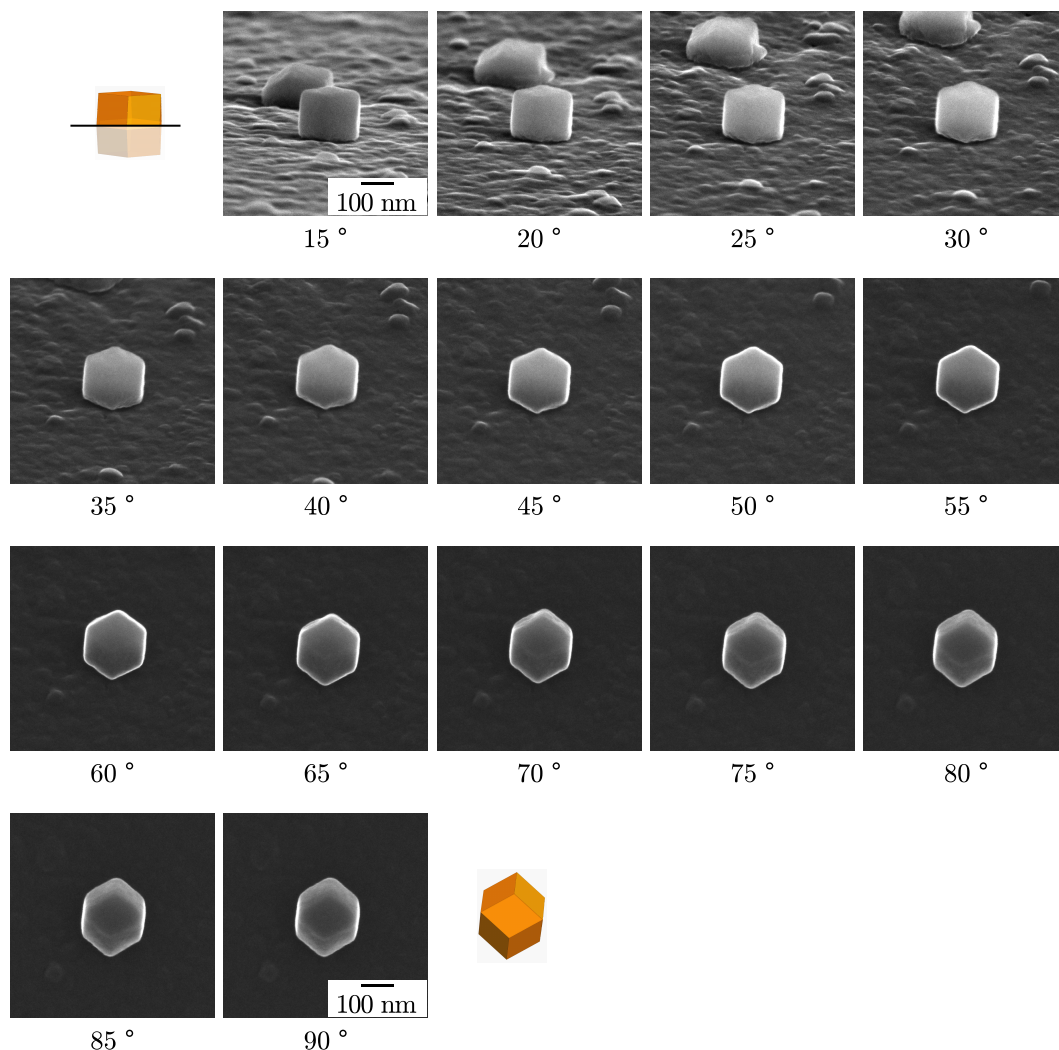


Figure 6.7. Tilt series of a single lbl-grown ZIF-8 crystal. The tilt angle ranges from 15° between the viewing direction and the support film to 90° (top view). The 10 keV-SE images were taken in immersion mode with the TLD. In addition to the tilt series, the corresponding 15° and 90° views of a RD are shown.

ZIF-8 particle² with a size of around 220 nm. What looks like a full RD in top view (90° between the viewing direction and the support film) is in fact a halved RD with planar connection to the support film, as becomes obvious in the image with 15° tilt. The tilt angles around 60° show the hexagonal appearance of the [111]-direction of ZIF-8 particles. Many other, similar-looking particles are found on the sample. However, Figure 6.8 also shows a larger (around 600 nm), full RD particle, apart from smaller particles with a close connection to the support film. This indicates that outstandingly large particles can be synthesized in the dipping solutions and deposited without planar connection to the support film and a controlled number of growth cycles.

²I'd like to thank Qing Sun (LEM, KIT) for providing this sample.

Figure 6.8 SE-SEM image of a larger particle with full RD shape (10 keV, immersion mode, same sample as in Figure 6.7). The tilt angle with respect to the support film is 20°.

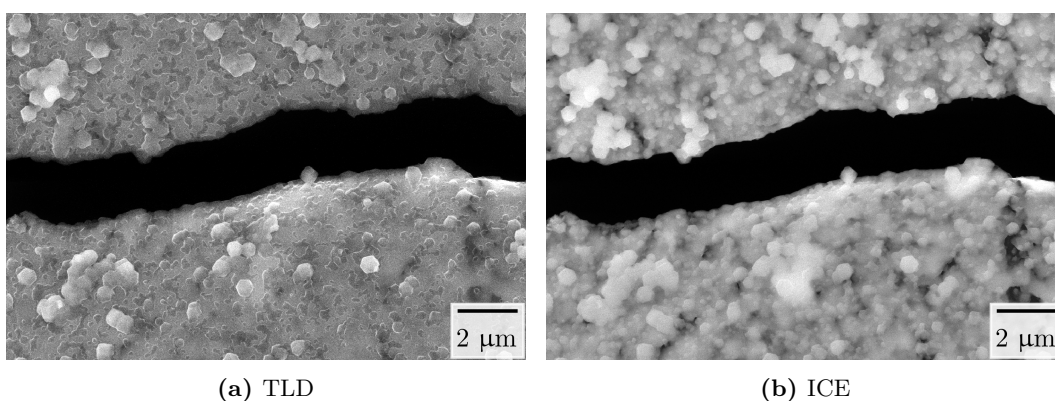
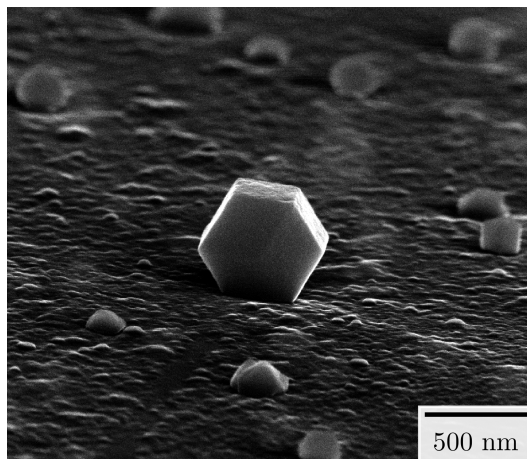


Figure 6.9. SE-SEM micrographs of lbl-grown ZIF-8 on aC film after 100 deposition cycles. A horizontal crack through the sample appears black. The images were taken in a single scan at 10 keV in the field-free mode [Hug+20].

Figure 6.9 shows two SE-SEM images of a ZIF-8 sample grown in 100 cycles, obtained in a single scan but with different detectors: The TLD (Figure 6.9a) and the ICE (Figure 6.9b). The sample is from the same batch as the sample grown in 50 cycles (Figure 6.5 on page 142), which makes them directly comparable. The morphology has changed compared to 50 deposition cycles: The support film is completely covered by the deposit that looks like a rough but closed film in the TLD image, which is dominated by topography contrast. The ICE image, which contains also subsurface information, reveals that the deposit consists of overgrown and coalesced particles of different sizes, ranging from some 10 nm to around 500 nm [Hug+20]. Apart from the dark horizontal crack through the film, a darker area on the right bottom is visible, where the ZIF-8 deposit is thinner. These images already indicate that the growth of ZIF-8 does not depend linearly on the number of cycles.

BF-STEM imaging was used to investigate the growth of ZIF-8 for smaller numbers of deposition cycles. The nonlinear growth as a function of deposition cycles is confirmed in Figure 6.10 on page 146, where samples grown in 25 and 50 cycles in

the same batch are shown at the same magnification. The 25 x sample looks nearly empty, only a few spots indicate that it is not an empty carbon support film. Still the question is not solved, if there is a thin homogeneous film of ZIF-8 deposited on the support, before the growth continues with the formation of islands (Stranski-Krastanow growth [Ven83]). The 50 x sample, however, shows many particles of different sizes. Some of the larger ones also have the typical RD shape. As mentioned on page 137, these BF-STEM images with strong contrast are well suited for automatic segmentation. Automatic segmentation of the images in particles and background gives quick and reliable information about particle sizes and the support coverage, which would be tedious to evaluate by hand.

The segmentation is performed using the open-source segmentation software ILASTIK, a machine-learning-based image analysis toolkit [Ber+19]. In the first step, every pixel is identified as either belonging to a particle or the background (pixel classification). In the second step, the particles in the image are separated when touching and the areas of each particle are calculated (object classification). This allows calculating coverage and particle diameters (assuming they are spherical). The separation is not possible anymore if particles are overgrown and large areas of the support are covered. As an example, Figure 6.11 on the next page shows the segmentation of the 50 x sample image in Figure 6.10. On the left, we recognize that most of the particles have been identified correctly, although some smaller ones are missing or appear smaller as in the original image. Such deviations can stem from an insufficient training of the algorithm, which was done on another image of this type. The pixel size of 3 nm was chosen to be able to detect very small particles despite the large horizontal field of view of 20 μm . The object classification then identifies individual particles based on the pixel classification. It yields a surface coverage of 10 % by 4348 particles in total. On the right, the diameters of all particles, assuming spherical shape, are shown in a histogram. It shows a wide range of particle sizes between 21 nm and 601 nm. The histogram can be fitted by a log-normal distribution, which is often used to describe particle-size distributions [Cha+11; Ebe+90]. It yields a maximum at a particle diameter of 50 nm.³ It is important to mention that the coverage differs in different areas on one sample, likely due to the remaining liquid between the dipping steps. In addition, the coverage achieved by a certain number of growth cycles in different sample batches differs due to uncontrollable changes in experimental conditions like air humidity. The segmentation shown here should be regarded as an example of the difficulties and, more importantly, the possibilities of automated image segmentation when used for the characterization of ZIF-8 SURMOF. In further studies, it would allow the quantification of its growth on a good statistical basis due to large numbers

³I want to thank Lukas Grünewald (LEM, KIT) for providing the base of the script used for the histogram evaluation.

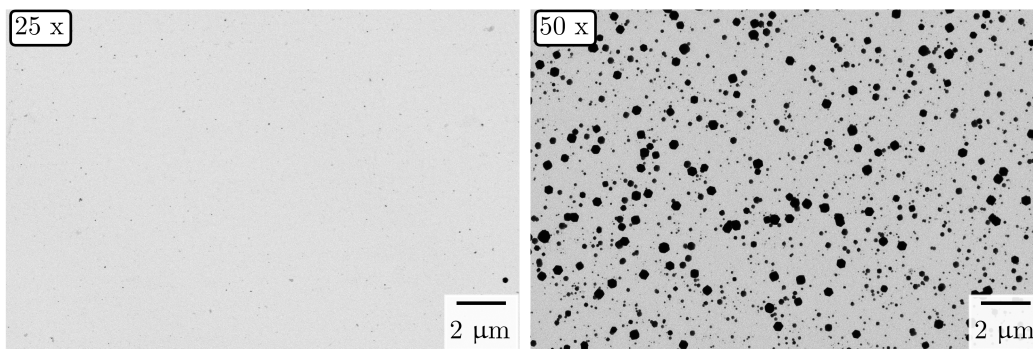


Figure 6.10. 30 keV-BF-STEM images of lbl-grown ZIF-8 after (left) 25 and (right) 50 deposition cycles.

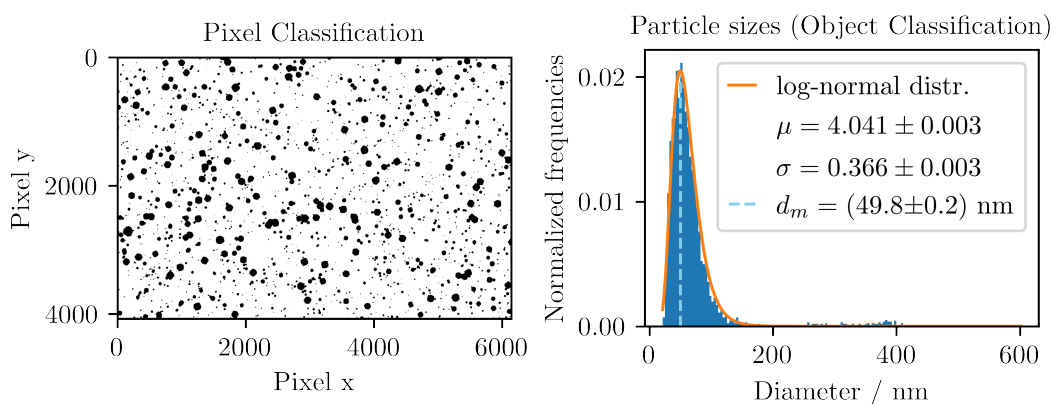


Figure 6.11. Segmentation and evaluation of particle sizes based on the BF-STEM image of the 50 cycles sample shown in Figure 6.10 (right).

of evaluated particles. Moreover, the object classification allows to automatically recognize particle shapes, which would help to identify the growth state of ZIF-8 from amorphous to cubes and finally RDs.

The investigation of the lbl-grown ZIF-8 samples by SEM has shown that the deposition of ZIF-8 on an aC film is not the deposition of an epitaxial, closed film. It is unclear if the growth starts with individual islands or if a closed thin film is formed first (Stranski-Krastanow or Volmer-Weber mode [Ven83]). After the initial nucleation, the growth proceeds with the formation of individual particles and later with the overgrowth of the particles to form a poly-crystalline, closed film. For ZIF-8 SURMOF, our findings thus indicate a similar, non-linear growth behavior like the one found for powder ZIF-8 by Venna, Jasinski, and Carreon [VJC10]. The results above also show that SEM and STEM-in-SEM are well suited for a detailed analysis of MOFs, including EDXS analyses, which are not shown here.

6.4.2. Crystallinity

The careful HRTEM imaging strategy described on page 138 allows obtaining HRTEM images of ZIF-8, even without a DDEC camera. Figure 6.12 a) shows a raw image taken at 71 000 x magnification. A zoom-in of one of the particles in Figure 6.12 b) reveals its crystallinity more clearly. Contributions from the amorphous background were removed here by an average background subtraction filter (ABSF) [Kil98; MS05]. The image is quite noisy due to the low dose, and lattice fringes are visible only with low SNR in the HRTEM image, even after filtering. The Fourier transform in Figure 6.12 b), however, reveals reflections up to the 3rd order that are consistent with the crystalline structure of ZIF-8 in [110] zone axis [Par+06a]. Looking back at Figure 6.1 on page 134, the particle indeed has the slightly rounded shape of the [110] viewing direction of the RD shape.

Since ZIF-8 consists mostly of light elements, the scattering power is low, and only a weak signal-to-noise ratio is achieved in HRTEM even with strong defocusing. As mass-thickness contrast is negligible, the inner of a particle looks quite homogeneous and only the contour of a ZIF-8 bears information about its shape. This is a source of confusion, as the [010] projection exactly looks like a cube. The RD and cubic shape of ZIF-8 particles can however be distinguished in HRTEM images using the knowledge about the orientation of their facets. Figure 6.13 shows two particles that both seem to be cubes with rounded corners. The top one (a) was grown in 39 cycles and has a width/height of 150 nm. The bottom one (b) was grown in 50 cycles and is 245 nm wide/high. The FTs of both HRTEM images correspond to ZIF-8 in [001] zone axis, with only little deviation from the theoretical values. A closer look at the direction of the facets now reveals the shape of the particles, using the prior knowledge that cubic ZIF-8 has (100)-type facets and RD-shaped ZIF-8 has (110)-type facets [Cra+12]. Indeed particle (a) is a cubic ZIF-8 particle, as revealed by the facet's orientation in (100) direction. Particle (b) however is an RD-shaped particle, since the facets are of the (110) type, although the intensity distribution inside the particle looks homogeneous and does not indicate the RD shape in [001] direction, due to the low mass-thickness contrast.

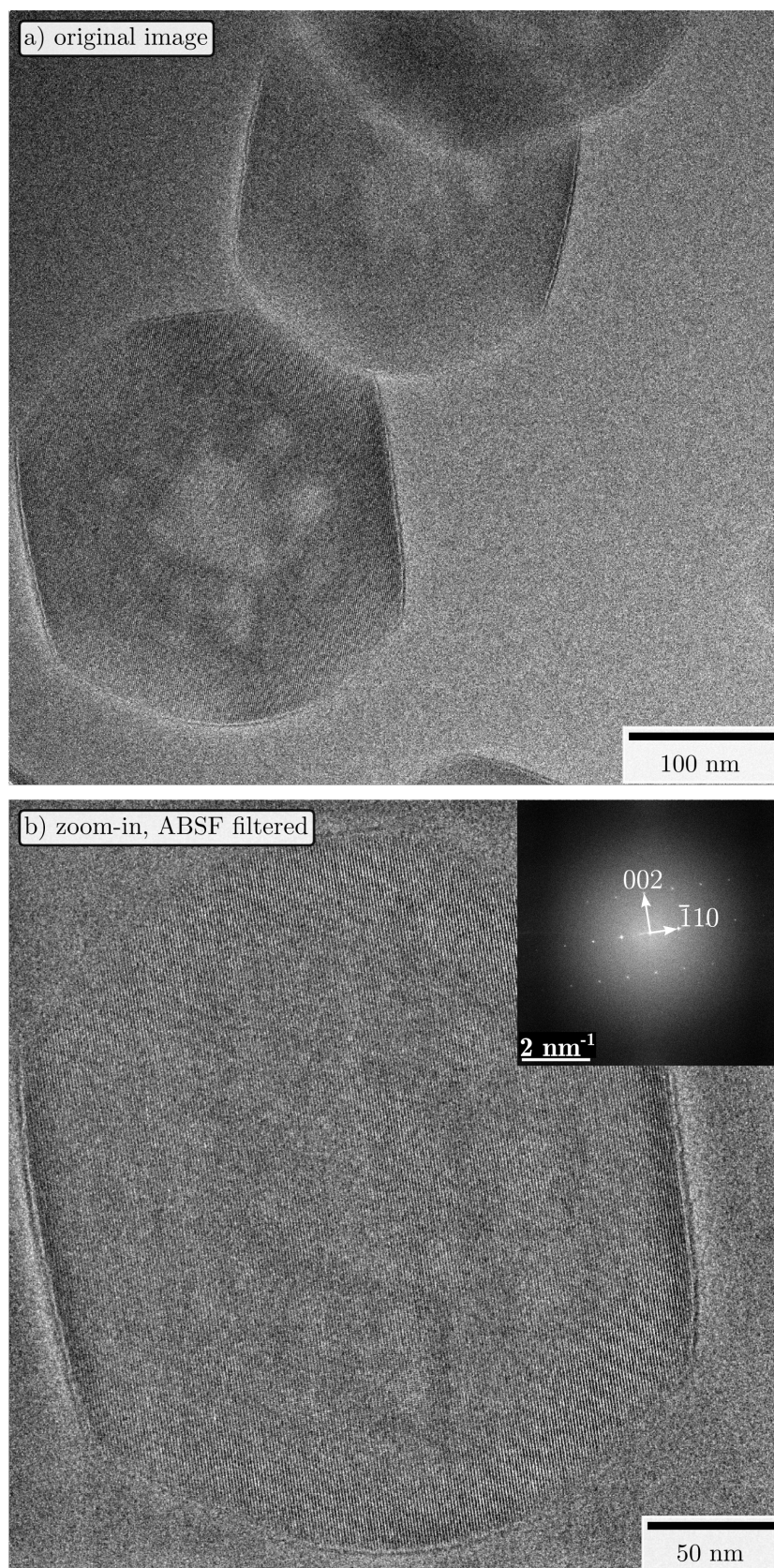


Figure 6.12. 300 keV HRTEM image of ZIF-8 crystallites after 46 deposition cycles. (a) original image, (b) magnified image, ABSF filtered. Fourier-transformed HRTEM image (magnitude) of the particle as inset, showing reflections that are compatible with the ZIF-8 [110] zone axis.

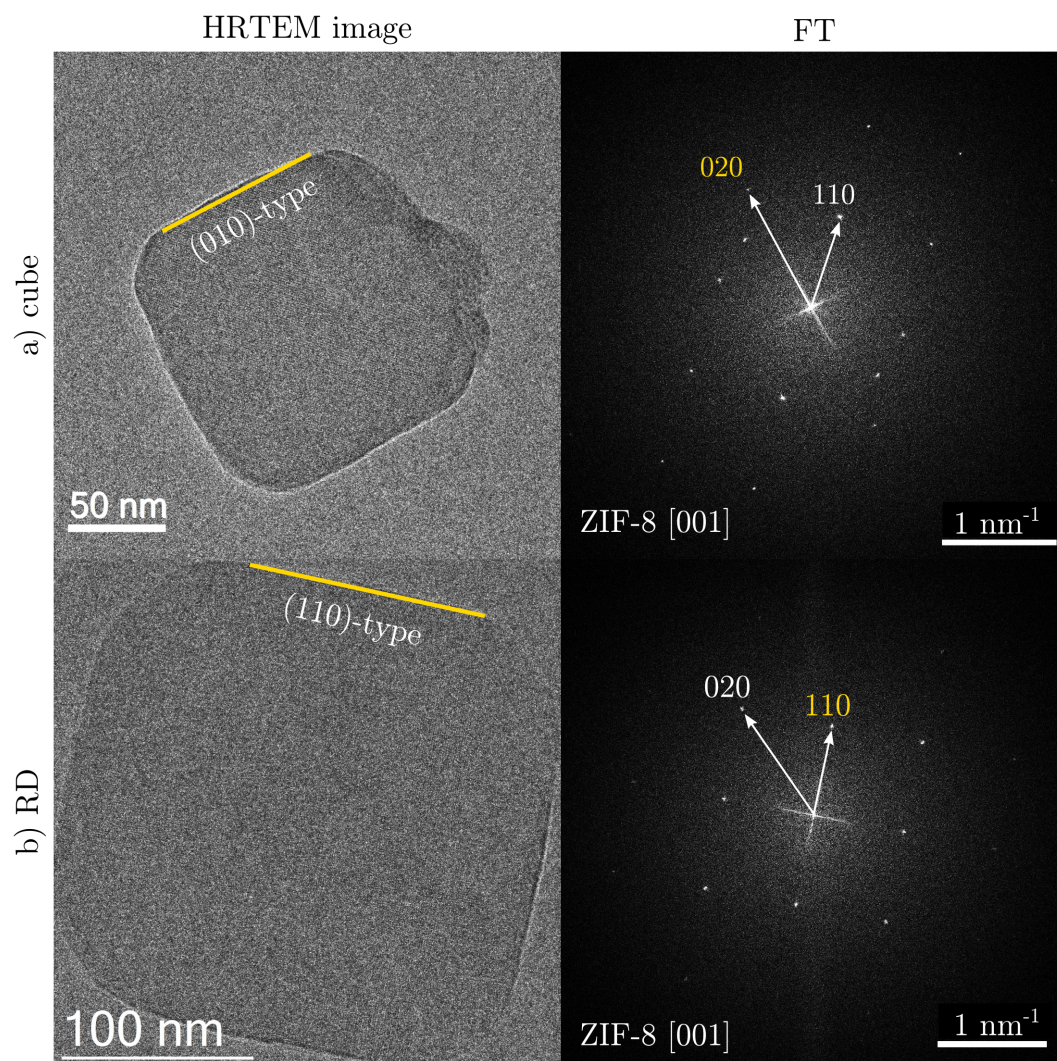


Figure 6.13. HRTEM images and Fourier-transformed images (power spectra) of a) a cubic particle (39 cycles sample), and b) a RD-shaped particle (50 cycles sample). The measured (theoretical) values of the marked reflections are: a) $d_{020} = 1.16 \text{ nm}^{-1}$ (1.18 nm^{-1}), $d_{110} = 0.82 \text{ nm}^{-1}$ (0.83 nm^{-1}), $\angle = 46 \text{ deg}$ (45 deg). b) $d_{020} = 1.18 \text{ nm}^{-1}$ (1.18 nm^{-1}), $d_{110} = 0.82 \text{ nm}^{-1}$ (0.83 nm^{-1}), $\angle = 46^\circ$ (45°). The reflections marked in yellow correspond to the directions of the facets of the particles. [Hug+20]

6.4.3. Nanoparticle Incorporation

The incorporation of Ag NP in ZIF-8 produced by the method described in Section 6.3.1 on page 135 was studied by STEM tomography and NBED. While tomography provides information on the location of the Ag NP (whether they are incorporated in the ZIF-8 or whether they are located on the surface), NBED could detect NP that are too small to resolve in STEM tomography.

Tomography / 3D reconstruction A tomogram obtained from a HAADF-STEM tilt series of an Ag/ZIF-8 sample is shown in Figure 6.14 on the next page. Figure 6.14a shows a HAADF-STEM image of the particle and its surroundings in top view. The ZIF-8 particle appears bright and resembles the shape of a cube, however, it agrees with the RD shape in the [111] viewing direction (see Figure 6.1 on page 134 for comparison). Bright dots are found all over the image and are presumed to be Ag NP with a diameter of 2 nm to 4 nm (some marked by arrows). Particles of this size are larger than the pore diameter (1.2 nm) and cannot fit into them. Still a number of NP is also found in the region of the ZIF-8 particle. Apart from the NP and the ZIF-8 particle, regions of contamination with cloud-resembling shapes are visible. After the reconstruction of the volume from the tilt series, slices through the volume can be checked for the incorporation of NP into the ZIF-8 particle (Figure 6.14b)). In the shown example, 3 NP are visible inside the particle (marked by arrows). Throughout the particle, only a few unevenly distributed NP are found. The intended incorporation of NP, “one NP @ one ZIF-8 pore” can therefore not be confirmed by this measurement. However, the resolution of the tomogram might be insufficient to resolve smaller NP.

The red line with many NP on the right side of the particle in Figure 6.14 on the next page b) is the intersection of the aC film, covered by NP, with the image plane. Surface reconstruction of the 3D volume reveals the RD shape of the ZIF-8 particle (Figure 6.14c,d, light blue). Instead of a full RD shape, it is a halved particle with a planar interface with the support film. This is consistent with the findings of the SEM tilt series (Figure 6.7 on page 143). The support film itself is not visible due to its weak scattering power, but its position is marked by the NP and contamination covering it (red). The characteristic RD shape indicates that the ZIF-8 structure is not damaged by the additional constituents for the NP synthesis.

NBED Figure 6.15 on page 152 shows an NBED pattern obtained from an Ag/ZIF-8 composite particle (shown as inset). It corresponds to the simulated ZIF-8 pattern in $[\bar{2}\bar{5}7]$ zone axis, which is overlaid on the experimental pattern. This confirms again that the synthesis route towards Ag/ZIF-8 does not hinder the growth of the ZIF-8 matrix. For a large number of Ag NP in different orientations

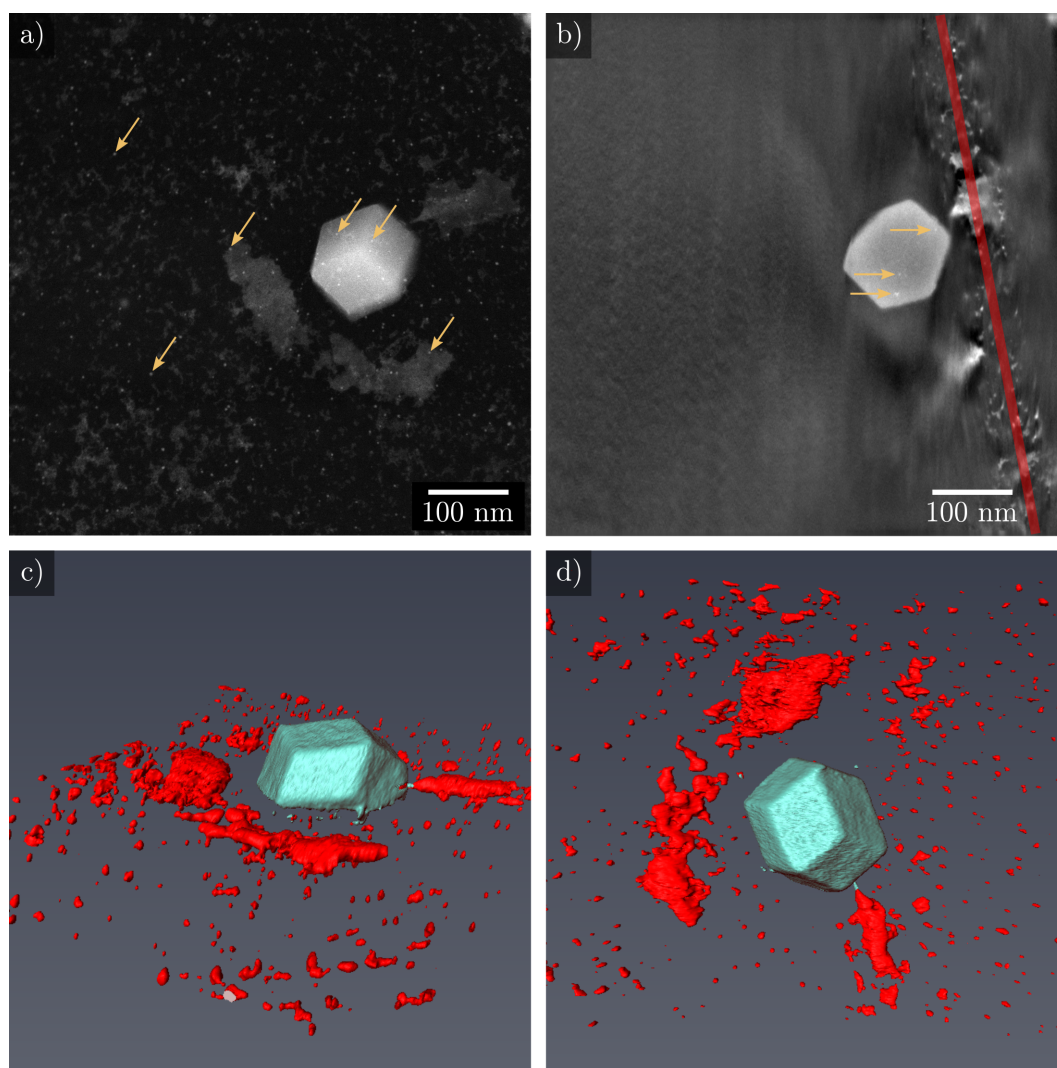


Figure 6.14. 300 keV HAADF-STEM tomography of an Ag/ZIF-8 composite particle (50 cycles ZIF-8, then 50 cycles Ag/ZIF-8). a) One HAADF-STEM image from the tilt series, showing a number of NP (marked by arrows). b) Slice through the reconstructed volume with three marked NP inside the ZIF-8 particle. c) Side view on the 3D surface representation of the tomogram with NP and contamination on the support film in red, ZIF-8 in light blue. d) top view on the reconstructed volume. [Hug+20]

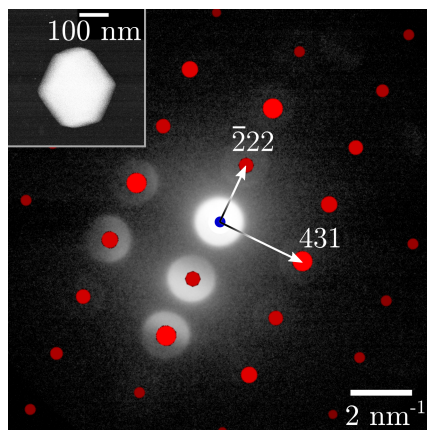


Figure 6.15. NBED pattern of an Ag/ZIF-8 crystallite (50 deposition cycles) obtained while scanning the particle which is shown in the HAADF-STEM image in the inset. The experimental pattern is overlaid by the simulated pattern of ZIF-8 in $[2\bar{5}7]$ zone axis. The measured (theoretical) values of the marked reflections are: a) $d_{\bar{2}22} = 2.05 \text{ nm}^{-1}$ (2.04 nm^{-1}), $d_{431} = 3.01 \text{ nm}^{-1}$ (3.00 nm^{-1}), $\angle = 89^\circ$ (90°). [Hug+20]

embedded in the ZIF-8 matrix, diffraction rings corresponding to the distinct lattice distances of Ag would be expected in the diffraction image. However, no sign of reflections from Ag NP is observed in the diffraction pattern, again indicating that the incorporation of Ag NP in the ZIF-8 pores was not successful.

Elemental distribution Finally, the Ag NP inside the Ag/ZIF-8 are searched by examining the elemental distribution within a particle using EDXS. Figure 6.16 shows a HAADF-STEM image of the investigated particle, along with elemental maps of Zn, N, C, Ag, O, and Na. The projected shape of the particle is an octagon, which is not consistent with the cubic or RD shape, but with the geometry of the truncated RD in $[010]$ direction, when the (100) facets are still comparatively large as compared to the (110) facets (compare Figure 6.1 and Figure 6.2 on page 134). Zn, N, and C are constituents of ZIF-8 and show the highest signal within the particle, as expected. O and Na can be remnants from the preparation process and are still present in the ZIF-8 particle [Hug+20]. The Ag map now clearly demonstrates that there is no homogenous incorporation of Ag into the particle. In this case, the maps should show the same intensity distributions as the other elemental maps, as outlined in Section 6.3.2.5 on page 141. Instead, the small particle that is marked by an arrow in the STEM image seems to be an Ag-rich agglomerate. The preserved shape of the ZIF-8 particle after a mapping time of one hour again validates that the material preserves its characteristic shape even if the crystalline structure is most likely destroyed.

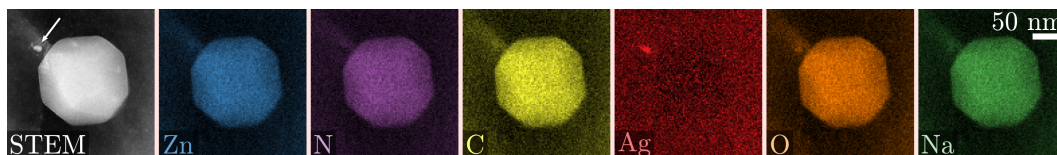


Figure 6.16. EDXS mapping of an Ag/ZIF-8 composite particle (50 deposition cycles), with a HAADF-STEM image and elemental maps for constituents of ZIF-8, Ag, and two contaminants (O, Na). The arrow in the STEM image points to an agglomerate with increased Ag signal.

6.5. Summary

Layer-by-layer synthesis was successfully used to deposit ZIF-8 SURMOF directly on aC-covered TEM grids. The direct synthesis renders TEM preparation steps to remove the SURMOF from its typically bulk support obsolete. That completely avoids damage of the material before it is studied by electron microscopy, and the pristine material can be analyzed [Hug+20]. SEM imaging revealed that ZIF-8 grows as individual particles, with a slow starting phase below 25 growth cycles, where a homogeneous coverage with a thin film cannot be excluded. After around 50 growth cycles, the material gain increases strongly and individual particles coalesce and overgrow to form a polycrystalline, closed film. Individual particles undergo the same shape development as powder ZIF-8 from cubic to the distinctive RD shape. However, the shape is not fully developed at the interface between particle and aC film, where a planar interface is formed. Imaging the crystalline structure of ZIF-8 by HRTEM is possible with a CMOS camera using a low-dose procedure. The obtained images confirm the crystalline structure to be ZIF-8. Although cubic and RD shape may look the same in HRTEM images, depending on their orientation, they can be distinguished through their facets' orientation. BF-STEM imaging at low electron energies in a SEM was tested and found to be a versatile tool to study the growth process of ZIF-8, especially during the early stages where only little material has been deposited. Combined with machine learning-based segmentation algorithms, large numbers of particles can be analyzed. Intensive investigations of the intended Ag/ZIF-8 composite by tomography, NBED, and EDXS have shown that the incorporation of Ag NP into the pores of ZIF-8 is not possible by the synthesis described in Section 6.3.1 on page 135.

The two-in-one synthesis and sample preparation technique combined with electron microscopy could promote the analysis of other SURMOFs, NP/SURMOF composites, and their growth processes as well.

Chapter 7. Summary

Scanning transmission electron microscopy (STEM) at low electron energies in scanning electron microscopes has several advantages: The lower energies in scanning electron microscopy (SEM, typically ≤ 30 keV) yield enhanced contrast for light materials and reduced knock-on damage [Kai+11]. The large number of available detectors enables correlative imaging of surface and bulk properties of the same specimen regions [Gui+04; KBF12; Sun+20]. Due to the lower price compared to classical STEM, and a large number of scanning electron microscopes, STEM in scanning electron microscopes, abbreviated as STEM-in-SEM, can in some cases replace STEM in transmission electron microscopes at high electron energies. However, some characteristics of STEM-in-SEM, like contamination and electron-beam broadening in specimens, require special attention. These topics were treated in this thesis.

Electron-beam broadening is enhanced at low energies due to the increased probability for scattering events in the sample. The topic is of interest as beam broadening degrades the resolution and contrast in STEM images [MM07]. Although beam broadening cannot be avoided, it is helpful to have suitable models to estimate its effect. A recent theoretical model by Gauvin and Rudinsky, based on anomalous diffusion, was tested for thin carbon films in earlier work [GR16; Dre+17]. The authors presented a new technique to directly measure beam broadening in electron-transparent specimens, without the need for test objects like nanoparticles. However, measurements for a broader range of materials and higher thicknesses were still missing. In this work, beam broadening was measured in different materials (MgO, Si, SrTiO₃, and Ge) with sample thicknesses up to 900 nm for a range of primary electron energies ($15 \text{ keV} \leq E_0 \leq 30 \text{ keV}$). Beam diameters for the same parameters were simulated by Monte Carlo (MC) methods and agreed well with the experimental data.

BEAM
BROADENING

Experimental and simulated beam diameters were compared with calculated beam diameters from the Gauvin and Rudinsky model. Different from the more traditional models (e.g., Goldstein [Gol+77]), it takes different scattering regimes into account by introducing the Hurst exponent H , which ranges from 1 for very thin specimens

(ballistic scattering regime) to $H = 0.5$ for thicker samples (random walk, normal diffusion) [GR16]. The value of H also depends on the fraction R of electrons that are considered for the definition of the beam diameter: It increases with decreasing R [GR16]. Fitting the experimental and simulated data with the theoretical, analytical equation yields

- $H = 0.75$ for the experimental data and
- $H = 0.80$ for the simulated data.

Plural scattering dominates for our experimental conditions, which would suggest values closer to 0.5. However, our definition of the diameter-defining parameter, $R = 68\%$, is smaller compared to the common definition of $R = 90\%$, which may explain the higher values of H .

The model by Gauvin and Rudinsky represents the experimental and simulated data well. It is thus more versatile than previous models and should be used for estimations of beam broadening. However, the restriction of Gauvin and Rudinsky's model to amorphous specimens (or crystalline specimens when Bragg diffraction is negligible) limits its applicability. Also, its usability to describe beam broadening in thick specimens is limited as it does not consider electron energy loss. To further improve the model, the effect of electron-energy loss could be incorporated in the future.

CARBON CONTAMINA- TION

Electron-beam-induced carbon contamination impedes the imaging process as it covers structures of interest, complicates chemical analyses of the sample, and can lead to charging problems [Ege19; Hei63; Rei98]. Carbon contamination has been the subject of many studies in the past decades. Contamination is attributed to the polymerization of hydrocarbon molecules, denoted as contaminants, which are adsorbed at the specimen surface. However, there is little information on the contamination growth in STEM-in-SEM, which is a more severe problem than for higher electron energies. This deficiency was addressed by a systematic study of contamination growth depending on different imaging parameters and contamination-mitigation strategies. For this purpose, it was necessary to develop a method to measure contamination quantitatively and verify the reproducibility of measurement results.

Amorphous carbon films were the predominant test specimens as they are widely used as a support for nanoparticles and other samples in electron microscopy. Different test patterns, either emulating SEM-like or transmission electron microscopy-like (TEM-like) irradiation, were used to deposit contamination. The contamination thickness was measured by quantitative SEM-in-SEM imaging. The reproducibility of the measurement conditions, like the state of the sample and microscope, was monitored by reference measurements always using the same imaging parameters. These reference measurements enable the comparison of measurements performed over long time intervals.

A test pattern with 3×3 scanned squares of $1 \mu\text{m}^2$ (SEM-like test) and different irradiation times up to 10 min was used to investigate the influence of the primary electron energy (0.35 keV – 30 keV), electron dose rate, and the material of the support film (C, Au, Pd, and Si_3N_4). The main findings are:

- **Morphology:** The typical SEM deposit has a rather homogeneous thickness. In some cases, more pronounced contamination at the border of the irradiated region (frame-like contamination) is observed, which can be understood by slow-diffusing contaminants.
- Higher **electron energies** lead to reduced contamination thicknesses, which is attributed to a lower probability for primary electrons to crack contaminants and a lower secondary electron yield. The morphology changes at primary electron energies below 1 keV, simultaneously with a reduction of the contamination thickness. This reduction may be caused by charging effects. It is suggested to maximize the electron energy to minimize contamination if knock-on damage is not an issue.
- Contamination decreases with increasing **dose rate** (dose per area and time). Hence, it is preferable to apply a specific dose with a high current in a short time instead of using a low current for a long time.
- Contamination strongly depends on the **material** of the support film. A reduction of specimen thickness, likely by etching, is observed for an Au film and, even more pronounced, for a Pd film. Etching is attributed to the catalytic properties of the film materials and contaminants that act as etch precursors. Contamination is absent on the Si_3N_4 film, which is tentatively assigned to a charging of Si_3N_4 under electron irradiation.

A continuously scanned single square ($1 \mu\text{m}^2$) was used to test the influence of the **irradiation time** up to 140 min. The contamination thickness begins to saturate after about 50 min and shows a frame-like morphology, which can be understood by the depletion of contaminants.

The single square was also used to compare contamination-mitigation strategies. All subsequently described cleaning methods were applied for 10 to 15 min. The results of three tested cleaning strategies are summarized as follows:

- **Beam showering** can reduce contamination growth strongly, but the effect only lasts for a limited time. Its efficiency is suggested to depend on the mobility of the contaminants. This explanation rationalizes largely different efficiencies of beam showering in different microscopes. If beam showering is effective, it is advisable to leave out the region of interest while showering to protect it from beam damage. Beam showering was also used to estimate the diffusion coefficient of contaminants on the specimen surface ($D \approx 10^{-14} \text{m}^2\text{s}^{-1}$).

- In-situ **plasma cleaning** is the most effective cleaning method with a long-lasting effect. However, it requires a separate device, in contrast to beam showering.
- **Sample baking** at 100 °C in an external vacuum recipient was found to be least effective but may perform better when applied for a longer time or in-situ in the microscope.

Experimental contamination data were compared with a theoretical model by Müller [Mül69; Hir+94]. The model is only applicable for irradiation with a stationary electron beam (TEM-like contamination) and required the irradiation with a homogeneous, defocused electron beam with a circular area of $1 \mu\text{m}^2$. The comparison of experimental and calculated contamination thicknesses yields the residence time of contaminants on the surface (here 84 s), which is hardly accessible otherwise. However, this estimation depends highly on a reasonable selection of other parameters in the model, and a theoretical description with a reduced number of parameters would be preferable.

In general, the results of this study are best explained by the importance of surface diffusion. Due to the high number of parameters that influence carbon contamination, it will not be quantitatively reproducible in different microscopes and depends, of course, on the sample material. However, this work provides an extensive quantitative study of contamination in STEM-in-SEM and the conclusions are likely to hold in many cases.

The test patterns and the method for contamination quantification developed in this work enable further systematic studies on cleaning methods and the influence of parameters like, e.g., the composition of mobile contaminants. Furthermore, the insight into the processes of contamination obtained in this work provides an incentive to develop a theoretical contamination model with fewer parameters compared to the Müller model.

In conclusion, it should be emphasized that STEM-in-SEM is a beneficial approach for the investigation of diverse materials. If the obstacles that come with the lower beam energies are thoughtfully dealt with, its strengths, like the increased flexibility and enhanced contrast generation for light materials, render it a valuable addition to the palette of electron microscopy techniques.

ZIF-8

While the previous topics were methodological in character, the third part of this thesis is concerned with the study of a material. It focuses on the analysis of the surface-mounted metal-organic framework (SURMOF) ZIF-8 by (S)TEM at (standard) electron energies of 200 and 300 keV, including STEM tomography and energy-dispersive X-ray spectroscopy (EDXS). These techniques were combined with SEM and STEM-in-SEM.

ZIF-8 is of interest in the cluster of excellence 3DMM2O¹, which contributed to the funding of this work. As ZIF-8 shows high susceptibility to damage by electron irradiation, low-dose imaging conditions need to be used to preserve its crystalline structure. In addition, it is usually prepared on bulk substrates, from which it needs to be detached for TEM imaging by a potentially damaging procedure. To turn this preparation step obsolete, ZIF-8 was deposited directly on TEM grids covered by amorphous carbon films in a layer-by-layer synthesis approach. Another advantage of this technique is the precise control of the number of growth cycles, which was varied between 25 and 100 cycles. The most important results of this study are:

- In the initial growth stage, the material grows as individual particles with a planar interface to the substrate.
- The particles develop from (halved) cubic to (halved) rhombic dodecahedron shape during growth, which is typical for ZIF-8 if it is synthesized as a powder.
- First small particles are observed after 25 growth cycles, although the formation of a thin (continuous) layer cannot be excluded for a lower number of growth cycles.
- After 50 cycles, the growth is accelerated and individual particles form a polycrystalline, closed film.
- The deposit has the crystalline structure of ZIF-8.

An attempt was made to incorporate Ag nanoparticles into the pores of ZIF-8. While standard characterization techniques like X-ray diffraction did not yield information on the success of the synthesis procedure, EDXS-STEM and STEM tomography clearly showed that Ag nanoparticles were not present in ZIF-8.

In the future, further studies on SURMOF growth, like the analysis of growth on different substrates (e.g., graphene) or amorphous carbon films with different surface functionalizations, can be envisioned. These studies will profit from the TEM-sample preparation techniques and correlative microscopy that were described and applied in this work.

¹Cluster of Excellence (EXC-2082/1 – 390761711)

List of Figures

2.1. Signals generated by the interaction between the specimen and the electron beam	4
2.2. Schematic energy spectrum of electrons emitted from a bulk sample	5
2.3. Interaction volume from which signals emerge and the teardrop-shaped penetration volume of the PE	6
2.4. Elastic scattering at an atom	7
2.5. Differential unscreened and screened Rutherford cross-section	7
2.6. Bragg description of diffraction between two lattice planes	14
2.7. Diffraction and imaging mode in TEM	20
2.8. $\sin(\chi)$ for different defocus values	25
2.9. Contrast transfer function $H(u)$	26
2.10. Scheme of the STEM detector's imaging principle	33
2.11. Simulated relative HAADF-STEM intensities for Si and Ge	33
2.12. Scheme of a scanning electron microscope equipped with a STEM detector for STEM-in-SEM	35
3.1. Scheme of the STEM detector in the STRATA microscope	41
3.2. Schematic representation of the STEM detector and the detection angles in STEM-in-SEM	42
3.3. HAADF-STEM image of the STEM detector in the HELIOS microscope	45
3.4. STEM image of the STEM detector in the STRATA microscope	45
4.1. Visualization of electron paths in a Si sample	50
4.2. Geometry behind the Goldstein model	52
4.3. Geometry behind the anomalous diffusion model	53
4.4. Domains of anomalous diffusion	54
4.5. MgO wedge for the measurement of beam broadening	58
4.6. Normalized STEM intensities of different detector segments for MgO, 20 keV	60
4.7. Normalized STEM intensities for different scattering angles for Si, 25 keV	61
4.8. Experimentally determined beam broadening for MgO, Si, SrTiO ₃ , and Ge at 25 keV	64
4.9. Compilation of the data for SrTiO ₃ with $H = 0.81$	65
4.10. Compilation of all experimental data with $H = 0.75$	67
4.11. Compilation of all simulated data with $H = 0.8$	68
5.1. Contamination growth and diffusion of contaminants	73
5.2. Cross-section of electron-impact-induced dissociation and ionization for C ₃ H ₈	76
5.3. Electron-limited and precursor-limited regime	79
5.4. Calculated contamination thicknesses according to the Müller model	85

5.5. Floating process to deposit aC films on TEM grids	88
5.6. Storage box for aC films	89
5.7. Contamination test patterns	90
5.8. Schematic representation of beam showering	92
5.9. 20 keV HAADF-STEM image of the contamination cross-section lamella . .	94
5.10. 200 keV TEM image of the cross-section lamella prepared from the support film	95
5.11. Simulated relative HAADF-STEM intensities at 20 keV for aC	95
5.12. Overview on the evaluation of contamination thicknesses	97
5.13. Simulated relative HAADF-STEM intensities I_{rel} as a function of aC thickness t for the HELIOS and STRATA microscope	99
5.14. Comparison between a commercial and a self-made carbon film	100
5.15. TEM grid window covered by an aC film	100
5.16. Contamination reference test at the HELIOS microscope	101
5.17. Simulated relative intensities I_{rel} on the HAADF detector for large sample thicknesses	102
5.18. Contamination growth on one sample and chamber pressure in the HELIOS microscope over a period of 3 months	104
5.19. Contamination thickness maps of reference measurements on the same sample on two different dates	105
5.20. Mean contamination thickness measured on the same day and the same sam- ple in the HELIOS and STRATA microscope	105
5.21. Test of the evaluation method's stability towards sample drift	106
5.22. Mean contamination thicknesses grown with the SEM-like pattern using the usual distance d of 1 μm and a smaller distance of 0.5 μm	107
5.23. Energy dependence of contamination between 0.35 keV and 30 keV	109
5.24. Contamination thickness maps of deposits grown on the same sample using the same setting except E_0	110
5.25. Mean contamination thickness as a function of irradiation time for different beam currents	111
5.26. Contamination test with a variation of the dose rate and constant total dose	112
5.27. Contamination thickness of a single square for times up to 140 min	114
5.28. Contamination thickness maps of a single deposit after 10 and 100 min irra- diation	114
5.29. Contamination thickness maps for different dwell times	116
5.30. BF-STEM images of an Au and Pd thin film after contamination tests . . .	117
5.31. BF-STEM image of the Si_3N_4 film after irradiation	117
5.32. SE image and thickness map of a deposit grown in 140 min	117
5.33. Morphology of a contamination deposit grown in 10 min, investigated by a cross-section TEM lamella	118
5.34. Comparison of measured and theoretical contamination thicknesses for TEM- like irradiation	120
5.35. Mass spectrum of the residual gas	121
5.36. Result of BS measurements in comparison with the reference measurement .	123
5.37. Spread (standard deviations σ) of the slopes of the beam showering measu- rement	124

5.38. Mean contamination thicknesses after frame showering and without cleaning	125
5.39. Mean contamination thicknesses after sample baking and without cleaning	126
5.40. Mean contamination thicknesses after plasma cleaning and without cleaning	126
5.41. Comparison of contamination-mitigation strategies for up to 6 min	127
5.42. Comparison of contamination-mitigation strategies for up to 20 min	128
6.1. Scheme of the RD shape of ZIF-8	134
6.2. Scheme of the truncated RD shape undergone by ZIF-8 particles during their shape development	134
6.3. Dipping synthesis of ZIF-8 SURMOF on TEM grids	137
6.4. Dipping synthesis of Ag/ZIF-8 SURMOF on TEM grids	137
6.5. SE-SEM images of ZIF-8 on an aC film after 50 deposition cycles	142
6.6. SE-SEM images of ZIF-8 grown in 39 and 46 deposition cycles	142
6.7. SE-SEM tilt series of a single lbl-grown ZIF-8 crystal	143
6.8. SE-SEM image of a larger particle with full RD shape	144
6.9. SE-SEM images of lbl-grown ZIF-8 after 100 deposition cycles	144
6.10. BF-STEM images of ZIF-8 after 25 and 50 deposition cycles	146
6.11. Segmentation and evaluation of particle sizes	146
6.12. 300 keV HRTEM image of ZIF-8 crystallites after 46 deposition cycles	148
6.13. HRTEM images and Fourier-transformed images (power spectra) of a cubic particle (39 cycles sample), and a RD-shaped particle (50 cycles sample)	149
6.14. 300 keV HAADF-STEM tomography of an Ag/ZIF-8 composite particle	151
6.15. NBED pattern of an Ag/ZIF-8 crystallite (50 deposition cycles)	152
6.16. EDXS mapping of an Ag/ZIF-8 composite particle (50 deposition cycles)	153

List of Tables

4.1. Material properties of sample materials for the determination of beam broadening	58
4.2. Hurst exponents and the normalized mean absolute error (nMAE) as a measure of deviations between Equation (4.30) and the experimental and simulated data	64
4.3. Elastic mean free path lengths	66
5.1. Parameters for measurements of beam-induced carbon contamination with the SEM-like pattern	91
5.2. Parameters for the contamination thickness evaluation and their uncertainties	98
5.3. Parameters for measurements of the dose rate dependence of the contamination thickness	111
5.4. Parameters for the calculation of contamination thicknesses	120

Bibliography

- [Abb73] E. Abbe. “Beiträge zur Theorie des Mikroskops und der mikroskopischen Wahrnehmung”. In: *Archiv für Mikroskopische Anatomie* 9.1 (1873), pp. 413–468. DOI: 10.1007/BF02956173.
- [Adr12] K. Adrion. *Contamination on Pd thin film: Raw data*. In collab. with M. Hugenschmidt. 2020-08-12.
- [Adr21] K. Adrion. *Contamination on Silicon Nitride thin film: Raw data*. In collab. with M. Hugenschmidt. 2020-09-21.
- [Adr23] K. Adrion. *Contamination on Au thin film: Raw data*. In collab. with M. Hugenschmidt. 2020-07-23.
- [Amm96] M. Amman. “Atomic force microscopy study of electron beam written contamination structures”. In: *Journal of Vacuum Science & Technology, B: Microelectronics and Nanometer Structures – Processing, Measurement, and Phenomena* 14.1 (1996), p. 54. DOI: 10.1116/1.588429.
- [ARB00] D. A. Alman, D. N. Ruzic, and J. N. Brooks. “A hydrocarbon reaction model for low temperature hydrogen plasmas and an application to the Joint European Torus”. In: *Physics of Plasmas* 7.5 (2000), pp. 1421–1432. DOI: 10.1063/1.873960.
- [Ard38] M. von Ardenne. “Das Elektronen-Rastermikroskop”. In: *Zeitschrift für Physik* 109.9 (1938), pp. 553–572. DOI: 10.1007/BF01341584.
- [Ban+78] U. R. Bance, I. W. Drummond, D. Finbow, E. H. Harden, and P. Kenway. “27. Hydrocarbon contamination in vacuum dependent scientific instruments”. In: *Vacuum* 28.10-11 (1978), pp. 489–496. DOI: 10.1016/S0042-207X(78)80029-3.
- [BB13] W. H. Bragg and W. L. Bragg. “The Reflection of X-rays by Crystals”. In: *Proceedings of the Royal Society A: Mathematical, Physical and Engineering Sciences* 88.605 (1913), pp. 428–438. DOI: 10.1098/rspa.1913.0040.
- [BDG13] N. Brodusch, H. Demers, and R. Gauvin. “Nanometres-resolution Kikuchi patterns from materials science specimens with transmission electron forward scatter diffraction in the scanning electron microscope”. In: *Journal of Microscopy* 250.1 (2013), pp. 1–14. DOI: 10.1111/jmi.12007.
- [BDG18] N. Brodusch, H. Demers, and R. Gauvin. *Field Emission Scanning Electron Microscopy*. Singapore: Springer Singapore, 2018. DOI: 10.1007/978-981-10-4433-5.
- [Béc+09] A. Béché, J. L. Rouvière, L. Clément, and J. M. Hartmann. “Improved precision in strain measurement using nanobeam electron diffraction”. In: *Applied Physics Letters* 95.12 (2009), p. 123114. DOI: 10.1063/1.3224886.

- [Ber+19] S. Berg, D. Kutra, T. Kroeger, C. N. Straehle, B. X. Kausler, C. Haubold, M. Schiegg, J. Ales, T. Beier, M. Rudy, K. Eren, J. I. Cervantes, B. Xu, F. Beuttenmueller, A. Wolny, C. Zhang, U. Koethe, F. A. Hamprecht, and A. Kreshuk. “ilastik: interactive machine learning for (bio)image analysis”. In: *Nature Methods* 16.12 (2019), pp. 1226–1232. DOI: 10.1038/s41592-019-0582-9.
- [Bet] H. A. Bethe. “Zur Theorie des Durchgangs schneller Korpuskularstrahlen durch Materie”. München, Phil. Hab.-Schr., 1930. Leipzig.
- [BG20] N. Brodusch and R. Gauvin. “Is a 30 kV CFE-SEM in STEM-in-SEM Mode Suitable for Characterizing Real Materials?” In: *Microscopy and Microanalysis* 26.S2 (2020), pp. 1218–1219. DOI: 10.1017/S1431927620017377.
- [BH21] M. Boese and L. Han. “Cryo-SEM as an effective method for avoiding contamination”. In: *Microscopy and Microanalysis* 27.S1 (2021), pp. 1652–1653. DOI: 10.1017/S1431927621006097.
- [BH86] G. F. Bastin and H. J. M. Heijligers. “Quantitative electron probe microanalysis of carbon in binary carbides I: principles and procedures”. In: *X-Ray Spectrometry* 15.2 (1986), pp. 135–141. DOI: 10.1002/xrs.1300150212.
- [BR10] L. A. Baker and J. L. Rubinstein. “Radiation Damage in Electron Cryomicroscopy”. In: *Cryo-EM*. Ed. by G. J. Jensen. Vol. 481. Methods in enzymology 0076-6879. Amsterdam: Elsevier Acad. Press, 2010, pp. 371–388. DOI: 10.1016/S0076-6879(10)81015-8.
- [Bre+05] T. Bret, S. Mauron, I. Utke, and P. Hoffmann. “Characterization of focused electron beam induced carbon deposits from organic precursors”. In: *Microelectronic Engineering* 78-79 (2005), pp. 300–306. DOI: 10.1016/j.mee.2005.01.006.
- [Bro+19] N. Brodusch, H. Demers, A. Gellé, A. Moores, and R. Gauvin. “Electron energy-loss spectroscopy (EELS) with a cold-field emission scanning electron microscope at low accelerating voltage in transmission mode”. In: *Ultramicroscopy* 203 (2019), pp. 21–36. DOI: 10.1016/j.ultramic.2018.12.015.
- [Bro27] L. de Broglie. “La mécanique ondulatoire et la structure atomique de la matière et du rayonnement”. In: *J. Phys. Radium* 8.5 (1927), pp. 225–241.
- [Bru97] W. H. Bruenger. “Contamination reduction in low voltage electron-beam microscopy for dimensional metrology”. In: *Journal of Vacuum Science & Technology, B: Microelectronics and Nanometer Structures – Processing, Measurement, and Phenomena* 15.6 (1997), p. 2181. DOI: 10.1116/1.589349.
- [BS64] M. J. Berger and S. M. Seltzer. *Tables of energy losses and ranges of electrons and positrons*. Washington, D.C., 1964. URL: <https://ntrs.nasa.gov/api/citations/19650002905/downloads/19650002905.pdf>.
- [BT08] J. Barthel and A. Thust. “Quantification of the information limit of transmission electron microscopes”. In: *Physical Review Letters* 101.20 (2008), p. 200801. DOI: 10.1103/PhysRevLett.101.200801.
- [But+16] V. V. Butova, A. P. Budnik, E. A. Bulanova, and A. V. Soldatov. “New microwave-assisted synthesis of ZIF-8”. In: *Mendeleev Communications* 26.1 (2016), pp. 43–44. DOI: 10.1016/j.mencom.2016.01.017.
- [Bux+09] H. Bux, F. Liang, Y. Li, J. Cravillon, M. Wiebcke, and J. Caro. “Zeolitic imidazolate framework membrane with molecular sieving properties by microwave-assisted solvothermal synthesis”. In: *Journal of the American Chemical Society* 131.44 (2009), pp. 16000–16001. DOI: 10.1021/ja907359t.

- [BZ89] C. R. Bradley and N. J. Zaluzec. “Atomic sputtering in the Analytical Electron Microscope”. In: *Ultramicroscopy* 28.1-4 (1989), pp. 335–338. DOI: 10.1016/0304-3991(89)90320-3.
- [BZK66] G. F. Bahr, E. H. Zeitler, and K. Kobayashi. “High-Voltage Electron Microscopy”. In: *Journal of Applied Physics* 37.7 (1966), pp. 2900–2907. DOI: 10.1063/1.1782147.
- [Cal+18] P. G. Callahan, J.-C. Stinville, E. R. Yao, M. P. Echlin, M. S. Titus, M. de Graef, D. S. Gianola, and T. M. Pollock. “Transmission scanning electron microscopy: Defect observations and image simulations”. In: *Ultramicroscopy* 186 (2018), pp. 49–61. DOI: 10.1016/j.ultramicro.2017.11.004.
- [Čal+19] M. Čalkovský, E. Müller, M. Hugenschmidt, and D. Gerthsen. “Differential electron scattering cross-sections at low electron energies: The influence of screening parameter”. In: *Ultramicroscopy* 207 (2019), p. 112843. DOI: 10.1016/j.ultramicro.2019.112843.
- [Caz10] J. Cazaux. “Material contrast in SEM: Fermi energy and work function effects”. In: *Ultramicroscopy* 110.3 (2010), pp. 242–253. DOI: 10.1016/j.ultramicro.2009.12.002.
- [Cha+11] S. R. Challa, A. T. Delariva, T. W. Hansen, S. Helveg, J. Sehested, P. L. Hansen, F. Garzon, and A. K. Datye. “Relating rates of catalyst sintering to the disappearance of individual nanoparticles during Ostwald ripening”. In: *Journal of the American Chemical Society* 133.51 (2011), pp. 20672–20675. DOI: 10.1021/ja208324n.
- [Cha+98] P. Chatwin, G. Dagan, J. List, C. Mei, S. Savage, and P. Grathwohl. *Diffusion in Natural Porous Media: Contaminant Transport, Sorption/Desorption and Dissolution Kinetics*. Vol. 1. Boston, MA: Springer US, 1998. DOI: 10.1007/978-1-4615-5683-1.
- [Che+14] B. Chen, Z. Yang, Y. Zhu, and Y. Xia. “Zeolitic imidazolate framework materials: recent progress in synthesis and applications”. In: *Journal of Materials Chemistry A* 2.40 (2014), pp. 16811–16831. DOI: 10.1039/C4TA02984D.
- [CHK18] B. W. Caplins, J. D. Holm, and R. R. Keller. “Transmission imaging with a programmable detector in a scanning electron microscope”. In: *Ultramicroscopy* 196 (2018), pp. 40–48. DOI: 10.1016/j.ultramicro.2018.09.006.
- [Chr60] R. W. Christy. “Formation of Thin Polymer Films by Electron Bombardment”. In: *Journal of Applied Physics* 31.9 (1960), pp. 1680–1683. DOI: 10.1063/1.1735915.
- [CL70] B. J. Crawford and C. R. W. Liley. “A simple transmission stage using the standard collection system in the scanning electron microscope”. In: *Journal of Physics E: Scientific Instruments* 3.6 (1970), pp. 461–462. DOI: 10.1088/0022-3735/3/6/314.
- [CL75] H. W. Conru and P. C. Laberge. “Oil contamination with the SEM operated in the spot scanning mode”. In: *Journal of Physics E: Scientific Instruments* 8.2 (1975), pp. 136–138. DOI: 10.1088/0022-3735/8/2/021.
- [CMS90] P. A. Crozier, M. R. McCartney, and D. J. Smith. “Observation of exit surface sputtering in TiO₂ using biased secondary electron imaging”. In: *Surface Science* 237.1-3 (1990), pp. 232–240. DOI: 10.1016/0039-6028(90)90534-F.
- [Cór14] R. Córdoba Castillo. *Functional Nanostructures Fabricated by Focused Electron/Ion Beam Induced Deposition*. Cham: Springer International Publishing, 2014. DOI: 10.1007/978-3-319-02081-5.
- [Cos47] V. E. Cosslett. “Particle “Growth” in the Electron Microscope”. In: *Journal of Applied Physics* 18.9 (1947), pp. 844–845. DOI: 10.1063/1.1697852.

- [Cra+09] J. Cravillon, S. Münzer, S.-J. Lohmeier, A. Feldhoff, K. Huber, and M. Wiebcke. “Rapid Room-Temperature Synthesis and Characterization of Nanocrystals of a Prototypical Zeolitic Imidazolate Framework”. In: *Chemistry of Materials* 21.8 (2009), pp. 1410–1412. DOI: 10.1021/cm900166h.
- [Cra+11] J. Cravillon, R. Nayuk, S. Springer, A. Feldhoff, K. Huber, and M. Wiebcke. “Controlling Zeolitic Imidazolate Framework Nano- and Microcrystal Formation: Insight into Crystal Growth by Time-Resolved In Situ Static Light Scattering”. In: *Chemistry of Materials* 23.8 (2011), pp. 2130–2141. DOI: 10.1021/cm103571y.
- [Cra+12] J. Cravillon, C. A. Schröder, H. Bux, A. Rothkirch, J. Caro, and M. Wiebcke. “Formate modulated solvothermal synthesis of ZIF-8 investigated using time-resolved in situ X-ray diffraction and scanning electron microscopy”. In: *CrystEngComm* 14.2 (2012), pp. 492–498. DOI: 10.1039/C1CE06002C.
- [CS08] K. Chuntonov and J. Setina. “New lithium gas sorbents”. In: *Journal of Alloys and Compounds* 455.1-2 (2008), pp. 489–496. DOI: 10.1016/j.jallcom.2007.01.158.
- [CWW68] A. V. Crewe, J. Wall, and L. M. Welter. “A High-Resolution Scanning Transmission Electron Microscope”. In: *Journal of Applied Physics* 39.13 (1968), pp. 5861–5868. DOI: 10.1063/1.1656079.
- [Czy+90] Z. Czyżewski, D. O. MacCallum, A. Romig, and D. C. Joy. “Calculations of Mott scattering cross section”. In: *Journal of Applied Physics* 68.7 (1990), pp. 3066–3072. DOI: 10.1063/1.346400.
- [Dar+10] M. Darbandi, H. K. Arslan, O. Shekhah, A. Bashir, A. Birkner, and C. Wöll. “Fabrication of free-standing ultrathin films of porous metal-organic frameworks by liquid-phase epitaxy and subsequent delamination”. In: *physica status solidi (RRL) - Rapid Research Letters* 4.8-9 (2010), pp. 197–199. DOI: 10.1002/pssr.201004200.
- [Dem+12] H. Demers, R. Ramachandra, D. Drouin, and N. de Jonge. “The probe profile and lateral resolution of scanning transmission electron microscopy of thick specimens”. In: *Microscopy and Microanalysis* 18.3 (2012), pp. 582–590. DOI: 10.1017/S1431927612000232.
- [Din+05] W. Ding, D. A. Dikin, X. Chen, R. D. Piner, R. S. Ruoff, E. Zussman, X. Wang, and X. Li. “Mechanics of hydrogenated amorphous carbon deposits from electron-beam-induced deposition of a paraffin precursor”. In: *Journal of Applied Physics* 98.1 (2005), p. 014905. DOI: 10.1063/1.1940138.
- [DKL17] H. S. Dow, W. S. Kim, and J. W. Lee. “Thermal and electrical properties of silicon nitride substrates”. In: *AIP Advances* 7.9 (2017), p. 095022. DOI: 10.1063/1.4996314.
- [DLF80] P. Doig, D. Lonsdale, and P. E. J. Flewitt. “The spatial resolution of X-ray microanalysis in the scanning transmission electron microscope”. In: *Philosophical Magazine A* 41.5 (1980), pp. 761–775. DOI: 10.1080/01418618008239347.
- [Dre+17] H. Drees, E. Müller, M. Dries, and D. Gerthsen. “Electron-beam broadening in amorphous carbon films in low-energy scanning transmission electron microscopy”. In: *Ultramicroscopy* 185 (2017), pp. 65–71. DOI: 10.1016/j.ultramicro.2017.11.005.
- [Dyc+18] O. Dyck, S. Kim, S. V. Kalinin, and S. Jesse. “Mitigating e-beam-induced hydrocarbon deposition on graphene for atomic-scale scanning transmission electron microscopy studies”. In: *Journal of Vacuum Science & Technology B: Nanotechnology and Microelectronics: Materials, Processing, Measurement, & Phenomena* 36.1 (2018), p. 011801. DOI: 10.1116/1.5003034.

- [Ebe+90] D. D. Eberl, J. Sacuterodonacuta, M. Kralik, B. E. Taylor, and Z. E. Peterman. “Ostwald ripening of clays and metamorphic minerals”. In: *Science (New York, N.Y.)* 248.4954 (1990), pp. 474–477. DOI: 10.1126/science.248.4954.474.
- [Ege12] R. F. Egerton. “Mechanisms of radiation damage in beam-sensitive specimens, for TEM accelerating voltages between 10 and 300 kV”. In: *Microscopy research and technique* 75.11 (2012), pp. 1550–1556. DOI: 10.1002/jemt.22099.
- [Ege19] R. F. Egerton. “Radiation damage to organic and inorganic specimens in the TEM”. In: *Micron (Oxford, England : 1993)* 119 (2019), pp. 72–87. DOI: 10.1016/j.micron.2019.01.005.
- [ELM04] R. F. Egerton, P. Li, and M. Malac. “Radiation damage in the TEM and SEM”. In: *Micron (Oxford, England : 1993)* 35.6 (2004), pp. 399–409. DOI: 10.1016/j.micron.2004.02.003.
- [Enn53] A. E. Ennos. “The origin of specimen contamination in the electron microscope”. In: *British Journal of Applied Physics* 4.4 (1953), pp. 101–106. DOI: 10.1088/0508-3443/4/4/302.
- [Enn54] A. E. Ennos. “The sources of electron-induced contamination in kinetic vacuum systems”. In: *British Journal of Applied Physics* 5.1 (1954), pp. 27–31. DOI: 10.1088/0508-3443/5/1/307.
- [ER76] R. F. Egerton and C. J. Rossouw. “Direct measurement of contamination and etching rates in an electron beam”. In: *Journal of Physics D: Applied Physics* 9.4 (1976), pp. 659–663. DOI: 10.1088/0022-3727/9/4/016.
- [Esk+10] D. Esken, S. Turner, O. I. Lebedev, G. van Tendeloo, and R. A. Fischer. “Au@ZIFs: Stabilization and Encapsulation of Cavity-Size Matching Gold Clusters inside Functionalized Zeolite Imidazolate Frameworks, ZIFs”. In: *Chemistry of Materials* 22.23 (2010), pp. 6393–6401. DOI: 10.1021/cm102529c.
- [FH08] B. Fultz and J. M. Howe. *Transmission electron microscopy and diffractometry of materials*. 3rd ed. Vol. 1439-2674. Advanced texts in physics. Berlin and New York: Springer, 2008.
- [FHN77] R. G. Faulkner, T. C. Hopkins, and K. Norrgård. “Improved spatial resolution microanalysis in a scanning transmission electron microscope”. In: *X-Ray Spectrometry* 6.2 (1977), pp. 73–79. DOI: 10.1002/xrs.1300060205.
- [FMD94] L. Frank, I. Müllerová, and A. Delong. “Microscopy with slow electrons”. In: *Czechoslovak Journal of Physics* 44.3 (1994), pp. 195–238. DOI: 10.1007/BF01694486.
- [FN78] R. G. Faulkner and K. Norgård. “X-ray microanalytical sensitivity and spatial resolution in scanning transmission electron microscopes”. In: *X-Ray Spectrometry* 7.4 (1978), pp. 184–189. DOI: 10.1002/xrs.1300070403.
- [Fou78] J. T. Fourie. “High contamination rates from strongly adsorbed hydrocarbon molecules and a suggested solution”. In: *Optik* 52.1 (1978), pp. 91–95.
- [FRR05] J. D. Fowlkes, S. J. Randolph, and P. D. Rack. “Growth and simulation of high-aspect ratio nanopillars by primary and secondary electron-induced deposition”. In: *Journal of Vacuum Science & Technology, B: Microelectronics and Nanometer Structures – Processing, Measurement, and Phenomena* 23.6 (2005), p. 2825. DOI: 10.1116/1.2101732.
- [GGR74] P. Gentsch, H. Gilde, and L. Reimer. “Measurement of the top bottom effect in scanning transmission electron microscopy of thick amorphous specimens”. In: *Journal of Microscopy* 100.1 (1974), pp. 81–92. DOI: 10.1111/j.1365-2818.1974.tb03915.x.

- [Gho+19] S. Ghosh, P. Kumar, S. Conrad, M. Tsapatsis, and K. A. Mkhoyan. “Electron-Beam Damage in Metal Organic Frameworks in the TEM”. In: *Microscopy and Microanalysis* 25.S2 (2019), pp. 1704–1705. DOI: 10.1017/S1431927619009255.
- [Gho+21] S. Ghosh, H. Yun, P. Kumar, S. Conrad, M. Tsapatsis, and K. A. Mkhoyan. “Two Distinct Stages of Structural Modification of ZIF-L MOF under Electron-Beam Irradiation”. In: *Chemistry of Materials* (2021). DOI: 10.1021/acs.chemmater.1c01332.
- [GM09] H. Geiger and E. Marsden. “On a diffuse reflection of the α -particles”. In: *Proceedings of the Royal Society of London Series A* 82.557 (1909), pp. 495–500. DOI: 10.1098/rspa.1909.0054.
- [Goh+20] Y. M. Goh, J. Schwartz, T. Ma, B. Kerns, and R. Hovden. “Open-hardware, High-vacuum Storage for TEM Holders Remedies and Quantifies Hydrocarbon Contamination”. In: *Microscopy and Microanalysis* 26.S2 (2020), pp. 3120–3123. DOI: 10.1017/S1431927620023879.
- [Gol+18] J. I. Goldstein, D. E. Newbury, J. R. Michael, N. W. Ritchie, J. H. J. Scott, and D. C. Joy. *Scanning Electron Microscopy and X-Ray Microanalysis*. 4th ed. 2018. New York, NY: Springer New York, 2018. DOI: 10.1007/978-1-4939-6676-9.
- [Gol+77] J. I. Goldstein, J. L. Costley, G. W. Lorimer, and S. Reed. “Quantitative X-ray analysis in the electron microscope”. In: *Scanning Electron Microscopy* 1 (1977), pp. 315–324.
- [GR16] R. Gauvin and S. Rudinsky. “A universal equation for computing the beam broadening of incident electrons in thin films”. In: *Ultramicroscopy* 167 (2016), pp. 21–30. DOI: 10.1016/j.ultramicro.2016.04.007.
- [GRK13] R. H. Geiss, K. P. Rice, and R. R. Keller. “Transmission EBSD in the Scanning Electron Microscope”. In: *Microscopy Today* 21.3 (2013), pp. 16–20. DOI: 10.1017/S1551929513000503.
- [Gro75] T. Groves. “Thick specimens in the CEM and STEM. Resolution and image formation”. In: *Ultramicroscopy* 1.1 (1975), pp. 15–31. DOI: 10.1016/S0304-3991(75)80005-2.
- [Grü+20] L. Grünwald, M. Langer, S. Meyer, D. Nerz, J. Hänisch, B. Holzapfel, and D. Gerthsen. *Supplementary information for 'Structural and chemical properties of superconducting Co-doped BaFe₂As₂ thin films grown on CaF₂'*. 2020. DOI: 10.5281/zenodo.4058145.
- [GS13] E. D. German and M. Sheintuch. “Predicting CH₄ Dissociation Kinetics on Metals: Trends, Sticking Coefficients, H Tunneling, and Kinetic Isotope Effect”. In: *The Journal of Physical Chemistry C* 117.44 (2013), pp. 22811–22826. DOI: 10.1021/jp406937r.
- [GS40] S. Goudsmit and J. L. Saunderson. “Multiple Scattering of Electrons”. In: *Physical Review* 57.1 (1940), pp. 24–29. DOI: 10.1103/PhysRev.57.24.
- [GSP11] O. Guise, C. Strom, and N. Preschilla. “STEM-in-SEM method for morphology analysis of polymer systems”. In: *Polymer* 52.5 (2011), pp. 1278–1285. DOI: 10.1016/j.polymer.2011.01.030.
- [Gu+16] Z.-G. Gu, H. Fu, T. Neumann, Z.-X. Xu, W.-Q. Fu, W. Wenzel, L. Zhang, J. Zhang, and C. Wöll. “Chiral Porous Metacrystals: Employing Liquid-Phase Epitaxy to Assemble Enantiopure Metal-Organic Nanoclusters into Molecular Framework Pores”. In: *ACS Nano* 10.1 (2016), pp. 977–983. DOI: 10.1021/acsnano.5b06230.

- [Gui+04] O. Guise, H. Marbach, J. Levy, J. Ahner, and J. T. Yates. “Electron-beam-induced deposition of carbon films on Si(100) using chemisorbed ethylene as a precursor molecule”. In: *Surface Science* 571.1-3 (2004), pp. 128–138. DOI: 10.1016/j.susc.2004.07.053.
- [Guo+16] W. Guo, Z. Chen, C. Yang, T. Neumann, C. Kübel, W. Wenzel, A. Welle, W. Pflöging, O. Shekhah, C. Wöll, and E. Redel. “Bi₂O₃ nanoparticles encapsulated in surface mounted metal-organic framework thin films”. In: *Nanoscale* 8.12 (2016), pp. 6468–6472. DOI: 10.1039/C6NR00532B.
- [GW10] A. J. V. Griffiths and T. Walther. “Quantification of carbon contamination under electron beam irradiation in a scanning transmission electron microscope and its suppression by plasma cleaning”. In: *Journal of Physics: Conference Series* 241 (2010), p. 012017. DOI: 10.1088/1742-6596/241/1/012017.
- [HB02] S. Havlin and D. Ben-Avraham. “Diffusion in disordered media”. In: *Advances in Physics* 51.1 (2002), pp. 187–292. DOI: 10.1080/00018730110116353.
- [Hei+15] L. Heinke, M. Tu, S. Wannapaiboon, R. A. Fischer, and C. Wöll. “Surface-mounted metal-organic frameworks for applications in sensing and separation”. In: *Microporous and Mesoporous Materials* 216 (2015), pp. 200–215. DOI: 10.1016/j.micromeso.2015.03.018.
- [Hei60] H. G. Heide. “Elektronenmikroskopie von Objekten unter Atmosphärendruck oder unter Drucken, welche ihre Austrocknung verhindern”. In: *Die Naturwissenschaften* 47.14 (1960), pp. 313–317. DOI: 10.1007/BF00628703.
- [Hei63] H. G. Heide. “Die Objektverschmutzung im Elektronenmikroskop und das Problem der Strahlenschädigung durch Kohlenstoffabbau”. In: *Zeitschrift für angewandte Physik* 15.2 (1963), pp. 116–128.
- [HEM08] J. K. Hyun, P. Ercius, and D. A. Muller. “Beam spreading and spatial resolution in thick organic specimens”. In: *Ultramicroscopy* 109.1 (2008), pp. 1–7. DOI: 10.1016/j.ultramicro.2008.07.003.
- [Het+17] S. Hettler, M. Dries, P. Hermann, M. Obermair, D. Gerthsen, and M. Malac. “Carbon contamination in scanning transmission electron microscopy and its impact on phase-plate applications”. In: *Micron (Oxford, England : 1993)* 96 (2017), pp. 38–47. DOI: 10.1016/j.micron.2017.02.002.
- [Het+18] S. Hettler, E. Kano, M. Dries, D. Gerthsen, L. Pfaffmann, M. Bruns, M. Beleggia, and M. Malac. “Charging of carbon thin films in scanning and phase-plate transmission electron microscopy”. In: *Ultramicroscopy* 184.Pt A (2018), pp. 252–266. DOI: 10.1016/j.ultramicro.2017.09.009.
- [Hil48] J. Hillier. “On the Investigation of Specimen Contamination in the Electron Microscope”. In: *Journal of Applied Physics* 19.3 (1948), pp. 226–230. DOI: 10.1063/1.1715049.
- [Hir+94] P. Hirsch, M. Kässens, M. Püttmann, and L. Reimer. “Contamination in a scanning electron microscope and the influence of specimen cooling”. In: *Scanning* 16.2 (1994), pp. 101–110. DOI: 10.1002/sca.4950160207.
- [Hir60] E. H. Hirsch. “Image formation by electron bombardment of metal targets”. In: *British Journal of Applied Physics* 11.12 (1960), pp. 547–550. DOI: 10.1088/0508-3443/11/12/305.
- [Hir77] E. H. Hirsch. “The growth of carbonaceous contamination on surfaces undergoing ion bombardment”. In: *Journal of Physics D: Applied Physics* 10.15 (1977), pp. 2069–2076. DOI: 10.1088/0022-3727/10/15/010.

- [HKM70] R. K. Hart, T. F. Kassner, and J. K. Maurin. “The contamination of surfaces during high-energy electron irradiation”. In: *Philosophical Magazine* 21.171 (1970), pp. 453–467. DOI: 10.1080/14786437008238431.
- [HMG19] M. Hugenschmidt, E. Müller, and D. Gerthsen. “Electron beam broadening in electron-transparent samples at low electron energies”. In: *Journal of Microscopy* 274.3 (2019), pp. 150–157. DOI: 10.1111/jmi.12793.
- [Hol21] J. Holm. “A Brief Overview of Scanning Transmission Electron Microscopy in a Scanning Electron Microscope (STEM-in-SEM)”. In: *Electronic Device Failure Analysis* 23.4 (2021). URL: https://tsapps.nist.gov/publication/get_pdf.cfm?pub_id=932860 (visited on 12/19/2021).
- [Hor+09] S. Horiuchi, T. Hanada, M. Ebisawa, Y. Matsuda, M. Kobayashi, and A. Takahara. “Contamination-free transmission electron microscopy for high-resolution carbon elemental mapping of polymers”. In: *ACS Nano* 3.5 (2009), pp. 1297–1304. DOI: 10.1021/nn9001598.
- [Hoy+11] D. Hoyle, M. Malac, M. Trudeau, and P. Woo. “UV Treatment of TEM/STEM Samples for Reduced Hydrocarbon Contamination”. In: *Microscopy and Microanalysis* 17.S2 (2011), pp. 1026–1027. DOI: 10.1017/S1431927611006003.
- [Hre78] J. J. Hren. “Specimen contamination in analytical electron microscopy: Sources and solutions”. In: *Ultramicroscopy* 3 (1978), pp. 375–380. DOI: 10.1016/S0304-3991(78)80057-6.
- [Hre79] J. J. Hren. “Barriers to AEM: Contamination and Etching”. In: *Introduction to Analytical Electron Microscopy*. Ed. by J. J. Hren, J. I. Goldstein, and D. C. Joy. Boston, MA: Springer US, 1979, pp. 481–505. DOI: 10.1007/978-1-4757-5581-7_18.
- [Hri+14] R. Hristu, D. E. Tranca, S. G. Stanciu, M. Gregor, T. Plecenik, M. Truchly, T. Roch, S. A. M. Tofail, and G. A. Stanciu. “Surface charge and carbon contamination on an electron-beam-irradiated hydroxyapatite thin film investigated by photoluminescence and phase imaging in atomic force microscopy”. In: *Microscopy and Microanalysis* 20.2 (2014), pp. 586–595. DOI: 10.1017/S1431927614000191.
- [Hri+15] R. Hristu, S. G. Stanciu, D. E. Tranca, and G. A. Stanciu. “Electron beam influence on the carbon contamination of electron irradiated hydroxyapatite thin films”. In: *Applied Surface Science* 346 (2015), pp. 342–347. DOI: 10.1016/j.apsusc.2015.03.214.
- [HS19] P. W. Hawkes and J. C. H. Spence. *Springer Handbook of Microscopy*. Cham: Springer International Publishing, 2019. DOI: 10.1007/978-3-030-00069-1.
- [Hüb+92] B. Hübner, H. Koops, H. Pagnia, N. Sotnik, J. Urban, and M. Weber. “Tips for scanning tunneling microscopy produced by electron-beam-induced deposition”. In: *Ultramicroscopy* 42-44 (1992), pp. 1519–1525. DOI: 10.1016/0304-3991(92)90476-Z.
- [Hug+20] M. Hugenschmidt, K. Kutonova, E. P. Valadez Sánchez, S. Moulai, H. Gliemann, S. Bräse, C. Wöll, and D. Gerthsen. “Direct Synthesis of ZIF-8 on Transmission Electron Microscopy Grids Allows Structure Analysis and 3D Reconstruction”. In: *Particle & Particle Systems Characterization* 37.11 (2020), p. 2000209. DOI: 10.1002/ppsc.202000209.
- [Hug18] M. Hugenschmidt. “Elektronenstrahlaufweitung in kristallinen Materialien in der Rastertransmissionselektronenmikroskopie bei niedrigen Elektronenenergien”. Master thesis. Karlsruhe: Karlsruhe Institute of Technology, 2018.

- [HW19] L. Heinke and C. Wöll. “Surface-Mounted Metal-Organic Frameworks: Crystalline and Porous Molecular Assemblies for Fundamental Insights and Advanced Applications”. In: *Advanced Materials* 31.26 (2019), p. 1806324. DOI: 10.1002/adma.201806324.
- [IL03] H. Ibach and H. Lüth. *Solid-State Physics: An Introduction to Principles of Materials Science*. Third Extensively Updated and Enlarged Edition. Springer eBook Collection. Berlin and Heidelberg: Springer, 2003. DOI: 10.1007/978-3-662-05342-3.
- [Isa+99] T. C. Isabell, P. E. Fischione, C. O’Keefe, M. U. Guruz, and V. P. Dravid. “Plasma Cleaning and Its Applications for Electron Microscopy”. In: *Microscopy and Microanalysis* 5.2 (1999), pp. 126–135. DOI: 10.1017/S1431927699000094.
- [Iwa02] M. Iwaki. “Estimation of the atomic density of amorphous carbon using ion implantation, SIMS and RBS”. In: *Surface and Coatings Technology* 158-159 (2002), pp. 377–381. DOI: 10.1016/S0257-8972(02)00247-5.
- [Jen+96] A. D. Jenkins, P. Kratochvíl, R. F. T. Stepto, and U. W. Suter. “Glossary of basic terms in polymer science (IUPAC Recommendations 1996)”. In: *Pure and Applied Chemistry* 68.12 (1996), pp. 2287–2311. DOI: 10.1351/pac199668122287.
- [Jia+11] H.-L. Jiang, T. Akita, T. Ishida, M. Haruta, and Q. Xu. “Synergistic catalysis of Au@Ag core-shell nanoparticles stabilized on metal-organic framework”. In: *Journal of the American Chemical Society* 133.5 (2011), pp. 1304–1306. DOI: 10.1021/ja1099006.
- [Jia+15] M. Jian, B. Liu, R. Liu, J. Qu, H. Wang, and X. Zhang. “Water-based synthesis of zeolitic imidazolate framework-8 with high morphology level at room temperature”. In: *RSC Advances* 5.60 (2015), pp. 48433–48441. DOI: 10.1039/C5RA04033G.
- [Jia16a] N. Jiang. “Beam damage by the induced electric field in transmission electron microscopy”. In: *Micron (Oxford, England : 1993)* 83 (2016), pp. 79–92. DOI: 10.1016/j.micron.2016.02.007.
- [Jia16b] N. Jiang. “Electron beam damage in oxides: a review”. In: *Reports on progress in physics. Physical Society (Great Britain)* 79.1 (2016), p. 016501. DOI: 10.1088/0034-4885/79/1/016501.
- [Jin+20] Y. Jing, Q. Lei, C. Xia, Y. Guan, Y. Yang, J. He, Y. Yang, Y. Zhang, and M. Yan. “Synthesis of Ag and AgCl co-doped ZIF-8 hybrid photocatalysts with enhanced photocatalytic activity through a synergistic effect”. In: *RSC Advances* 10.2 (2020), pp. 698–704. DOI: 10.1039/C9RA10100D.
- [JJ96] D. C. Joy and C. S. Joy. “Low voltage scanning electron microscopy”. In: *Micron (Oxford, England : 1993)* 27.3-4 (1996), pp. 247–263. DOI: 10.1016/0968-4328(96)00023-6.
- [JL89] D. C. Joy and S. Luo. “An empirical stopping power relationship for low-energy electrons”. In: *Scanning* 11.4 (1989), pp. 176–180. DOI: 10.1002/sca.4950110404.
- [Jon+10] N. de Jonge, N. Poirier-Demers, H. Demers, D. B. Peckys, and D. Drouin. “Nanometer-resolution electron microscopy through micrometers-thick water layers”. In: *Ultramicroscopy* 110.9 (2010), pp. 1114–1119. DOI: 10.1016/j.ultramicro.2010.04.001.
- [Jon18] N. de Jonge. “Sample Dependent Resolution of Transmission Electron Microscopy in Water or Ice”. In: *Microscopy and Microanalysis* 24.S1 (2018), pp. 1978–1979. DOI: 10.1017/S1431927618010371.
- [Joy06] D. C. Joy. “What EBID Can Tell Us About Contamination ?” In: *Microscopy and Microanalysis* 12.S02 (2006), pp. 1660–1661. DOI: 10.1017/S1431927606069285.

- [JVD18] N. de Jonge, A. Verch, and H. Demers. “The Influence of Beam Broadening on the Spatial Resolution of Annular Dark Field Scanning Transmission Electron Microscopy”. In: *Microscopy and Microanalysis* 24.1 (2018), pp. 8–16. DOI: 10.1017/S1431927618000077.
- [Kai+11] U. Kaiser, J. Biskupek, J. C. Meyer, J. Leschner, L. Lechner, H. Rose, M. Stöger-Pollach, A. N. Khlobystov, P. Hartel, H. Müller, M. Haider, S. Eyhusen, and G. Benner. “Transmission electron microscopy at 20 kV for imaging and spectroscopy”. In: *Ultramicroscopy* 111.8 (2011), pp. 1239–1246. DOI: 10.1016/j.ultramicro.2011.03.012.
- [Kan+88] K. Kanaya, E. Oho, N. Osaki, and T. Oda. “A contamination reducing method by ion beam bombardment of the specimen in high resolution electron microscopy”. In: *Micron and Microscopica Acta* 19.3 (1988), pp. 163–173. DOI: 10.1016/0739-6260(88)90026-3.
- [Kan+90] K. Kanaya, K. Yonehara, E. Oho, N. Inoue, and M. Izumida. “A cone formation theory of contamination in high resolution transmission electron microscopy”. In: *Micron and Microscopica Acta* 21.1-2 (1990), pp. 13–28. DOI: 10.1016/0739-6260(90)90004-Y.
- [Kas16] S. Kaskel, ed. *The Chemistry of Metal-Organic Frameworks: Synthesis, Characterization, and Applications: Synthesis and characterization of functional nano-objects*. Weinheim, Germany: Wiley-VCH Verlag GmbH & Co. KGaA, 2016. DOI: 10.1002/9783527693078.
- [KBF12] T. Klein, E. Buhr, and C. G. Frase. “TSEM: A Review of Scanning Electron Microscopy in Transmission Mode and Its Applications”. In: *Advances in imaging and electron physics*. Ed. by P. W. Hawkes. Vol. 171. Amsterdam: Elsevier/Academic Press, 2012, pp. 297–356. DOI: 10.1016/B978-0-12-394297-5.00006-4.
- [KH68] S. Kimoto and H. Hashimoto. “On the contrast and resolution of the scanning electron microscope”. In: *Proceedings of the Symposium on the Scanning Electron Microscope*. Chicago, Illinois, USA, 1968, pp. 63–78.
- [KHS81] A. Kumao, H. Hashimoto, and Shiraishi. “Studies on Specimen Contamination by Transmission Electron Microscopy”. In: *Journal of Electron Microscopy* 30.3 (1981), pp. 161–170. DOI: 10.1093/oxfordjournals.jmicro.a050301.
- [Kil98] R. Kilaas. “Optimal and near-optimal filters in high-resolution electron microscopy”. In: *Journal of Microscopy* 190.1-2 (1998), pp. 45–51. DOI: 10.1046/j.1365-2818.1998.3070861.x.
- [Kle+11] T. Klein, E. Buhr, K.-P. Johnsen, and C. G. Frase. “Traceable measurement of nanoparticle size using a scanning electron microscope in transmission mode (TSEM)”. In: *Measurement Science and Technology* 22.9 (2011), p. 094002. DOI: 10.1088/0957-0233/22/9/094002.
- [Kno76] W. A. Knox. “Contamination formed around a very narrow electron beam”. In: *Ultramicroscopy* 1.3-4 (1976), pp. 175–180. DOI: 10.1016/0304-3991(76)90031-0.
- [Kon+14] M. Konno, T. Ogashiwa, T. Sunaoshi, Y. Orai, and M. Sato. “Lattice imaging at an accelerating voltage of 30kV using an in-lens type cold field-emission scanning electron microscope”. In: *Ultramicroscopy* 145 (2014), pp. 28–35. DOI: 10.1016/j.ultramicro.2013.09.001.
- [Kön48] H. König. “Die Rolle der Kohle bei elektronenmikroskopischen Abbildungen”. In: *Die Naturwissenschaften* 35.9 (1948), pp. 261–265. DOI: 10.1007/BF00599571.

- [Kon79] H. Konuma. “Rate of Carbon Contamination on Al Targets in a High Vacuum Electron Excitation X-Ray Tube”. In: *Japanese Journal of Applied Physics* 18.2 (1979), pp. 357–362. DOI: 10.1143/JJAP.18.357.
- [Koo88] H. W. P. Koops. “High-resolution electron-beam induced deposition”. In: *Journal of Vacuum Science & Technology, B: Microelectronics and Nanometer Structures – Processing, Measurement, and Phenomena* 6.1 (1988), p. 477. DOI: 10.1116/1.584045.
- [KR32] M. Knoll and E. Ruska. “Das Elektronenmikroskop”. In: *Z. Physik (Zeitschrift für Physik)* 78.5-6 (1932), pp. 318–339. DOI: 10.1007/BF01342199.
- [Kut+09] K. Kutsuki, G. Okamoto, T. Hosoi, T. Shimura, and H. Watanabe. “Nitrogen plasma cleaning of Ge(100) surfaces”. In: *Applied Surface Science* 255.12 (2009), pp. 6335–6337. DOI: 10.1016/j.apsusc.2009.02.011.
- [La +19] F. D. La Peña, E. Prestat, V. T. Fauske, P. Burdet, P. Jokubauskas, M. Nord, T. Ostasevicius, K. E. MacArthur, M. Sarahan, D. N. Johnstone, J. Taillon, J. Lähne-mann, V. Migunov, A. Eljarrat, J. Caron, T. Aarholt, S. Mazzucco, M. Walls, T. Slater, F. Winkler, pquinn-dls, B. Martineau, G. Donval, R. McLeod, E. R. Hoglund, I. Alxneit, D. Lundeby, T. Henninen, Luiz Fernando Zagonel, and A. Garmannslund. *HyperSpy v1.5.2*. 2019. DOI: 10.5281/zenodo.3396791.
- [Lai+16] L. S. Lai, Y. F. Yeong, K. K. Lau, and A. M. Shariff. “Effect of Synthesis Parameters on the Formation of ZIF-8 Under Microwave-assisted Solvothermal”. In: *Procedia Engineering* 148 (2016), pp. 35–42. DOI: 10.1016/j.proeng.2016.06.481.
- [Lau+10] D. Lau, A. E. Hughes, T. H. Muster, T. J. Davis, and A. M. Glenn. “Electron-beam-induced carbon contamination on silicon: characterization using Raman spectroscopy and atomic force microscopy”. In: *Microscopy and Microanalysis* 16.1 (2010), pp. 13–20. DOI: 10.1017/S1431927609991206.
- [Lau13] M. Laue. “Eine quantitative Prüfung der Theorie für die Interferenzerscheinungen bei Röntgenstrahlen”. In: *Annalen der Physik* 346.10 (1913), pp. 989–1002. DOI: 10.1002/andp.19133461005.
- [Len+02] M. Lentzen, B. Jahnen, C. L. Jia, A. Thust, K. Tillmann, and K. Urban. “High-resolution imaging with an aberration-corrected transmission electron microscope”. In: *Ultramicroscopy* 92.3-4 (2002), pp. 233–242. DOI: 10.1016/S0304-3991(02)00139-0.
- [Lev+18] B. D. Levin, Y. Jiang, E. Padgett, S. Waldon, C. Quammen, C. Harris, U. Ayachit, M. Hanwell, P. Ercius, D. A. Muller, and R. Hovden. “Tutorial on the Visualization of Volumetric Data Using tomviz”. In: *Microscopy Today* 26.1 (2018), pp. 12–17. DOI: 10.1017/S1551929517001213.
- [Li+20] Y. Li, Y. Li, Y. Wang, G. Ma, X. Liu, Y. Li, and J. Soar. “Application of zeolitic imidazolate frameworks (ZIF-8)/ionic liquid composites modified nano-carbon paste electrode as sensor for electroanalytical sensing of 1-hydroxypyrene”. In: *Microchemical Journal* 159 (2020), p. 105433. DOI: 10.1016/j.microc.2020.105433.
- [Li+21] C. Li, A. P. Tardajos, Da Wang, D. Choukroun, K. van Daele, T. Breugelmanns, and S. Bals. “A simple method to clean ligand contamination on TEM grids”. In: *Ultramicroscopy* 221 (2021), p. 113195. DOI: 10.1016/j.ultramic.2020.113195. URL: <https://www.sciencedirect.com/science/article/pii/S0304399120303375>.
- [Lid05] D. R. Lide, ed. *CRC handbook of chemistry and physics: Internet Version 2005*. Boca Raton FL: CRC Press, 2005. URL: <http://hbcponline.com> (visited on 09/21/2017).

- [Lin66] J. Ling. “An approximate expression for the growth rate of surface contamination on electron microscope specimens”. In: *British Journal of Applied Physics* 17.4 (1966), pp. 565–568. DOI: 10.1088/0508-3443/17/4/419.
- [Liu+11] S. Liu, Z. Xiang, Z. Hu, X. Zheng, and D. Cao. “Zeolitic imidazolate framework-8 as a luminescent material for the sensing of metal ions and small molecules”. In: *Journal of Materials Chemistry* 21.18 (2011), p. 6649. DOI: 10.1039/c1jm10166h.
- [Liu+13] Z. Liu, N. Fujita, K. Miyasaka, L. Han, S. M. Stevens, M. Suga, S. Asahina, B. Slater, C. Xiao, Y. Sakamoto, M. W. Anderson, R. Ryoo, and O. Terasaki. “A review of fine structures of nanoporous materials as evidenced by microscopic methods”. In: *Microscopy (Oxford, England)* 62.1 (2013), pp. 109–146. DOI: 10.1093/jmicro/dfs098.
- [Liu+20] L. Liu, D. Zhang, Y. Zhu, and Y. Han. “Bulk and local structures of metal–organic frameworks unravelled by high-resolution electron microscopy”. In: *Communications Chemistry* 3.1 (2020). DOI: 10.1038/s42004-020-00361-6.
- [Liu+21] X. Liu, S. W. Chee, S. Raj, M. Sawczyk, P. Král, and U. Mirsaidov. “Three-step nucleation of metal-organic framework nanocrystals”. In: *Proceedings of the National Academy of Sciences of the United States of America* 118.10 (2021). DOI: 10.1073/pnas.2008880118.
- [LJ05] Y. Lin and D. C. Joy. “A new examination of secondary electron yield data”. In: *Surface and Interface Analysis* 37.11 (2005), pp. 895–900. DOI: 10.1002/sia.2107.
- [LJ06] W. Li and D. C. Joy. “Study of temperature influence on electron beam induced deposition”. In: *Journal of Vacuum Science & Technology, A: Vacuum, Surfaces, and Films* 24.3 (2006), pp. 431–436. DOI: 10.1116/1.2187995.
- [Lob+08] C. J. Lobo, M. Toth, R. Wagner, B. L. Thiel, and M. Lysaght. “High resolution radially symmetric nanostructures from simultaneous electron beam induced etching and deposition”. In: *Nanotechnology* 19.2 (2008), p. 025303. DOI: 10.1088/0957-4484/19/02/025303.
- [Lov+81] G. Love, v. d. Scott, N. M. T. Dennis, and L. Laurenson. “Sources of contamination in electron optical equipment”. In: *Scanning* 4.1 (1981), pp. 32–39. DOI: 10.1002/sca.4950040105.
- [Mal+05] M. Malac, R. Egerton, M. Freeman, J. Lau, Y. Zhu, and L. Wu. “Electron-beam patterning with sub-2 nm line edge roughness”. In: *Journal of Vacuum Science & Technology, B: Microelectronics and Nanometer Structures – Processing, Measurement, and Phenomena* 23.1 (2005), p. 271. DOI: 10.1116/1.1856466.
- [Mar21] A. Marx. “Quantitative Analyse von Kontamination im Rasterelektronenmikroskop”. Master thesis. Karlsruhe: Karlsruhe Institute of Technology, 2021.
- [McG+12] C. M. McGilvery, A. E. Goode, M. S. P. Shaffer, and D. W. McComb. “Contamination of holey/lacey carbon films in STEM”. In: *Micron (Oxford, England : 1993)* 43.2-3 (2012), pp. 450–455. DOI: 10.1016/j.micron.2011.10.026.
- [MDG08] M. Maazouz, T. Dingle, and R. Gerlach. “In-chamber electron detector”. EP2006881. 2008. URL: <https://data.epo.org/publication-server/document?iDocId=3386559&iFormat=0> (visited on 12/28/2021).
- [Met+14] R. Metzler, J.-H. Jeon, A. G. Cherstvy, and E. Barkai. “Anomalous diffusion models and their properties: non-stationarity, non-ergodicity, and ageing at the centenary of single particle tracking”. In: *Physical chemistry chemical physics : PCCP* 16.44 (2014), pp. 24128–24164. DOI: 10.1039/c4cp03465a.

- [MH17] D. N. Mastronarde and S. R. Held. “Automated tilt series alignment and tomographic reconstruction in IMOD”. In: *Journal of structural biology* 197.2 (2017), pp. 102–113. DOI: 10.1016/j.jsb.2016.07.011.
- [MHG20] E. Müller, M. Hugenschmidt, and D. Gerthsen. “Electron-beam broadening in electron microscopy by solving the electron transport equation”. In: *Physical Review Research* 2.4 (2020), p. 043313. DOI: 10.1103/PhysRevResearch.2.043313.
- [Mik+16] E. Mikmeková, L. Frank, I. Müllerová, B. W. Li, R. S. Ruoff, and M. Lejeune. “Study of multi-layered graphene by ultra-low energy SEM/STEM”. In: *Diamond and Related Materials* 63 (2016), pp. 136–142. DOI: 10.1016/j.diamond.2015.12.012.
- [Mit+05] K. Mitsuishi, Z. Q. Liu, M. Shimojo, M. Han, and K. Furuya. “Dynamic profile calculation of deposition resolution by high-energy electrons in electron-beam-induced deposition”. In: *Ultramicroscopy* 103.1 (2005), pp. 17–22. DOI: 10.1016/j.ultramicro.2004.11.011.
- [Mit15] D. R. G. Mitchell. “Contamination mitigation strategies for scanning transmission electron microscopy”. In: *Micron (Oxford, England : 1993)* 73 (2015), pp. 36–46. DOI: 10.1016/j.micron.2015.03.013.
- [MK00] R. Metzler and J. Klafter. “The random walk’s guide to anomalous diffusion: A fractional dynamics approach”. In: *Physics Reports* 339.1 (2000), pp. 1–77. DOI: 10.1016/S0370-1573(00)00070-3.
- [MM07] V. Morandi and P. G. Merli. “Contrast and resolution versus specimen thickness in low energy scanning transmission electron microscopy”. In: *Journal of Applied Physics* 101.11 (2007), p. 114917. DOI: 10.1063/1.2745333.
- [MM65] N. F. Mott and H. S. W. Massey. *The Theory of atomic collisions*. 3. (The international Series of monographs on physics). Oxford: Clarendon Pr, 1965.
- [Mog+17] P. Z. Moghadam, A. Li, S. B. Wiggin, A. Tao, A. G. P. Maloney, P. A. Wood, S. C. Ward, and D. Fairen-Jimenez. “Development of a Cambridge Structural Database Subset: A Collection of Metal–Organic Frameworks for Past, Present, and Future”. In: *Chemistry of Materials* 29.7 (2017), pp. 2618–2625. DOI: 10.1021/acs.chemmater.7b00441.
- [MS05] D. R. G. Mitchell and B. Schaffer. “Scripting-customized microscopy tools for Digital Micrograph”. In: *Ultramicroscopy* 103.4 (2005), pp. 319–332. DOI: 10.1016/j.ultramicro.2005.02.003.
- [Mül+20] J. Müller, B. Haas, W. van den Broek, S. Shabih, and C. T. Koch. “Features of Our SEM Transmission Diffraction Sub-stage with 6-axis Sample Control and a Camera with Variable Camera Length”. In: *Microscopy and Microanalysis* 26.S2 (2020), pp. 1906–1907. DOI: 10.1017/S1431927620019789.
- [Mül69] K.-H. Müller. “Elektronen-Mikroschreiber mit geschwindigkeitsgesteuerter Strahlführung”. Dissertation. Tübingen: Eberhard-Karls-Universität zu Tübingen, 1969.
- [Mv68] B. B. Mandelbrot and J. W. van Ness. “Fractional Brownian Motions, Fractional Noises and Applications”. In: *SIAM Review* 10.4 (1968), pp. 422–437. DOI: 10.1137/1010093.
- [Nag+87] T. Nagatani, S. Saito, M. Sato, and M. Yamada. “Development of an Ultra High Resolution Scanning Electron Microscope by Means of a Field Emission Source and In-Lens System”. In: *Scanning Microscopy* 1.3 (1987), pp. 901–909. URL: <https://digitalcommons.usu.edu/microscopy/vol1/iss3/3> (visited on 12/28/2021).

- [Neg+05] C. Negreanu, X. Llovet, R. Chawla, and F. Salvat. “Calculation of multiple-scattering angular distributions of electrons and positrons”. In: *Radiation Physics and Chemistry* 74.5 (2005), pp. 264–281. DOI: 10.1016/j.radphyschem.2005.07.006.
- [Oat82] C. W. Oatley. “The early history of the scanning electron microscope”. In: *British Journal of Applied Physics* 53.2 (1982), R1–R13. DOI: 10.1063/1.331666.
- [OGT18] M. Oster, R. Ghadimi, and H. Tietz. “Performance of a Novel Detector for TEM Employing a 4T Pixel Design for On-Chip Correlated Double Sampling and a Selectable Full-Well Capacity”. In: *Microscopy and Microanalysis* 24.S1 (2018), pp. 896–897. DOI: 10.1017/S143192761800497X.
- [OKe92] M. A. O’Keefe. ““Resolution” in high-resolution electron microscopy”. In: *Ultramicroscopy* 47.1-3 (1992), pp. 282–297. DOI: 10.1016/0304-3991(92)90203-V.
- [Ore+03] A. Orekhov, D. Jannis, N. Gauquelin, G. Guzzinati, A. N. Mehta, S. Psilodimitrakopoulos, L. Mouchliadis, P. K. Sahoo, I. Paradisanos, A. C. Ferrari, G. Kioseoglou, E. Stratakis, and J. Verbeeck. *Wide field of view crystal orientation mapping of layered materials*. 2020-11-03. URL: <http://arxiv.org/pdf/2011.01875v1>.
- [Par+06a] K. S. Park, Z. Ni, A. P. Cote, J. Y. Choi, R. Huang, F. J. Uribe-Romo, H. K. Chae, M. O’Keeffe, and O. M. Yaghi. *CCDC 602542: Experimental Crystal Structure Determination*. 2006. DOI: 10.5517/ccn6zvn.
- [Par+06b] K. S. Park, Z. Ni, A. P. Côté, J. Y. Choi, R. Huang, F. J. Uribe-Romo, H. K. Chae, M. O’Keeffe, and O. M. Yaghi. “Exceptional chemical and thermal stability of zeolitic imidazolate frameworks”. In: *Proceedings of the National Academy of Sciences of the United States of America* 103.27 (2006), pp. 10186–10191. DOI: 10.1073/pnas.0602439103.
- [Pin16] P. T. Pinard. “Electron probe microanalysis of carbon containing steels at a high spatial resolution”. Dissertation. Aachen: RWTH Aachen University, 2016. DOI: 10.18154/RWTH-2016-08543.
- [PL11] Y. Pan and Z. Lai. “Sharp separation of C2/C3 hydrocarbon mixtures by zeolitic imidazolate framework-8 (ZIF-8) membranes synthesized in aqueous solutions”. In: *Chemical Communications* 47.37 (2011), pp. 10275–10277. DOI: 10.1039/c1cc14051e.
- [Poo53] K. M. Poole. “Electrode Contamination in Electron Optical Systems”. In: *Proceedings of the Physical Society. Section B* 66.7 (1953), pp. 542–547. DOI: 10.1088/0370-1301/66/7/303.
- [Pos96] M. T. Postek. “An approach to the reduction of hydrocarbon contamination in the scanning electron microscope”. In: *Scanning* 18.4 (1996), pp. 269–274. DOI: 10.1002/sca.1996.4950180402.
- [Ree82] S. Reed. “The single-scattering model and spatial resolution in X-ray analysis of thin foils”. In: *Ultramicroscopy* 7.4 (1982), pp. 405–409. DOI: 10.1016/0304-3991(82)90263-7.
- [Rei98] L. Reimer. *Scanning Electron Microscopy: Physics of Image Formation and Microanalysis*. Second Completely Revised and Updated Edition. Vol. 45. Springer series in optical sciences. Berlin, Heidelberg: Springer Berlin Heidelberg, 1998. DOI: 10.1007/978-3-540-38967-5.
- [Rez83] P. Rez. “A transport equation theory of beam spreading in the electron microscope”. In: *Ultramicroscopy* 12.1-2 (1983), pp. 29–38. DOI: 10.1016/0304-3991(83)90302-9.

- [RFR06] S. J. Randolph, J. D. Fowlkes, and P. D. Rack. “Focused, Nanoscale Electron-Beam-Induced Deposition and Etching”. In: *Critical Reviews in Solid State and Materials Sciences* 31.3 (2006), pp. 55–89. DOI: 10.1080/10408430600930438.
- [RH18] C. J. Russo and R. Henderson. “Charge accumulation in electron cryomicroscopy”. In: *Ultramicroscopy* 187 (2018), pp. 43–49. DOI: 10.1016/j.ultramicro.2018.01.009.
- [Rit05] N. W. M. Ritchie. “A new Monte Carlo application for complex sample geometries”. In: *Surface and Interface Analysis* 37.11 (2005), pp. 1006–1011. DOI: 10.1002/sia.2093.
- [RK08] L. Reimer and H. Kohl. *Transmission electron microscopy: Physics of image formation*. 5th ed. Vol. 36. Springer series in optical sciences. New York NY: Springer, 2008.
- [Roe+09] P. Roediger, H. D. Wanzenboeck, G. Hochleitner, and E. Bertagnolli. “Evaluation of chamber contamination in a scanning electron microscope”. In: *Journal of Vacuum Science & Technology, B: Microelectronics and Nanometer Structures – Processing, Measurement, and Phenomena* 27.6 (2009), p. 2711. DOI: 10.1116/1.3244628.
- [Rös+14] C. Rösler, D. Esken, C. Wiktor, H. Kobayashi, T. Yamamoto, S. Matsumura, H. Kitagawa, and R. A. Fischer. “Encapsulation of Bimetallic Nanoparticles into a Metal-Organic Framework: Preparation and Microstructure Characterization of Pd/Au@ZIF-8”. In: *European Journal of Inorganic Chemistry* 2014.32 (2014), pp. 5514–5521. DOI: 10.1002/ejic.201402409.
- [Ros48] A. Rose. “The Sensitivity Performance of the Human Eye on an Absolute Scale”. In: *Journal of the Optical Society of America* 38.2 (1948), p. 196. DOI: 10.1364/JOSA.38.000196.
- [Ros75] H. Rose. “The influence of plural scattering on the limit of resolution in electron microscopy”. In: *Ultramicroscopy* 1.2 (1975), pp. 167–169. DOI: 10.1016/S0304-3991(75)80022-2.
- [RR87] L. Reimer and M. Ross-Messemer. “Top-bottom effect in energy-selecting transmission electron microscopy”. In: *Ultramicroscopy* 21.4 (1987), pp. 385–387. DOI: 10.1016/0304-3991(87)90037-4.
- [RS66] G. V. T. Ranzetta and V. D. Scott. “Specimen contamination in electron-probe microanalysis and its prevention using a cold trap”. In: *Journal of Scientific Instruments* 43.11 (1966), pp. 816–819. DOI: 10.1088/0950-7671/43/11/307.
- [Rut11] E. Rutherford. “The scattering of α - and β -particles by matter and the structure of the atom”. In: *Philosophical Magazine Series 6* 21.125 (1911), pp. 669–688. DOI: 10.1080/14786440508637080.
- [RW78] L. Reimer and M. Wächter. “Contribution to the contamination problem in transmission electron microscopy”. In: *Ultramicroscopy* 3 (1978), pp. 169–174. DOI: 10.1016/S0304-3991(78)80023-0.
- [RWF07] K. Rykaczewski, W. B. White, and A. G. Fedorov. “Analysis of electron beam induced deposition (EBID) of residual hydrocarbons in electron microscopy”. In: *Journal of Applied Physics* 101.5 (2007), p. 054307. DOI: 10.1063/1.2437065.
- [Ryk+08] K. Rykaczewski, A. Marshall, W. B. White, and A. G. Fedorov. “Dynamic growth of carbon nanopillars and microrings in electron beam induced dissociation of residual hydrocarbons”. In: *Ultramicroscopy* 108.9 (2008), pp. 989–992. DOI: 10.1016/j.ultramicro.2008.04.006.

- [SA18] I. P. Silverwood and J. Armstrong. “Surface diffusion of cyclic hydrocarbons on nickel”. In: *Surface Science* 674 (2018), pp. 13–17. DOI: 10.1016/j.susc.2018.03.012.
- [Sas+14] T. Sasaki, H. Sawada, F. Hosokawa, Y. Sato, and K. Suenaga. “Aberration-corrected STEM/TEM imaging at 15kV”. In: *Ultramicroscopy* 145 (2014), pp. 50–55. DOI: 10.1016/j.ultramicro.2014.04.006.
- [SBS69] J. A. Swift, A. C. Brown, and C. A. Saxton. “Scanning transmission electron microscopy with the Cambridge Stereoscan Mk II”. In: *Journal of Physics E: Scientific Instruments* 2.8 (1969), pp. 744–746. DOI: 10.1088/0022-3735/2/8/441.
- [Sch+05] M. Schowalter, J. T. Titantah, D. Lamoen, and P. Kruse. “Ab initio computation of the mean inner Coulomb potential of amorphous carbon structures”. In: *Applied Physics Letters* 86.11 (2005), p. 112102. DOI: 10.1063/1.1885171.
- [Sch+10] P. Schlossmacher, D. O. Klenov, B. Freitag, and H. S. von Harrach. “Enhanced Detection Sensitivity with a New Windowless XEDS System for AEM Based on Silicon Drift Detector Technology”. In: *Microscopy Today* 18.4 (2010), pp. 14–20. DOI: 10.1017/S1551929510000404.
- [Sch+12] J. Schindelin, I. Arganda-Carreras, E. Frise, V. Kaynig, M. Longair, T. Pietzsch, S. Preibisch, C. Rueden, S. Saalfeld, B. Schmid, J.-Y. Tinevez, D. J. White, V. Hartenstein, K. Eliceiri, P. Tomancak, and A. Cardona. “Fiji: an open-source platform for biological-image analysis”. In: *Nature Methods* 9.7 (2012), pp. 676–682. DOI: 10.1038/nmeth.2019.
- [Sch+20a] P. Schweizer, P. Denninger, C. Dolle, and E. Spiecker. “Low energy nano diffraction (LEND) - A versatile diffraction technique in SEM”. In: *Ultramicroscopy* 213 (2020), p. 112956. DOI: 10.1016/j.ultramicro.2020.112956.
- [Sch+20b] P. Schweizer, C. Dolle, D. Dasler, G. Abellán, F. Hauke, A. Hirsch, and E. Spiecker. “Mechanical cleaning of graphene using in situ electron microscopy”. In: *Nature Communications* 11.1 (2020), p. 1743. DOI: 10.1038/s41467-020-15255-3.
- [Sch93] K. I. Schiffmann. “Investigation of fabrication parameters for the electron-beam-induced deposition of contamination tips used in atomic force microscopy”. In: *Nanotechnology* 4.3 (1993), pp. 163–169. DOI: 10.1088/0957-4484/4/3/006.
- [SE13] O. Shekhah and M. Eddaoudi. “The liquid phase epitaxy method for the construction of oriented ZIF-8 thin films with controlled growth on functionalized surfaces”. In: *Chemical communications (Cambridge, England)* 49.86 (2013), pp. 10079–10081. DOI: 10.1039/C3CC45343J.
- [She+07] O. Shekhah, H. Wang, S. Kowarik, F. Schreiber, M. Paulus, M. Tolan, C. Sternermann, F. Evers, D. Zacher, R. A. Fischer, and C. Wöll. “Step-by-step route for the synthesis of metal-organic frameworks”. In: *Journal of the American Chemical Society* 129.49 (2007), pp. 15118–15119. DOI: 10.1021/ja076210u.
- [She+11] O. Shekhah, J. Liu, R. A. Fischer, and C. Wöll. “MOF thin films: existing and future applications”. In: *Chemical Society reviews* 40.2 (2011), pp. 1081–1106. DOI: 10.1039/C0CS00147C.
- [She+14] O. Shekhah, R. Swaidan, Y. Belmabkhout, M. du Plessis, T. Jacobs, L. J. Barbour, I. Pinnau, and M. Eddaoudi. “The liquid phase epitaxy approach for the successful construction of ultra-thin and defect-free ZIF-8 membranes: pure and mixed gas transport study”. In: *Chemical Communications* 50.17 (2014), pp. 2089–2092. DOI: 10.1039/C3CC47495J.

- [Smi07] D. A. Smith. “Elucidating the Growth Mechanisms of Electron Beam Induced Deposition via a Three Dimensional, Monte-Carlo Based Simulation”. Dissertation. Knoxville: University of Tennessee, 2007. URL: https://trace.tennessee.edu/utk_graddiss/320/ (visited on 11/03/2021).
- [Sou+09] A. A. Sousa, M. F. Hohmann-Marriott, G. Zhang, and R. D. Leapman. “Monte Carlo electron-trajectory simulations in bright-field and dark-field STEM: implications for tomography of thick biological sections”. In: *Ultramicroscopy* 109.3 (2009), pp. 213–221. DOI: 10.1016/j.ultramicro.2008.10.005.
- [SSR12] M. Schaffer, B. Schaffer, and Q. Ramasse. “Sample preparation for atomic-resolution STEM at low voltages by FIB”. In: *Ultramicroscopy* 114 (2012), pp. 62–71. DOI: 10.1016/j.ultramicro.2012.01.005.
- [Sta87] P. A. Stadelmann. “EMS - a software package for electron diffraction analysis and HREM image simulation in materials science”. In: *Ultramicroscopy* 21.2 (1987), pp. 131–145. DOI: 10.1016/0304-3991(87)90080-5.
- [Ste34] R. L. Stewart. “Insulating Films Formed Under Electron and Ion Bombardment”. In: *Physical Review* 45.7 (1934), pp. 488–490. DOI: 10.1103/PhysRev.45.488.
- [Sud+06] Y. Sudaryanto, S. B. Hartono, W. Irawaty, H. Hindarso, and S. Ismadji. “High surface area activated carbon prepared from cassava peel by chemical activation”. In: *Bioresource Technology* 97.5 (2006), pp. 734–739. DOI: 10.1016/j.biortech.2005.04.029.
- [Sun+16] T. Sunaoshi, K. Kaji, Y. Orai, C. T. Schamp, and E. Voelkl. “STEM/SEM, Chemical Analysis, Atomic Resolution and Surface Imaging At ≤ 30 kV with No Aberration Correction for Nanomaterials on Graphene Support”. In: *Microscopy and Microanalysis* 22.S3 (2016), pp. 604–605. DOI: 10.1017/S1431927616003871.
- [Sun+19] C. Sun, E. Müller, M. Meffert, and D. Gerthsen. “Analysis of crystal defects by scanning transmission electron microscopy (STEM) in a modern scanning electron microscope”. In: *Advanced Structural and Chemical Imaging* 5.1 (2019), p. 247. DOI: 10.1186/s40679-019-0065-1.
- [Sun+20] C. Sun, S. Lux, E. Müller, M. Meffert, and D. Gerthsen. “Versatile application of a modern scanning electron microscope for materials characterization”. In: *Journal of Materials Science* 55.28 (2020), pp. 13824–13835. DOI: 10.1007/s10853-020-04970-3.
- [SWH12] C. Soong, P. Woo, and D. Hoyle. “Contamination Cleaning of TEM/SEM Samples with the ZONE Cleaner”. In: *Microscopy Today* 20.6 (2012), pp. 44–48. DOI: 10.1017/S1551929512000752.
- [Tay+92] P. A. Taylor, R. M. Wallace, C. C. Cheng, W. H. Weinberg, M. J. Dresser, W. J. Choyke, and J. T. Yates. “Adsorption and decomposition of acetylene on silicon(100)-(2×1)”. In: *Journal of the American Chemical Society* 114.17 (1992), pp. 6754–6760. DOI: 10.1021/ja00043a020.
- [TBH68] A. R. Taylor, C. A. Baechler, and M. A. Holcomb. “Improved Vacuum System for Electron Microscopes”. In: *Review of Scientific Instruments* 39.5 (1968), pp. 780–781. DOI: 10.1063/1.1683510.
- [Tie+20] E. Tiesinga, P. J. Mohr, D. B. Newell, and B. N. Taylor. *The 2018 CODATA Recommended Values of the Fundamental Physical Constants: Web Version 8.1: Database developed by J. Baker, M. Douma, and S. Kotochigova*. 2020. URL: <http://physics.nist.gov/constants>.

- [Tom+79] T. Tomita, Y. Harada, H. Watanabe, and T. Etoh. “Reduction of Contamination in Analytical Electron Microscopy”. In: *Shinku (1958-2007)* 22.4 (1979), pp. 158–164. DOI: 10.3131/jvsj.22.158.
- [Tot+07] M. Toth, C. J. Lobo, G. Hartigan, and W. R. Knowles. “Electron flux controlled switching between electron beam induced etching and deposition”. In: *Journal of Applied Physics* 101.5 (2007), p. 054309. DOI: 10.1063/1.2437667.
- [Tro+19] J. Troyano, A. Carné-Sánchez, C. Avci, I. Imaz, and D. Maspoch. “Colloidal metal-organic framework particles: the pioneering case of ZIF-8”. In: *Chemical Society reviews* 48.23 (2019), pp. 5534–5546. DOI: 10.1039/c9cs00472f.
- [Ugu+11] O. Ugurlu, J. Haus, A. A. Gunawan, M. G. Thomas, S. Maheshwari, M. Tsapatsis, and K. A. Mkhoyan. “Radiolysis to knock-on damage transition in zeolites under electron beam irradiation”. In: *Physical Review B* 83.11 (2011). DOI: 10.1103/PhysRevB.83.113408.
- [UHM08] I. Utke, P. Hoffmann, and J. Melngailis. “Gas-assisted focused electron beam and ion beam processing and fabrication”. In: *Journal of Vacuum Science & Technology, B: Microelectronics and Nanometer Structures – Processing, Measurement, and Phenomena* 26.4 (2008), p. 1197. DOI: 10.1116/1.2955728.
- [Usu+04] K. Usuda, T. Mizuno, T. Tezuka, N. Sugiyama, Y. Moriyama, S. Nakaharai, and S.-i. Takagi. “Strain relaxation of strained-Si layers on SiGe-on-insulator (SGOI) structures after mesa isolation”. In: *Applied Surface Science* 224.1-4 (2004), pp. 113–116. DOI: 10.1016/j.apsusc.2003.11.058.
- [UY04] K. Ueda and M. Yoshimura. “Fabrication of nanofigures by focused electron beam-induced deposition”. In: *Thin Solid Films* 464-465 (2004), pp. 331–334. DOI: 10.1016/j.tsf.2004.06.078.
- [Val+16] E. P. Valadez Sánchez, H. Gliemann, K. Haas-Santo, C. Wöll, and R. Dittmeyer. “ZIF-8 SURMOF Membranes Synthesized by Au-Assisted Liquid Phase Epitaxy for Application in Gas Separation”. In: *Chemie Ingenieur Technik* 88.11 (2016), pp. 1798–1805. DOI: 10.1002/cite.201600061.
- [Val+20] E. P. Valadez Sánchez, H. Gliemann, K. Haas-Santo, W. Ding, E. Hansjosten, J. Wohlgemuth, C. Wöll, and R. Dittmeyer. “Alpha-Al₂O₃-supported ZIF-8 SURMOF membranes: Diffusion mechanism of ethene/ethane mixtures and gas separation performance”. In: *Journal of Membrane Science* 594 (2020), p. 117421. DOI: 10.1016/j.memsci.2019.117421.
- [van+07] V. van Ngo, M. Hernandez, B. Roth, and D. C. Joy. “STEM Imaging of Lattice Fringes and beyond in a UHR In-Lens Field-Emission SEM”. In: *Microscopy Today* 15.2 (2007), pp. 12–17. DOI: 10.1017/S1551929500050951.
- [VC05] R. Vane and V. Carlino. “Environmental Contamination Sources and Control in High Resolution Scanning Electron Microscopy”. In: *Microscopy and Microanalysis* 11.S02 (2005). DOI: 10.1017/S1431927605501661.
- [Ven83] J. A. Venables. “Nucleation and growth of thin films: recent progress”. In: *Vacuum* 33.10-12 (1983), pp. 701–705. DOI: 10.1016/0042-207X(83)90595-X.
- [vH08] W. F. van Dorp and C. W. Hagen. “A critical literature review of focused electron beam induced deposition”. In: *Journal of Applied Physics* 104.8 (2008), p. 081301. DOI: 10.1063/1.2977587.
- [VJC10] S. R. Venna, J. B. Jasinski, and M. A. Carreon. “Structural evolution of zeolitic imidazolate framework-8”. In: *Journal of the American Chemical Society* 132.51 (2010), pp. 18030–18033. DOI: 10.1021/ja109268m.

- [VKC20] R. Vane, E. Kosmowska, and M. Cable. “Plasma Cleaning with Alternate Gases”. In: *Microscopy and Microanalysis* 26.S2 (2020), pp. 2704–2706. DOI: 10.1017/S1431927620022497.
- [VMG14] T. Volkenandt, E. Müller, and D. Gerthsen. “Sample thickness determination by scanning transmission electron microscopy at low electron energies”. In: *Microscopy and Microanalysis* 20.1 (2014), pp. 111–123. DOI: 10.1017/S1431927613013913.
- [VP05] A. E. Vladár and M. Postek. “Electron Beam-Induced Sample Contamination in the SEM”. In: *Microscopy and Microanalysis* 11.S02 (2005). DOI: 10.1017/S1431927605507785.
- [VPP08] A. E. Vladár, K. P. Purushotham, and M. T. Postek. “Contamination specification for dimensional metrology SEMs”. In: *Metrology, Inspection, and Process Control for Microlithography XXII*. Ed. by J. A. Allgair and C. J. Raymond. SPIE Proceedings. SPIE, 2008, p. 692217. DOI: 10.1117/12.774015.
- [VPV01] A. E. Vladár, J. T. Postek, and R. Vane. “Active monitoring and control of electron-beam-induced contamination”. In: *Metrology, Inspection, and Process Control for Microlithography XV*. Ed. by N. T. Sullivan. SPIE Proceedings. SPIE, 2001, p. 835. DOI: 10.1117/12.436724.
- [Wal80] J. S. Wall. “Contamination in the STEM at Ultra High Vacuum”. In: *Scanning Electron Microscopy* 1 (1980), pp. 99–106.
- [Wan+06] M. Wanner, D. Bach, D. Gerthsen, R. Werner, and B. Tesche. “Electron holography of thin amorphous carbon films: measurement of the mean inner potential and a thickness-independent phase shift”. In: *Ultramicroscopy* 106.4-5 (2006), pp. 341–345. DOI: 10.1016/j.ultramic.2005.10.004.
- [Wan+10] H. D. Wanzenboeck, P. Roediger, G. Hochleitner, E. Bertagnolli, and W. Buehler. “Novel method for cleaning a vacuum chamber from hydrocarbon contamination”. In: *Journal of Vacuum Science & Technology, A: Vacuum, Surfaces, and Films* 28.6 (2010), pp. 1413–1420. DOI: 10.1116/1.3484242.
- [Wat47] J. H. L. Watson. “An Effect of Electron Bombardment upon Carbon Black”. In: *Journal of Applied Physics* 18.2 (1947), pp. 153–161. DOI: 10.1063/1.1697597.
- [WC09] D. B. Williams and C. B. Carter. *Transmission Electron Microscopy: A Textbook for Materials Science*. 2. ed. Boston, MA: Springer US, 2009. DOI: 10.1007/978-0-387-76501-3.
- [WCH91] J. K. Weiss, R. W. Carpenter, and A. A. Higgs. “A study of small electron probe formation in a field emission gun TEM/STEM”. In: *Ultramicroscopy* 36.4 (1991), pp. 319–329. DOI: 10.1016/0304-3991(91)90124-0.
- [Wen80] M. Wendt. “The role of contamination layers in electron probe microanalysis”. In: *Kristall und Technik* 15.12 (1980), pp. 1367–1375. DOI: 10.1002/crat.19800151206.
- [Wet+98] S. M. Wetterer, D. J. Lavrich, T. Cummings, S. L. Bernasek, and G. Scoles. “Energetics and Kinetics of the Physisorption of Hydrocarbons on Au(111)”. In: *The journal of physical chemistry. B* 102.46 (1998), pp. 9266–9275. DOI: 10.1021/jp982338+.
- [Wil+92] D. B. Williams, J. R. Michael, J. I. Goldstein, and A. D. Romig. “Definition of the spatial resolution of X-ray microanalysis in thin foils”. In: *Ultramicroscopy* 47.1-3 (1992), pp. 121–132. DOI: 10.1016/0304-3991(92)90189-Q.
- [Win21] M. Winter. *WebElements*. 1993-2021. URL: <https://www.webelements.com> (visited on 12/28/2021).

- [WM20] M. Weyland and D. A. Muller. *Tuning the convergence angle for optimum STEM performance*. 2020. URL: <http://arxiv.org/pdf/2008.12870v1>.
- [Wu+17] R. J. Wu, A. Mittal, M. L. Odlyzko, and K. A. Mkhoyan. “Simplifying Electron Beam Channeling in Scanning Transmission Electron Microscopy (STEM)”. In: *Microscopy and Microanalysis* 23.4 (2017), pp. 794–808. DOI: 10.1017/S143192761700068X.
- [WW06] M. Watanabe and D. B. Williams. “The quantitative analysis of thin specimens: a review of progress from the Cliff-Lorimer to the new zeta-factor methods”. In: *Journal of Microscopy* 221.Pt 2 (2006), pp. 89–109. DOI: 10.1111/j.1365-2818.2006.01549.x.
- [Yam+16] T. Yamashita, Y. Tanaka, M. Yagoshi, and K. Ishida. “Novel technique to suppress hydrocarbon contamination for high accuracy determination of carbon content in steel by FE-EPMA”. In: *Scientific reports* 6 (2016), p. 29825. DOI: 10.1038/srep29825.
- [Yam+18] S. Yamashita, J. Kikkawa, K. Yanagisawa, T. Nagai, K. Ishizuka, and K. Kimoto. “Atomic number dependence of Z contrast in scanning transmission electron microscopy”. In: *Scientific reports* 8.1 (2018), p. 12325. DOI: 10.1038/s41598-018-30941-5.
- [Yan+18] F. Yang, H. Mu, C. Wang, L. Xiang, K. X. Yao, L. Liu, Y. Yang, Y. Han, Y. Li, and Y. Pan. “Morphological Map of ZIF-8 Crystals with Five Distinctive Shapes: Feature of Filler in Mixed-Matrix Membranes on C₃H₆/C₃H₈ Separation”. In: *Chemistry of Materials* 30.10 (2018), pp. 3467–3473. DOI: 10.1021/acs.chemmater.8b01073.
- [Yan+20] Y. Yang, Z. Guo, W. Huang, S. Zhang, J. Huang, H. Yang, Y. Zhou, W. Xu, and S. Gu. “Fabrication of multifunctional textiles with durable antibacterial property and efficient oil-water separation via in situ growth of zeolitic imidazolate framework-8 (ZIF-8) on cotton fabric”. In: *Applied Surface Science* 503 (2020), p. 144079. DOI: 10.1016/j.apsusc.2019.144079.
- [Ye+21] Z. Ye, Y. Jiang, L. Li, F. Wu, and R. Chen. “Rational Design of MOF-Based Materials for Next-Generation Rechargeable Batteries”. In: *Nano-micro letters* 13.1 (2021), p. 203. DOI: 10.1007/s40820-021-00726-z.
- [YHE83] N. Yoshimura, H. Hirano, and T. Etoh. “Mechanism of contamination build-up induced by fine electron probe irradiation”. In: *Vacuum* 33.7 (1983), pp. 391–395. DOI: 10.1016/0042-207X(83)90658-9.
- [YLL95] O. M. Yaghi, G. Li, and H. Li. “Selective binding and removal of guests in a microporous metal-organic framework”. In: *Nature* 378.6558 (1995), pp. 703–706. DOI: 10.1038/378703a0.
- [Yu+06] S. Yu, B. Eder, R. Dennis, S.-H. Chu, and S. E. Schwartz. “New unbiased symmetric metrics for evaluation of air quality models”. In: *Atmospheric Science Letters* 7.1 (2006), pp. 26–34. DOI: 10.1002/asl.125.
- [Zha+14] K. Zhang, A. Nalaparaju, Y. Chen, and J. Jiang. “Biofuel purification in zeolitic imidazolate frameworks: the significant role of functional groups”. In: *Physical chemistry chemical physics : PCCP* 16.20 (2014), pp. 9643–9655. DOI: 10.1039/C4CP00739E.
- [Zha+15] J. Zhao, B. Gong, W. T. Nunn, P. C. Lemaire, E. C. Stevens, F. I. Sidi, P. S. Williams, C. J. Oldham, H. J. Walls, S. D. Shepherd, M. A. Browe, G. W. Peterson, M. D. Losego, and G. N. Parsons. “Conformal and highly adsorptive metal-organic framework thin films via layer-by-layer growth on ALD-coated fiber mats”. In: *Journal of Materials Chemistry A* 3.4 (2015), pp. 1458–1464. DOI: 10.1039/C4TA05501B.

- [Zha+18] D. Zhang, Y. Zhu, L. Liu, X. Ying, C.-E. Hsiung, R. Sougrat, K. Li, and Y. Han. “Atomic-resolution transmission electron microscopy of electron beam-sensitive crystalline materials”. In: *Science (New York, N.Y.)* 359.6376 (2018), pp. 675–679. DOI: 10.1126/science.aao0865.
- [Zha19] P. Zhang. “Study on EEBS for Linewidth Imaging by a Monte Carlo Method”. In: *Results in Physics* (2019), p. 102712. DOI: 10.1016/j.rinp.2019.102712.
- [Zho+19] L. Zhou, N. Li, G. Owens, and Z. Chen. “Simultaneous removal of mixed contaminants, copper and norfloxacin, from aqueous solution by ZIF-8”. In: *Chemical Engineering Journal* 362 (2019), pp. 628–637. DOI: 10.1016/j.cej.2019.01.068.
- [ZHS42] V. K. Zworykin, J. Hiller, and R. L. Snyder. “A scanning electron microscope”. In: *ASTM Bulletin* 117 (1942), pp. 15–23.
- [Zhu+17] Y. Zhu, J. Ciston, B. Zheng, X. Miao, C. Czarnik, Y. Pan, R. Sougrat, Z. Lai, C.-E. Hsiung, K. Yao, I. Pinnau, M. Pan, and Y. Han. “Unravelling surface and interfacial structures of a metal-organic framework by transmission electron microscopy”. In: *Nature materials* 16.5 (2017), pp. 532–536. DOI: 10.1038/nmat4852.
- [ZKH97] N. J. Zaluzec, B. J. Kestel, and D. Henriks. “Reactive Gas Plasma Specimen Processing for Use in Microanalysis and Imaging in Analytical Electron Microscopy”. In: *Microscopy and Microanalysis* 3.S2 (1997), pp. 983–984. DOI: 10.1017/S1431927600011806.
- [ZZ18] G. Zhan and H. C. Zeng. “Hydrogen spillover through Matryoshka-type (ZIFs@)_{n-1}ZIFs nanocubes”. In: *Nature Communications* 9.1 (2018), p. 3778. DOI: 10.1038/s41467-018-06269-z.

Publications and Conference Contributions

Reviewed Publications

- Olivia Wenzel, Viktor Rein, **Milena Hugenschmidt**, Frank Schilling, Claus Feldmann, and Dagmar Gerthsen: “Impact of synthesis conditions on the morphology and crystal structure of tungsten nitride nanomaterials”. *RSC Advances* 11.45, pp. 28198 – 28210 (2021). DOI: 10.1039/D1RA04448F
- Erich Müller, **Milena Hugenschmidt**, and Dagmar Gerthsen: “Electron-beam broadening in electron microscopy by solving the electron transport equation”. *Physical Review Research* 2.4, p. 043313 (2020). DOI: 10.1103/PhysRevResearch.2.043313
- **Milena Hugenschmidt**, Ksenia Kutonova, Elvia P. Valadez Sánchez, Sarah Moulai, Hartmut Gliemann, Stefan Bräse, Christof Wöll, and Dagmar Gerthsen: “Direct Synthesis of ZIF-8 on Transmission Electron Microscopy Grids Allows Structure Analysis and 3D Reconstruction”. *Particle & Particle Systems Characterization* 37.11, p. 2000209 (2020). DOI: 10.1002/ppsc.202000209
- **Milena Hugenschmidt**, Erich Müller, and Dagmar Gerthsen: “Electron beam broadening in electron-transparent samples at low electron energies”. *Journal of Microscopy* 274.3, pp. 150 – 157 (2019). DOI: 10.1111/jmi.12793
- Martin Čalkovský, Erich Müller, **Milena Hugenschmidt**, and Dagmar Gerthsen: “Differential electron scattering cross-sections at low electron energies: The influence of screening parameter”. *Ultramicroscopy* 207, p. 112843 (2019). DOI: 10.1016/j.ultramicro.2019.112843

Contributions to Conferences

- 08/2021 **Oral Presentation.** Aaron Marx, Milena Hugenschmidt, Katharina Adrion, Erich Müller, Dagmar Gerthsen: *Determination of Key Parameters for Carbon Contamination – Quantitative Measurement of Contamination Thickness and Comparison with Theory*, Microscopy Conference 2021 (virtual).
- 08/2021 **Poster Presentation.** Milena Hugenschmidt, Ksenia Kutonova, Elvia P. Valadez Sánchez, Sarah Moulai, Hartmut Gliemann, Stefan Bräse, Christof Wöll, Dagmar Gerthsen: *Direct Synthesis of ZIF-8 on Transmission Electron Microscopy Grids Allows Insights into the Growth Process*. Microscopy Conference 2021 (virtual). DOI: 10.5445/IR/1000136027.
- 08/2021 **Invited Presentation.** Milena Hugenschmidt, Katharina Adrion, Aaron Marx, Erich Müller, Dagmar Gerthsen: *Quantification and Mitigation of Electron-Beam-Induced Carbon Contamination*. Microscopy & Microanalysis Virtual Meeting. DOI: 10.1017/S1431927621007352. M&M Student Scholar Award.
- 08/2021 **Oral Presentation.** Milena Hugenschmidt, Ksenia Kutonova, Elvia P. Valadez Sánchez, Sarah Moulai, Hartmut Gliemann, Stefan Bräse, Christof Wöll, Dagmar Gerthsen: *Direct Synthesis of ZIF-8 on Transmission Electron Microscopy Grids Allows Structure Analysis and 3D Reconstruction*. Microscopy & Microanalysis Virtual Meeting. DOI: 10.1017/S1431927621010771.
- 07/2021 **Invited Presentation.** Milena Hugenschmidt, Katharina Adrion, Aaron Marx, Erich Müller, Dagmar Gerthsen: *Mitigation of Electron-Beam-Induced Carbon Contamination*. Annual Pre-Meeting Congress for Students, Post-Docs, and Early-Career Professionals in Microscopy and Microanalysis (virtual).
- 11/2020 **Oral Presentation.** Milena Hugenschmidt, Aaron Marx, Katharina Adrion, Erich Müller, Dagmar Gerthsen: *Quantification and Mitigation of Electron-Beam-Induced Carbon Contamination*. Virtual Early Career European Microscopy Congress.
- 09/2019 **Poster Presentation.** Milena Hugenschmidt, Erich Müller, and Dagmar Gerthsen: *Beam Broadening Measured in Transmission Mode at Low Electron Energies in a Scanning Electron Microscope*. Microscopy Conference MC2019, Berlin.

- 06/2019 **Oral Presentation.** Milena Hugenschmidt, Erich Müller, and Dagmar Gerthsen: *Electron Beam Broadening in TEM Samples at Low Electron Energies*. Germany-Japan Joint Seminar on Advanced Electron Microscopy and Its Application, Nagoya.
- 09/2018 **Digital Poster Presentation.** Milena Hugenschmidt, Erich Müller, and Dagmar Gerthsen: *Electron Beam Broadening in Thin Samples in a Scanning Electron Microscope*. 19th International Microscopy Congress, Sydney.

Instrumentation List

Electron Microscopes

Thermo Scientific Helios G4 FX NanoLab	FIB and SEM/STEM combined system with FEG and Ga source, up to 30 keV. Detectors: ETD, STEM 4 BF-HAADF, ICE, TLD, mirror detector. EDXS detector: Bruker X-Flash 6 60 silicon-drift detector.
FEI Strata 400S	FIB and SEM/STEM combined system with FEG and Ga source, up to 30 keV. Detectors: ETD, STEM 3 BF-HAADF, TLD. EDXS detector: Bruker X-Flash 5010 silicon-drift detector. FEI Company, today Thermo Fisher Scientific.
FEI Titan³ 80-300	(Scanning) transmission electron microscope FEI Titan ³ 80-300. FEG, 80 – 300 keV. Monochromator, spherical aberration (C_s) corrector for the imaging-lens system CETCOR (CEOS GmbH), TVIPS TemCam-XF416(R) CMOS camera (Tietz Video and Image Processing Systems GmbH), post-column spectrometer GIF Tridiem 865 ER (Gatan), HAADF-STEM detector Fischione Model 3000 ADF. Single-tilt tomography holder (E.A. Fischione Instruments Inc.).
FEI Tecnai Osiris	(Scanning) transmission electron microscope, X-FEG, 80 – 200 keV. Analytical-TWIN lens ($C_s = 1.2$ mm). Super-X EDXS detection system with four windowless silicon-drift detectors (Bruker Corporation). HAADF-STEM detector Fischione Model 3000 ADF. On-axis FEI BF/DF STEM detectors.
Philips CM200 FEG S/T	Transmission electron microscope CM200 FEG with a Super-TWIN lens ($C_s = 1.2$ mm). FEG, 200 keV (Philips, today Thermo Fisher Scientific). TVIPS TemCam-F416 CMOS camera (TVIPS).

Others

High-vacuum coater	Leica EM ACE600 for carbon-thread coating and Pt sputtering (Leica Microsystems)
Vacuum heating recipient	Binder drying station TS 716 (Klaus Binder Labortechnik)
External plasma cleaner	Binder plasma cleaner TPS 316, 25 W
In-chamber plasma cleaner	FEI plasma cleaning unit, 19 W

Appendix

A. Cross-Section for Scattering through Angles Larger than θ^*

The cross section for scattering through angles larger than θ^* is needed for the deviation of the Goldstein equation (4.6).

It is deviated from the differential unscreened elastic Rutherford cross section $\frac{d\sigma}{d\Omega}$ (2.2). For this calculation, it can be reduced by introducing a constant $c = \frac{e^4 Z^2}{4(4\pi\epsilon_0)^2 m^2 v^4}$ and reads then as

$$\frac{d\sigma}{d\Omega} = c \cdot \frac{1}{\sin^4(\theta/2)} \quad (\text{A.1})$$

It describes the probability of scattering through θ into a solid angle $d\Omega = 2\pi \sin(\theta)d\theta$. This gives

$$\frac{d\sigma}{d\theta} = c \cdot \frac{2\pi \sin(\theta)}{\sin^4(\theta/2)} \quad (\text{A.2})$$

Integration over θ with $\theta^* < \theta < \pi$ gives the total cross section for scattering through angles $> \theta^*$:

$$\sigma(\theta^*) = c \int_{\theta^*}^{\pi} \frac{2\pi \sin(\theta)}{\sin^4(\theta/2)} d\theta \quad (\text{A.3})$$

and by substituting $u = \sin(\theta/2) \Rightarrow \frac{du}{d\theta} = \frac{1}{2} \cos(\theta/2) \Leftrightarrow d\theta = du \cdot \frac{2}{\cos(\theta/2)}$:

$$\sigma(\theta^*) = c \int_{\sin(\theta^*/2)}^1 \frac{4\pi u}{u^4} \cos(\theta/2) \frac{2}{\cos(\theta/2)} du \quad (\text{A.4})$$

$$= c \int_{\sin(\theta^*/2)}^1 \frac{8\pi}{u^3} du \quad (\text{A.5})$$

$$= c \cdot 8\pi \left(\frac{1}{2} \sin^{-2}(\theta^*/2) - \frac{1}{2} \right) \quad (\text{A.6})$$

$$= 4\pi c \cot^2(\theta^*/2) \quad (\text{A.7})$$

$$\Leftrightarrow \sigma(\theta^*) = \frac{\pi e^4 Z^2}{(4\pi\epsilon_0)^2 m^2 v^4} \cot^2\left(\frac{\theta^*}{2}\right). \quad (\text{A.8})$$

This is the cross section for scattering through angles larger than θ^* , where $\cot(\alpha) = \cos(\alpha)/\sin(\alpha)$ and $\cos^2(\alpha) + \sin^2(\alpha) = 1$ was used.

B. Detector Correction in Monte Carlo Simulations

The simulation of the signal detected by the STEM detector by Monte Carlo (MC) methods, using a modified version of NISTMONTE1.2 [Rit05], was described in Section 5.3.5 on page 93. Before the STEM detector registers the electrons, they have to propagate through a protective layer on the detector's surface, where they lose some additional energy. For high electron energies, this is of little consequence. However, the lost energy can be a more significant part of the electron energy E for low energies. The cutoff energy E_{cut} is the energy below which the detector efficiency drops. The decrease of the detection efficiency below E_{cut} is assumed as linear. This detection efficiency below E_{cut} leads to an expression of the detected energy for $E < E_{\text{cut}}$:

$$E_{\text{det}} = \int_0^E \frac{E}{E_{\text{cut}}} dE = \frac{E^2}{2E_{\text{cut}}}. \quad (\text{B.1})$$

Above E_{cut} , the energy loss is assumed to be constant. Thus two cases for the detected energy are:

$$E_{\text{det}} = \begin{cases} \frac{E^2}{2E_{\text{cut}}} & \text{for } E < E_{\text{cut}} \\ E - \frac{1}{2}E_{\text{cut}} & \text{for } E \geq E_{\text{cut}}. \end{cases} \quad (\text{B.2})$$

With this, our modified version of NISTMonte1.2 calculates the normalized simulated intensity I_{rel} as the ratio of the simulated primary intensity I_0 and the detected intensity I :

$$I_{\text{rel,sim}} = \frac{I}{I_0} \quad (\text{B.3})$$

$$= \frac{\sum_i E_{\text{det},i}}{n_0(E_0 - E_{\text{cut}}/2)}, \quad (\text{B.4})$$

with the number n_0 of simulated electrons and the detected energy $E_{\text{det},i}$ of each electron according to Equation (B.2). $I_{\text{rel,sim}}$ is comparable with experimental relative intensities I_{rel} (see Section 3.2.2 for definition).

Acknowledgements

First of all, I would like to express my sincere gratitude to my supervisor Prof. Dagmar Gerthsen for her continuous support and guidance, the possibility to attend a number of conferences, and for allowing me to spend some enriching years at KIT-LEM and on this research. I wish her a happy retirement and lots of time for her travels.

I would like to thank Prof. Hans-Joachim Kleebe from TU Darmstadt for taking over the co-lecture and for the encouragement and valuable comments from another perspective.

Thank you to Dr. Erich Müller for the constant support and instructive exchange in my years at LEM. He was a wonderful mentor and colleague, and I will miss working with him.

Dr. Cheng Sun and Martin Čalkovský were my office neighbors during the PhD time and I would like to thank them very much for the scientific and non-scientific discussions and the nice time we had.

I also owe lots of thanks to Katharina Adrion and Aaron Marx, who were fantastic students to work with and who patiently endured my first attempts at supervision.

Many thanks to my cooperation partners in the cluster of excellence 3DMM2O. First and foremost to Dr. Ksenia Kutonova, as our extensive discussions contributed significantly to the successful cooperation and as she provided helpful guidance for my PhD time.

I would like to thank all the LEM employees for their friendliness, helpfulness, and the creative, enjoyable cooperation.

Finally, a big thank you to my family and friends who stood by me the whole time.